Appendices

Appendix 1

Supplementary materials to complement the data presented in Chapter 3

Appendix 2

Supplementary materials to complement the data presented in Chapter 5

Appendix 3

Published version of Chapter 2:

Bullock, R.J., De Paola, N., Holdsworth, R.E., Trabucho-Alexandre, J., 2014. Lithological controls on the deformation mechanisms operating within carbonate-hosted faults during the seismic cycle. Journal of Structural Geology 58, 22-42.

Appendix 4

Published version of Chapter 3:

Bullock, R.J., De Paola, N., Holdsworth, R.E., 2015. An experimental investigation into the role of phyllosilicate content on earthquake propagation during seismic slip in carbonate faults. Journal of Geophysical Research: Solid Earth 120, 3187-3207.

Appendix 5

Paper on which I am a co-author:

De Paola, N., Holdsworth, R.E., Viti, C., Collettini, C., Bullock, R.J. Can grain size sensitive creep lubricate faults during earthquake propagation? In review, EPSL.

Appendix 1

Supplementary materials to complement the data presented in Chapter 3

Appendix 1.1: Additional field observations (pp. 2-3)

Appendix 1.2: Details and results of experiments terminated at peak friction (pp. 4-6)

Appendix 1.3: Determination of initial friction (pp. 7-13)

Appendix 1.4: Additional initial microstructures (p.14)

Appendix 1.5: Additional peak friction microstructures (pp. 15-18)

Appendix 1.6: Additional steady-state microstructures (pp. 19-23)

Appendix 1.1

Additional field observations

Additional examples from the Gubbio fault zone (Northern Apennines of Italy) of pressure-solution concentrating phyllosilicates within principal slip zones.

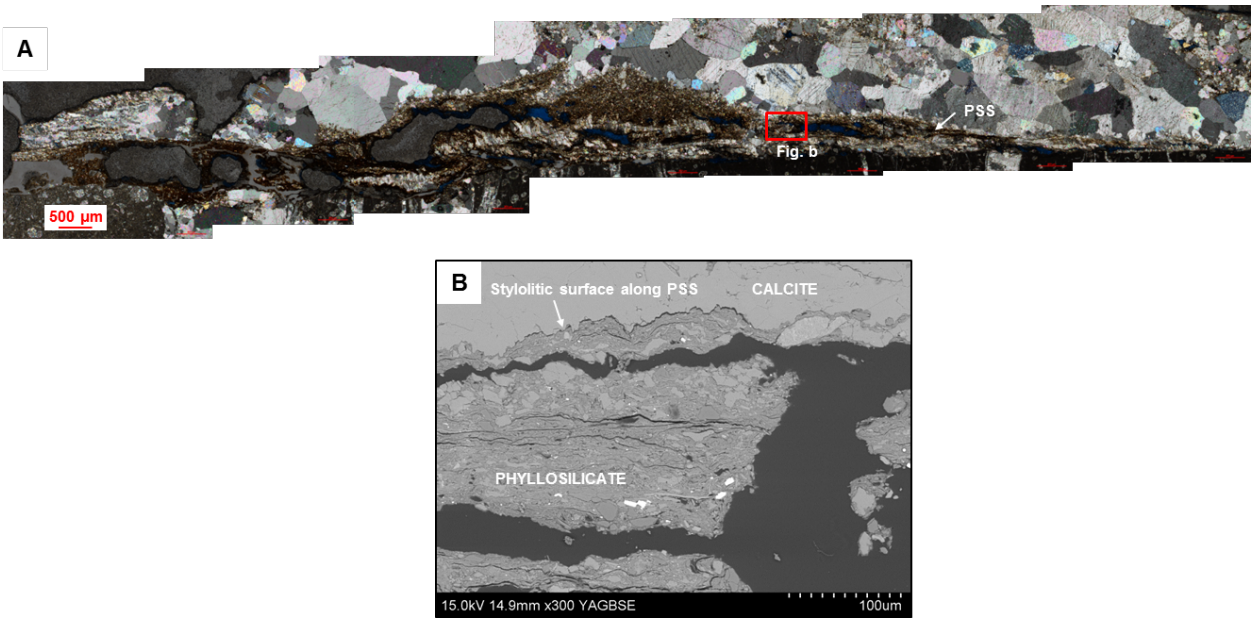

Fig. A1.1 a) Optical microscope image of a principal slip surface in marly limestone. **b)** SEM image of PSS in fig. **a**, showing stylolitic surface and an enrichment of phyllosilicate along the surface.

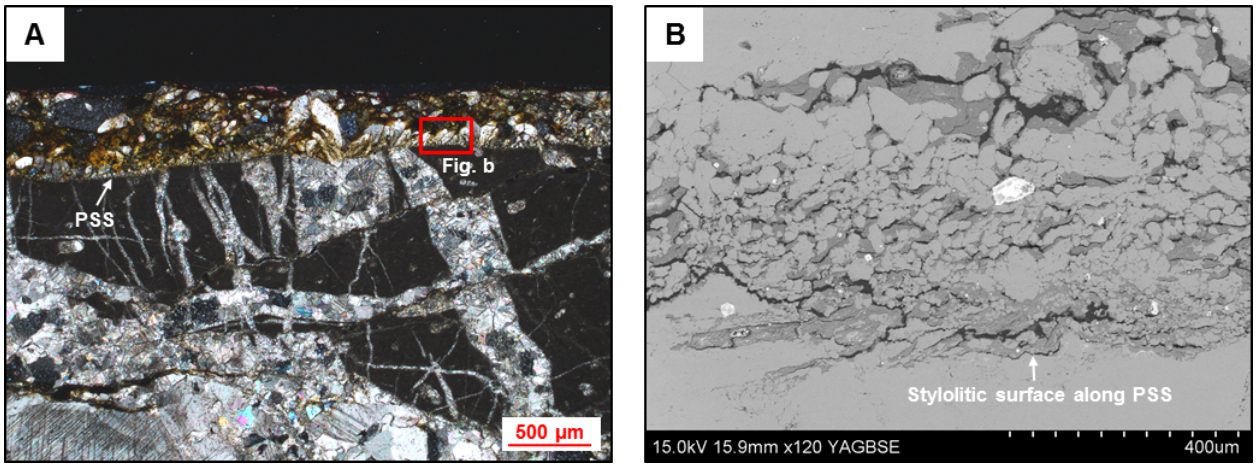

Fig. A1.2 a) Optical microscope image of a principal slip surface in micritic limestone. **b)** SEM image of PSS in fig. **a**, showing stylolitic surface and an enrichment of phyllosilicate along the surface and into the adjacent (overlying) slip zone.

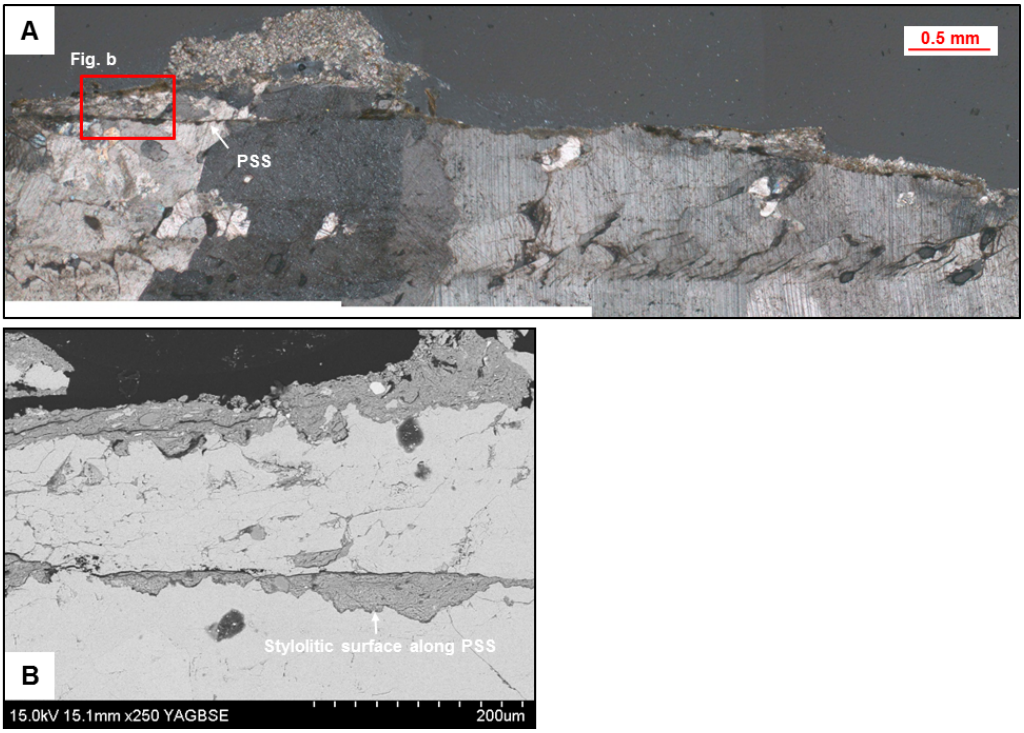

Fig. A1.3 a) Optical microscope image of a principal slip surface in marly limestone. **b)** SEM image of PSS in fig. **a**, showing stylolitic surface and enrichment of phyllosilicate along the surface.

Appendix 1.2

Details and results of experiments terminated at peak friction

Table A1.1 shows the details of experiments performed under the same conditions as those presented in the paper, but terminated close to peak friction, or in the early stages of weakening. The experimental results for the dry gouges are shown in Fig. A1.4 and for the wet gouges are shown in Fig. A1.5. The results we obtained are very similar to the experiments that were run until steady-state, demonstrating good reproducibility of results. Fewer of the wet experiments were repeated due to the fact that they typically do not exhibit a 'peak' in friction and so all microstructures produced are representative of steady-state.

Dry gouges

Calcite+illite-smectite

Exp. #	wt.% calcite	wt.% clay	μ_i	μ_p	Total displacement (m)
403	100	0	0.45	0.71	0.12
456	80	20	0.48	0.71	0.12
453	50	50	0.52	0.74	0.14
406	0	100	0.55	0.62	0.16

Calcite+montmorillonite

Exp. #	wt.% calcite	wt.% clay	μ_i	μ_p	Total displacement (m)
403	100	0	0.45	0.71	0.12
425	80	20	0.53	0.72	0.31
421	50	50	0.52	0.71	0.05
404	0	100	0.49	0.61	0.08

Wet gouges

Calcite+illite-smectite

Exp. #	wt.% calcite	wt.% clay	μ_i	μ_p	Total displacement (m)
415	100	0	0.6	0.7	0.03
458	80	20	0.41	0.46	0.12
459	50	50	0.29	0.35	0.12

Table A1.1: Summary of experiments terminated at peak friction and frictional parameters obtained.

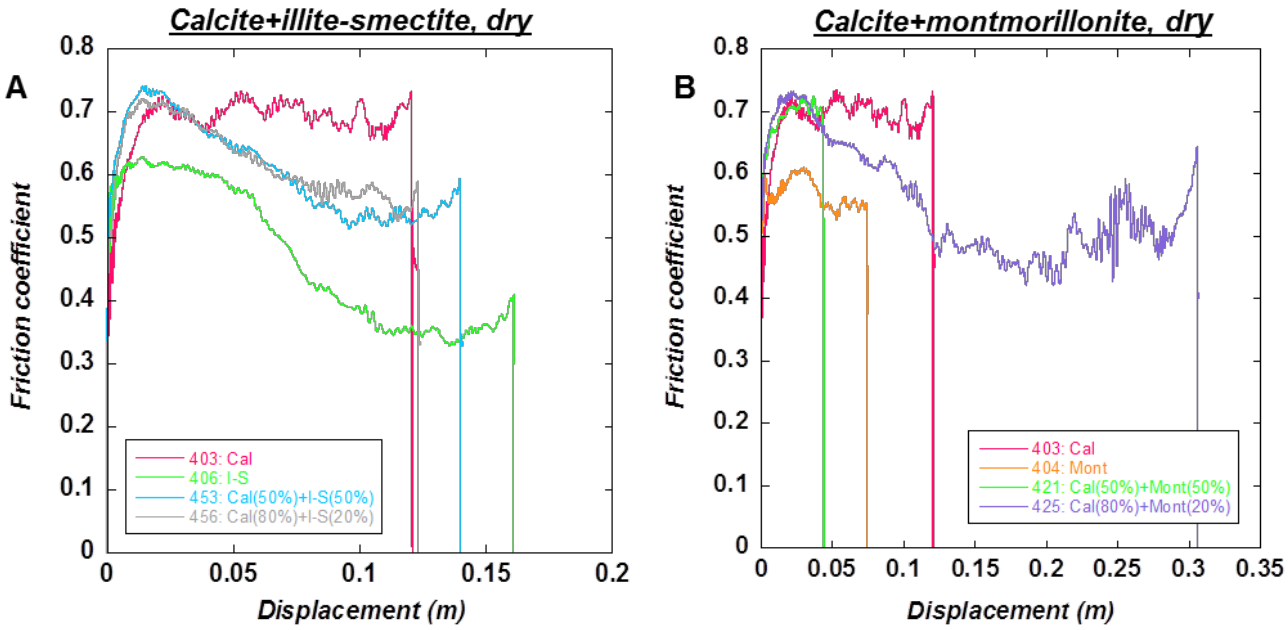

Fig. A1.4 Experimental results for dry gouges terminated at peak friction. **a)** Calcite and illite-smectite end-members and mixtures. **b)** Calcite and montmorillonite end-members and mixtures.

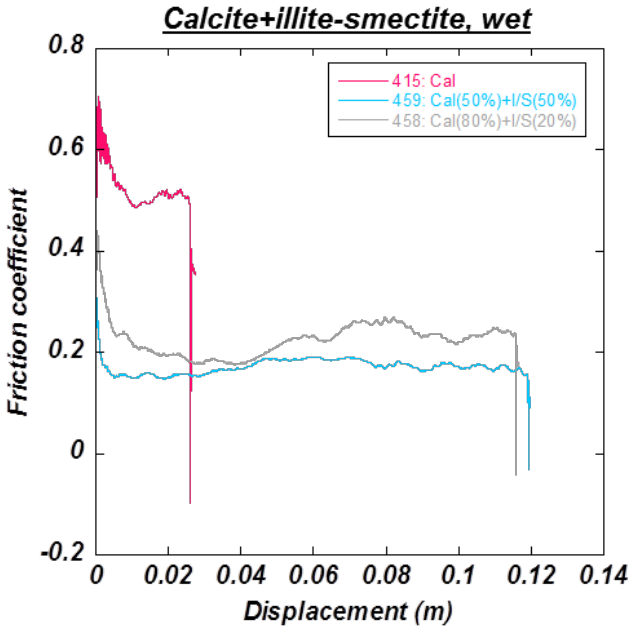

Fig. A1.5 Experimental results for wet gouges terminated at 'peak' friction.

Appendix 1.3

Determination of initial friction

Most high-velocity friction studies focus on the values of peak friction, steady-state friction and the slip-weakening distance as being the most important friction parameters. However, we draw attention also to the value of initial friction, which we also observe to be highly variable depending on gouge composition and deformation conditions. We define the initial friction as being equivalent to the yield strength of the gouge, i.e. the point at which gouge deformation ceases to be linear-elastic. On the following plots, we indicate this phase of linear-elastic deformation, which commences upon acceleration of the motor. A plot is included for all of the experiments discussed in the main manuscript. The linear increase in friction to μ_i is followed by either a slip-hardening phase, in the case of dry gouges (Figs. A1.6 to A1.8), or a slip-weakening phase, in the case of wet gouges (Figs. A1.9 to A1.11).

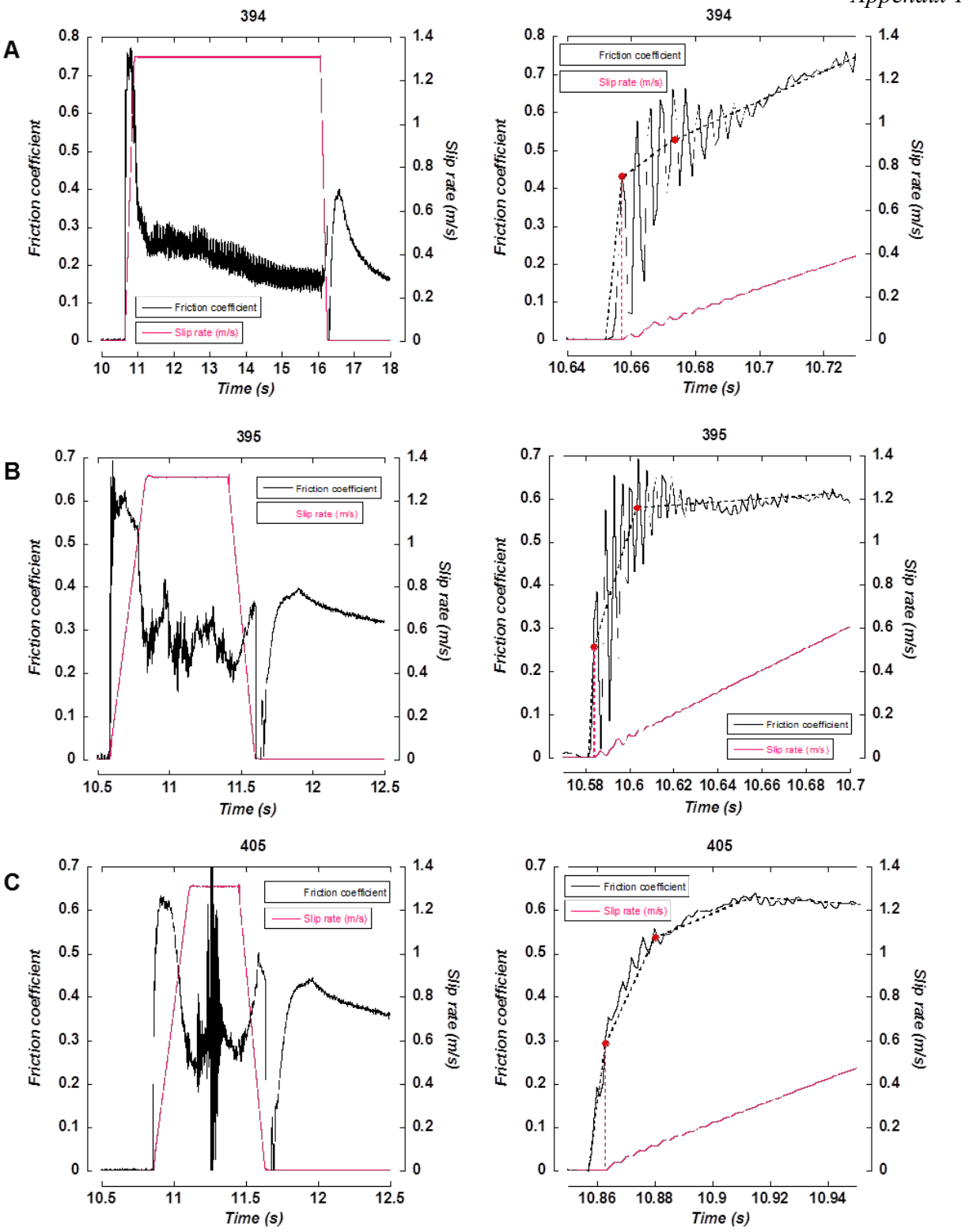

Fig. A1.6 Plots of slip rate and friction coefficient against time for dry end-member gouges. **a)** Experiment 394 = calcite. **b)** Experiment 395 = montmorillonite. **c)** Experiment 405 = illite-smectite. Plots on the right show a magnification of the early stage of the experiment. The first red dot marks the point at which the motor starts to accelerate, which is followed by a linear evolution of friction towards the initial friction value, μ_i, which is marked by the second red dot. After this point, friction evolution deviates from a linear behaviour.

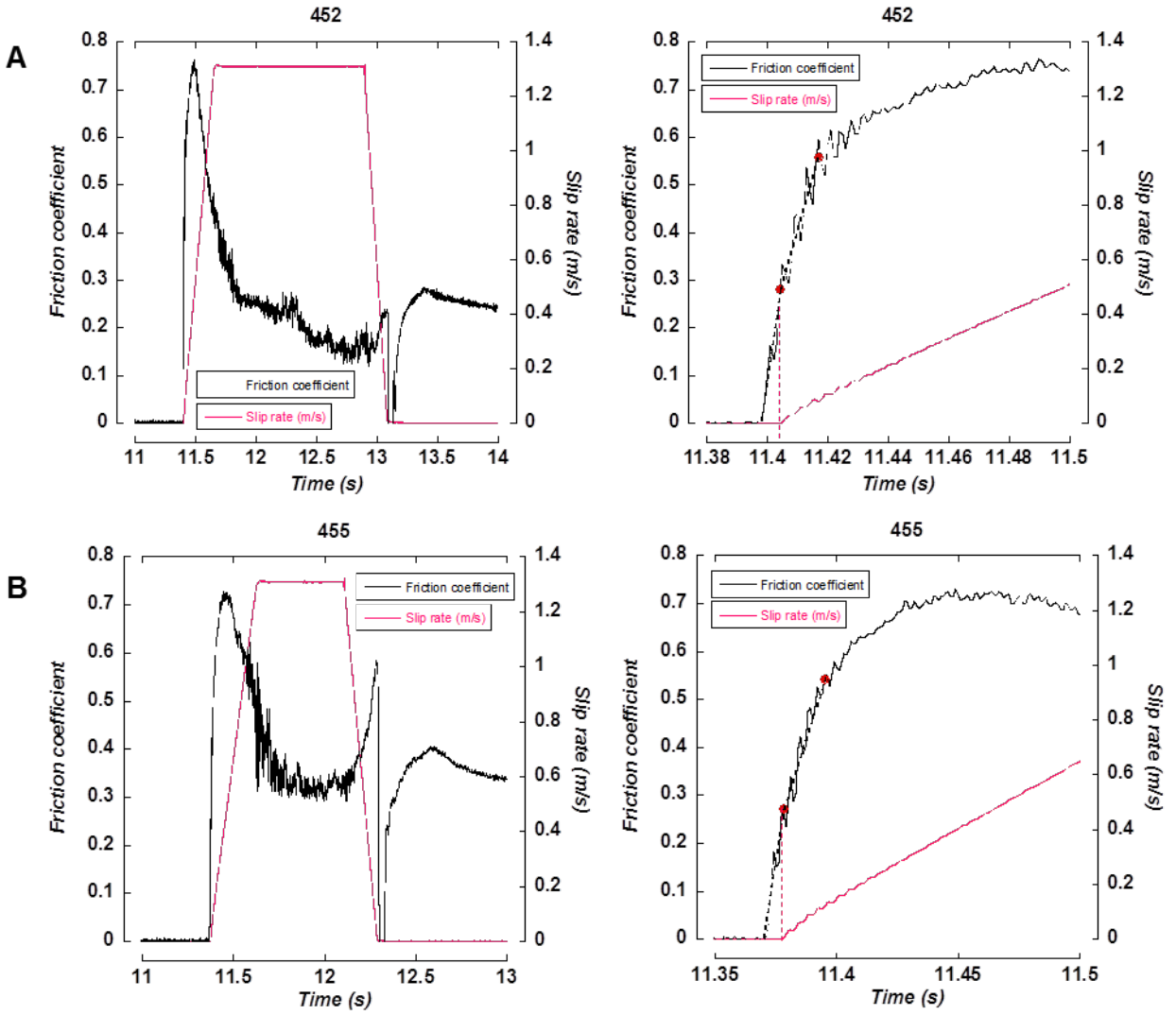

Fig. A1.7 Plots of slip rate and friction coefficient against time for dry calcite + illite-smectite mixtures. **a)** Experiment 452 = 50% calcite + 50% illite-smectite. **b)** Experiment 455 = 80% calcite + 20 % illite-smectite. Plots on the right show a magnification of the early stage of the experiment The first red dot marks the point at which the motor starts to accelerate, which is followed by a linear evolution of friction towards the initial friction value, μ_i, which is marked by the second red dot. After this point, friction evolution deviates from a linear behaviour.

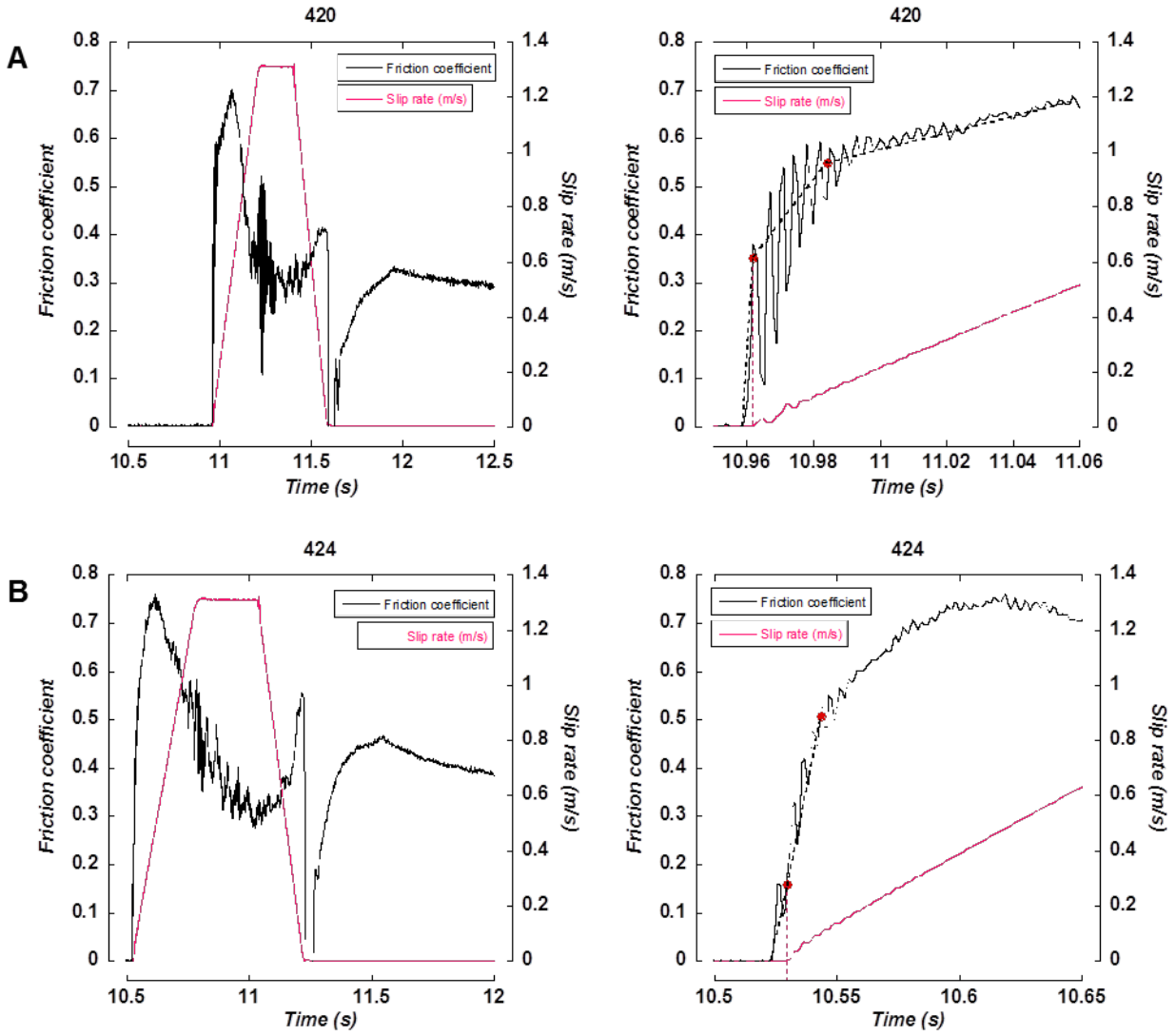

Fig. A1.8 Plots of slip rate and friction coefficient against time for dry calcite + montmorillonite mixtures. **a)** Experiment 420 = 50% calcite + 50% montmorillonite. **b)** Experiment 424 = 80% calcite + 20 % montmorillonite. Plots on the right show a magnification of the early stage of the experiment. The first red dot marks the point at which the motor starts to accelerate, which is followed by a linear evolution of friction towards the initial friction value, μ_i, which is marked by the second red dot. After this point, friction evolution deviates from a linear behaviour.

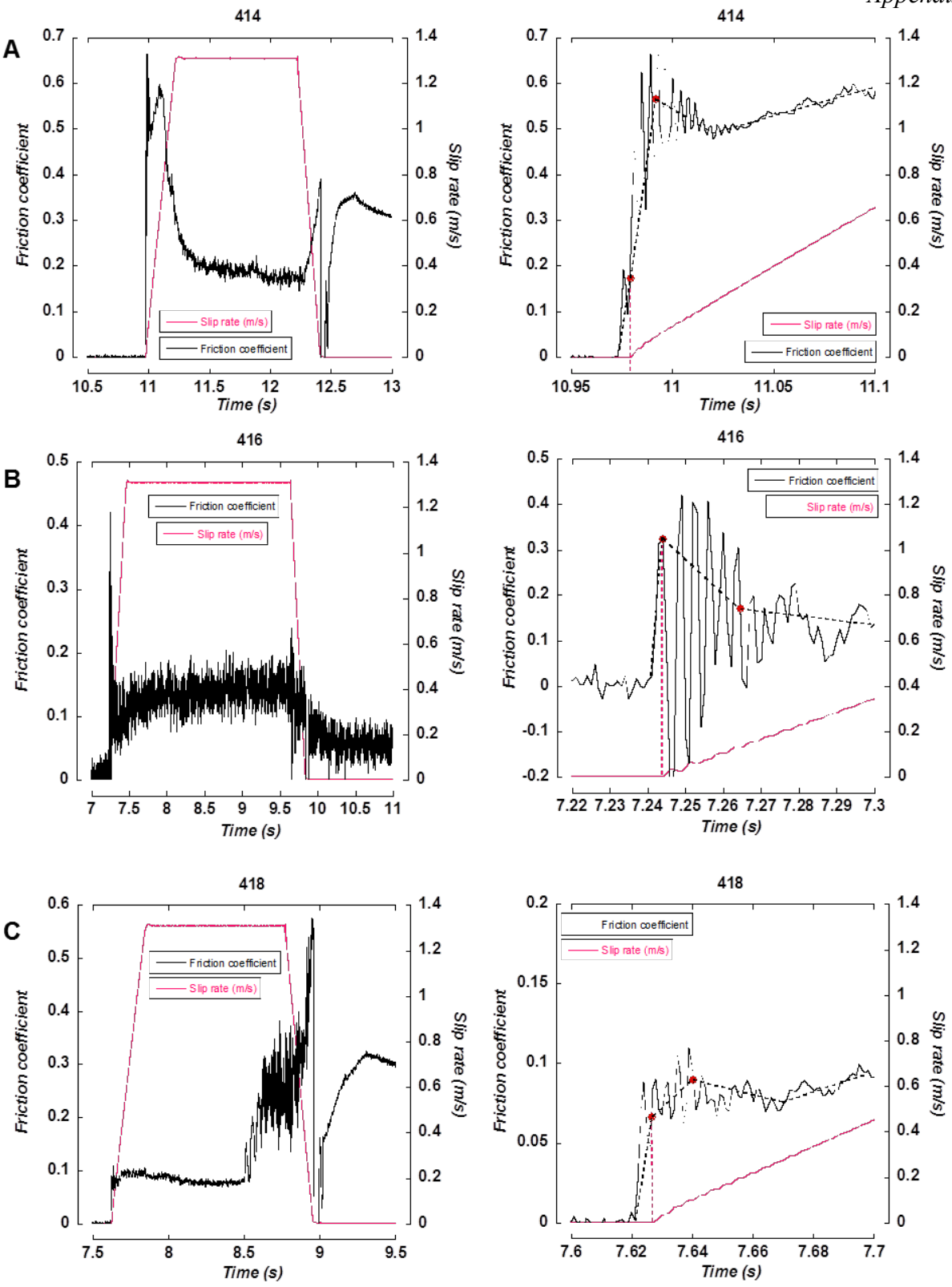

Fig. A1.9 Plots of slip rate and friction coefficient against time for wet end-member gouges. **a)** Experiment 414 = calcite. **b)** Experiment 416 = montmorillonite. **c)** Experiment 418 = illite-smectite. Plots on the right show a magnification of the early stage of the experiment. The first red dot marks the point at which the motor starts to accelerate, which is followed by a linear evolution of friction towards the initial friction value, μ_i, which is marked by the second red dot. After this point, friction evolution deviates from a linear behaviour.

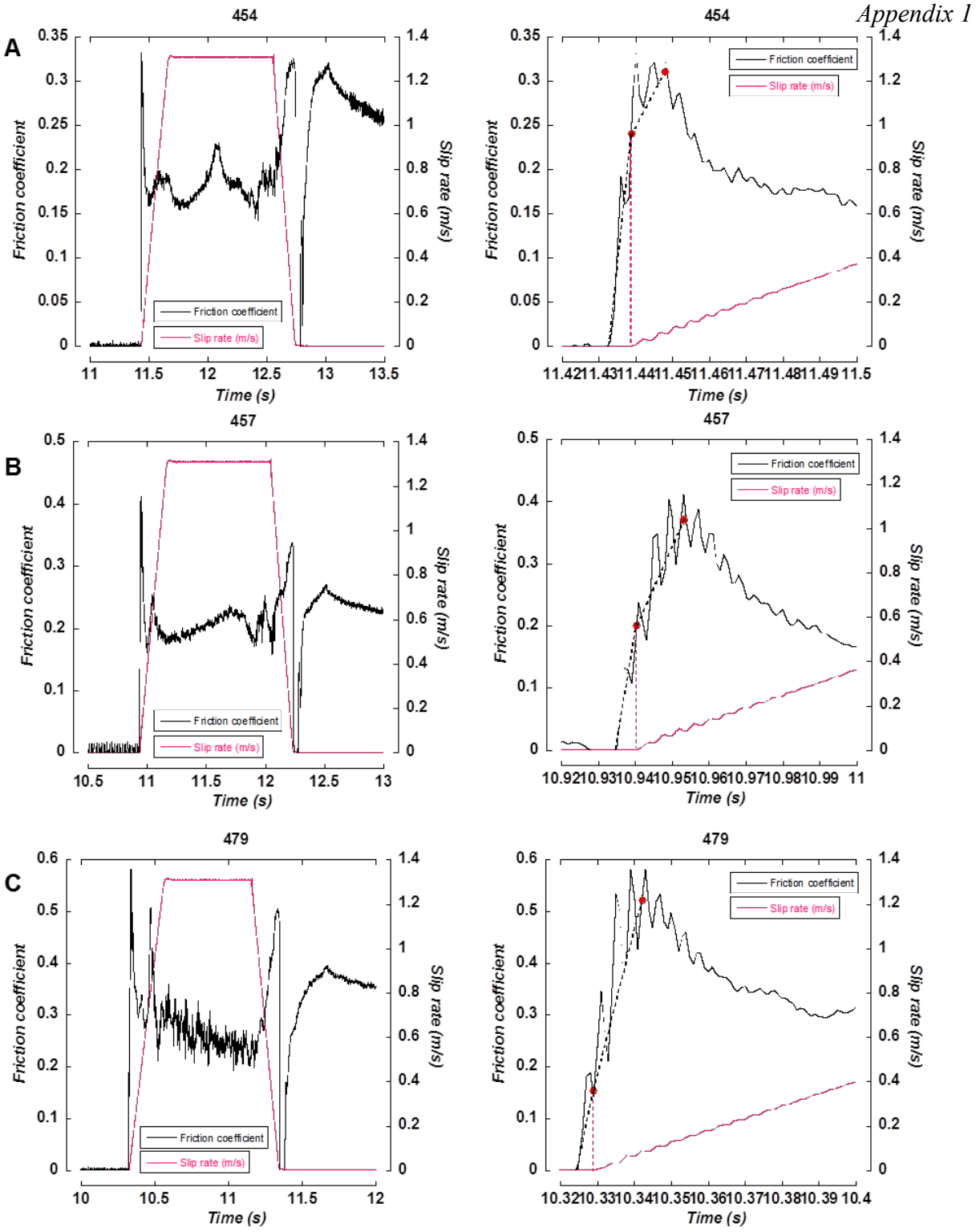

Fig. A1.10 Plots of slip rate and friction coefficient against time for wet calcite + illite-smectite mixtures. **a)** Experiment 454 = 50% calcite + 50% illite-smectite. **b)** Experiment 457 = 80% calcite + 20% illite-smectite. **c)** Experiment 479 = 90% calcite + 10% illite-smectite. Plots on the right show a magnification of the early stage of the experiment. The first red dot marks the point at which the motor starts to accelerate, which is followed by a linear evolution of friction towards the initial friction value, μ_i, which is marked by the second red dot. After this point, friction evolution deviates from a linear behaviour.

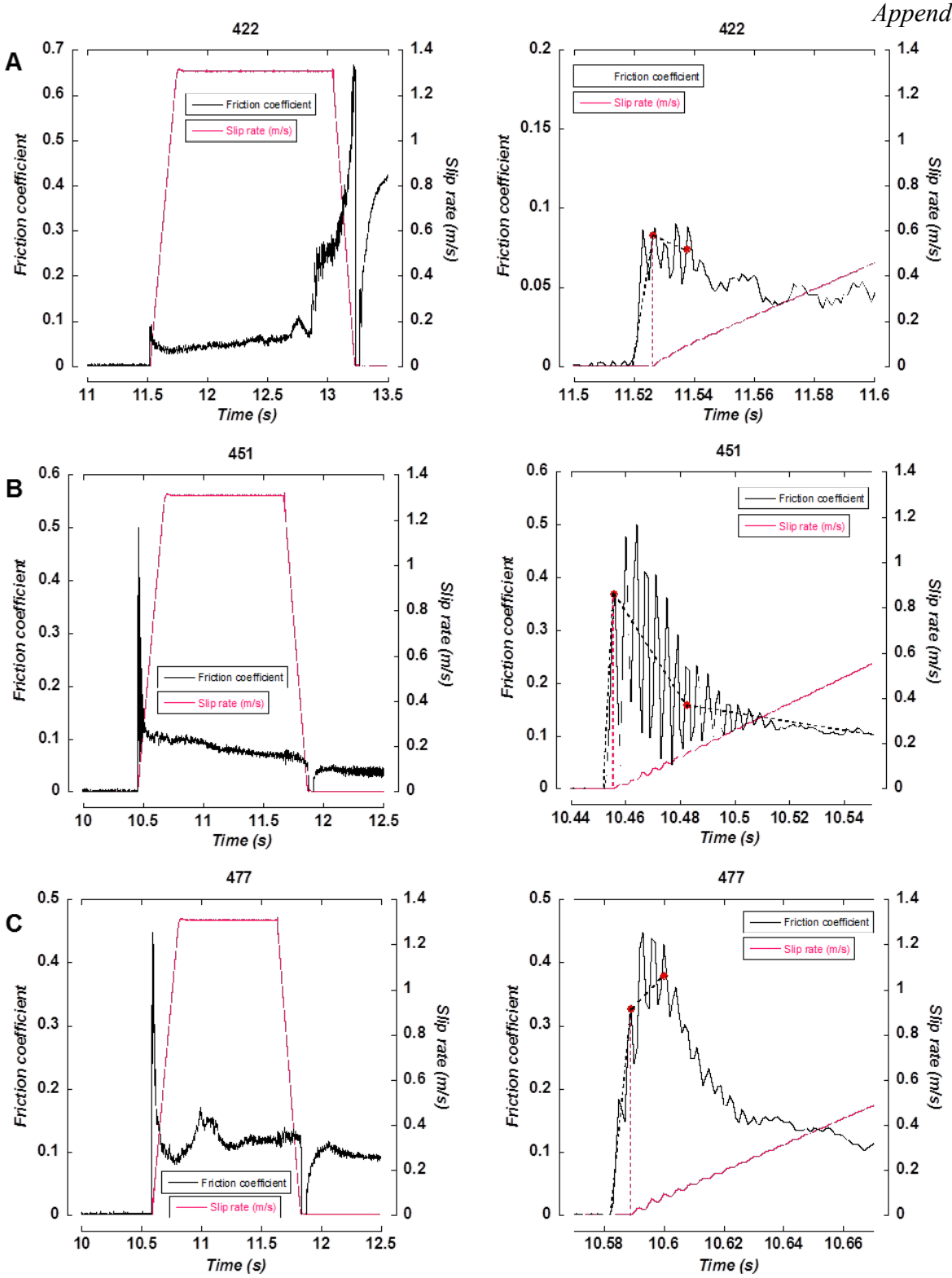

Fig. A1.11 Plots of slip rate and friction coefficient against time for wet calcite + montmorillonite mixtures. **a)** Experiment 422 = 50% calcite + 50% montmorillonite. **b)** Experiment 451 = 80% calcite + 20% montmorillonite. **c)** Experiment 479 = 90% calcite + 10% montmorillonite. Plots on the right show a magnification of the early stage of the experiment. The first red dot marks the point at which the motor starts to accelerate, which is followed by a linear evolution of friction towards the initial friction value, μ_i, which is marked by the second red dot. After this point, friction evolution deviates from a linear behaviour.

Appendix 1.4

Additional initial microstructures

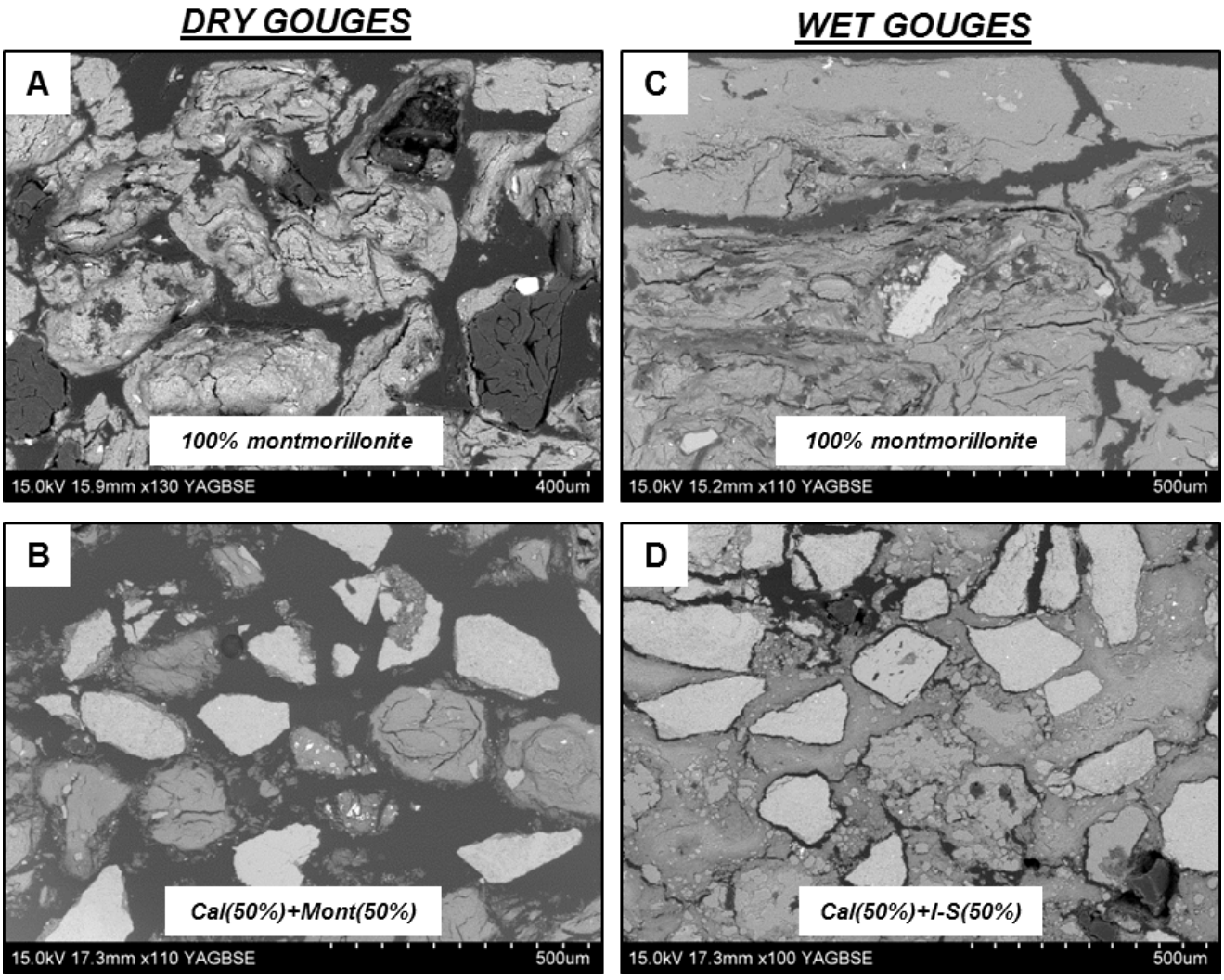

Fig. A1.12 Initial microstructure of gouges recovered after being held under 9 MPa normal load for 3 minutes, prior to shearing. See paper Section 3.3.2.1 for full description. **a)** 100% montmorillonite, dry. **b)** 50% calcite + 50% montmorillonite, dry. **c)** 100% montmorillonite, wet. **d)** 50% calcite + 50% illite-smectite, wet.

Appendix 1.5

Additional peak friction microstructures

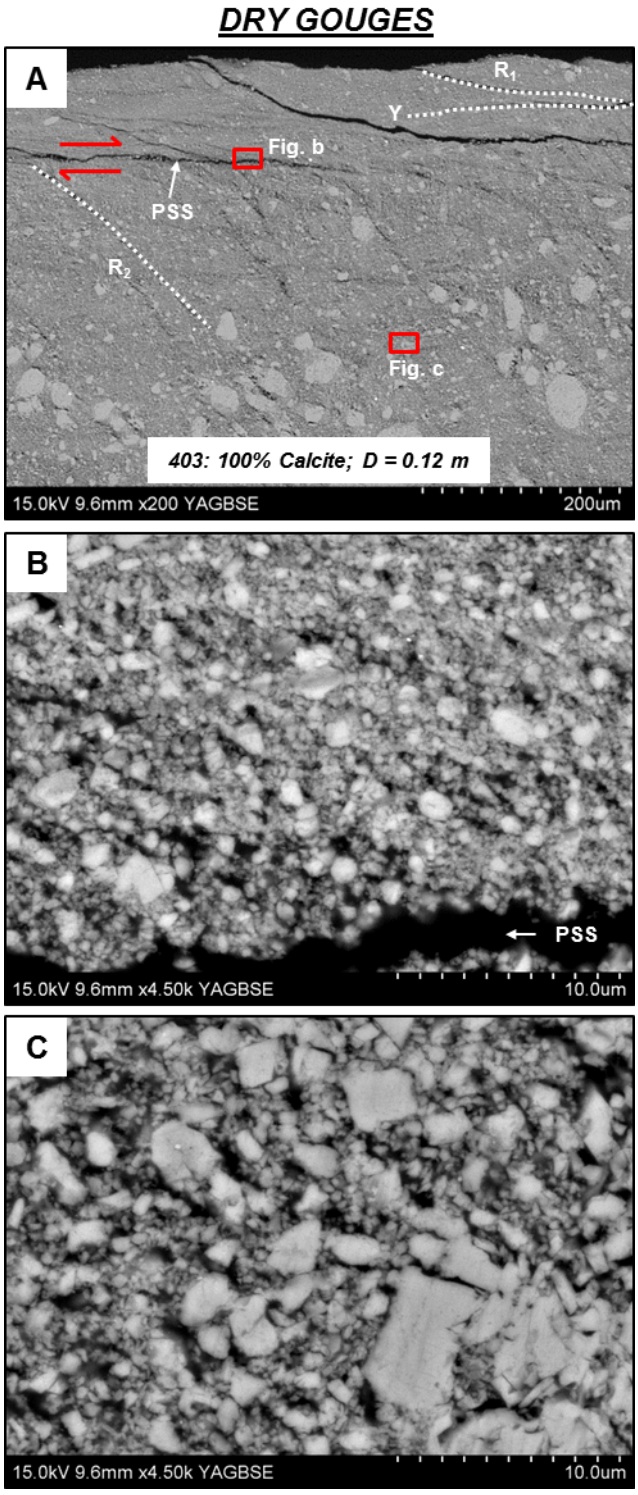

Fig. A1.13 Deformed microstructures after recovery of 100% dry calcite gouge at peak friction. See paper Section 3.3.2.2 for full description. **a)** Overview of slip zone, showing location of PSS. Fabric in the slip zone is characterized by R_1-, R_2- and incipient Y-shears (examples highlighted). **b)** Zoomed in image of PSS and adjacent region shown in fig. **a**. **c)** Zoomed in image of matrix within central slip zone of fig. **a**.

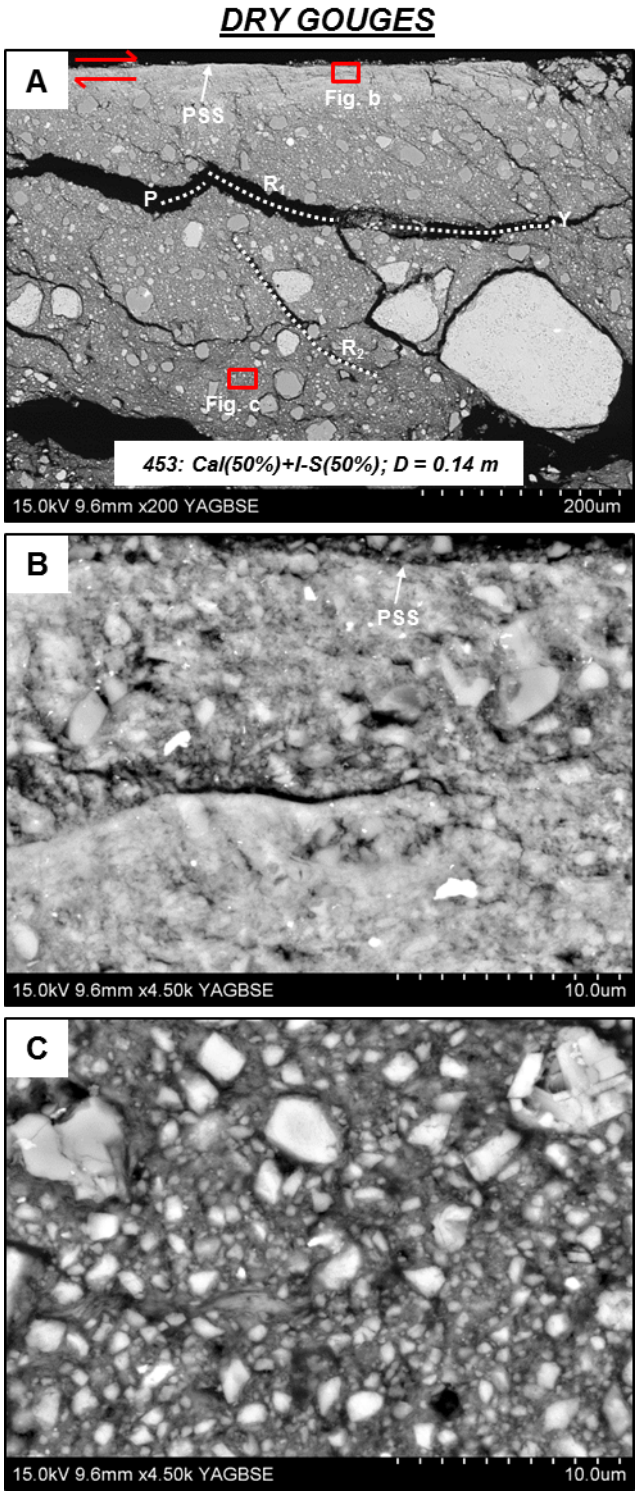

Fig. A1.14 Deformed microstructures after recovery of dry 50% calcite + 50% illite-smectite gouge at peak friction. See paper Section 3.3.2.2 for full description. **a)** Overview of slip zone, showing location of PSS. Examples of Riedel shear structures are labelled and the sense of shear inferred. **b)** Zoomed in image of PSS and adjacent region shown in fig. **a**. A P-shear transects the centre of the image. **c)** Zoomed in image of matrix within central slip zone of fig. **a**.

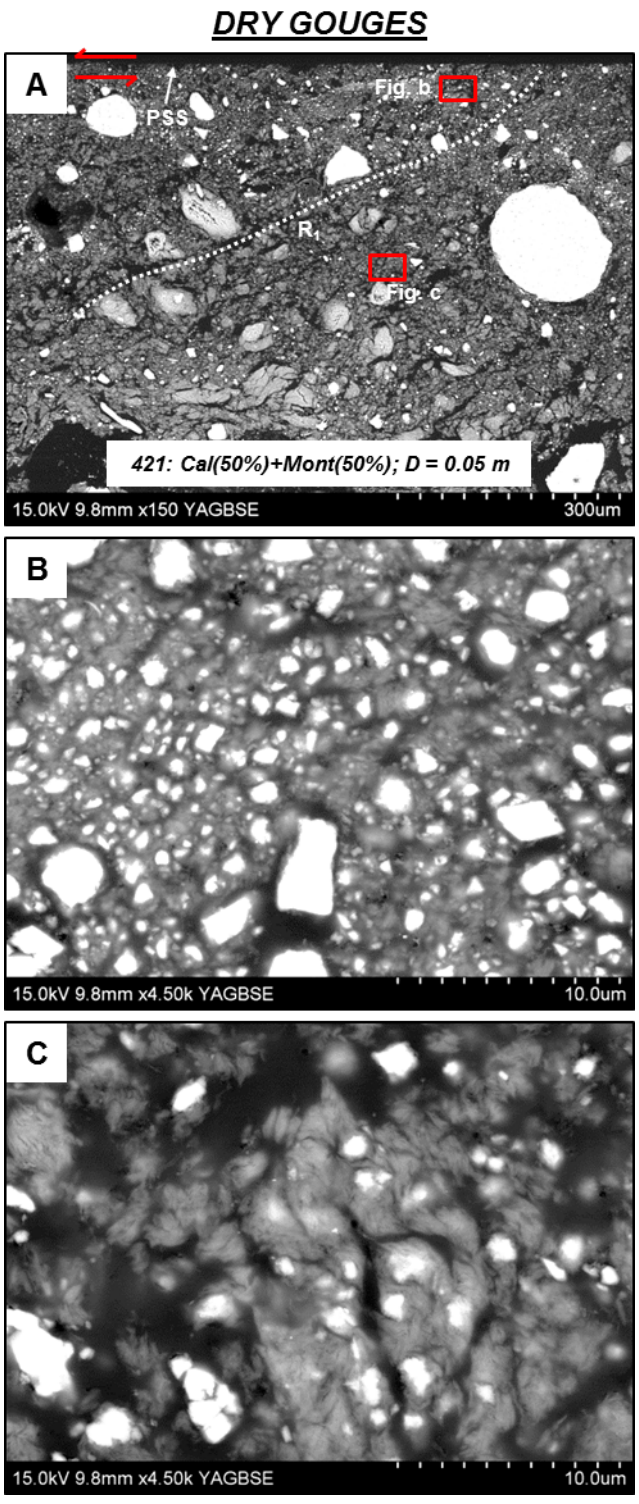

Fig. A1.15 Deformed microstructures after recovery of dry 50% calcite + 50% montmorillonite gouge at peak friction. See paper Section 3.3.2.2 for full description. **a)** Overview of slip zone, showing location of PSS. A weak fabric, characterized by R_1-shears is present. **b)** Zoomed in image of region adjacent to PSS shown in fig. **a**. **c)** Zoomed in image of matrix within central slip zone of fig. **a**.

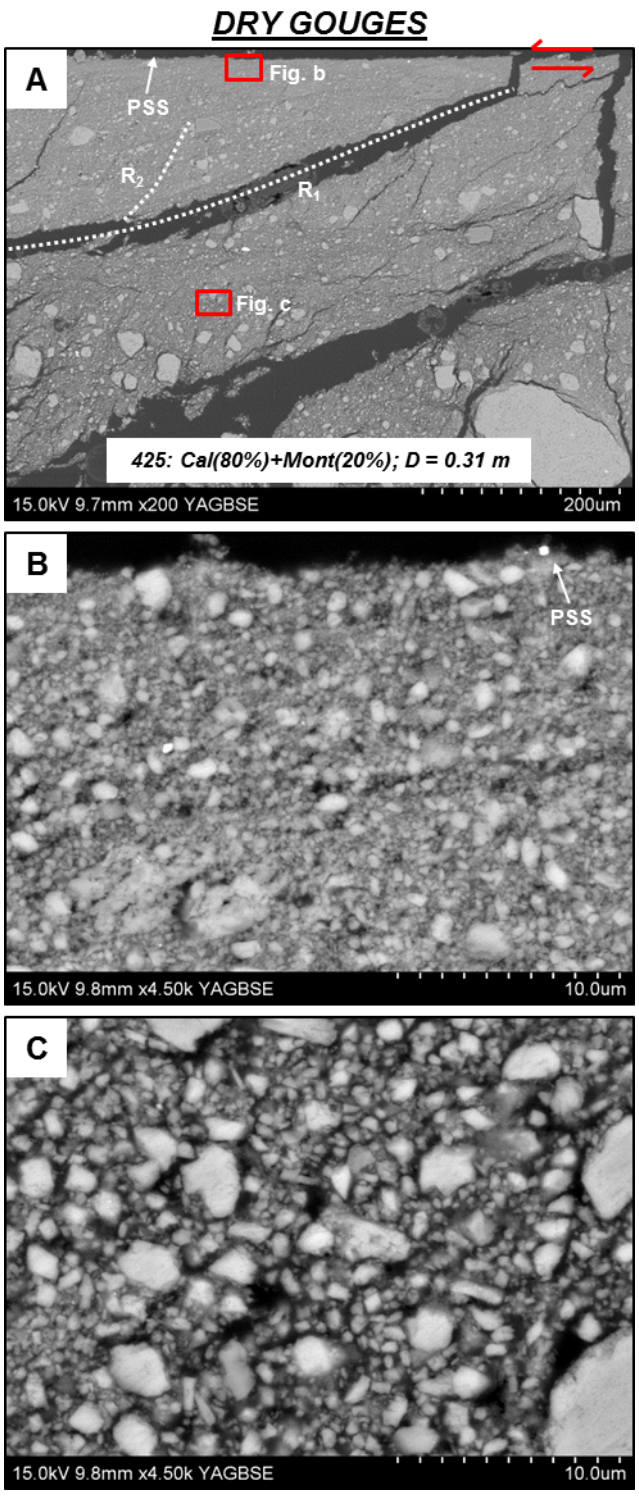

Fig. A1.16 Deformed microstructures after recovery of dry 80% calcite + 20% montmorillonite gouge at peak friction. See paper Section 3.3.2.2 for full description. **a)** Overview of slip zone, showing location of PSS. Fabric in the slip zone is dominated by R_1-shears, but R_2-shears are also common in the upper part of the slip zone. **b)** Zoomed in image of PSS and adjacent region shown in Fig. 4a-S6. **c)** Zoomed in image of matrix within central slip zone of Fig. 4a-S6.

Appendix 1.6

Additional steady-state microstructures

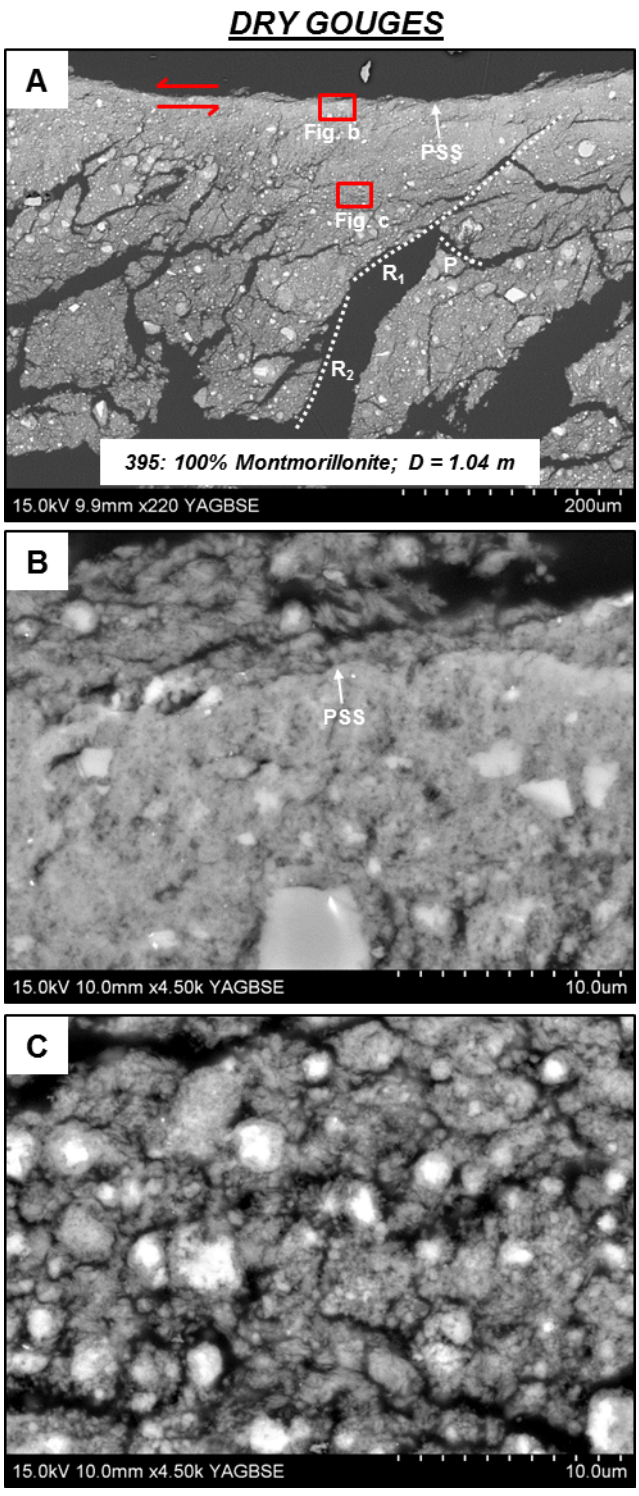

Fig. A1.17 Deformed microstructures after recovery of dry 100% montmorillonite gouge during steady-state sliding. See paper Section 3.3.2.3 for full description. **a)** Overview of slip zone, showing location of PSS. Fabric in the slip zone is dominated by R_1-shears. **b)** Zoomed in image of PSS and adjacent region shown in fig. **a**. **c)** Zoomed in image of matrix within central slip zone of fig. **a**.

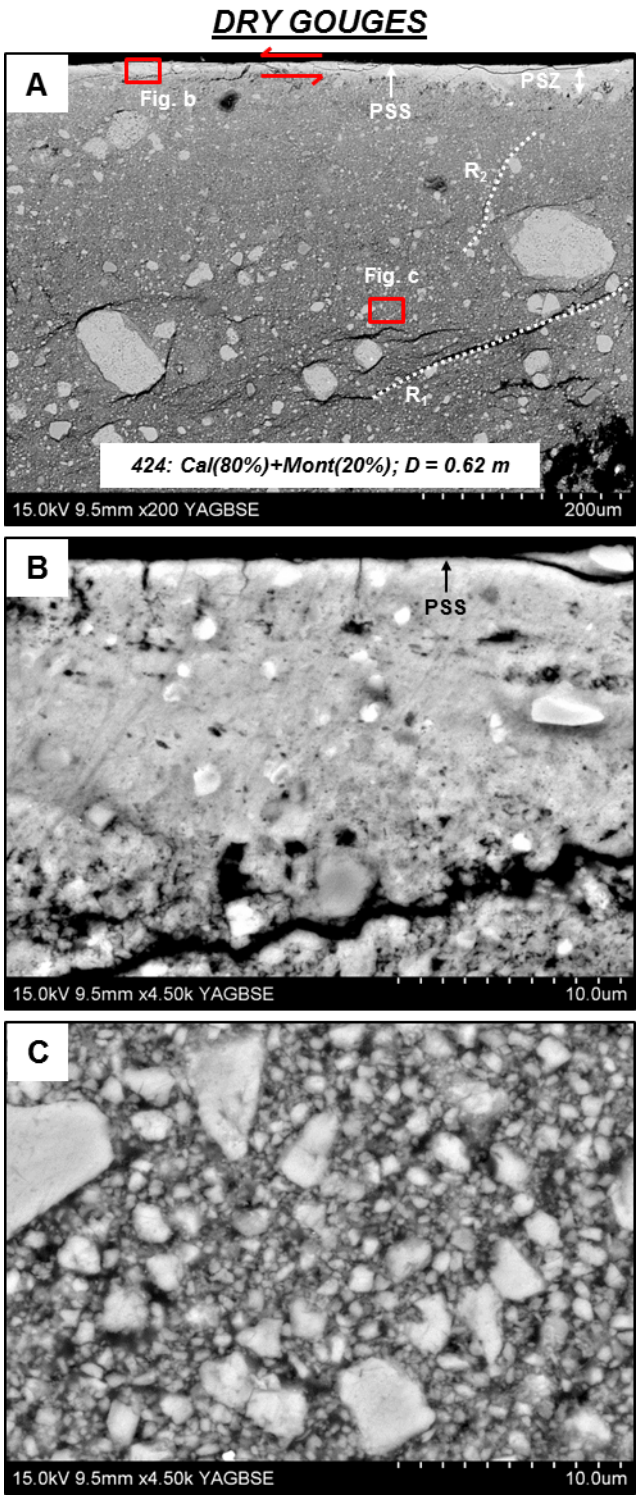

Fig. A1.18 Deformed microstructures after recovery of dry 80% calcite + 20% montmorillonite gouge during steady-state sliding. See paper Section 3.3.2.3 for full description. **a)** Overview of slip zone, showing location of PSS and PSZ. Fabric in the slip zone is dominated by R_1-shears, particularly in the lower part of the slip zone. **b)** Zoomed in image of PSS and adjacent PSZ shown in fig. **a**. The black spots within the PSZ are inferred to be degassing bubbles as a consequence of thermal decomposition of calcite. **c)** Zoomed in image of matrix within central slip zone of fig. **a**.

.

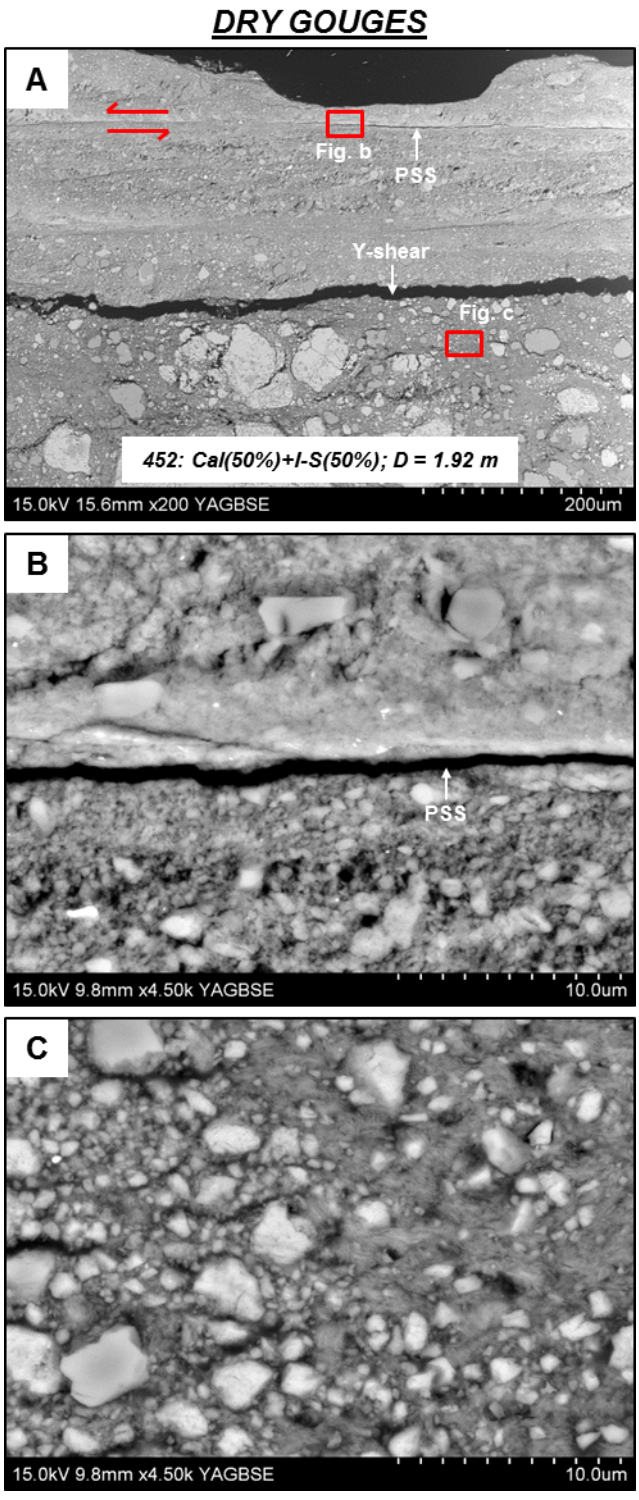

Fig. A1.19 Deformed microstructures after recovery of dry 50% calcite + 50% illite-smectite gouge during steady-state sliding. See paper Section 3.3.2.3 for full description. a) Overview of slip zone, showing location of PSS. A number of Y-shears are present in the region below the PSS. **b)** Zoomed in image of PSS and adjacent region shown in fig. **a**. **c)** Zoomed in image of matrix within central slip zone of fig. **a**.

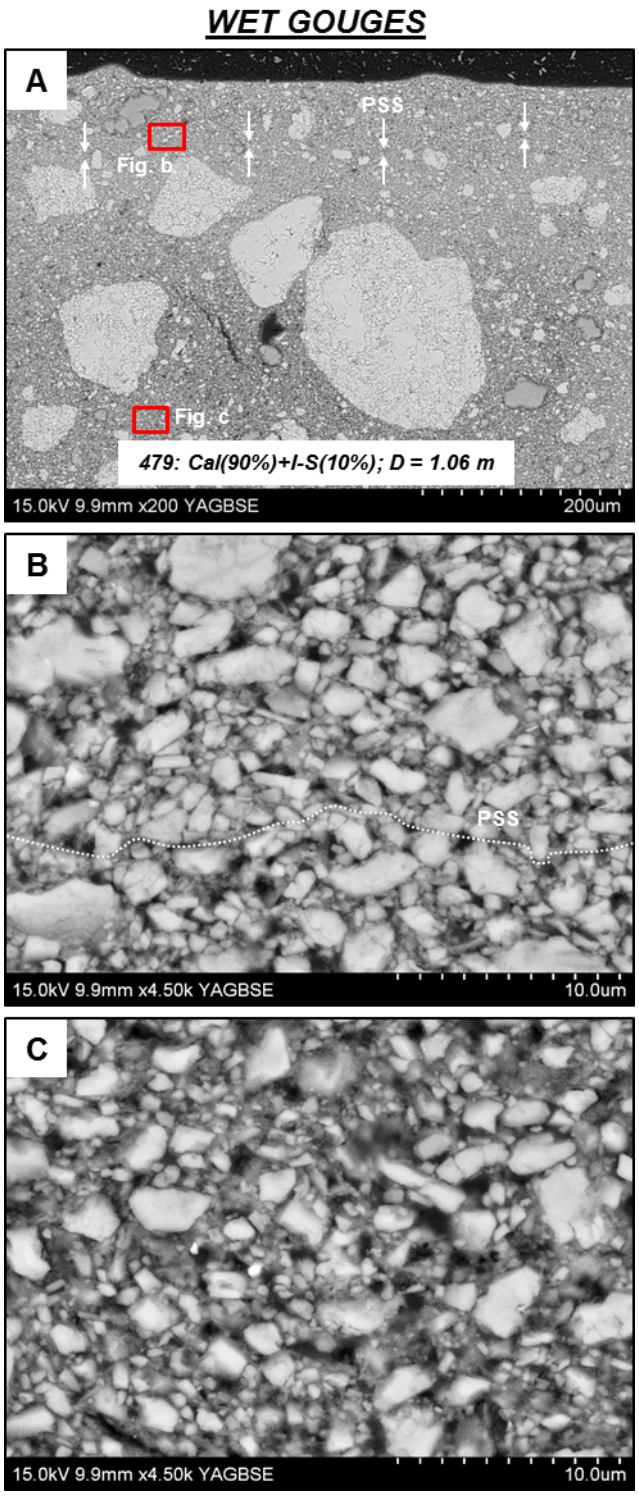

Fig. A1.20 Deformed microstructures after recovery of wet 90% calcite + 10% illite-smectite gouge during steady-state sliding. See paper Section 3.3.2.3 for full description. **a)** Overview of slip zone, showing location of PSS, although the PSS is very vague and hard to resolve. **b)** Zoomed in image of PSS and adjacent region shown in fig. **a**. **c)** Zoomed in image of matrix within central slip zone of fig. **a**.

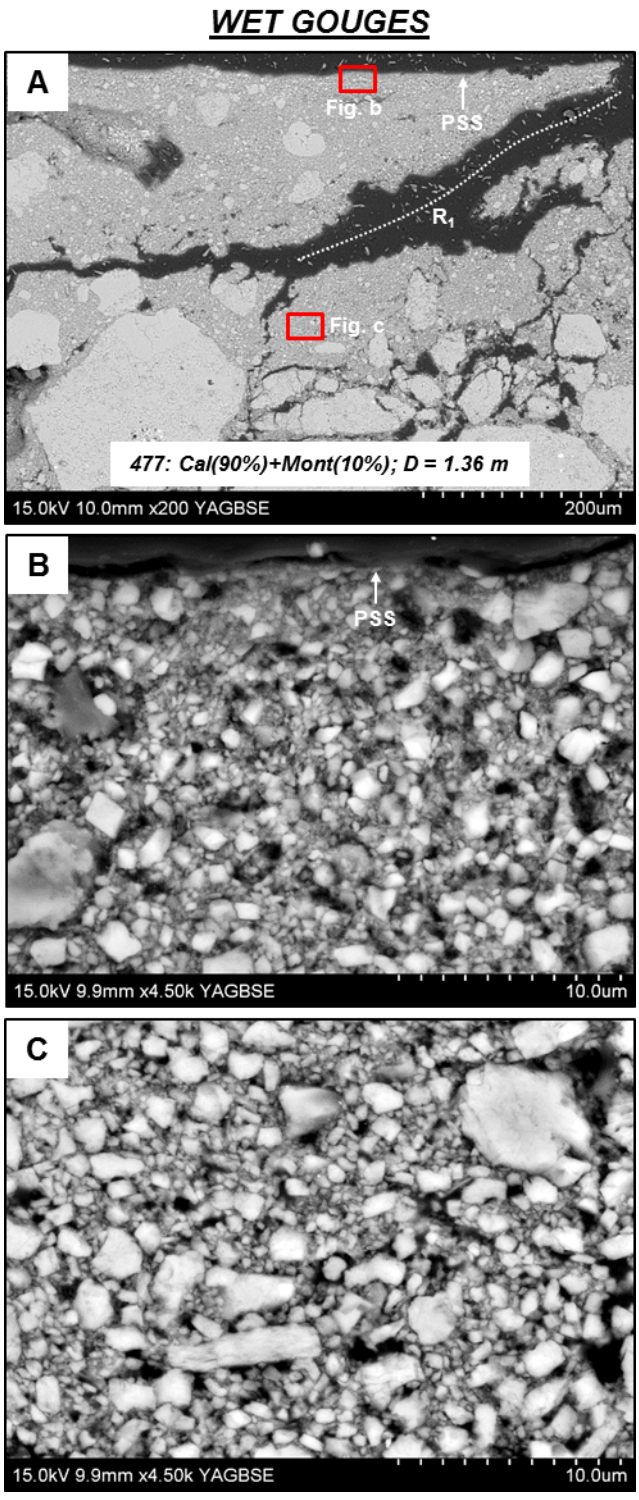

Fig. A1.21 Deformed microstructures after recovery of wet 90% calcite + 10% montmorillonite gouge during steady-state sliding. See paper Section 3.3.2.3 for full description. **a)** Overview of slip zone showing location of PSS. Clasts in the central part of the slip zone are much more angular than those in the slip zones of the wet clay-bearing gouges containing ≥20 wt.% clay (e.g. Figs. 3.8d and 3.9d in paper). Also, unlike the more clay-rich water-saturated gouges, which are void of any fabric, there is evidence in this sample of Riedel shears. **b)** Zoomed in image of PSS and adjacent region shown in fig. **a**. **c)** Zoomed in image of matrix within central slip zone of fig. **a**.

Appendix 2

Supplementary materials to complement the data presented in Chapter 5

Appendix 2.1: Mineralogical composition of starting material (pp. 2-3)

Appendix 2.2: Reproducibility of low-velocity experimental results and rate and state modelling data (pp. 4-34)

Appendix 2.3: Reproducibility of high-velocity friction experiments (pp. 35-39)

Appendix 2.1

Mineralogical composition of starting material

The following XRD spectra show the composition of the sieved gouge used in the experiments, plus the residual material which did not pass through the sieve (Fig. A2.1), and the composition of the clay fractions in the sieved gouge (Fig. A2.2) and residual material (Fig. A2.3).

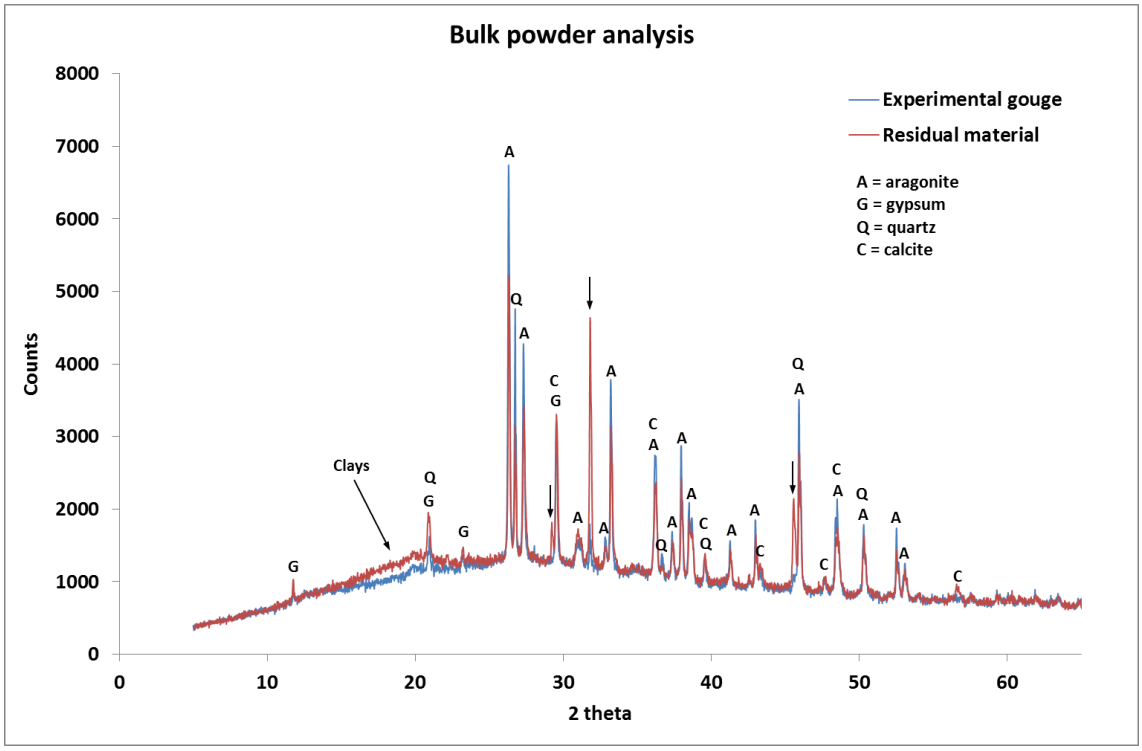

Fig. A2.1 XRD patterns of the sieved gouge (<1 mm) used in the experiments and the residual material, which did not pass through the sieve. The compositions are almost identical, with the exception of the arrowed peaks, which are relatively enriched in the residual material; these peaks are virtually absent in the sieved gouge. We were not able to unequivocally identify these peaks; possible matches are barite and basanite. Either of these would be consistent with the residual material being enriched in late-stage crystalline mineralisation products, which one would expect to be coarser and more resistant to disaggregation than the rest of the Lisan sediment. The broad 'bump' present at low values of 2 theta is typical of clay minerals, which are poorly crystalline and so do not produce strong, clear diffractions. To identify the clays, we separated the clay fraction to produce oriented mounts (see Figs. A2.2 and A2.3).

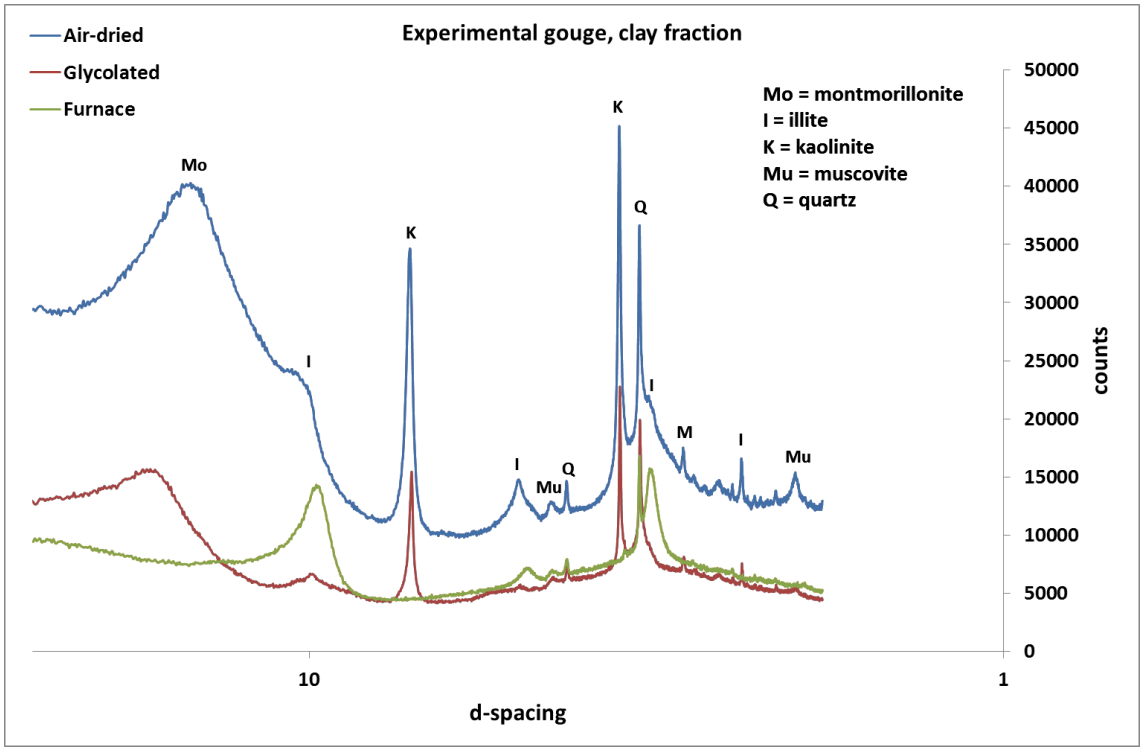

Fig. A2.2 XRD patterns of the air-dried, glycolated and furnace-treated (550˚C) clay fraction of the sieved Lisan sediment used in the experiments.

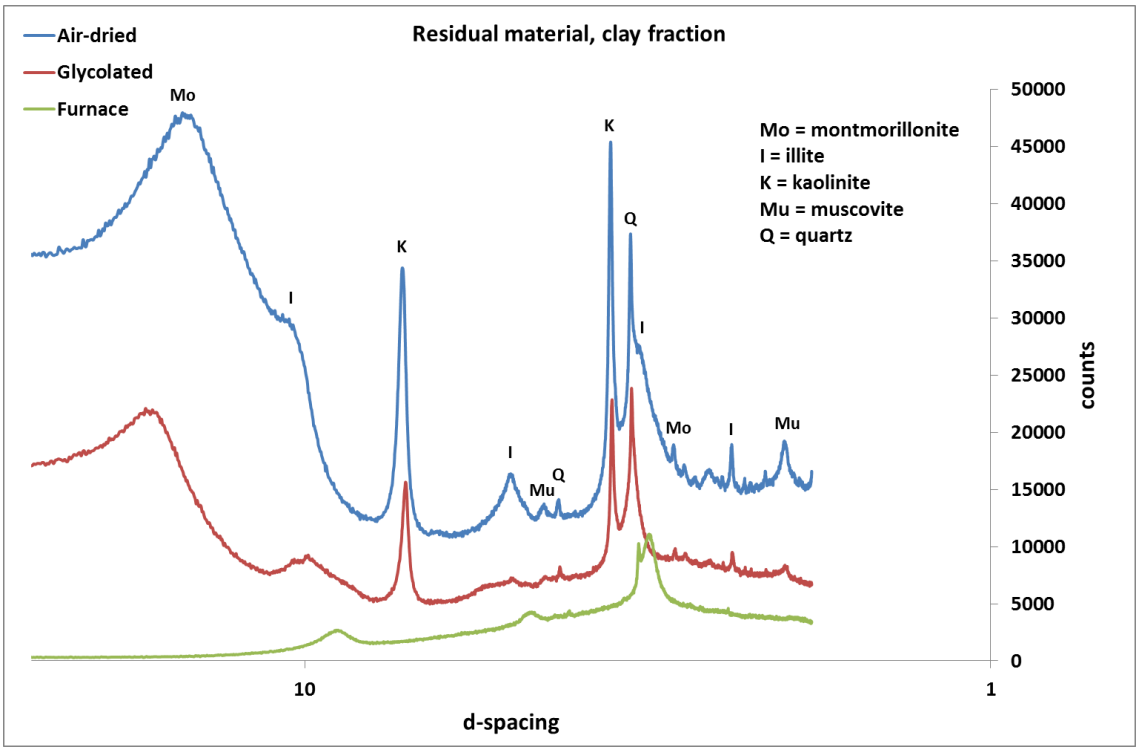

Fig. A2.3 XRD patterns of the air-dried, glycolated and furnace-treated (550˚C) clay fraction of the residual material, which did not pass through the sieve, and so was not used in the experiments. The composition is the same as that observed for the experimental gouge (Fig. A2.2).

Appendix 2.2

Reproducibility of low-velocity experimental results and rate and state modelling data

Experiments were performed twice for each of the imposed experimental conditions. In the main text we show only the results of one of the experiments performed under each set of conditions. Here we present the results of both experiments, to show that our data are highly reproducible, particularly in terms of the main trends in frictional stability and healing rates discussed in the main text.

The following pages show for each set of experimental conditions:

1) Friction vs. displacement plots of the experimental runs.
2) The results of rate and state modelling of the velocity step data, including representative example plots of the modelled velocity steps. Note that the data produced at 1 MPa is very noisy compared with that produced at 18 MPa, hence the greater uncertainties (reported as σ_2) associated with these data. However, despite the uncertainties associated with the individual parameters a, b, and D_c, the absolute values of the combined parameter (a-b) are consistent across numerous model runs.
3) The results of slide-hold-slide tests.

1 MPa, room humidity, experimental runs

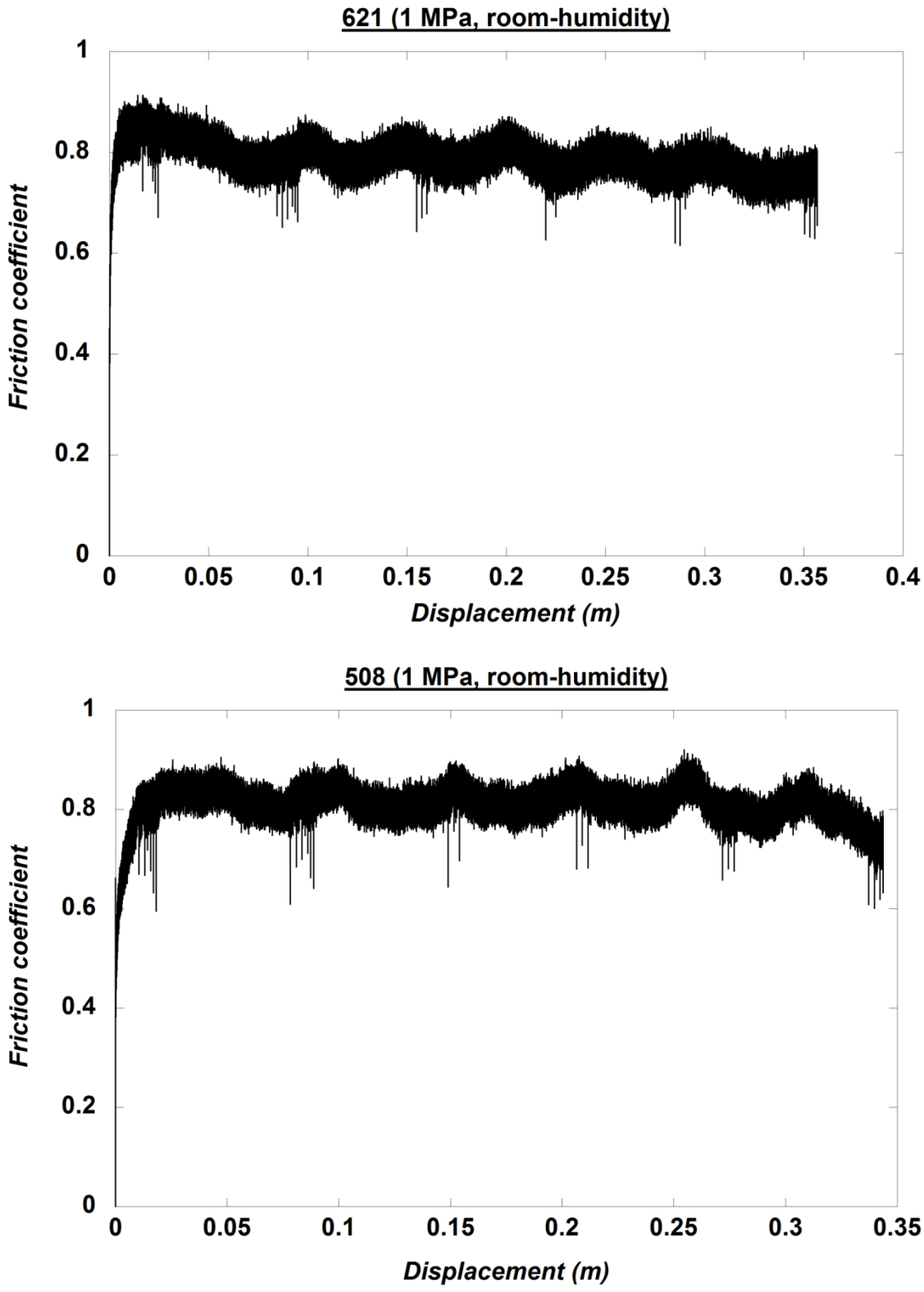

Figure A2.4 1 MPa, room humidity, experimental runs

1 MPa, room humidity. velocity-step data

Run 1: Experiment 508

Displacement (m)	V_0 (μm/s)	V (μm/s)	K (μ/m)	a	b_1	D_{c1} (m)	a-b	σ2 (k)	σ2 (a)	σ2 (b_1)	σ2 (D_{c1})	Propagated uncertainty (a-b)
0.0093	13	130	20664.6948	0.024974	0.013811	1.99E-07	0.0112	5.75E+02	9.58E+02	1.73E+03	1.54E+03	43949826.70
0.0119	13	130	21322.2007	0.026837	0.015054	1.04E-07	0.0118	6.11E+01	3.12E+02	5.55E+02	4.71E+02	4014996.67
0.0796	13	130	23403.6313	0.014989	0.011409	1.01E-07	0.0036	3.78E+02	4.71E+02	6.19E+02	6.17E+02	2651648.89
0.0823	13	130	19859.541	0.015764	0.010982	9.90E-08	0.0048	2.15E+02	3.86E+02	5.54E+02	9.39E+02	3050055.18
0.1502	13	130	20888.6812	0.013505	0.011816	1.05E-07	0.0017	1.78E+01	3.43E+01	3.92E+01	4.21E+01	5925.63
0.1528	13	130	21173.9242	0.014544	0.011399	9.59E-08	0.0031	2.31E+02	2.98E+02	3.81E+02	3.30E+02	887336.13
0.2078	13	130	16065.7705	0.0095589	0.007503	1.30E-07	0.0021	2.64E+02	2.79E+02	3.55E+02	3.91E+02	1165256.71
0.2103	13	130	17844.1337	0.010869	0.0053399	1.10E-07	0.0055	4.10E+03	4.08E+03	7.93E+03	4.08E+03	3046453595.12
0.2731	13	130	16133.3334	0.010332	0.0051374	1.04E-07	0.0052	1.36E+03	4.26E+03	8.57E+03	7.71E+03	3615295433.80
0.2757	13	130	16958.4847	0.0083796	0.0062591	1.13E-07	0.0021	5.30E+02	4.59E+02	6.08E+02	6.07E+02	5035217.98
0.3384	13	130	10867.2385	0.0072612	0.0058421	1.00E-07	0.0014	5.69E+02	4.80E+02	5.97E+02	1.10E+03	3733132.57
0.3411	13	130	10966.0433	0.01457	0.014143	6.90E-08	0.0004	4.93E+00	7.65E+00	7.78E+00	7.37E+00	294.85

Run 2: Experiment 621

Displacement (m)	V_0 (μm/s)	V (μm/s)	K (μ/m)	a	b_1	D_{c1} (m)	a-b	σ2 (k)	σ2 (a)	σ2 (b_1)	σ2 (D_{c1})	Propagated uncertainty (a-b)
0.01562	13	130	49832.1386	0.0047325	0.00063681	1.09E-05	0.0041	9.92E+03	1.72E+01	1.28E+02	4.72E+01	41253811.63
0.01805	13	130	39658.9671	0.0018833	0.0006327	1.93E-06	0.0013	1.14E+04	1.44E+02	4.28E+02	8.55E+01	143021828.51
0.08586	13	130	50005.0628	0.0032491	0.0006467	6.96E-06	0.0026	1.27E+04	3.51E+01	1.77E+02	5.53E+01	48510949.07
0.08845	13	130	23571.7435	0.0055785	0.0041316	1.70E-05	0.0014	3.01E+01	9.05E-01	1.21E+00	1.62E+00	112.37
0.1562	13	130	30139.7307	0.00191	0.00078876	2.98E-06	0.0011	4.67E+03	5.31E+01	1.31E+02	7.98E+01	7777808.19
0.1588	13	130	30059.8898	0.0026437	0.00073159	9.30E-06	0.0019	9.42E+03	3.66E+01	1.32E+02	3.53E+01	15625557.96
0.2212	13	130	29754.0325	0.00040507	0.0046752	9.23E-07	-0.0043	8.02E+03	2.39E+03	2.08E+02	1.48E+03	839412.85
0.2238	13	130	17595.3317	0.0028269	0.00090647	2.54E-07	0.0019	2.14E+05	1.91E+04	5.96E+04	5.80E+04	2072655501367.20
0.2865	13	130	21021.5138	0.00010451	0.00018675	3.40E-07	-0.0001	1.82E+05	6.26E+04	3.50E+04	1.04E+04	722693727018.49
0.2891	13	130	20009.5341	0.0016098	0.00039193	9.57E-07	0.0012	1.51E+02	6.16E+01	2.54E+02	2.33E+02	127704583.26
0.3518	13	130	20208.6382	0.0027191	0.00019019	9.53E-07	0.0025	6.00E+03	6.82E+01	9.76E+02	6.70E+02	16642554223.11
0.3544	13	130	20034.4441	0.0026079	0.00021732	9.94E-07	0.0024	6.21E+03	8.73E+01	1.05E+03	5.74E+02	13885211025.13

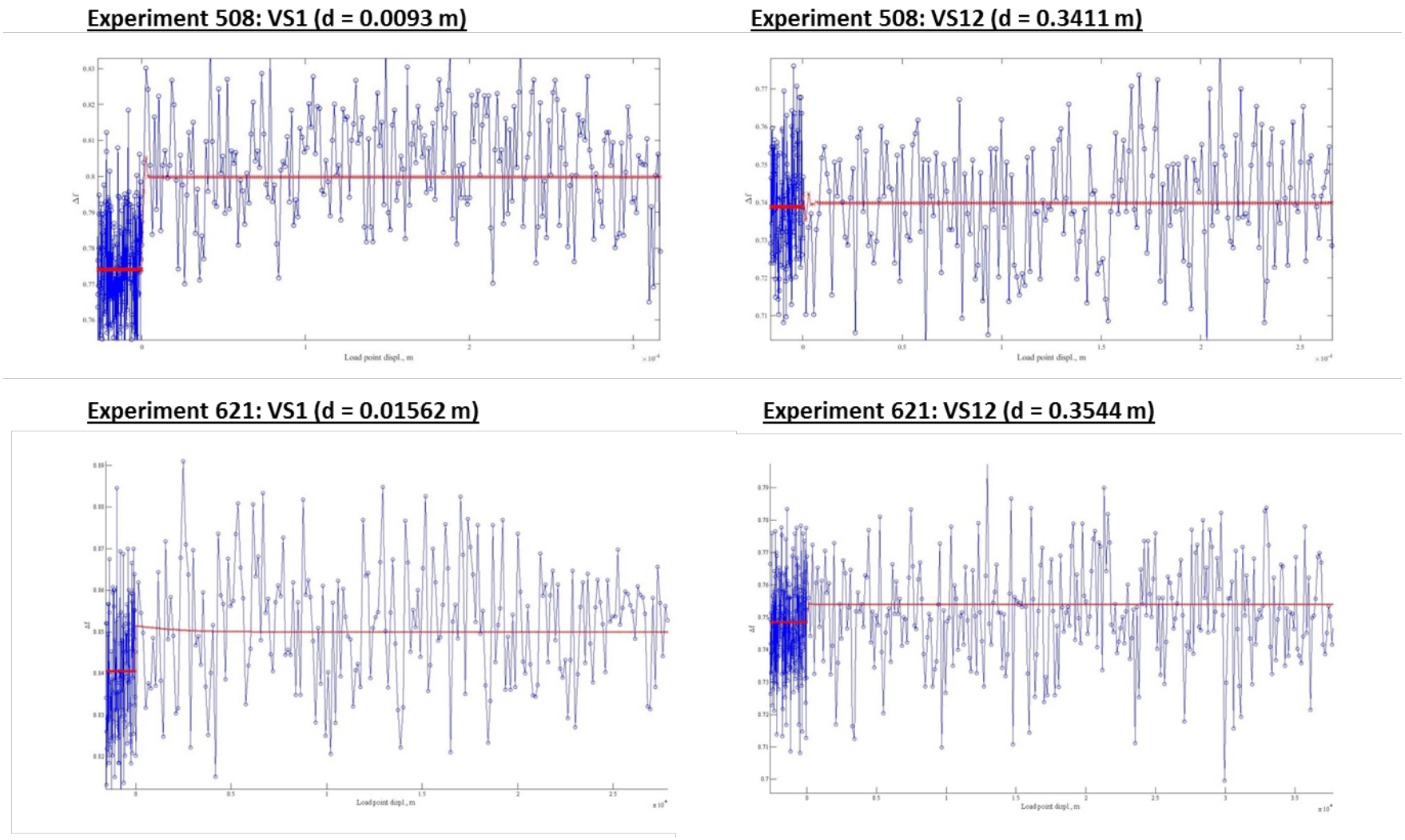

Figure A2.5 Examples of modelled velocity steps for experiments performed under room-humidity conditions at 1 MPa. Blue curve is the raw experimental data; red curve is the modelled data.

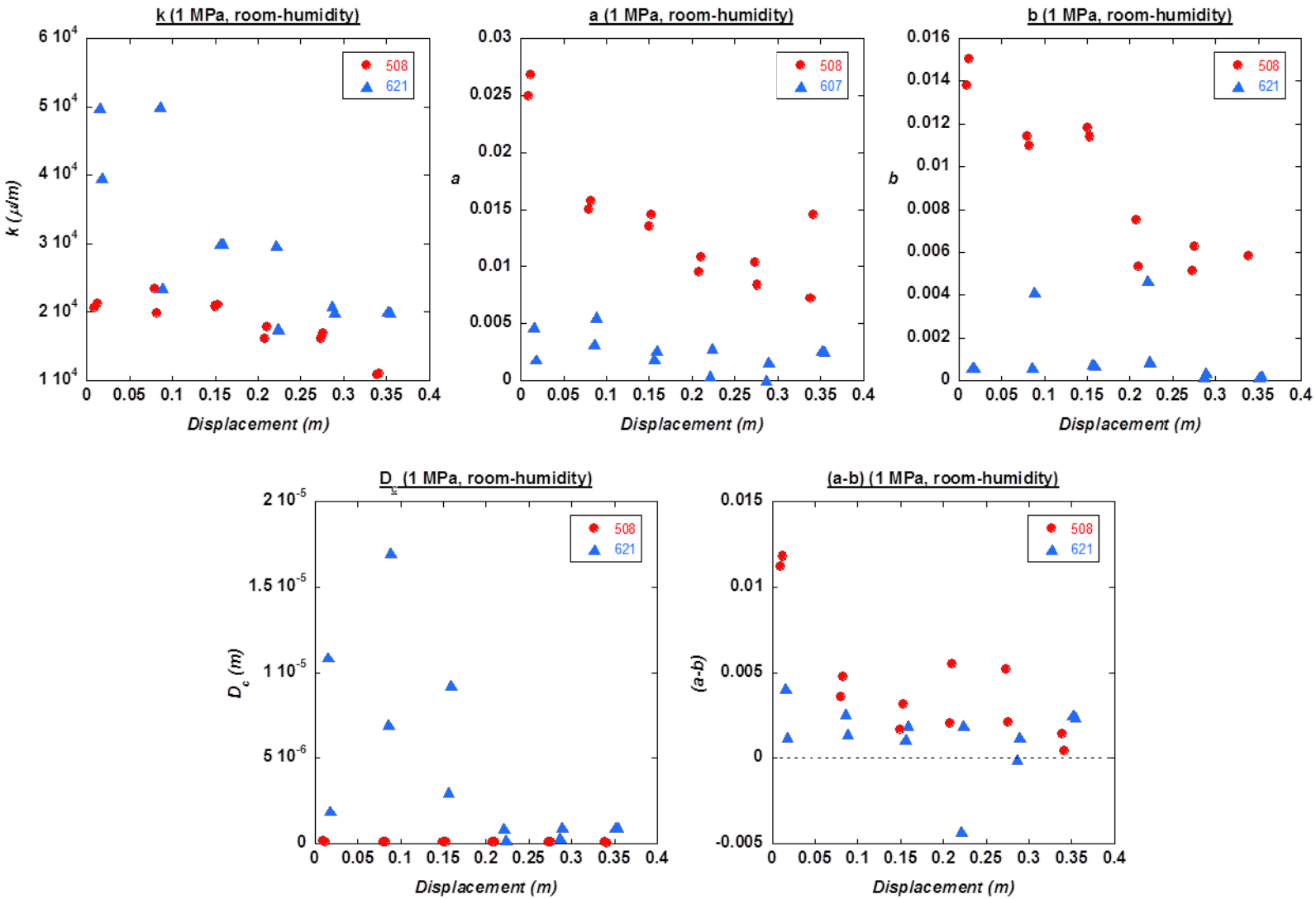

Figure A2.6 Graphical comparison of modelled data results for experiments performed under room-humidity conditions at 1 MPa.

1 MPa, room humidity, slide-hold-slide data
Run 1: Experiment 508

SHS	Displacement (m)	μ_d	μ_s	$\Delta\mu$	Δt (s)
1a	0.01445	0.802	0.8092	0.0072	0.82
1b	0.01574	0.8048	0.8145	0.0097	9.96
1c	0.01704	0.8075	0.8218	0.0143	99.84
1d	0.01834	0.8175	0.8436	0.0261	1000.6
2a	0.08487	0.8219	0.8251	0.0032	0.78
2b	0.08617	0.8213	0.8329	0.0116	9.95
2c	0.08747	0.8176	0.8338	0.0162	99.97
2d	0.08876	0.8066	0.8657	0.0591	999.04

Run 2: Experiment 621

SHS	Displacement (m)	μ_d	μ_s	$\Delta\mu$	Δt (s)
1a	0.02066	0.8404	0.8429	0.0025	0.8
1b	0.02196	0.8343	0.8375	0.0032	9.95
1c	0.02326	0.8324	0.8382	0.0058	99.98
1d	0.02456	0.8345	0.849	0.0145	999.9
2a	0.09103	0.785	0.7888	0.0038	0.77
2b	0.09233	0.7825	0.7892	0.0067	9.63
2c	0.09363	0.7857	0.7985	0.0128	99.92
2d	0.09492	0.7893	0.8267	0.0374	1001.26

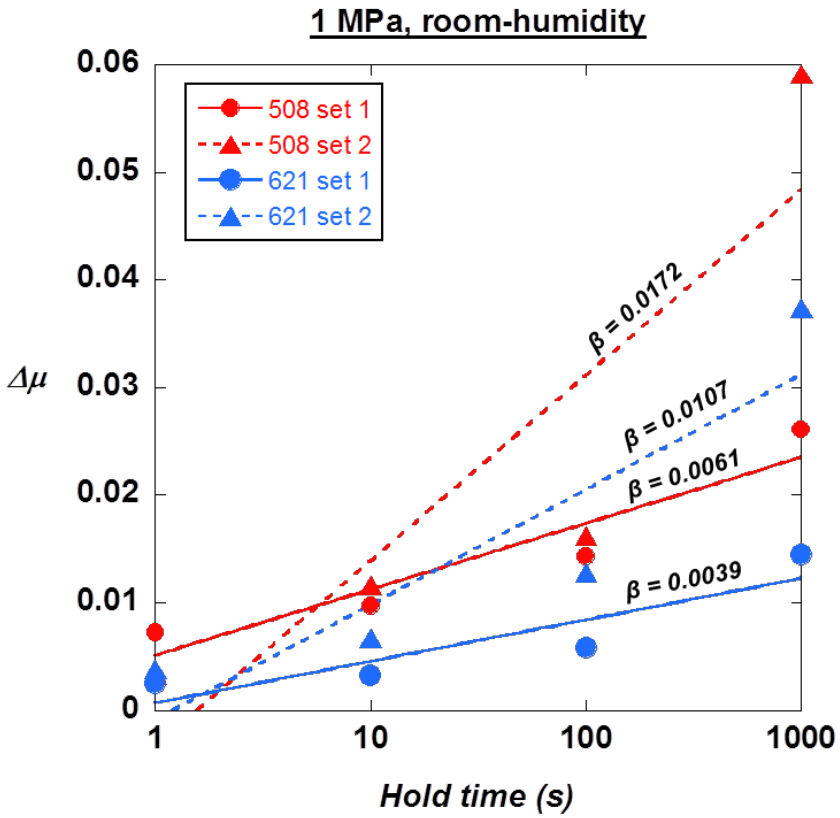

Fig. A2.7 1 MPa, room humidity, slide-hold-slide data

1 MPa, water-saturated, experimental runs

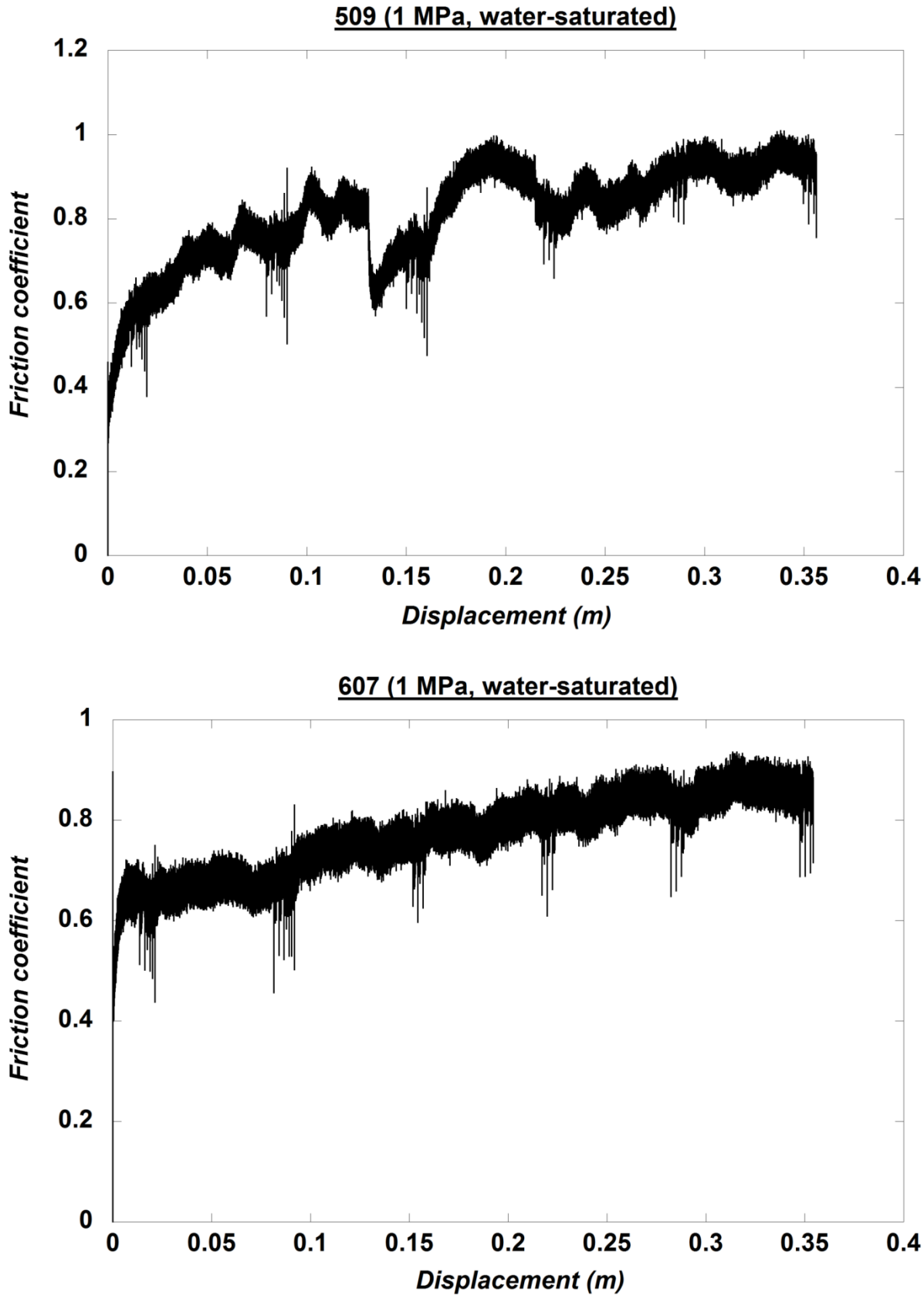

Figure A2.8 1 MPa, water-saturated, experimental runs

1 MPa, water-saturated, velocity-step data

Run 1: Experiment 509

Displacement (m)	V_0 (μm/s)	V (μm/s)	K (μ/m)	a	b_1	D_{c1} (m)	a-b	σ2 (k)	σ2 (a)	σ2 (b_1)	σ2 (D_{c1})	Propagated uncertainty (a-b)
0.0107	13	130	31049.4688	0.023301	0.013335	1.46E-07	0.0100	3.83E+02	9.28E+02	1.62E+03	1.01E+03	36836266.25
0.0133	13	130	25725.6224	0.021055	0.011226	1.03E-07	0.0098	2.08E+03	8.73E+03	1.64E+04	1.23E+04	5224693202
0.0811	13	130	23011.164	0.018807	0.010192	9.65E-08	0.0086	8.03E+01	4.06E+02	7.50E+02	6.82E+02	11660437.73
0.0837	13	130	25763.4664	0.023584	0.014232	1.63E-07	0.0094	1.86E+02	2.30E+02	3.82E+02	4.00E+02	1687850.987
0.1515	13	130	70587.8717	0.029575	0.013714	1.47E-07	0.0159	8.70E+03	1.02E+04	2.20E+04	2.24E+04	10177691472
0.154	13	130	142505.995	0.029765	0.01284	1.56E-05	0.0169	2.65E+01	4.78E-01	4.78E-01	5.86E-01	13.87456314
0.2205	13	130	27569.0281	0.017931	0.0099932	2.37E-05	0.0079	6.20E+00	2.51E-01	4.46E-01	6.06E-01	10.94794941
0.2231	13	130	154429.087	0.020083	0.013729	8.22E-06	0.0064	1.85E+02	4.78E-01	6.87E-01	1.98E+00	15.86459386
0.2858	13	130	249930.522	0.02998	0.012278	3.01E-06	0.0177	2.00E+00	4.97E-01	1.21E+00	1.41E+00	51.40324257
0.2884	13	130	42047.3204	0.018852	0.0059843	1.39E-05	0.0129	1.60E+00	2.78E-01	8.69E-01	1.15E+00	75.17787196
0.3511	13	130	218785.073	0.025563	0.014128	8.92E-06	0.0114	9.69E+00	2.69E-01	4.83E-01	6.11E-01	8.603028834
0.3537	13	130	269364.132	0.015151	0.0057332	4.72E-05	0.0094	1.85E+03	1.47E+00	4.22E+00	2.68E+00	1325.799667

Run 2: Experiment 607

Displacement (m)	V_0 (μm/s)	V (μm/s)	K (μ/m)	a	b_1	D_{c1} (m)	a-b	σ2 (k)	σ2 (a)	σ2 (b_1)	σ2 (D_{c1})	Propagated uncertainty (a-b)
0.01232	13	130	34954.5269	0.011376	0.0058125	1.45E-05	0.0056	9.56E+01	5.07E-01	9.84E-01	1.60E+00	62.14170813
0.01492	13	130	71318.899	0.016102	0.0056062	3.95E-05	0.0105	1.24E+01	2.03E-01	5.73E-01	8.00E-01	33.7066239
0.08275	13	130	43615.8267	0.023856	0.012368	1.61E-05	0.0115	5.23E+00	2.30E-01	4.41E-01	5.90E-01	8.468838382
0.08536	13	130	30522.1167	0.075714	0.061301	3.90E-07	0.0144	9.14E-01	1.57E+00	1.94E+00	2.56E+00	13.99228717
0.1531	13	130	246500.404	0.027187	0.016969	1.51E-05	0.0102	1.26E+02	5.27E-01	8.19E-01	4.82E-01	15.64134439
0.1557	13	130	172639.981	0.024862	0.01368	6.14E-06	0.0112	6.09E+01	1.74E+00	3.17E+00	1.54E+00	184.9148634
0.2185	13	130	173484.022	0.02787	0.018404	9.81E-06	0.0095	3.94E+01	5.03E-01	7.61E-01	4.78E-01	13.08189426
0.221	13	130	67703.2122	0.062004	0.049854	6.85E-07	0.0122	8.93E-01	5.34E-01	6.64E-01	9.81E-01	4.847698192
0.2838	13	130	203511.59	0.029791	0.019555	9.29E-06	0.0102	1.26E+01	2.47E-01	3.76E-01	4.46E-01	5.097006478
0.2863	13	130	44154.6973	0.022856	0.011593	1.14E-05	0.0113	4.34E+00	2.74E-01	5.38E-01	7.14E-01	12.05552106
0.3491	13	130	24135.7748	0.031689	0.017945	8.08E-06	0.0137	1.17E+00	2.49E-01	4.38E-01	5.79E-01	5.985803536
0.3517	13	130	189079.549	0.028297	0.019197	1.10E-05	0.0091	1.76E+01	2.92E-01	4.30E-01	4.45E-01	6.308024556

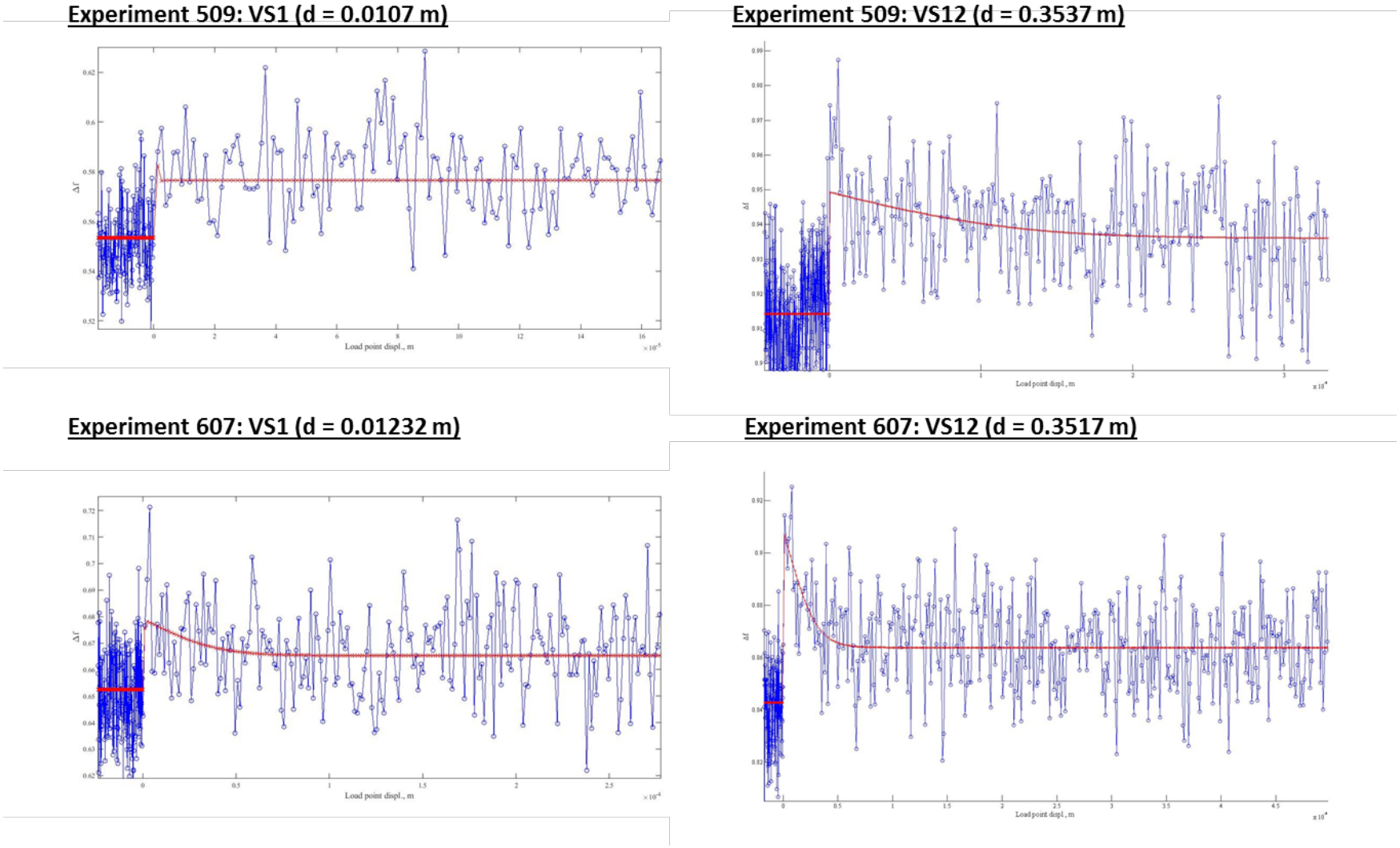

Figure A2.9 Examples of modelled velocity steps for experiments performed under water-saturated conditions at 1 MPa. Blue curve is the raw experimental data; red curve is the modelled data.

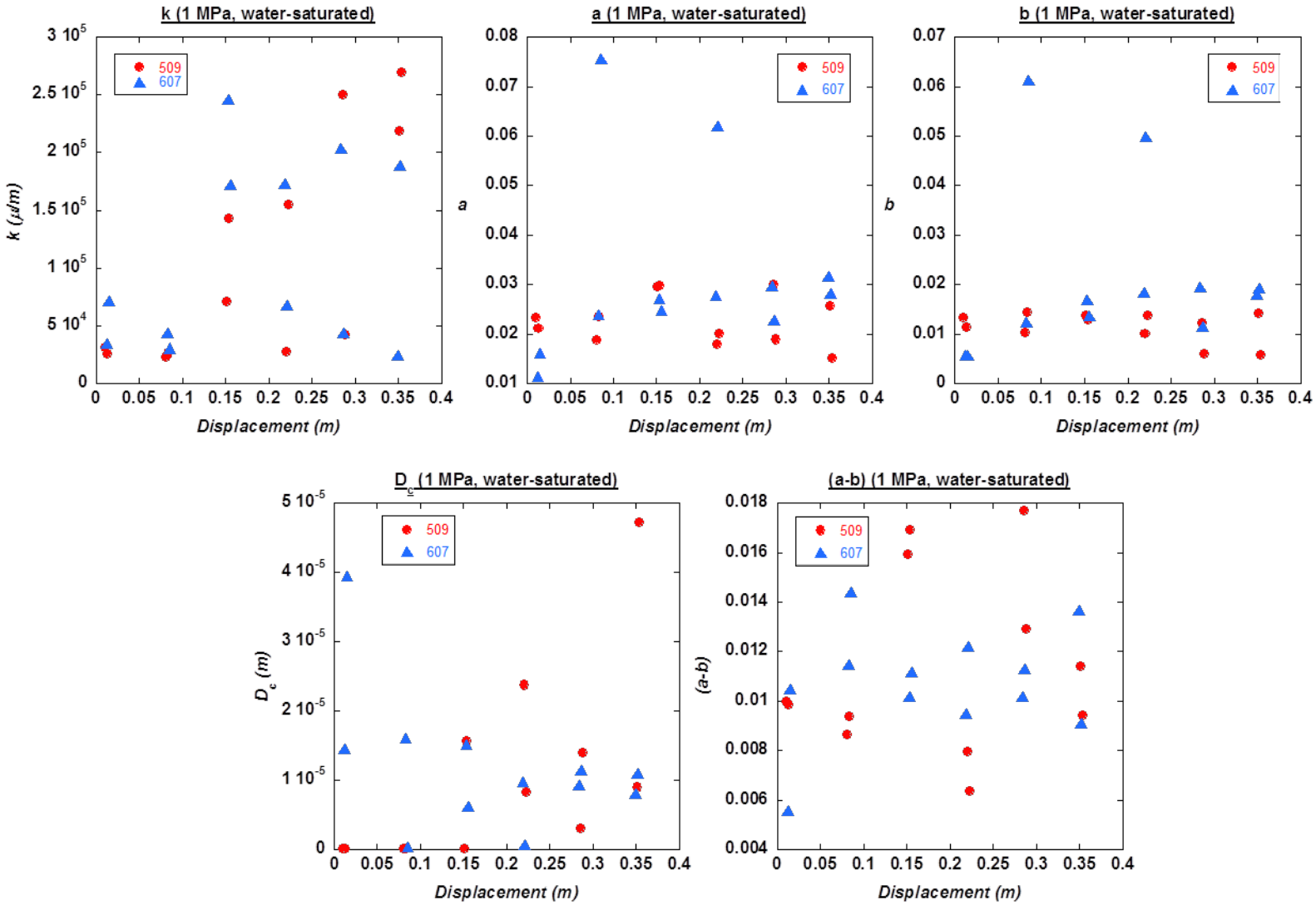

Figure A2.10 Graphical comparison of modelled data results for experiments performed under water-saturated conditions at 1 MPa.

1 MPa, water-saturated, slide-hold-slide data

Run 1: Experiment 509

SHS	Displacement (m)	μ_d	μ_s	$\Delta\mu$	Δt (s)
1a	0.01586	0.5848	0.5923	0.0075	0.79
1b	0.01716	0.5971	0.6145	0.0174	10.05
1c	0.01846	0.5992	0.628	0.0288	99.96
1d	0.01975	0.6042	0.6367	0.0325	999.96
2a	0.08627	0.7383	0.752	0.0137	0.8
2b	0.08757	0.7378	0.7921	0.0543	10.06
2c	0.08886	0.7375	0.83	0.0925	99.78
2d	0.09016	0.7377	0.8846	0.1469	1000.03

Run 2: Experiment 607

SHS	Displacement (m)	μ_d	μ_s	$\Delta\mu$	Δt (s)
1a	0.01754	0.6296	0.6328	0.0032	0.62
1b	0.01897	0.6258	0.6568	0.031	10.83
1c	0.02012	0.6296	0.6758	0.0462	100.02
1d	0.02142	0.6252	0.7118	0.0866	999.69
2a	0.08795	0.6647	0.6892	0.0245	1.49
2b	0.08924	0.6644	0.697	0.0326	10.02
2c	0.09054	0.6747	0.7455	0.0708	99.93
2d	0.09184	0.6785	0.8018	0.1233	999.81

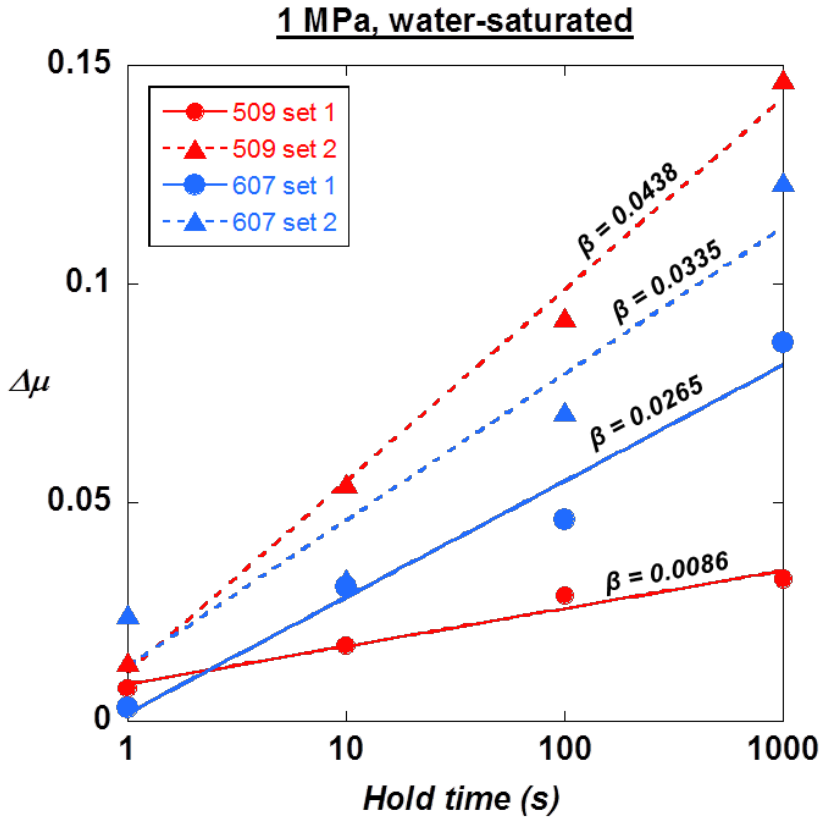

Fig. A2.11 1 MPa, water-saturated, slide-hold-slide data

1 MPa, brine-saturated, experimental runs

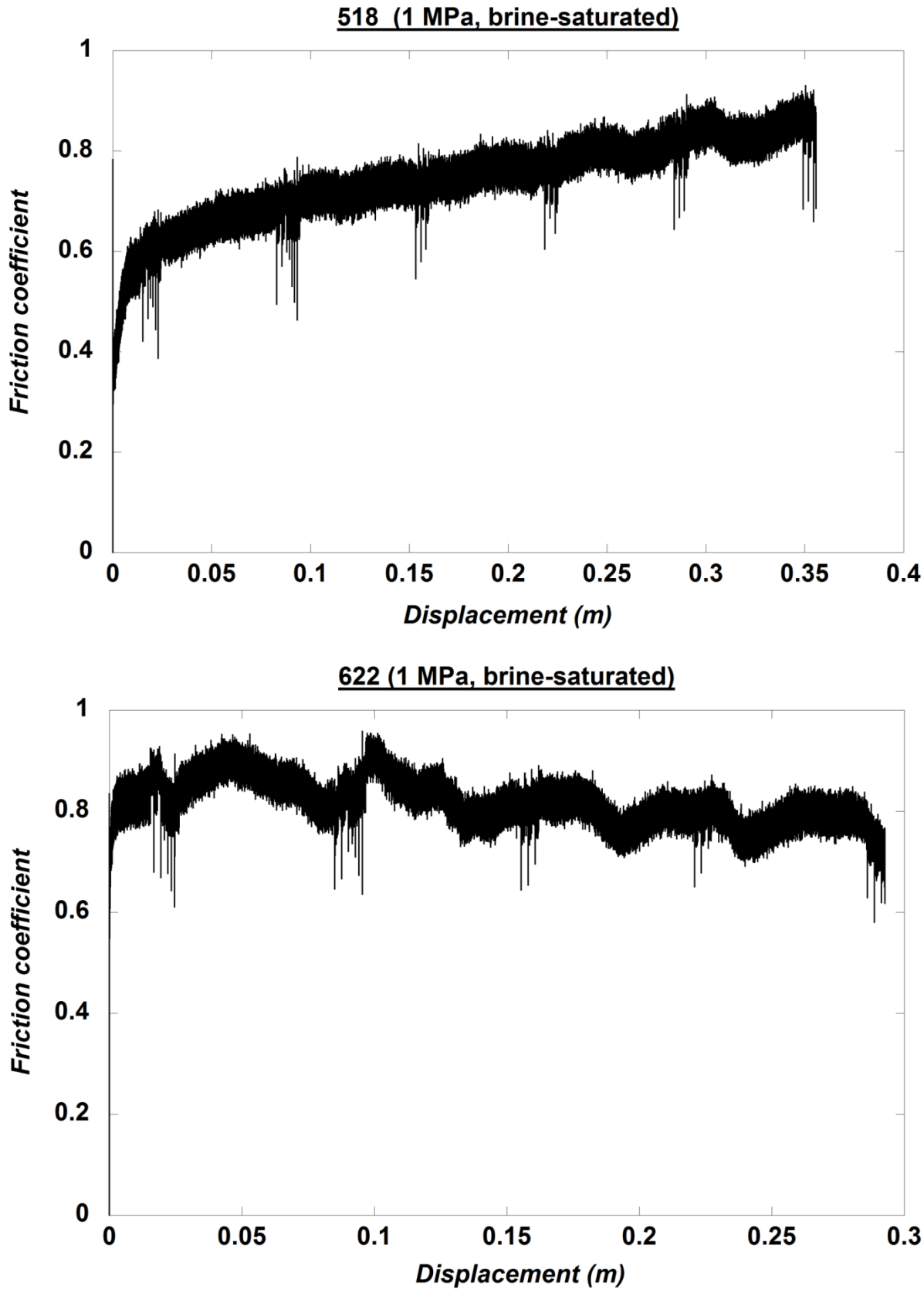

Figure A2.12 1 MPa, brine-saturated, experimental runs

1 MPa, brine-saturated, velocity-step data

Run 1: Experiment 518

Displacement (m)	V_0 (μm/s)	V (μm/s)	K (μ/m)	a	b_1	D_{c1} (m)	a-b	σ2 (k)	σ2 (a)	σ2 (b_1)	σ2 (D_{c1})	Propagated uncertainty (a-b)
0.0139	13	130	154984.433	0.013813	0.0022891	1.26E-04	0.0115	1.06E+04	1.82E+00	1.11E+01	4.14E+00	68064.25257
0.0165	13	130	16845.3341	0.027377	0.015254	5.62E-06	0.0121	5.87E-01	3.13E-01	5.60E-01	7.38E-01	9.794922053
0.0843	13	130	311821.159	0.021579	0.0098982	4.88E-05	0.0117	3.12E+02	1.42E-01	2.99E-01	4.61E-01	5.968109665
0.0868	13	130	154709.545	0.027285	0.011453	1.62E-05	0.0158	1.56E+02	5.06E-01	1.21E+00	5.91E-01	53.32623904
0.1546	13	130	41350.3562	0.025946	0.012856	2.08E-05	0.0131	1.84E+00	1.73E-01	3.46E-01	4.60E-01	5.706221735
0.1572	13	130	50016.5537	0.030109	0.016128	1.89E-05	0.0140	3.47E+00	1.57E-01	2.90E-01	3.90E-01	3.728138823
0.22	13	130	270604.992	0.022686	0.014069	2.94E-05	0.0086	5.26E+02	1.41E+00	2.33E+00	1.91E+00	90.3823076
0.2225	13	130	552311.353	0.023761	0.015064	3.65E-05	0.0087	3.69E+00	1.47E-01	2.29E-01	3.06E-01	3.60218865
0.2853	13	130	14494.977	0.021284	0.010967	2.81E-05	0.0103	8.11E-01	1.89E-01	3.62E-01	4.90E-01	7.251083532
0.2879	13	130	179358.488	0.024009	0.01133	3.44E-05	0.0127	2.13E+01	1.46E-01	3.04E-01	4.14E-01	5.321003107
0.3506	13	130	77498.5148	0.028455	0.018312	1.31E-05	0.0101	2.74E+00	1.98E-01	3.06E-01	4.12E-01	4.186888991
0.3532	13	130	51539.3094	0.027277	0.014799	1.33E-05	0.0125	1.34E+00	2.07E-01	3.79E-01	5.03E-01	5.832379662

Run 2: Experiment 622

Displacement (m)	V_0 (μm/s)	V (μm/s)	K (μ/m)	a	b_1	D_{c1} (m)	a-b	σ2 (k)	σ2 (a)	σ2 (b_1)	σ2 (D_{c1})	Propagated uncertainty (a-b)
0.01551	13	130	59768.5546	0.033192	0.011668	1.25E-07	0.0215	8.60E+03	2.10E+04	5.98E+04	3.83E+04	1.41508E+11
0.01821	13	130	22211.1794	0.02861	0.010579	1.05E-07	0.0180	7.61E+00	4.59E+01	1.24E+02	7.52E+01	621119.6425
0.0864	13	130	137426.683	0.018697	0.0094921	1.05E-04	0.0092	2.42E+01	1.11E-01	2.08E-01	3.06E-01	4.063222174
0.08902	13	130	21428.1571	0.021927	0.010535	1.13E-07	0.0114	3.55E+02	8.88E+02	1.85E+03	1.28E+03	87768552.53
0.1568	13	130	176752.21	0.015021	0.0083031	9.95E-05	0.0067	1.13E+01	1.39E-01	2.41E-01	3.52E-01	6.037536175
0.1594	13	130	163748.57	0.02203	0.013391	1.81E-05	0.0086	3.03E+01	2.46E-01	4.02E-01	4.65E-01	7.530096322
0.2222	13	130	23193.8285	0.018839	0.010825	1.06E-07	0.0080	3.72E+03	1.15E+04	2.00E+04	1.42E+04	6811307732
0.2248	13	130	56996.792	0.014573	0.0077949	5.17E-05	0.0068	1.41E+02	2.00E-01	3.64E-01	5.57E-01	10.55358806
0.2875	13	130	128658.672	0.01989	0.01877	1.20E-05	0.0011	2.10E+02	6.73E-01	7.15E-01	2.27E+00	17.32360026
0.2901	13	130	190686.88	0.01153	0.010486	8.75E-05	0.0010	4.59E+01	2.00E-01	2.11E-01	3.05E-01	8.761015626

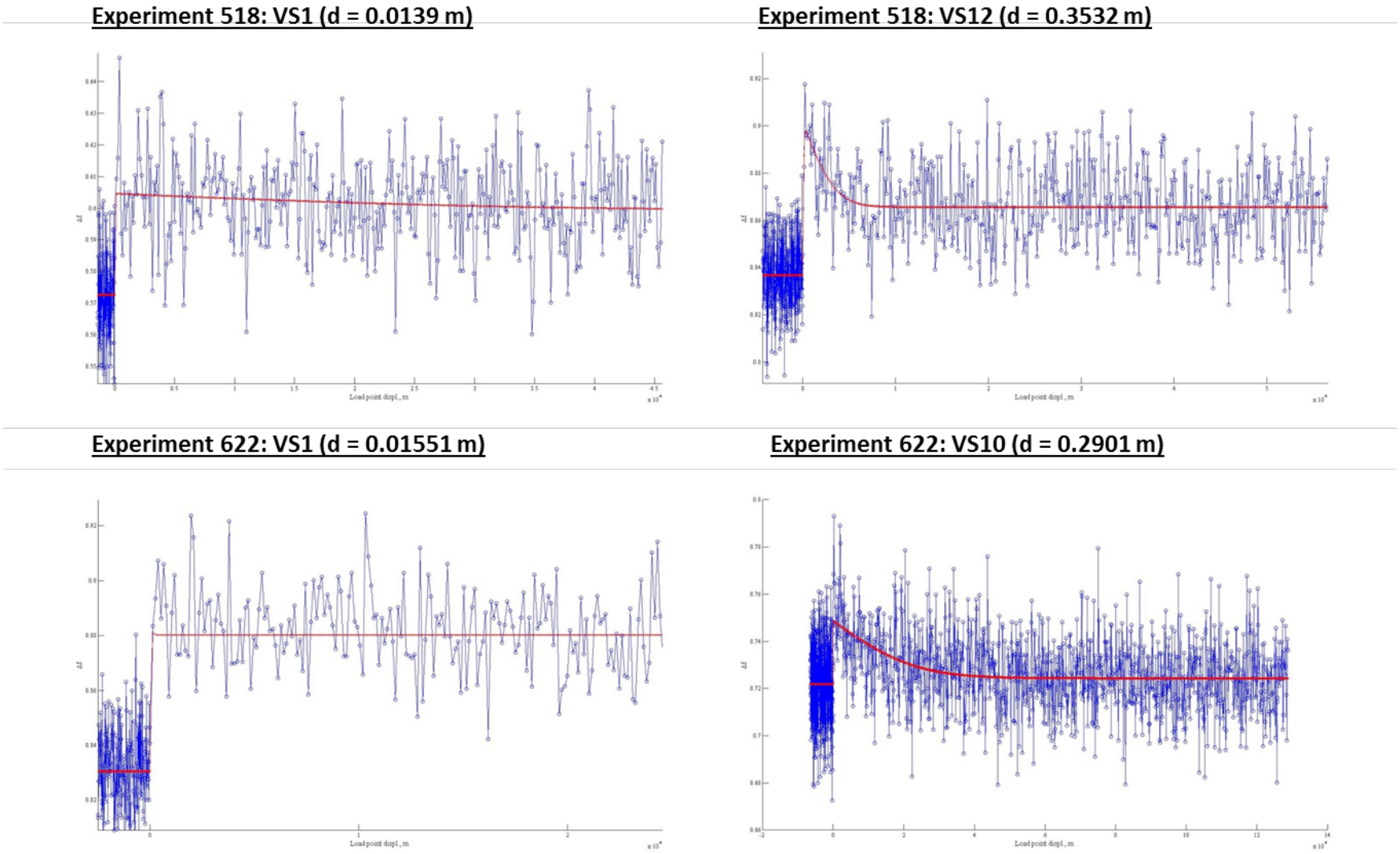

Figure A2.13 Examples of modelled velocity steps for experiments performed under brine-saturated conditions at 1 MPa. Blue curve is the raw experimental data; red curve is the modelled data.

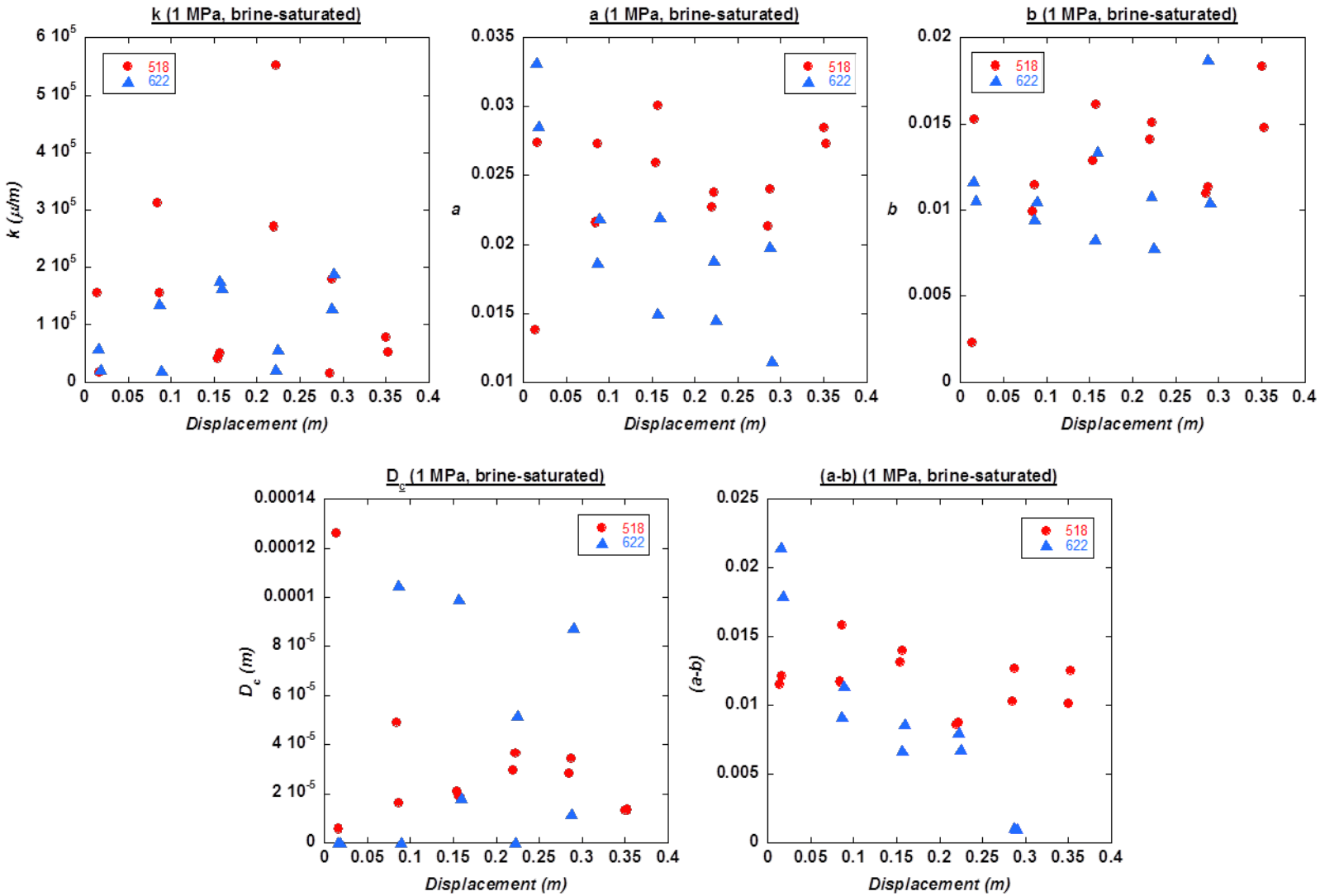

Figure A2.14 Graphical comparison of modelled data results for experiments performed under brine-saturated conditions at 1 MPa.

1 MPa, brine-saturated, slide-hold-slide data
Run 1: Experiment 518

SHS	Displacement (m)	μ_d	μ_s	$\Delta\mu$	Δt (s)
1a	0.01911	0.5959	0.615	0.0191	0.65
1b	0.02041	0.6057	0.6241	0.0184	10.11
1c	0.02171	0.6059	0.6385	0.0326	100.01
1d	0.023	0.6038	0.6426	0.0388	999.79
2a	0.0894	0.6758	0.6837	0.0079	0.81
2b	0.0907	0.6771	0.7034	0.0263	10.12
2c	0.092	0.6779	0.7287	0.0508	99.81
2d	0.09329	0.6766	0.7509	0.0743	1000.13

Run 2: Experiment 622

SHS	Displacement (m)	μ_d	μ_s	$\Delta\mu$	Δt (s)
1a	0.02082	0.8243	0.833	0.0087	0.78
1b	0.02212	0.8119	0.8287	0.0168	9.92
1c	0.02342	0.8046	0.8301	0.0255	99.95
1d	0.02472	0.8043	0.8714	0.0671	1000.07
2a	0.09161	0.8199	0.8296	0.0097	0.79
2b	0.09291	0.8282	0.8686	0.0404	9.97
2c	0.09421	0.8293	0.8831	0.0538	99.83
2d	0.0955	0.842	0.9172	0.0752	999.83

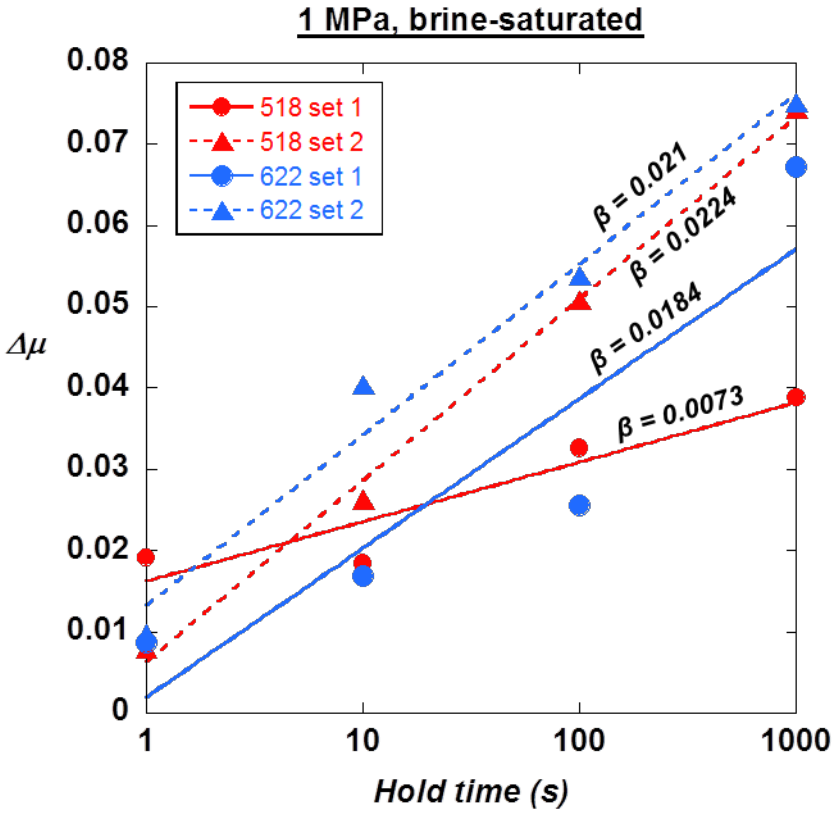

Fig. A2.15 1 MPa, brine-saturated, slide-hold-slide data

18 MPa, room-humidity, experimental runs

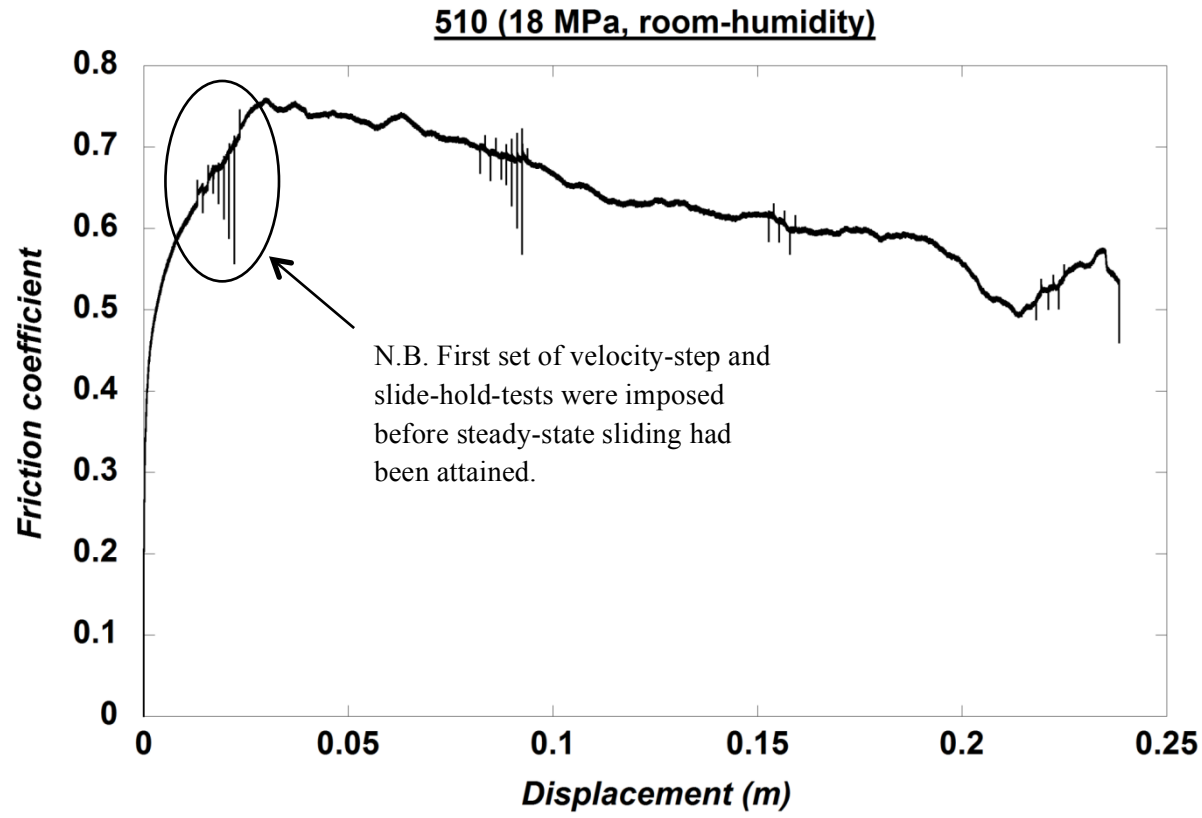

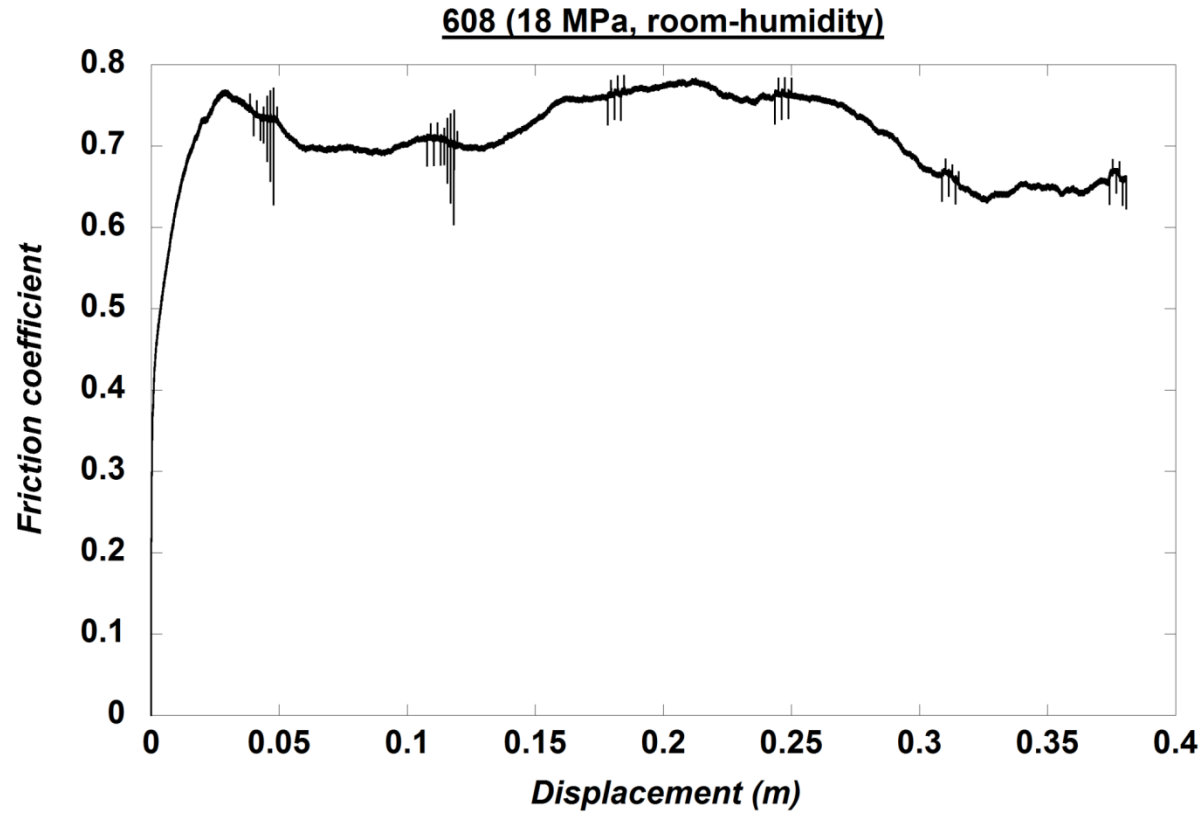

Figure A2.16 1 MPa, room humidity, experimental runs

Appendix 2

18 MPa, room-humidity, velocity-step data

Run 1: Experiment 510

Displacement (m)	V_0 (μm/s)	V (μm/s)	K (μ/m)	a	b_1	b_2	D_{c1} (m)	D_{c2} (m)	b_1+b_2	$D_{c1}+D_{c2}$ (m)	a-b	σ2 (k)	σ2 (a)	σ2 (b_1)	σ2 (b_2)	σ2 (D_{c1})	σ2 (D_{c2})	Propagated uncertainty (a-b)
0.0132	13	130	20145.247	0.010932	0.0034269	4.66E-06	2.72E-03	3.54E-05	6.14E-03	4.01E-05	0.0048	3.21E-01	6.04E-02	1.93E-01	1.44E-01	3.09E-01	1.43E-01	809.2099616
0.0157	13	130	15683.4634	0.01149	0.004254	3.36E-06	3.63E-03	5.32E-05	7.88E-03	5.65E-05	0.0036	2.29E-01	7.42E-02	1.93E-01	6.66E-02	2.78E-01	8.31E-02	520.7033169
0.0835	13	130	9957.1433	0.01047	0.0088464	9.46E-07	1.20E-03	1.44E-05	1.00E-02	1.54E-05	0.0004	1.52E-01	1.33E-01	1.47E-01	3.63E-01	2.45E-01	4.08E-01	79.91973914
0.0861	13	130	9665.2002	0.011681	0.010249	1.07E-06	1.64E-03	2.63E-05	1.19E-02	2.74E-05	-0.0002	1.89E-01	9.98E-02	1.08E-01	1.65E-01	1.68E-01	1.98E-01	31.29440515
0.154	13	130	10748.844	0.0089724	0.0077933	1.27E-06	1.65E-03	7.96E-05	9.44E-03	8.09E-05	-0.0005	4.19E-01	1.20E-01	1.35E-01	9.05E-02	1.89E-01	1.23E-01	79.89656011
0.1566	13	130	14927.5986	0.0078208	0.006852	1.69E-06	3.40E-03	2.46E-04	1.02E-02	2.48E-04	-0.0024	7.29E-01	1.14E-01	1.26E-01	2.43E-02	1.66E-01	5.00E-02	90.7809986
0.2194	13	130	8848.408	0.0096532	0.0061637	8.83E-07	2.08E-03	3.37E-05	8.24E-03	3.45E-05	0.0014	3.92E-01	2.28E-01	3.49E-01	1.15E-01	4.93E-01	1.44E-01	834.6590148
0.2224	13	130	148304.34	0.0054266	0.0036931	6.00E-06	2.53E-03	1.70E-04	6.22E-03	1.76E-04	-0.0008	1.40E+00	1.02E-01	1.48E-01	5.39E-02	1.97E-01	1.30E-01	408.4836721

Run 2: Experiment 608

Displacement (m)	V_0 (μm/s)	V (μm/s)	K (μ/m)	a	b_1	b_2	D_{c1} (m)	D_{c2} (m)	b_1+b_2	$D_{c1}+D_{c2}$ (m)	a-b	σ2 (k)	σ2 (a)	σ2 (b_1)	σ2 (b_2)	σ2 (D_{c1})	σ2 (D_{c2})	Propagated uncertainty (a-b)
0.03878	13	130	8021.6758	0.016988	0.015151	5.33E-07	1.45E-03	1.18E-05	1.66E-02	1.24E-05	0.0004	1.99E-01	2.43E-01	2.58E-01	2.91E-01	3.92E-01	3.44E-01	86.71458039
0.04138	13	130	10308.4509	0.012521	0.011395	9.01E-07	1.72E-03	1.09E-04	1.31E-02	1.10E-04	-0.0006	2.43E-01	9.28E-02	9.84E-02	6.68E-02	1.39E-01	1.16E-01	21.36425922
0.1092	13	130	9082.095	0.010713	0.010115	9.44E-07	1.00E-03	1.91E-05	1.11E-02	2.00E-05	-0.0004	3.07E-01	1.10E-01	1.10E-01	3.50E-01	1.68E-01	4.19E-01	31.98173574
0.1118	13	130	8113.5824	0.011046	0.010596	1.07E-06	7.38E-04	7.13E-05	1.13E-02	7.24E-05	-0.0003	1.82E-01	1.01E-01	1.01E-01	2.11E-01	1.40E-01	2.97E-01	24.74537524
0.1796	13	130	6360.9059	0.012815	0.0096318	6.49E-07	3.79E-03	7.64E-05	1.34E-02	7.70E-05	-0.0006	2.50E-01	2.85E-01	3.75E-01	3.67E-02	4.84E-01	5.39E-02	388.33279
0.1822	13	130	10627.0676	0.012638	0.01013	9.51E-07	3.45E-03	1.47E-04	1.36E-02	1.48E-04	-0.0009	1.96E-01	1.21E-01	1.48E-01	3.20E-02	2.16E-01	5.21E-02	57.02652592
0.2449	13	130	8616.5275	0.012367	0.011145	1.02E-06	1.48E-03	2.06E-05	1.26E-02	2.16E-05	-0.0003	1.91E-01	1.10E-01	1.14E-01	2.40E-01	1.83E-01	2.84E-01	29.59883735
0.2475	13	130	12821.5484	0.012971	0.012098	1.05E-06	1.55E-03	2.86E-05	1.36E-02	2.97E-05	-0.0007	2.27E-01	8.63E-02	8.88E-02	1.72E-01	1.29E-01	2.12E-01	15.62385386
0.3102	13	130	13485.6948	0.0085477	0.0085952	1.37E-06	1.03E-03	1.01E-04	9.63E-03	1.02E-04	-0.0011	2.47E-01	1.07E-01	1.04E-01	1.22E-01	1.37E-01	2.37E-01	38.07507573
0.3128	13	130	8887.449	0.007792	0.008176	1.43E-06	7.88E-04	5.88E-05	8.96E-03	6.02E-05	-0.0012	2.71E-01	1.26E-01	1.17E-01	2.32E-01	1.53E-01	3.17E-01	47.88626323
0.3756	13	130	8757.429	0.0093373	0.0081608	1.02E-06	1.30E-03	2.09E-05	9.46E-03	2.19E-05	-0.0001	2.28E-01	1.26E-01	1.36E-01	2.28E-01	2.20E-01	2.74E-01	75.59062038
0.3782	13	130	11207.1818	0.0096369	0.0095719	1.31E-06	1.96E-03	5.48E-05	1.15E-02	5.61E-05	-0.0019	2.29E-01	1.11E-01	1.08E-01	9.97E-02	1.48E-01	1.51E-01	34.98164393

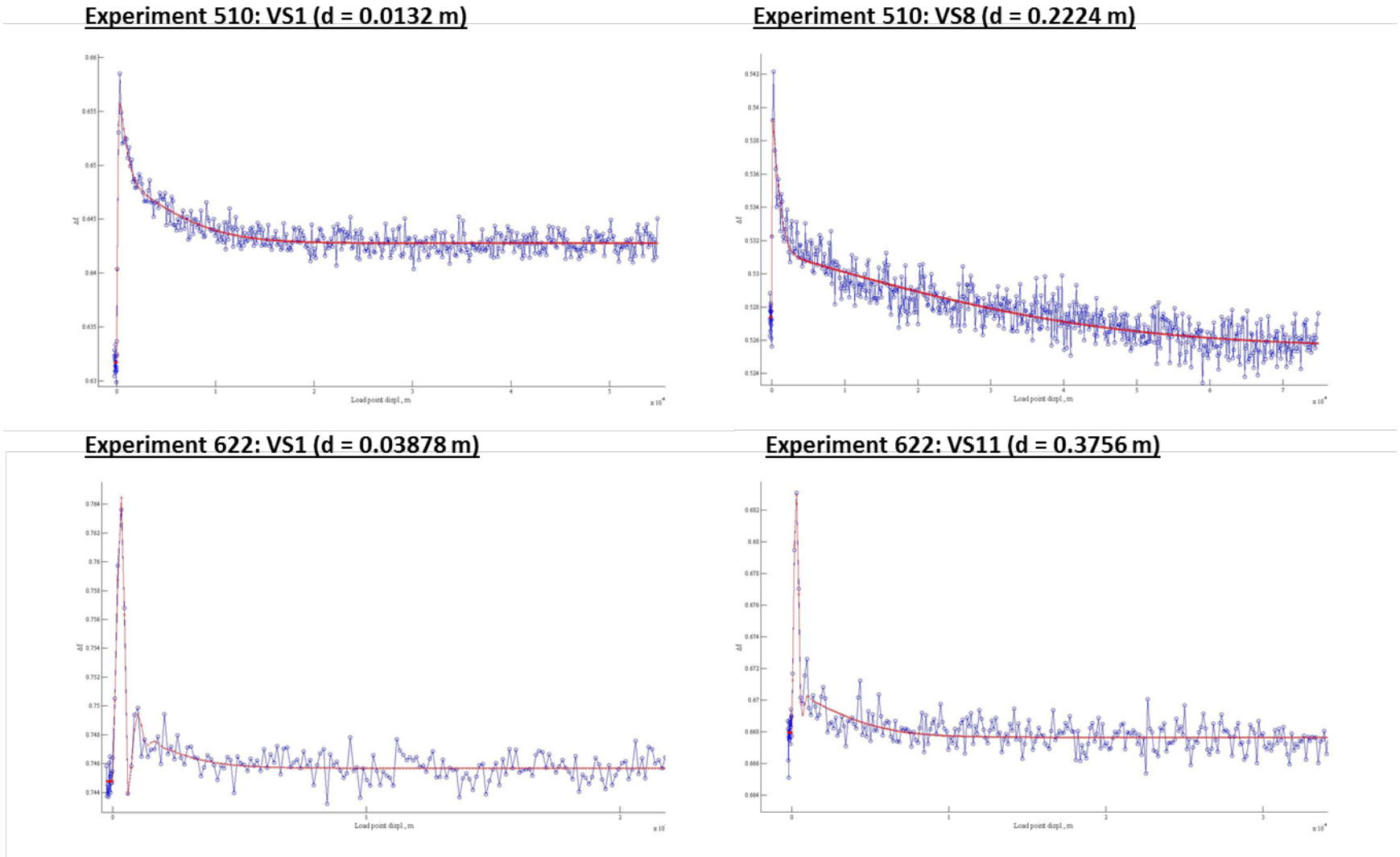

Figure A2.17 Examples of modelled velocity steps for experiments performed under room-humidity conditions at 18 MPa. Blue curve is the raw experimental data; red curve is the modelled data.

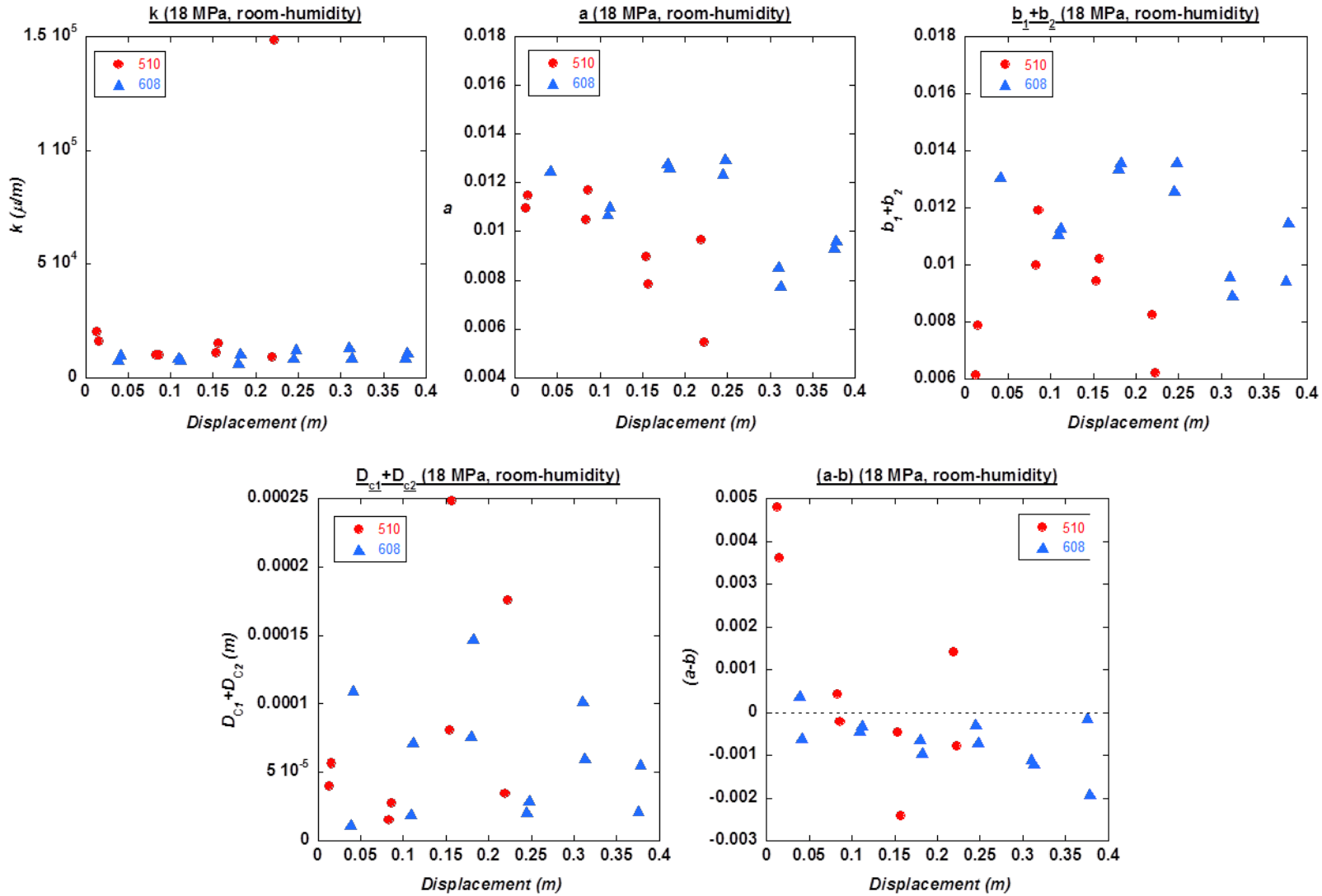

Figure A2.18 Graphical comparison of modelled data results for experiments performed under room-humidity conditions at 18 MPa.

18 MPa, room-humidity, slide-hold-slide data

Run 1: Experiment 510

SHS	Displacement (m)	μ_d	μ_s	$\Delta\mu$	Δt (s)
1a	0.01833	0.6746	0.6775	0.0029	1.49
1b	0.01961	0.6813	0.6864	0.0051	10.65
1c	0.02091	0.6943	0.7017	0.0074	100.06
1d	0.0222	0.7058	0.7117	0.0059	999.77
2a	0.08867	0.6892	0.7014	0.0122	1.1
2b	0.08997	0.6853	0.7076	0.0223	10.05
2c	0.09127	0.6831	0.7147	0.0316	99.28
2d	0.09257	0.6839	0.7201	0.0362	999.85

Run 2: Experiment 608

SHS	Displacement (m)	μ_d	μ_s	$\Delta\mu$	Δt (s)
1a	0.044	0.7342	0.7463	0.0121	0.76
1b	0.04529	0.7341	0.7603	0.0262	10.02
1c	0.04659	0.7329	0.7659	0.033	99.98
1d	0.04789	0.7323	0.7691	0.0368	1000.12
2a	0.1144	0.7076	0.721	0.0134	0.75
2b	0.1157	0.7055	0.7322	0.0267	9.94
2c	0.117	0.7022	0.7376	0.0354	99.89
2d	0.1183	0.7011	0.7426	0.0415	999.83

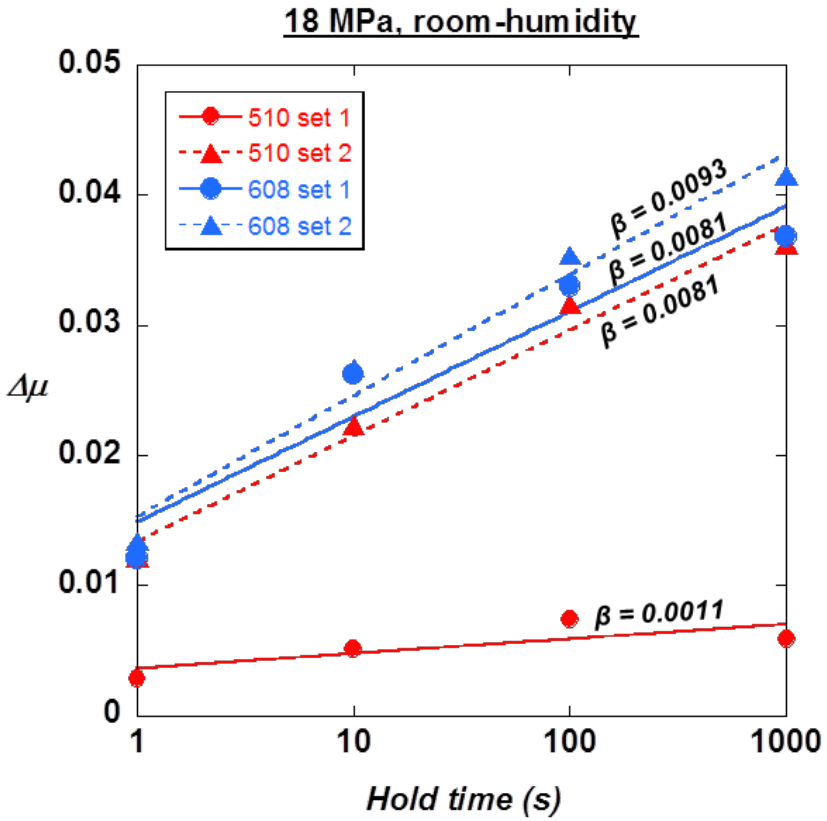

Fig. A2.19 18 MPa, room humidity, slide-hold-slide data

18 MPa, water-saturated, experimental runs

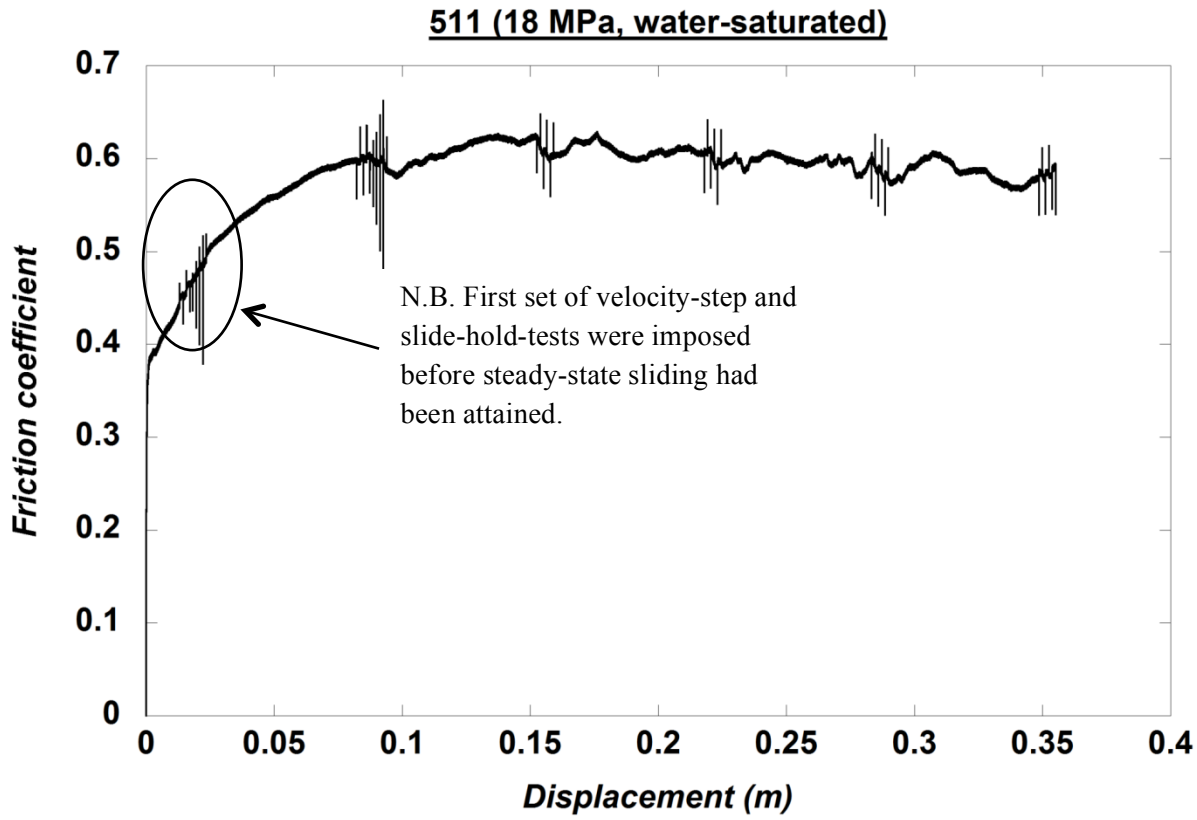

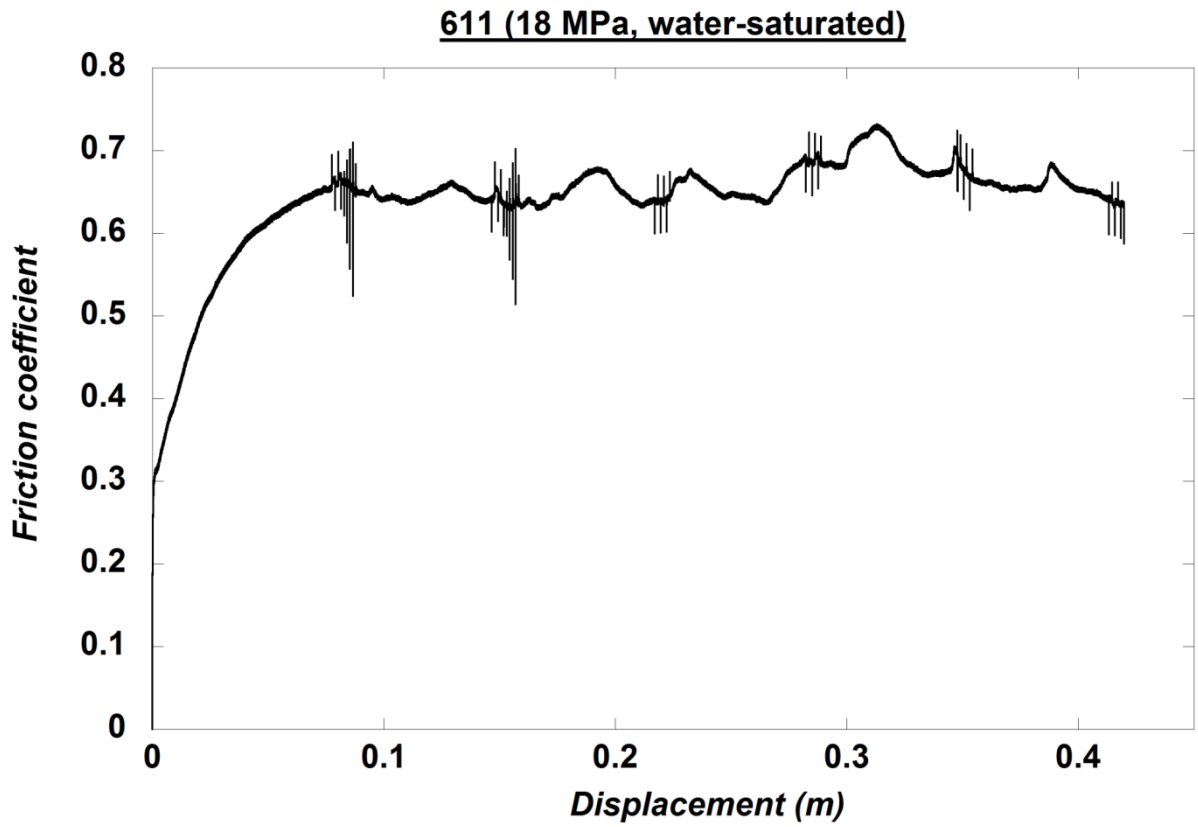

Figure A2.20 18 MPa, room humidity, experimental runs

18 MPa, water-saturated, velocity-step data

Run 1: Experiment 511

Displacement (m)	V_0 (μm/s)	V (μm/s)	K (μ/m)	a	b_1	b_2	D_{c1} (m)	D_{c2} (m)	b_1+b_2	$D_{c1}+D_{c2}$ (m)	a-b	σ2 (k)	σ2 (a)	σ2 (b_1)	σ2 (b_2)	σ2 (D_{c1})	σ2 (D_{c2})	Propagated uncertainty (a-b)
0.0132	13	130	19259.9841	0.010713	0.0058643	2.32E-06	1.99E-03	2.23E-05	7.86E-03	2.46E-05	0.0029	4.34E-01	8.93E-02	1.59E-01	2.26E-01	2.65E-01	2.32E-01	199.591811
0.0157	13	130	11986.9623	0.010773	0.0067279	3.07E-06	1.57E-03	3.12E-05	8.30E-03	3.43E-05	0.0025	1.78E-01	6.94E-02	1.07E-01	2.14E-01	1.72E-01	2.26E-01	74.2684201
0.0836	13	130	24760.2157	0.017592	0.012429	2.66E-06	3.69E-03	2.03E-05	1.61E-02	2.30E-05	0.0015	2.03E-01	4.61E-02	6.62E-02	1.41E-01	1.11E-01	1.35E-01	8.735224782
0.0862	13	130	20417.1945	0.016102	0.013632	4.33E-06	2.25E-03	9.89E-05	1.59E-02	1.03E-04	0.0002	1.23E-01	3.93E-02	4.39E-02	6.91E-02	6.26E-02	9.66E-02	3.856538934
0.1539	13	130	95839.1026	0.016797	0.014945	3.54E-06	4.48E-03	1.24E-04	1.94E-02	1.28E-04	-0.0026	9.17E+00	3.48E-01	3.96E-01	3.41E-02	2.14E-01	4.76E-02	184.157201
0.1565	13	130	26438.1232	0.017168	0.01528	3.05E-06	3.35E-03	6.72E-05	1.86E-02	7.03E-05	-0.0015	1.66E-01	4.28E-02	4.63E-02	5.65E-02	6.61E-02	7.10E-02	3.394726697
0.2193	13	130	21672.1301	0.016759	0.013759	2.96E-06	2.61E-03	5.42E-05	1.64E-02	5.71E-05	0.0004	1.74E-01	4.76E-02	5.56E-02	8.94E-02	8.19E-02	1.11E-01	5.601480276
0.2219	13	130	20870.4326	0.015791	0.014342	3.32E-06	4.62E-03	1.03E-04	1.90E-02	1.07E-04	-0.0032	1.53E-01	4.88E-02	5.12E-02	3.40E-02	7.12E-02	4.93E-02	4.54337285
0.2846	13	130	20690.4318	0.016439	0.014853	2.18E-06	3.27E-03	1.12E-04	1.81E-02	1.15E-04	-0.0017	1.28E-01	5.22E-02	5.56E-02	4.04E-02	7.60E-02	5.74E-02	4.859961334
0.2873	13	130	22737.3006	0.015956	0.015318	2.60E-06	3.08E-03	1.03E-04	1.84E-02	1.06E-04	-0.0024	1.64E-01	5.39E-02	5.39E-02	4.99E-02	7.33E-02	6.94E-02	4.434639681
0.35	13	130	17477.0934	0.015536	0.015522	1.61E-06	2.57E-03	1.72E-04	1.81E-02	1.74E-04	-0.0026	1.80E-01	6.87E-02	6.63E-02	4.49E-02	8.65E-02	7.68E-02	6.052503194
0.3526	13	130	20144.5018	0.015526	0.014995	1.76E-06	0.002883	8.03E-05	1.79E-02	8.21E-05	-0.0024	1.68E-01	6.24E-02	6.26E-02	5.69E-02	8.45E-02	7.68E-02	5.869334711

Run 2: Experiment 611

Displacement (m)	V_0 (μm/s)	V (μm/s)	K (μ/m)	a	b_1	b_2	D_{c1} (m)	D_{c2} (m)	b_1+b_2	$D_{c1}+D_{c2}$ (m)	a-b	σ2 (k)	σ2 (a)	σ2 (b_1)	σ2 (b_2)	σ2 (D_{c1})	σ2 (D_{c2})	Propagated uncertainty (a-b)
0.07768	13	130	16173.2219	0.018878	0.011063	2.48E-06	4.95E-03	1.86E-05	1.60E-02	2.11E-05	0.0029	1.11E-01	5.56E-02	9.16E-02	1.23E-01	1.57E-01	1.17E-01	19.34949529
0.08029	13	130	17940.2872	0.018233	0.011892	2.73E-06	3.92E-03	2.06E-05	1.58E-02	2.34E-05	0.0024	1.29E-01	4.78E-02	7.23E-02	1.37E-01	1.24E-01	1.29E-01	11.14726504
0.1481	13	130	23010.2047	0.018297	0.012393	2.62E-06	2.67E-03	2.09E-05	1.51E-02	2.35E-05	0.0032	1.63E-01	4.49E-02	6.61E-02	1.84E-01	1.12E-01	1.78E-01	9.739853997
0.1506	13	130	30478.4131	0.015943	0.012859	3.69E-06	3.80E-03	1.13E-04	1.67E-02	1.16E-04	-0.0007	3.29E-01	4.54E-02	5.38E-02	3.88E-02	7.56E-02	5.38E-02	5.729728235
0.2184	13	130	20066.0401	0.018124	0.013924	1.40E-06	3.24E-03	7.26E-05	1.72E-02	7.40E-05	0.0010	1.66E-01	6.36E-02	8.03E-02	5.08E-02	1.17E-01	7.33E-02	10.38011515
0.221	13	130	25717.9738	0.017147	0.013887	1.41E-06	3.19E-03	7.58E-05	1.71E-02	7.73E-05	0.0001	2.66E-01	6.31E-02	7.59E-02	5.01E-02	1.08E-01	7.20E-02	9.321026054
0.2838	13	130	21496.8758	0.019572	0.01508	1.75E-06	3.49E-03	6.91E-05	1.86E-02	7.08E-05	0.0010	1.21E-01	5.17E-02	6.47E-02	4.94E-02	9.32E-02	6.89E-02	6.100008634
0.2865	13	130	17568.0072	0.019729	0.014967	1.31E-06	2.95E-03	7.06E-05	1.79E-02	7.20E-05	0.0018	1.30E-01	6.46E-02	8.23E-02	5.65E-02	1.21E-01	8.03E-02	9.95736833
0.3493	13	130	21268.6912	0.019793	0.015817	1.41E-06	4.19E-03	7.67E-05	2.00E-02	7.81E-05	-0.0002	1.16E-01	5.64E-02	6.82E-02	3.77E-02	9.80E-02	5.49E-02	6.049027948
0.3519	13	130	26509.7209	0.018385	0.015153	1.85E-06	3.28E-03	7.04E-05	1.84E-02	7.22E-05	0.0000	1.95E-01	5.01E-02	5.89E-02	5.10E-02	8.34E-02	7.23E-02	5.128472999
0.4147	13	130	10765.4815	0.013815	0.01128	9.02E-07	2.69E-03	6.02E-05	1.40E-02	6.11E-05	-0.0002	1.75E-01	1.10E-01	1.31E-01	6.33E-02	1.97E-01	8.75E-02	37.3842656
0.4173	13	130	16397.5127	0.012783	0.010297	1.30E-06	3.02E-03	8.88E-05	1.33E-02	9.01E-05	-0.0005	2.01E-01	8.16E-02	9.84E-02	4.38E-02	1.40E-01	6.45E-02	25.73621672

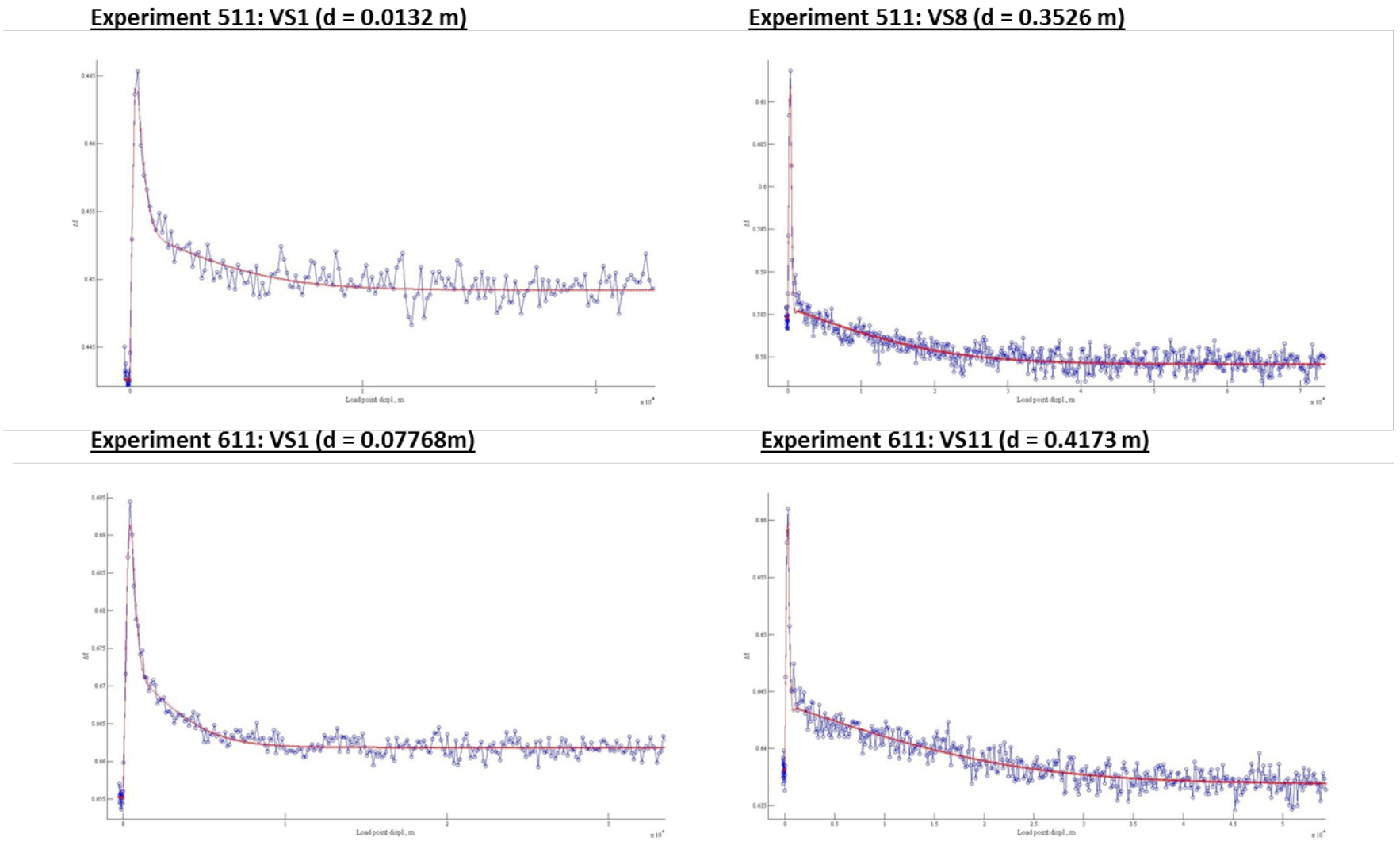

Figure A2.21 Examples of modelled velocity steps for experiments performed under water-saturated conditions at 18 MPa. Blue curve is the raw experimental data; red curve is the modelled data.

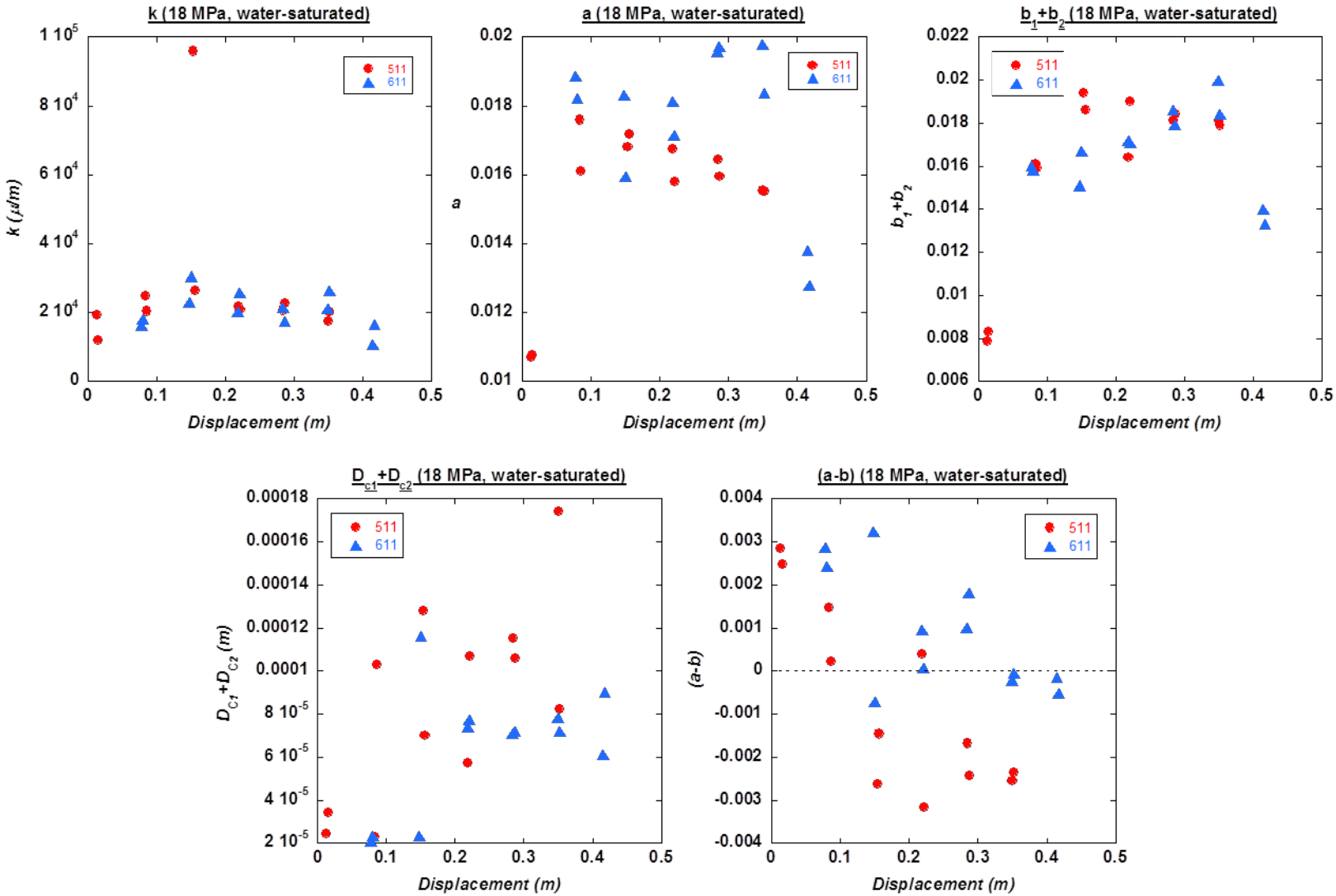

Figure A2.22 Graphical comparison of modelled data results for experiments performed under water-saturated conditions at 18 MPa.

18 MPa, water-saturated, slide-hold-slide data

Run 1: Experiment 511

SHS	Displacement (m)	μ_d	μ_s	$\Delta\mu$	Δt (s)
1a	0.01834	0.4686	0.4755	0.0069	0.86
1b	0.01963	0.4742	0.4874	0.0132	10.13
1c	0.02093	0.4803	0.5026	0.0223	100.24
1d	0.02222	0.4863	0.5147	0.0284	1000.06
2a	0.08877	0.5978	0.6173	0.0195	2.04
2b	0.09004	0.5942	0.6271	0.0329	10.12
2c	0.09134	0.5947	0.6452	0.0505	100.08
2d	0.09263	0.5986	0.6613	0.0627	999.88

Run 2: Experiment 611

SHS	Displacement (m)	μ_d	μ_s	$\Delta\mu$	Δt (s)
1a	0.08288	0.6626	0.6725	0.0099	0.86
1b	0.08418	0.6597	0.6865	0.0268	9.86
1c	0.08548	0.6558	0.6995	0.0437	100.03
1d	0.08676	0.6516	0.7085	0.0569	1001.09
2a	0.1532	0.6335	0.6484	0.0149	0.73
2b	0.1545	0.6304	0.6635	0.0331	9.84
2c	0.1558	0.6306	0.683	0.0524	100.07
2d	0.1571	0.6318	0.7007	0.0689	1000.05

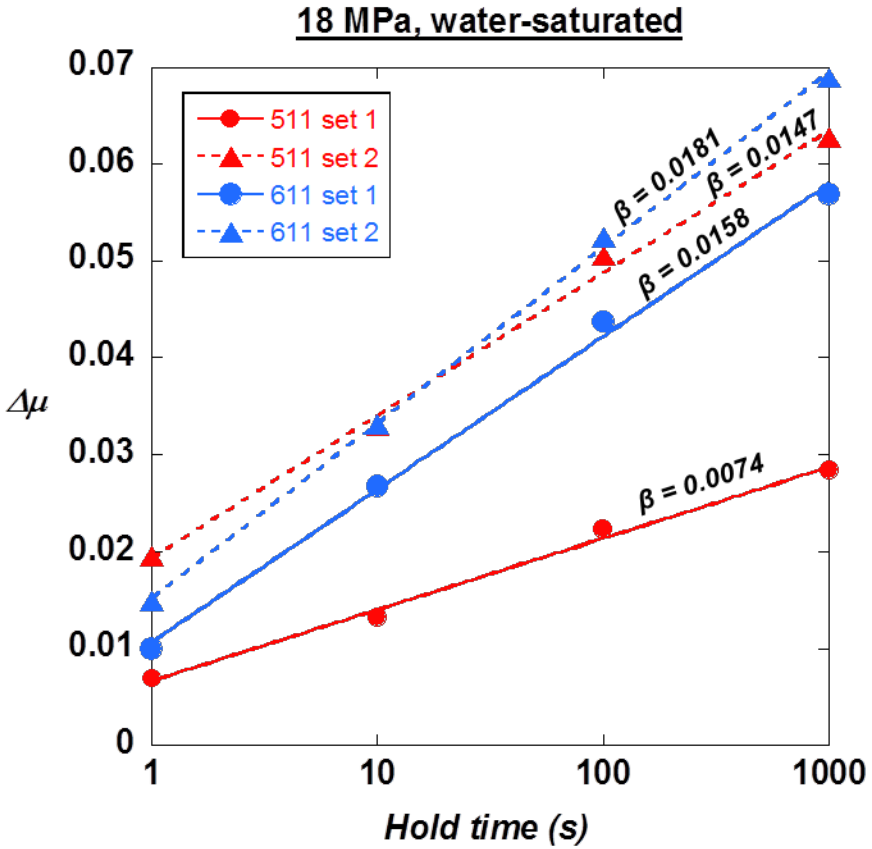

Fig. A2.23 18 MPa, water-saturated, slide-hold-slide data

18 MPa, brine-saturated, experimental runs

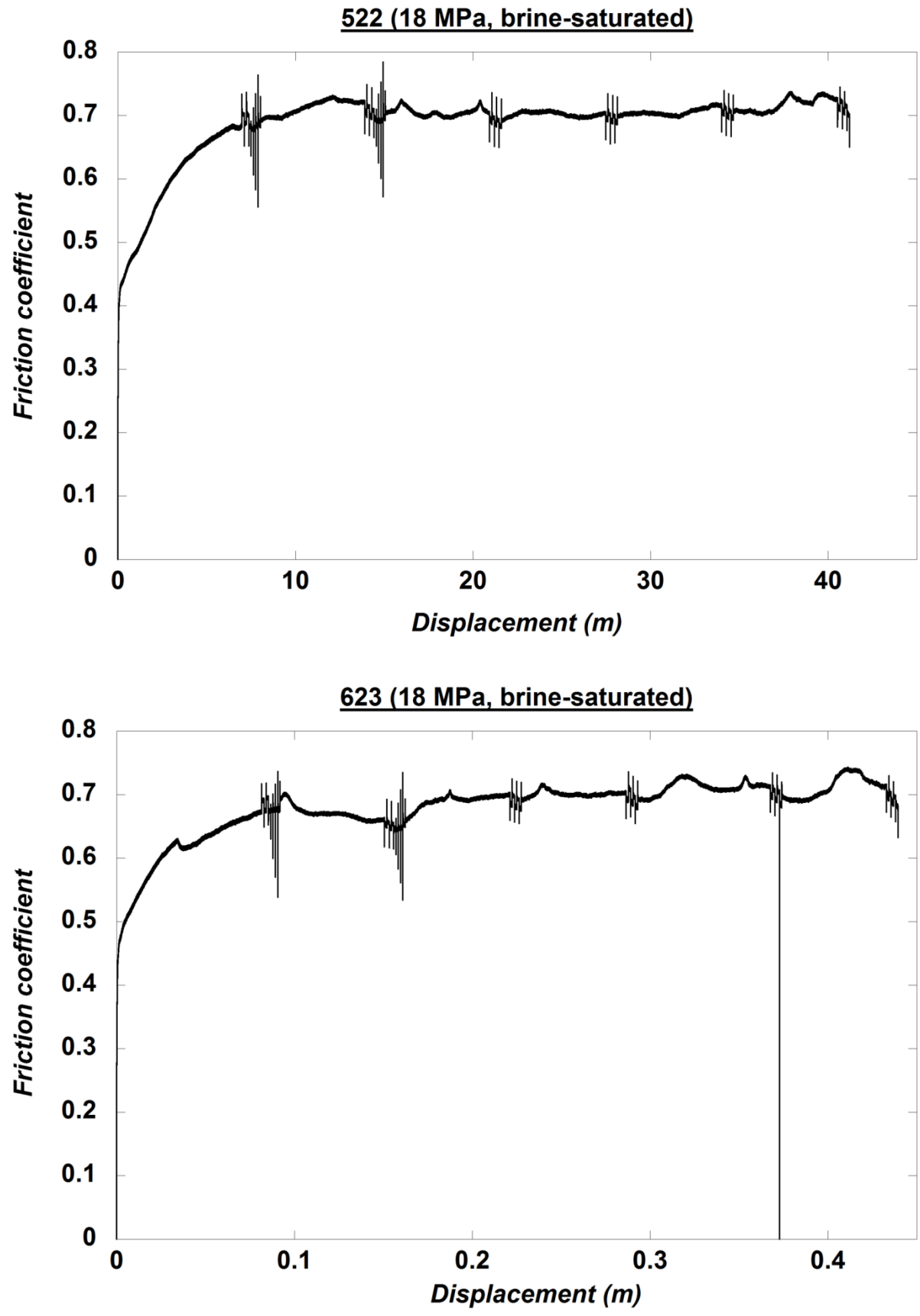

Figure A2.24 18 MPa, water-saturated, experimental runs

18 MPa, brine-saturated, velocity-step data

Run 1: Experiment 522

Displacement (m)	V_0 (μm/s)	V (μm/s)	K (μ/m)	a	b_1	b_2	D_{c1} (m)	D_{c2} (m)	b_1+b_2	$D_{c1}+D_{c2}$ (m)	a-b	σ2 (k)	σ2 (a)	σ2 (b_1)	σ2 (b_2)	σ2 (D_{c1})	σ2 (D_{c2})	Propagated uncertainty (a-b)
0.0699	13	130	21616.3003	0.021511	0.010915	7.46E-06	3.98E-03	6.59E-05	1.49E-02	7.33E-05	0.0066	1.06E-01	2.53E-02	4.83E-02	6.99E-02	7.73E-02	1.11E-01	6.11369402
0.0725	13	130	22343.2859	0.020264	0.010397	8.29E-06	3.27E-03	1.03E-04	1.37E-02	1.12E-04	0.0066	1.10E-01	2.56E-02	4.60E-02	5.77E-02	6.97E-02	6.91E-02	6.282137893
0.1404	13	130	20722.4976	0.021082	0.013128	4.05E-06	2.49E-03	1.05E-04	1.56E-02	1.10E-04	0.0055	9.59E-02	3.66E-02	5.56E-02	6.64E-02	7.92E-02	1.06E-01	6.725617947
0.143	13	130	29230.3195	0.021634	0.012995	3.12E-06	3.62E-03	5.42E-05	1.66E-02	5.74E-05	0.0050	1.45E-01	3.88E-02	6.18E-02	6.62E-02	9.25E-02	8.20E-02	7.370791139
0.2108	13	130	29276.0212	0.021186	0.013809	3.26E-06	4.37E-03	1.26E-04	1.82E-02	1.29E-04	0.0030	1.34E-01	3.61E-02	5.29E-02	2.96E-02	7.44E-02	4.28E-02	4.738113148
0.2134	13	130	25943.5048	0.019825	0.012444	3.64E-06	3.98E-03	7.57E-05	1.64E-02	7.93E-05	0.0034	1.58E-01	3.85E-02	5.86E-02	4.86E-02	8.59E-02	6.46E-02	6.908998636
0.2762	13	130	26944.8389	0.020608	0.013378	1.80E-06	3.00E-03	1.57E-04	1.64E-02	1.59E-04	0.0042	1.54E-01	4.95E-02	7.42E-02	3.77E-02	1.04E-01	7.96E-02	10.17696178
0.2788	13	130	26590.5843	0.019295	0.012519	2.47E-06	2.82E-03	1.07E-04	1.53E-02	1.09E-04	0.0040	1.79E-01	4.45E-02	6.61E-02	4.79E-02	9.39E-02	7.32E-02	9.213499408
0.3441	13	130	23518.9503	0.019283	0.012703	1.47E-06	1.52E-03	9.42E-05	1.42E-02	9.57E-05	0.0051	1.77E-01	6.06E-02	8.98E-02	9.06E-02	1.29E-01	1.41E-01	23.1324338
0.406	13	130	18294.1704	0.020021	0.012266	1.05E-06	2.31E-03	1.27E-04	1.46E-02	1.28E-04	0.0054	1.48E-01	9.19E-02	1.48E-01	5.06E-02	2.01E-01	8.70E-02	48.73753832
0.4094	13	130	12947.7438	0.017013	0.0099256	1.64E-06	2.98E-03	1.30E-04	1.29E-02	1.32E-04	0.0041	1.42E-01	7.89E-02	1.32E-01	3.91E-02	1.80E-01	6.37E-02	50.36875427

Run 2: Experiment 623

Displacement (m)	V_0 (μm/s)	V (μm/s)	K (μ/m)	a	b_1	b_2	D_{c1} (m)	D_{c2} (m)	b_1+b_2	$D_{c1}+D_{c2}$ (m)	a-b	σ2 (k)	σ2 (a)	σ2 (b_1)	σ2 (b_2)	σ2 (D_{c1})	σ2 (D_{c2})	Propagated uncertainty (a-b)
0.08157	13	130	23463.7811	0.019985	0.0098323	5.15E-06	2.61E-03	7.73E-05	1.24E-02	8.25E-05	0.0075	1.25E-01	3.29E-02	6.34E-02	7.89E-02	9.42E-02	1.01E-01	13.66062966
0.08418	13	130	25909.0396	0.019733	0.0082878	4.26E-06	2.97E-03	3.20E-05	1.13E-02	3.63E-05	0.0085	1.40E-01	3.36E-02	8.00E-02	1.35E-01	1.31E-01	1.40E-01	28.26085295
0.152	13	130	21869.5667	0.019699	0.012042	2.88E-06	5.87E-03	1.30E-04	1.79E-02	1.33E-04	0.0018	1.19E-01	4.34E-02	6.82E-02	2.19E-02	9.54E-02	3.58E-02	9.230554581
0.1546	13	130	29534.6555	0.018928	0.011685	3.44E-06	4.95E-03	1.07E-04	1.66E-02	1.11E-04	0.0023	2.17E-01	4.14E-02	6.41E-02	3.06E-02	9.17E-02	4.54E-02	8.815172955
0.2225	13	130	22057.9838	0.019794	0.010842	3.19E-06	2.91E-03	1.34E-04	1.38E-02	1.37E-04	0.0060	1.22E-01	4.04E-02	7.06E-02	4.24E-02	9.83E-02	7.13E-02	13.35584873
0.2251	13	130	21075.9821	0.018941	0.010601	3.36E-06	2.50E-03	1.45E-04	1.31E-02	1.48E-04	0.0058	1.03E-01	3.83E-02	6.55E-02	4.51E-02	9.07E-02	8.16E-02	12.4821499
0.2879	13	130	15681.896	0.025389	0.010487	9.36E-07	5.85E-03	5.90E-06	1.63E-02	6.84E-06	0.0090	1.35E-01	1.81E-01	4.00E-01	2.11E-01	5.58E-01	1.73E-01	388.2836592
0.2905	13	130	29167.0717	0.018527	0.010436	4.15E-06	3.59E-03	1.83E-04	1.40E-02	1.87E-04	0.0045	2.47E-01	3.87E-02	6.54E-02	3.13E-02	9.15E-02	5.58E-02	11.60721947
0.3689	13	130	19638.9209	0.019766	0.011031	1.93E-06	3.47E-03	2.25E-04	1.45E-02	2.27E-04	0.0053	1.09E-01	5.50E-02	9.60E-02	2.65E-02	1.29E-01	5.44E-02	22.14880398
0.3715	13	130	24602.767	0.019098	0.010445	2.20E-06	2.52E-03	1.37E-04	1.30E-02	1.39E-04	0.0061	1.77E-01	5.02E-02	8.92E-02	4.47E-02	1.24E-01	6.79E-02	23.2306411
0.4343	13	130	21998.4175	0.016317	0.0086006	3.14E-06	3.40E-03	1.55E-04	1.20E-02	1.58E-04	0.0043	2.01E-01	5.04E-02	9.18E-02	3.38E-02	1.27E-01	5.34E-02	31.55154299
0.4369	13	130	21540.1315	0.016072	0.0089191	3.17E-06	1.98E-03	1.42E-04	1.09E-02	1.45E-04	0.0052	1.56E-01	5.07E-02	8.76E-02	6.34E-02	1.21E-01	1.21E-01	30.53459082

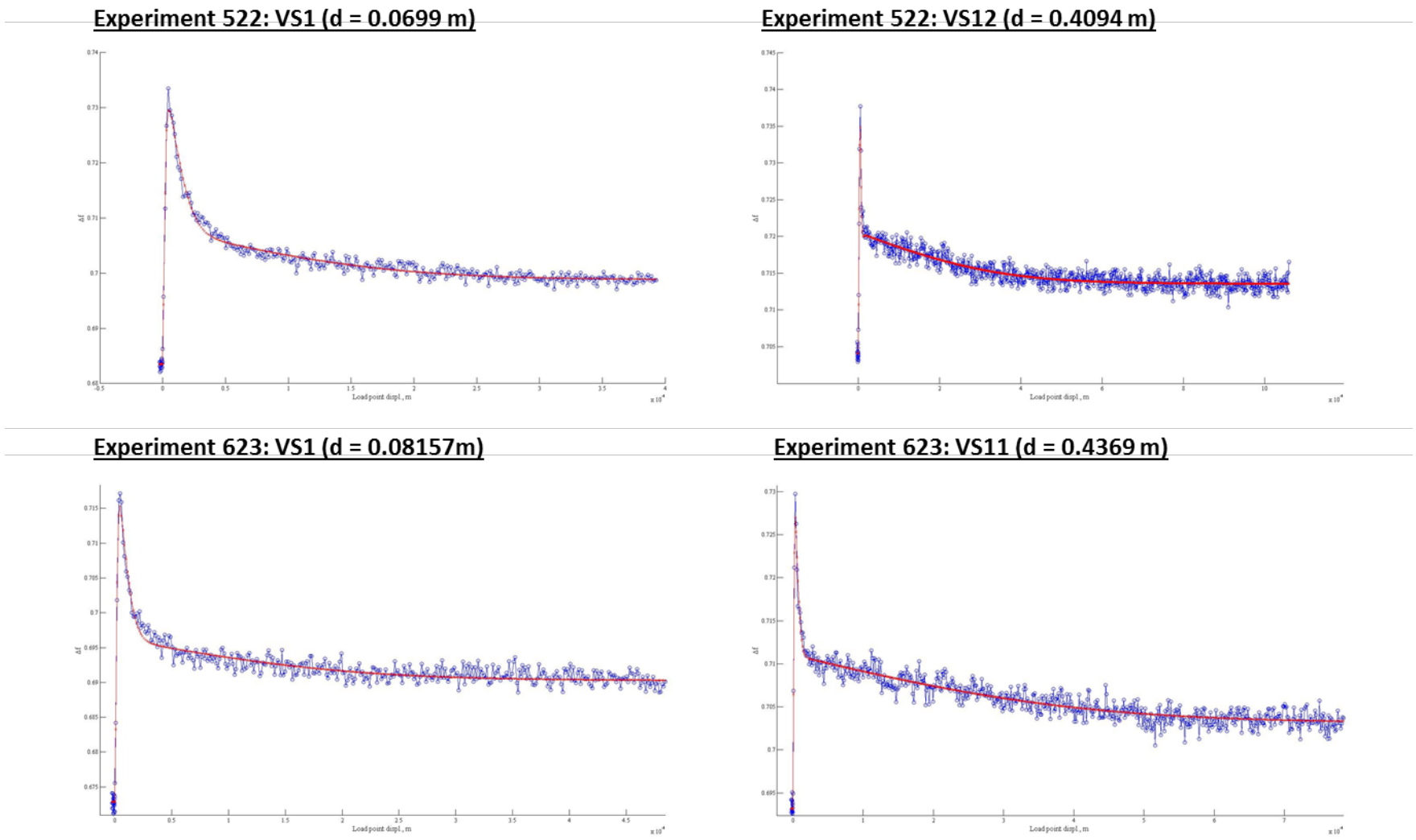

Figure A2.25 Examples of modelled velocity steps for experiments performed under brine-saturated conditions at 18 MPa. Blue curve is the raw experimental data; red curve is the modelled data.

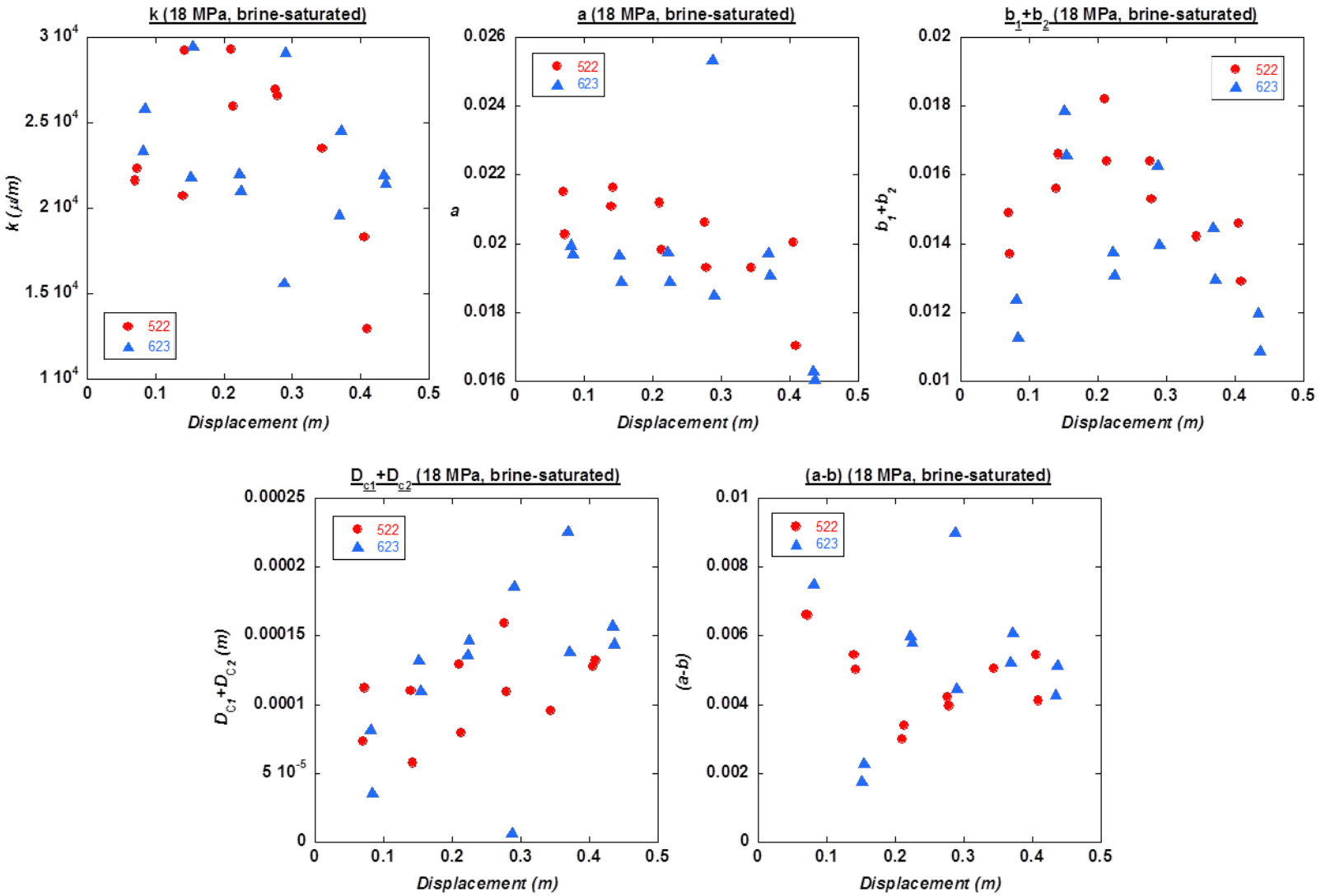

Figure A2.26 Graphical comparison of modelled data results for experiments performed under brine-saturated conditions at 18 MPa.

18 MPa, brine-saturated, slide-hold-slide data

Run 1: Experiment 522

SHS	Displacement (m)	μ_d	μ_s	$\Delta\mu$	Δt (s)
1a	0.07515	0.6802	0.6896	0.0094	0.74
1b	0.07645	0.679	0.7105	0.0315	9.84
1c	0.07775	0.6778	0.7327	0.0549	99.94
1d	0.07905	0.6813	0.7621	0.0808	1000.01
2a	0.1456	0.6932	0.709	0.0158	0.8
2b	0.1469	0.691	0.7322	0.0412	9.95
2c	0.1482	0.6892	0.743	0.0538	100.06
2d	0.1495	0.6913	0.7828	0.0915	1000

Run 2: Experiment 623

SHS	Displacement (m)	μ_d	μ_s	$\Delta\mu$	Δt (s)
1a	0.08678	0.6749	0.6827	0.0078	0.76
1b	0.08808	0.675	0.6991	0.0241	9.94
1c	0.08938	0.6757	0.6914	0.0157	99.9
1d	0.09067	0.6763	0.7349	0.0586	1000.03
2a	0.1572	0.6453	0.661	0.0157	0.76
2b	0.1585	0.6458	0.685	0.0392	10.43
2c	0.1598	0.646	0.706	0.06	100.06
2d	0.1611	0.6475	0.7321	0.0846	988.78

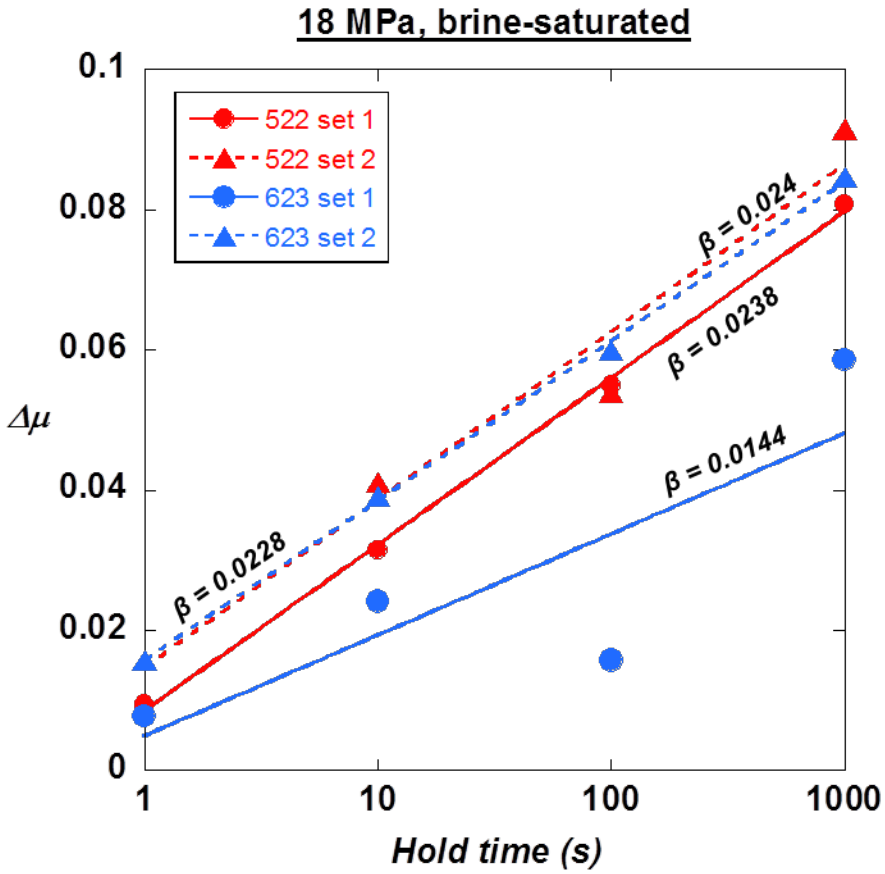

Fig. A2.27 18 MPa, brine-saturated, slide-hold-slide data

Appendix 2.3

Reproducibility of high-velocity friction experiments

The following pages contain:

1) Tables summarising the data obtained during the high-velocity friction experiments.
2) Friction vs. displacement plots not included in the main text, which were obtained during repeat runs of the high-velocity friction experiments, demonstrating good reproducibility of data.

1 MPa, high-velocity friction results

Exp. #	μ_p	μ_r*	μ_{ss}	D_w (m)	Final displacement (m)
Room-humidity					
512	1.1358	0.6224			7.53
513	1.1263	0.5416			13.46
514	1.2848		0.3996	19.2	26.68
532	1.2348		0.3784	21.3	36.77
Water-saturated					
515	0.8714		0.2408		27.22
533	0.6975		0.1972		27.54
534	0.8686		0.2112	33.2	39.03
Brine-saturated					
516	0.9423				16.72
517	0.7243		0.3155	16.7	30.02
535	0.8511		0.2174	16.5	33.35

* μr = the residual friction value, reported for experiments terminated before steady-state sliding was fully established

9 MPa, high-velocity friction results

Exp. #	μ_p	μ_{ss}	D_w (m)	Final displacement (m)
Room-humidity				
523	0.8079	0.2322	0.56	1.005
624	0.7865	0.2035	1.67	4.579
Water-saturated				
524	0.3068	0.0983	0.75	1.401
625	0.3699	0.1057	0.05	2.12
Brine-saturated				
525	0.2966	0.0963	0.013	1.732
626	0.3534	0.1117	0.053	1.214
627	0.3575	0.1048	0.057	1.066

18 MPa, high-velocity friction results

Exp. #	μ_p	μ_{ss}	D_w (m)	Final displacement (m)
Room-humidity				
519	0.753	0.1579	0.29	0.7193
Water-saturated				
520	0.311	0.0905	0.034	1.079
Brine-saturated				
521	0.2886	0.0783	0.033	2.248

Fig. A2.28: 1 MPa, room-humidity, high-velocity friction plots

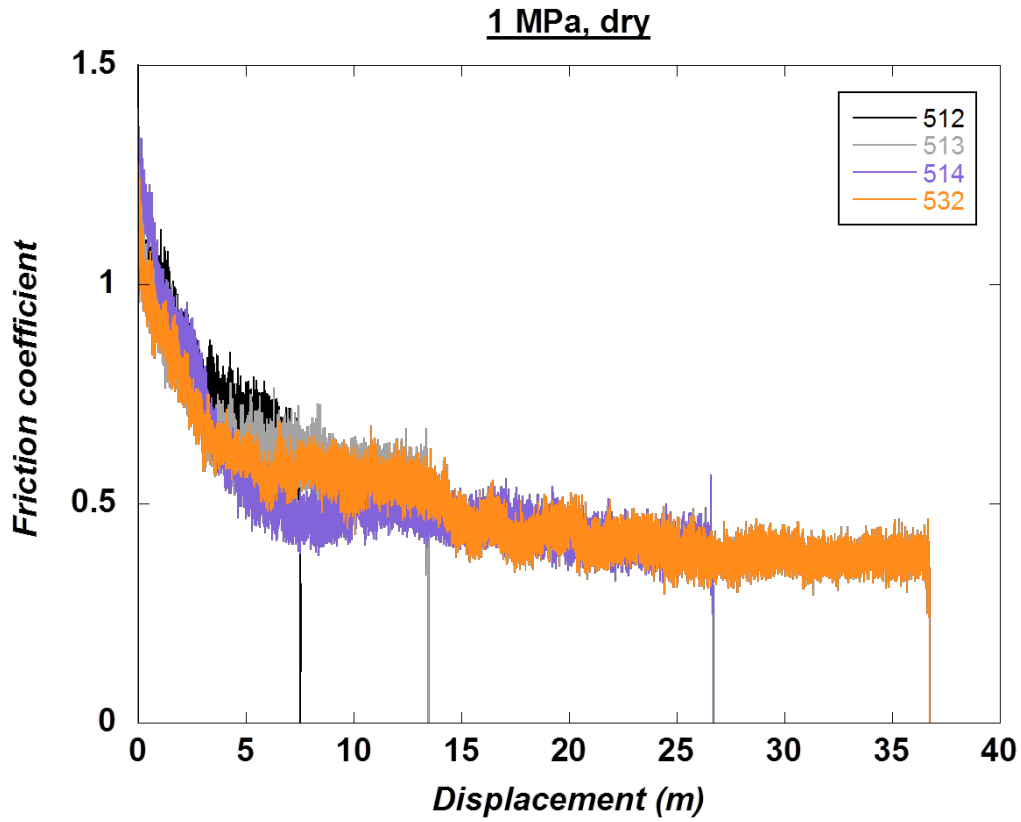

Fig. A2.29: 1 MPa, water-saturated, high-velocity friction plots

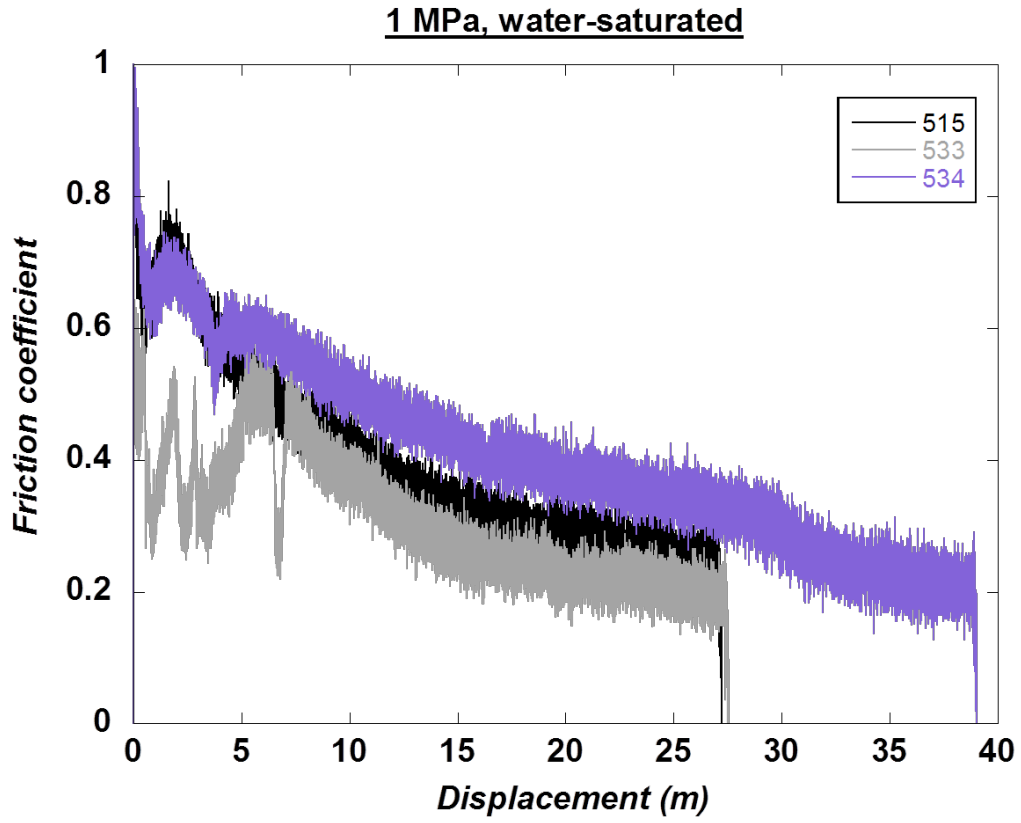

Fig. A2.30: 1 MPa, brine-saturated, high-velocity friction plots

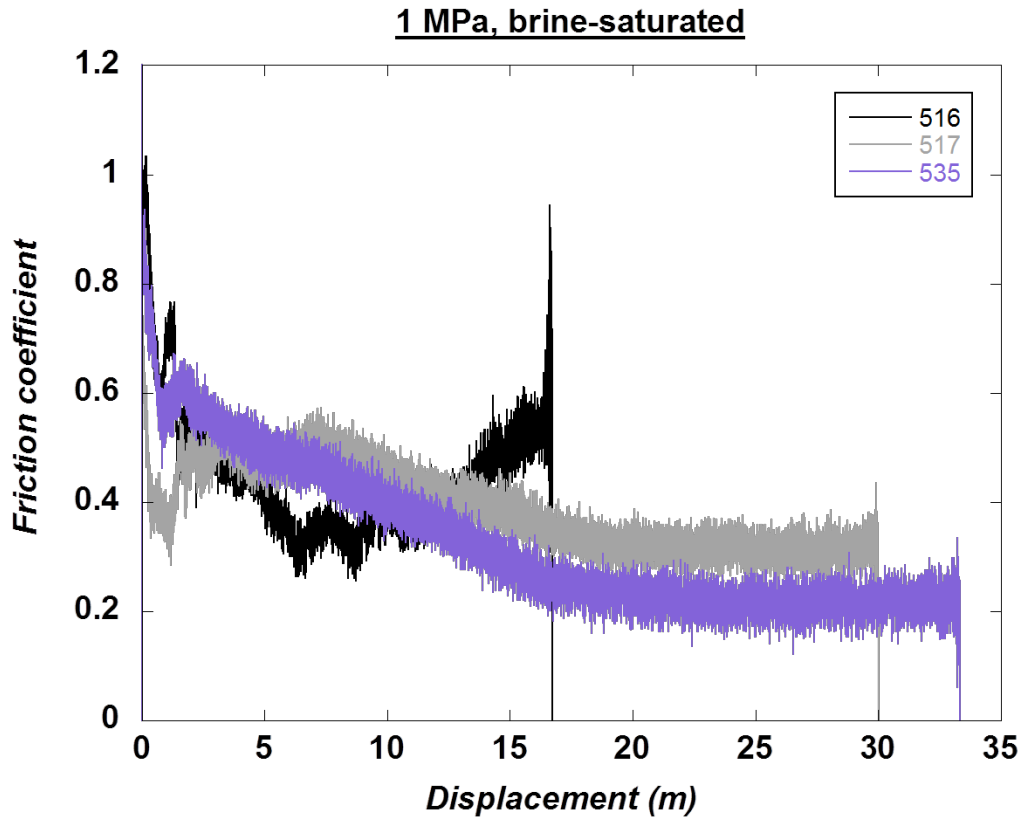

Fig. A2.31: 9 MPa, room-humidity, high-velocity friction plots

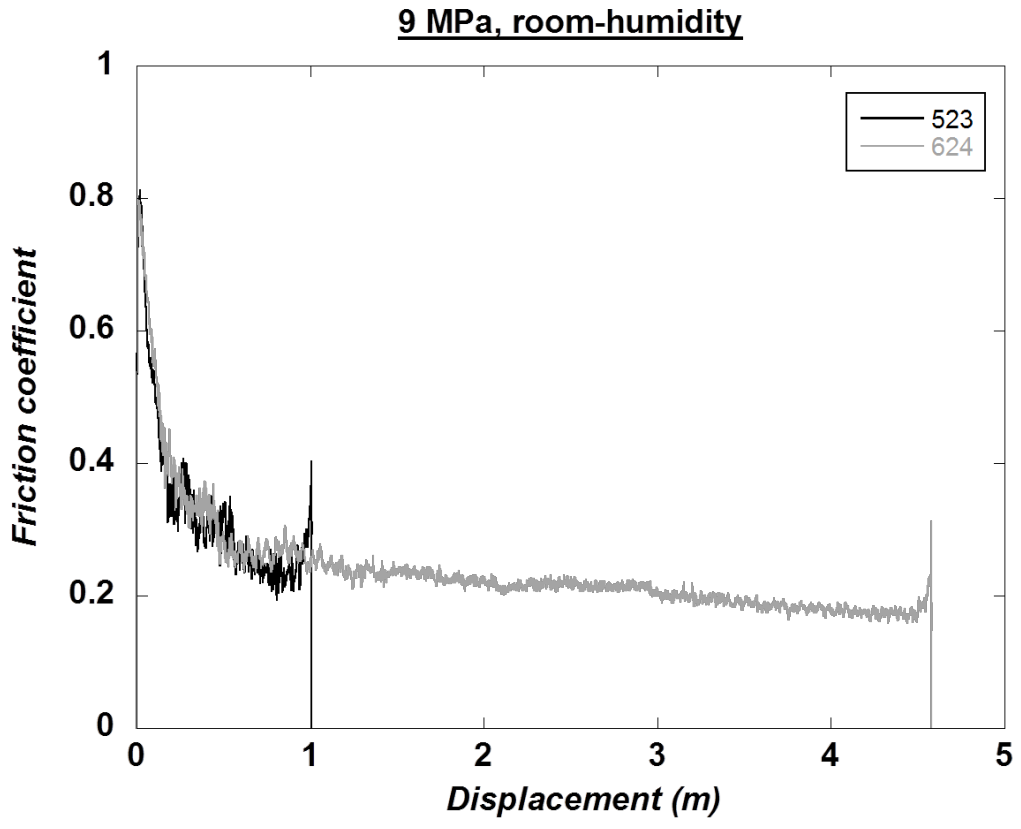

Fig. A2.32: 9 MPa, water-saturated, high-velocity friction plots

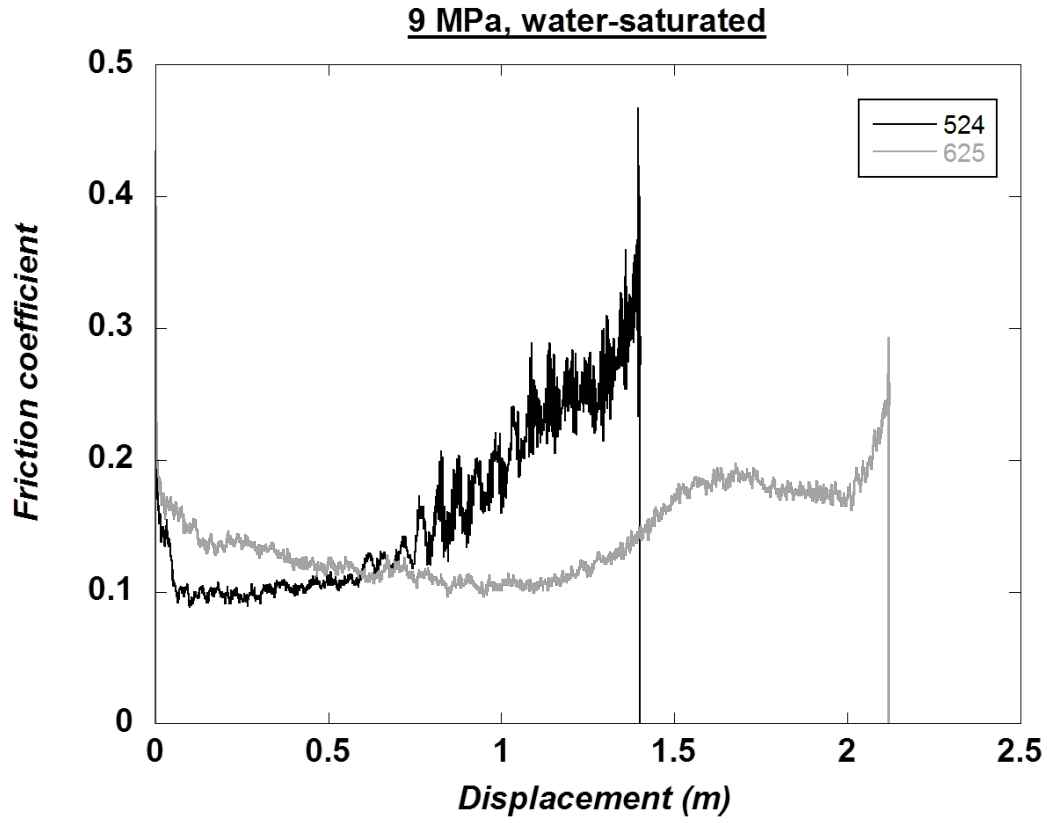

Fig. A2.33: 9 MPa, brine-saturated, high-velocity friction plots

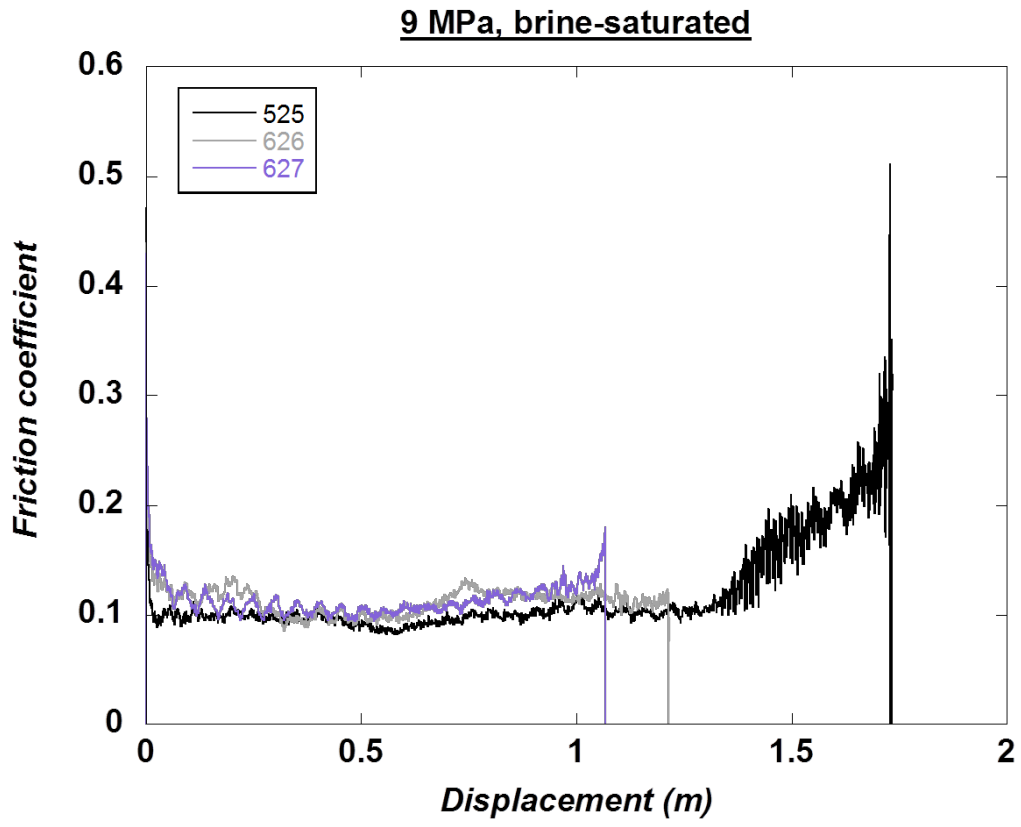

Appendix 3

Published version of Chapter 2

Journal of Structural Geology 58 (2014) 22–42

Contents lists available at ScienceDirect

Journal of Structural Geology

journal homepage: www.elsevier.com/locate/jsg

Lithological controls on the deformation mechanisms operating within carbonate-hosted faults during the seismic cycle☆

Rachael J. Bullock*, Nicola De Paola, Robert E. Holdsworth, João Trabucho-Alexandre

Rock Mechanics Laboratory, Earth Sciences Department, Durham University, South Road, Durham DH1 3LE, UK

ARTICLE INFO

Article history:
Received 5 July 2013
Received in revised form
7 October 2013
Accepted 20 October 2013
Available online 2 November 2013

Keywords:
Carbonate fault
Phyllosilicate
Fault zone heterogeneity
Seismic behaviour
Microstructure
Deformation mechanisms

ABSTRACT

A significant proportion of moderate-large earthquakes, plus aftershocks, nucleate within and propagate through upper-crustal carbonate-dominated sequences, where the effects of lithological variations on fault behaviour are poorly understood. The Gubbio fault is an active (1984, Ms = 5.2) normal fault in Italy, hosted in Mesozoic–Cenozoic limestones and interbedded marls. Fault core domains derived from limestone at the studied outcrop are characterised by fractures/hydrofractures and breccias and host a number of localised (<1.5 mm wide) principal slip zones (PSZs). The majority of displacement of up to 230 m is concentrated in these PSZs, which comprise cataclasites, gouges, and calcite veins. Degassing bubbles, 'quenched' calcite, and the transformation of smectite to illite, are also observed within PSZs, implying frictional heating and seismic slip. In contrast, marl-rich domains exhibit distributed shear planes bounding a continuous and pervasive foliation, defined by phyllosilicate-rich pressure-solution seams. Microstructures in the seams include folds/kinks of phyllosilicates and pressure shadows around clasts, consistent with aseismic fault creep. A model is proposed for the behaviour of lithologically complex carbonate-hosted faults during the seismic cycle, whereby limestone-dominated fault core domains behave in a predominantly seismic manner, whereas phyllosilicate-rich domains behave in a predominantly aseismic manner.

1. Introduction

The large-scale architecture of upper-crustal faults at <5 km depth comprises either a single high-strain fault core surrounded by a damage zone (e.g. Chester et al., 1993), or multiple high-strain cores, which bound lenses of damaged material (e.g. Faulkner et al., 2003). The differentiation between fault core and damage zone is generally based on the presence and spatial distribution of deformation products (Chester and Logan, 1986; Chester et al., 1993; Shipton et al., 2006). The fault core, which ranges from a few metres up to a few tens of metres wide, consists of cataclastically deformed fault rocks and typically contains one or more principal slip surfaces (PSSs) (Shipton et al., 2006; Faulkner et al., 2010). Damage zones, which are up to a few hundred metres in width, consist of fractured protolith rocks and smaller displacement subsidiary slip surfaces (Faulkner et al., 2010). The fault core is where most of the displacement is accommodated, and the deformation processes occurring here are the focus of the present paper.

Fault core architectures vary widely between faults and appear to be controlled, in part, by the composition of the protolith. Upper-crustal faults derived from carbonates (e.g. Agosta and Aydin, 2006; Micarelli et al., 2006; De Paola et al., 2008; Bastesen and Braathen, 2010; Molli et al., 2010; Smith et al., 2011a; Fondriest et al., 2012) and crystalline rocks (e.g. Chester and Chester, 1998; Wibberley and Shimamoto, 2003; Walker et al., 2013) tend to exhibit narrow fault cores that are less than a few metres in width, comprising cohesive and incohesive random-fabric fault rocks such as breccias, cataclasites and gouges (Sibson, 1977). The majority of the displacement within these fault cores is localised along discrete PSSs and within their associated principal slip zones (PSZs).

Numerous field studies of major seismogenic faults suggest that slip during individual earthquake events is localised along these PSZs, which are typically no more than a few cm thick (see Sibson, 2003, for a review). Notable examples include: the PSZ associated with the 1999 Mw 7.6 Chi Chi thrust earthquake in Taiwan, which has been estimated to be just 1 mm thick (Kuo et al., 2013); the Nojima fault, responsible for the 1995 M 7.2 Kobe earthquake in Japan, which contains several gouge and pseudotachylyte layers,

* Corresponding author. Tel.: +44 (0)191 3342300.
E-mail addresses: r.j.bullock@durham.ac.uk (R.J. Bullock), nicola.de-paola@durham.ac.uk (N. De Paola), r.e.holdsworth@durham.ac.uk (R.E. Holdsworth), joao.trabucho@durham.ac.uk (J. Trabucho-Alexandre).

0191-8141/$ – see front matter © 2013 The Authors. Published by Elsevier Ltd. All rights reserved.
http://dx.doi.org/10.1016/j.jsg.2013.10.008

each less than a few mm thick (Otsuki et al., 2003); and the PSZ responsible for the 2008 Ms 8.0 Wenchuan earthquake in China, which comprises a ~1 cm thick layer of fault gouge (Li et al., 2013). At the microscale, PSZs are often observed to contain sub-zones, which range from a few hundred microns to a few millimetres in width, composed of variably developed cataclasites and gouges and frequently displaying Riedel shear geometries (e.g. Power and Tullis, 1989; Otsuki et al., 2003; De Paola et al., 2008; Smith et al., 2011a; Fondriest et al., 2012).

In contrast, upper-crustal fault zones rich in phyllosilicates typically display much wider fault cores, often adhering to the multiple fault cores model. For example, the exhumed Carboneras fault in SE Spain has a fault core up to 1 km wide (Faulkner et al., 2003), which comprises numerous high-strain gouge zones of a few metres in thickness (Faulkner et al., 2003). Similarly, the SAFOD (San Andreas Fault Observatory at Depth) borehole core and field studies of the Median Tectonic Line in Japan have revealed several phyllosilicate-rich fault core strands, each >1 m wide (Zoback et al., 2010; Holdsworth et al., 2011; Jefferies et al., 2006). Rather than displacement being localised within PSZs, it is uniformly distributed within each gouge band; and rather than random-fabric fault rocks being the dominant deformation products, phyllosilicate-rich fault cores typically display a continuous, highly foliated fabric, though Riedel shear geometries are still conspicuous features (e.g. Rutter et al., 1986, 2012; Faulkner et al., 2003).

Consequently, in lithologically heterogeneous, upper-crustal fault zones, where crystalline/carbonate and phyllosilicate-rich protoliths are interlayered, we might expect to see a complex fault zone architecture with separate domains of localised and distributed deformation. This geometry has been documented along ancient, exhumed examples of presently inactive major strike-slip faults (e.g. the Carboneras fault zone, Faulkner et al., 2003), low-angle normal faults (e.g. the Zuccale fault in Central Italy, Collettini and Holdsworth, 2004; Smith et al., 2011b) and in accretionary complexes (e.g. the Chrystalls Beach Complex mélange, New Zealand, Fagereng and Sibson, 2010). Attention now is turning to active fault zones, in an attempt to understand how lithological heterogeneities within multi-layered sequences cut by a fault may affect not only the fault zone architecture, but also the seismic behaviour of the fault (e.g. Nemser and Cowan, 2009; Chiaraluce, 2012; Gratier et al., 2013; Tesei et al., 2013).

Quartzo-feldspathic and carbonate rocks typically have sliding friction coefficients in the Byerlee range of 0.6–0.85 (Byerlee, 1978) and experimentally exhibit slip-weakening and velocity-weakening behaviour (Logan et al., 1992; Beeler et al., 1996; Marone et al., 1990; Gu and Wong, 1994; Verberne et al., 2010; Collettini et al., 2011), which is necessary for earthquake nucleation and unstable stick-slip behaviour (Dieterich and Kilgore, 1994; Marone, 1998; Scholz, 1998). These lithologies also display dynamic-weakening behaviour during high-velocity rotary shear experiments (see Di Toro et al., 2011, for a review), with the coefficient of friction reducing to sub-Byerlee values (<0.2) at seismic slip velocities, facilitating earthquake propagation.

In contrast, many phyllosilicates (e.g. talc, smectites) are weak, particularly when wet, (sliding friction ≪0.3, e.g. Behnsen and Faulkner, 2012) and most types exhibit velocity-strengthening behaviour (e.g. Saffer et al., 2001; Saffer and Marone, 2003; Moore and Lockner, 2004, 2011; Ikari et al., 2007, 2009, 2011; Morrow et al., 2007; Tembe et al., 2010; Behnsen and Faulkner, 2012; Sone et al., 2012; Tesei et al., 2012). Velocity-strengthening behaviour does not favour earthquake nucleation and rock units displaying this behaviour are expected to act as barriers to earthquake propagation due to a positive stress drop (Scholz, 1998). Thus, upper-crustal fault rocks rich in weak phyllosilicate minerals are thought to deform predominantly aseismically by fault creep. For example, the creeping behaviour of faults such as the San Andreas is attributed to the presence of smectitic phyllosilicates in fault gouges (e.g. Carpenter et al., 2011; Lockner et al., 2011; Holdsworth et al., 2011).

Over the course of the seismic cycle, a fault may experience a broad spectrum of slip rates. These range from mm/yr, during the interseismic period, to mm/day-week during the pre-seismic (earthquake nucleation) and post-seismic (afterslip) periods and, then, to slip rates of m/s during earthquake propagation. It seems reasonable to hypothesise that lithological heterogeneities within the fault core will strongly influence which parts of a fault zone deform seismically or aseismically during the different seismic intervals. To further investigate this proposal, we document here the deformational and microstructural characteristics of the Gubbio normal fault (1984, Ms = 5.2) in the northern Apennines of Italy (Fig. 1a). This upper-crustal, seismically active fault deforms a succession of alternating limestone and cm-scale marl beds. Outcrop to microscale deformation features within the Gubbio fault zone have previously been studied by Bussolotto et al. (2007), who characterised the spatial and temporal relationships of structures in the fault zone, together with a determination of the P/T conditions and fluid behaviour during deformation. Here, we use a combination of microstructural (optical microscopy and field emission scanning electron microscopy, SEM) and mineralogical analyses (energy-dispersive X-ray spectroscopy, EDX, and X-ray diffraction, XRD) to study the dominant deformation mechanisms active within the fault core, and to assess the likely influence of lithology on deformation style. We use these findings to propose a conceptual model for the long- (inter- and post-seismic period) and short-term (coseismic) frictional behaviour of the fault zone, which can then be tested by future experimental work.

2. Geological setting

The northern Apennines of Italy have undergone NE–SW shortening since the middle Miocene, resulting in the development of a NE-verging fold and thrust belt (Barchi et al., 1998b). In the Gubbio area, this deformation is represented by the NW–SE striking Gubbio anticline (De Paola et al., 2006 and references therein). An upper Pliocene–Quaternary late-orogenic extensional regime is superimposed upon the folds and thrusts, forming a series of extensional basins bounded by NNW–SSE trending normal faults (Barchi et al., 1998a; Boncio and Lavecchia, 2000) (Fig. 1a). This extensional regime currently dominates the tectonics of the northern Apennines, although it has a relatively slow separation rate of 2–3 mm/yr (D'Agostino et al., 2009).

The Gubbio fault is an active segment of a 150 km long fault system known as the Umbria Fault System (Collettini et al., 2003). The surface trace is 22 km long, striking NW–SE (~N130°) (Figs. 1a and 2a). Seismic reflection data suggest that it has a listric profile at depth, with average dips of ~60–70° to the SW at the surface, decreasing to 10–15° at ~6 km, where it reactivates a pre-existing thrust fault (Mirabella et al., 2004) (Fig. 1a). At the surface, the fault juxtaposes Jurassic-Oligocene carbonates, belonging to the Umbria–Marche succession, in the footwall against Quaternary fluvio-lacustrine deposits, of the Gubbio Basin, in the hangingwall (Collettini et al., 2003; Bussolotto et al., 2007) (Fig. 1b).

A maximum displacement of 3.2 km at the centre of the Gubbio Basin was estimated by Collettini et al. (2003), which accumulated during multiple tectonic phases. Historical and instrumental records of moderate-large earthquakes occurring on the Gubbio fault are limited, since no permanent station coverage exists (Collettini et al., 2003; Pucci et al., 2003). However in 1984, the Gubbio area experienced an Ms 5.2 (Haessler et al., 1988) earthquake, located ~10 km south of the town of Gubbio at 7 km depth (ISC, 2001), and

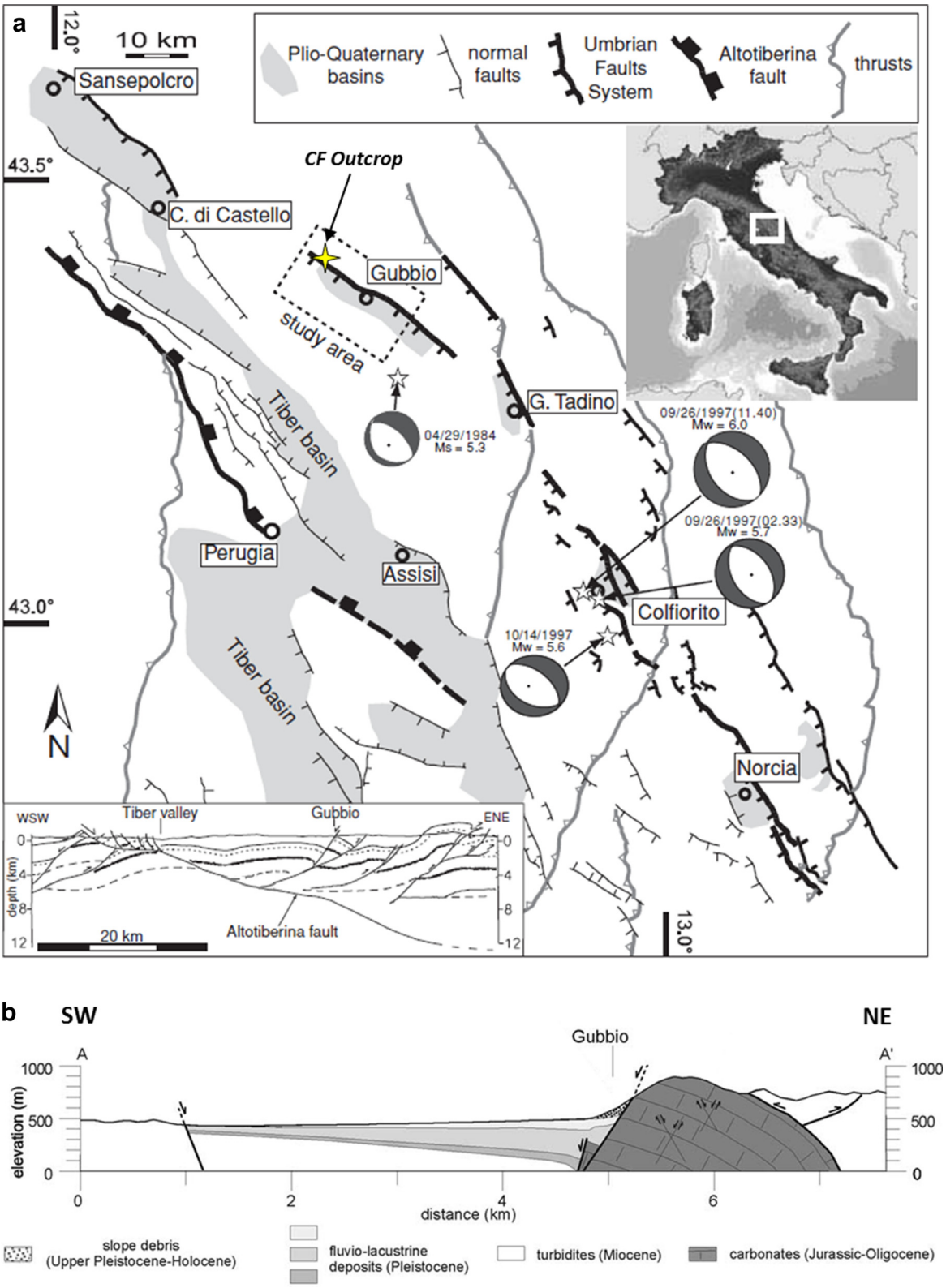

Fig. 1. a) Schematic structural map of the Umbria region (from Pucci et al., 2003, after Barchi et al., 2001), showing location of study area. Focal mechanisms and magnitudes are for the 1997 Colfiorito sequence (Ekström et al., 1998) and the 1984 Gubbio earthquake (Dziewonski et al., 1985). The location of the Cava Filippi (CF) outcrop is indicated. Inset is a schematic regional geologic section, constructed with the aid of seismic profile interpretations (modified from Boncio et al., 1998). b) Geological cross-section of the Gubbio fault, with the Gubbio Basin to the west in the hangingwall and the Gubbio anticline to the east in the footwall (modified from Collettini et al., 2003).

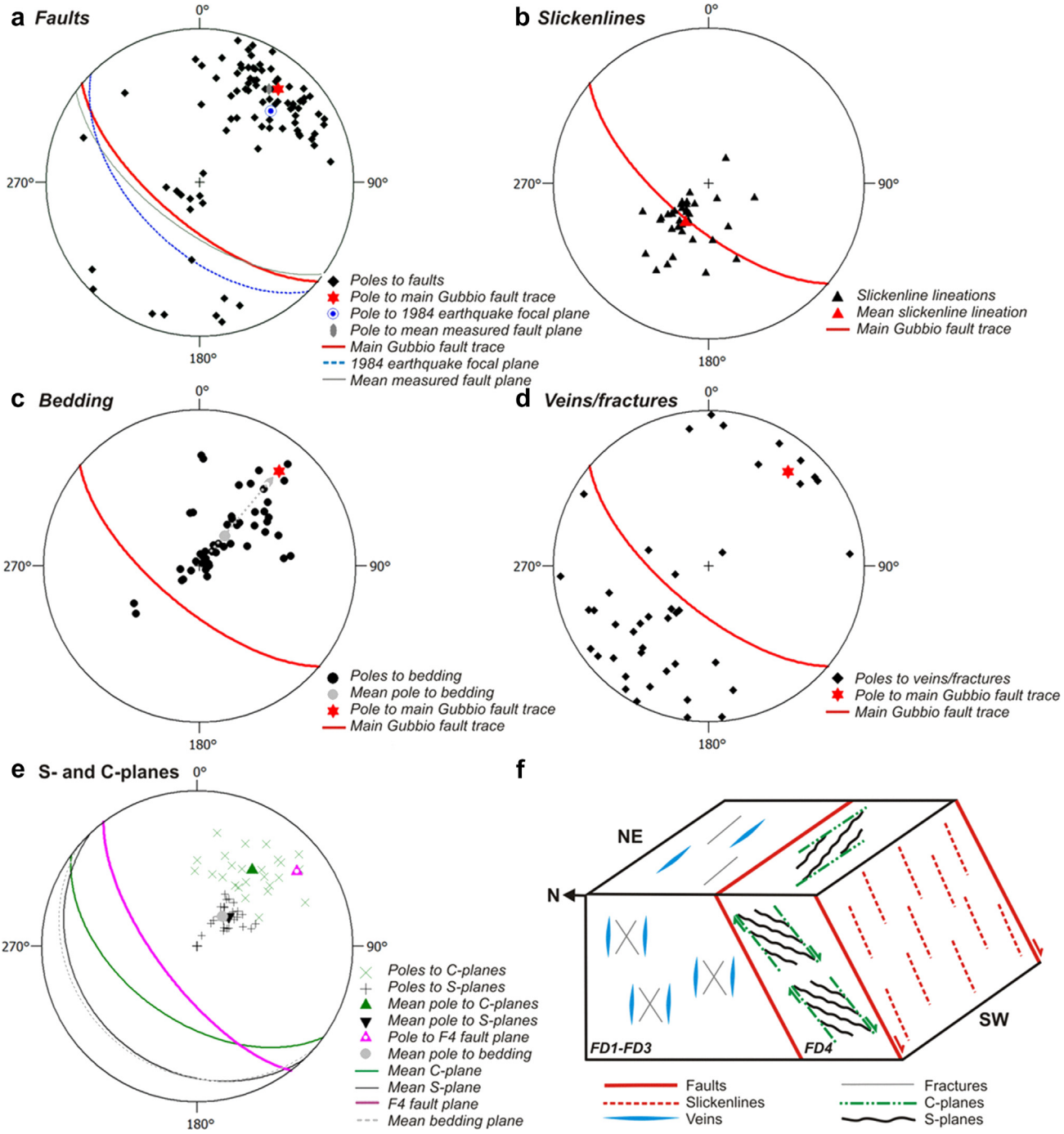

Fig. 2. a–e are equal area, lower hemisphere stereographic projections of the main structural features related to the Gubbio normal fault. Measurements are taken from both the damage zone (in the case of bedding, veins/fractures and faults) and from within the fault core. The trace of the main Gubbio fault is plotted on projections a–d as a reference. a) PSSs and subsidiary faults. The mean trend of the measured faults is consistent with the trend of the main Gubbio fault trace (Collettini et al., 2003) and the focal plane of the 1984 Gubbio earthquake (Westaway et al., 1989), which are also plotted. b) Slickenlines on fault surfaces, plunging steeply SW in a pure dip-slip geometry. c) Bedding: rotation of bedding from the protolith to the fault core is highlighted by the dashed arrow. d) Fractures and veins. e) C- and S-planes of the S–C fabric in FD4, and also observed within the slip zones of F3 and F4. The plane of F4 and the mean bedding plane are also plotted. f) Block diagram summarising the angular relationships between the structures observed at Gubbio, all of which have kinematics consistent with extension related to movement on the Gubbio normal fault.

this event was attributed to movement on the Gubbio fault (e.g. Collettini et al., 2003). A temporary seismic network installed three days after the main event recorded ~300 aftershocks ($M < 3.5$), arranged in two linear clusters trending sub-parallel to the strike of the Gubbio fault: a northern cluster (10 km long and 3 km wide in map view), where seismicity was limited to depths of 1–4 km, and a denser southern cluster (14 km long and 5 km wide), where seismicity was limited to depths of 4–6 km (Collettini et al., 2003). The aftershocks were located in the hangingwall of the Gubbio fault, rather than on the fault plane itself, and thus were interpreted to represent stress readjustments within the fault hangingwall (Pucci et al., 2003). Microseismicity has been recorded in the Gubbio area during a survey conducted from October 2000–May 2001 (Piccinini et al., 2003), which allowed

Chiaraluce et al. (2007) to clearly image the subsurface geometry of the northern portion of the Gubbio fault. The Umbria fault system has hosted two other major normal-faulting events during recent decades: the Norcia earthquake in 1979 (Mw = 5.8) (Deschamps et al., 1984), and the Colfiorito seismic sequence from 1997 to 1998 (Mw < 6.0) (Amato et al., 1998). In addition, the 2009 L'Aquila (Mw = 6.1) (Chiarabba et al., 2009) earthquake was located ~130 km SE of Gubbio on the Paganica fault, also part of the Apennine fault system. Real-time slip analyses using LiDAR-based methods showed that the latter earthquake was succeeded by slow, afterslip deformation in the months following the earthquake (Wilkinson et al., 2010; D'Agostino et al., 2012). All of these seismic events nucleated in and propagated through the Mesozoic–Cenozoic carbonatic multilayer bedrock sequence.

The outcrop that forms the focus of this present study is at Cava Filippi (43°23′21.95″N, 12°29′51.83″E), located ~1.5 km to the N of the village of Mocaiana, which lies near to the NW termination of the Gubbio fault and where the displacement on the fault is ~1.5 km (Mirabella et al., 2004). This outcrop is part of the footwall of the Gubbio fault. The fault rocks at Cava Filippi formed at depths of less than 2.5–3 km within a confined fluid system (Bussolotto et al., 2007).

3. Fault zone architecture

3.1. Terminology

Throughout this paper, certain terminologies and abbreviations are used, which we now define. Firstly, the fault core contains a number of *slip zones*, which are zones up to a few 10s of cm wide, containing variably developed brittle fault rocks (breccias, cataclasites; see below). These slip zones each contain a *principal slip zone* (PSZ), which at our study site is never greater than 1.5 mm thick. PSZs typically consist of ultracataclasite or gouge. Each PSZ is associated with a discrete *principal slip surface* (PSS), which sharply cuts the PSZ along one of its margins. The majority of displacement within the fault core is thought to be accommodated collectively along the PSSs and within the associated PSZs (e.g. Sibson, 2003; Smith et al., 2011a).

Secondly, we follow the classifications of Woodcock and Mort (2008) for brittle fault rocks that are defined primarily by grain size. A cohesive fault rock with ≥30% large clasts (≥2 mm in diameter) is classified as a breccia. Anything with <30% large clasts is a cataclasite, and different classes of cataclasite are defined according to the ratio of small clasts (0.1–2 mm in diameter) to cement/matrix (clasts < 0.1 mm in diameter). A fault gouge is defined as a fine-grained fault rock that is incohesive (Woodcock and Mort, 2008). The breccias are further subdivided based on how well the clasts fit together. In *crackle breccias*, the clasts are separated by thin seams of cement/matrix and have little evidence for rotation of clasts. In *mosaic breccias*, clasts display greater separations and rotations, but adjacent clasts can fit back to their original configuration. In *chaotic breccias*, clast separation and rotation are so large as to preclude reassembly by visual inspection. In addition to these random-fabric fault rocks, we also describe a number of foliated brittle fault rocks, where the fabrics are a result of pressure-solution processes dominating over brittle processes.

3.2. Protolith

Here we refer to the protolith as the "relatively undeformed" host rock, where brittle deformation is at a background level. The hangingwall rocks, which are not exposed in the study area, are Quaternary-age lacustrine and fluvial deposits of the Gubbio Basin, which range from clay-rich lignites through to sandstones and conglomerates (GE.MI.NA, 1963). Protolith rocks in the footwall of the Gubbio fault dip gently to the NE (Fig. 2c).

The rocks deformed within the fault core of the Gubbio fault belong to the Scaglia Rossa Formation. The Scaglia Rossa Formation is part of a Jurassic to Oligocene carbonate succession in the Umbria–Marche Apennines (Collettini et al., 2003). It consists of Turonian to Danian pale grey–red, micritic limestones with regular marl interbeds up to several cm thick (Bortolotti et al., 1970; Trabucho-Alexandre et al., 2011). The two deformed members in our study area are a "micritic limestone" member (Fig. 3a), which consists predominantly of beds (up to 20 cm thick) of micritic limestone (~5 wt.% clay; marl interbeds are infrequent), and the "marly limestone" member (Fig. 3b), which is generally more thinly bedded (beds average 5–10 cm thick) and contains frequent marl-rich horizons of up to 2 cm thick. Thus, portions of the fault core derived from the marly limestone have a more significant phyllosilicate content (up to ~20 wt.%) compared to those portions derived from the micritic limestone.

3.3. Damage zone

We refer to the damage zone as the portion of the fault zone in which the protolith has been variably fractured during fault-related deformation. Several fracture sets are present, some of which emanate from the earlier compressional phase of deformation that resulted in the formation of the Gubbio thrust and anticline (De Paola et al., 2006). Here, we describe only those features that are clearly attributed to the current extensional phase of deformation. The damage zone is ~220 m wide, corresponding to a region measured from the damage zone-fault core boundary, where fracture/vein density values peak at ~15 fractures counted per metre on a 1-D transect (Sagi, 2012), to the protolith, where fracture/vein density decays to background values (<2 fractures/m, Sagi, 2012). The fractures are predominantly pure dilational features (Sagi, 2012) and are often infilled by calcite; calcite mineralisation locally forms up to 75% of the rock volume. A few shear-extensional fractures are present with offsets up to 5 mm (Sagi, 2012), as well as some dip-slip faults with displacements of up to 5 m (Sagi, 2012). All fractures, veins and faults strike subparallel to the main Gubbio fault trace, with both synthetic and antithetic dips, often displaying an Andersonian geometry (Fig. 2d). Within 2 m of the fault core-damage zone boundary, bedding starts to become highly rotated with beds being dragged into the fault core to dip at steep angles of up to 75° to the SW (Fig. 2c).

Stylolites are also noteable features within the damage zone. Typically, they are either sub-parallel or sub-perpendicular to bedding, and thus are likely a combined product of diagenesis and the prior compressional deformation phase. The stylolites in the damage zone have a high-amplitude, sutured morphology, using the classification scheme of Logan and Semeniuk (1976), with very thin seams of insoluble residue (<100 μm thick) comprising <5% of the total rock volume.

3.4. Fault core

We refer to the fault core at Cava Filippi as the part of the fault zone where the majority of the normal displacement and associated fault rocks are concentrated (Fig. 3c and d). This outcrop was selected for its excellent exposures in an active quarry, orthogonal to the main PSSs. The damage zone-fault core boundary is marked by a PSS (F1) and thus is very sharp. The fault core has a width across-strike of ~15 m, and is bounded to the SW by a major escarpment that corresponds to the unexposed trace of the Gubbio fault. Following the practice of Bussolotto et al. (2007), we subdivide the fault core in the quarry into four structural domains

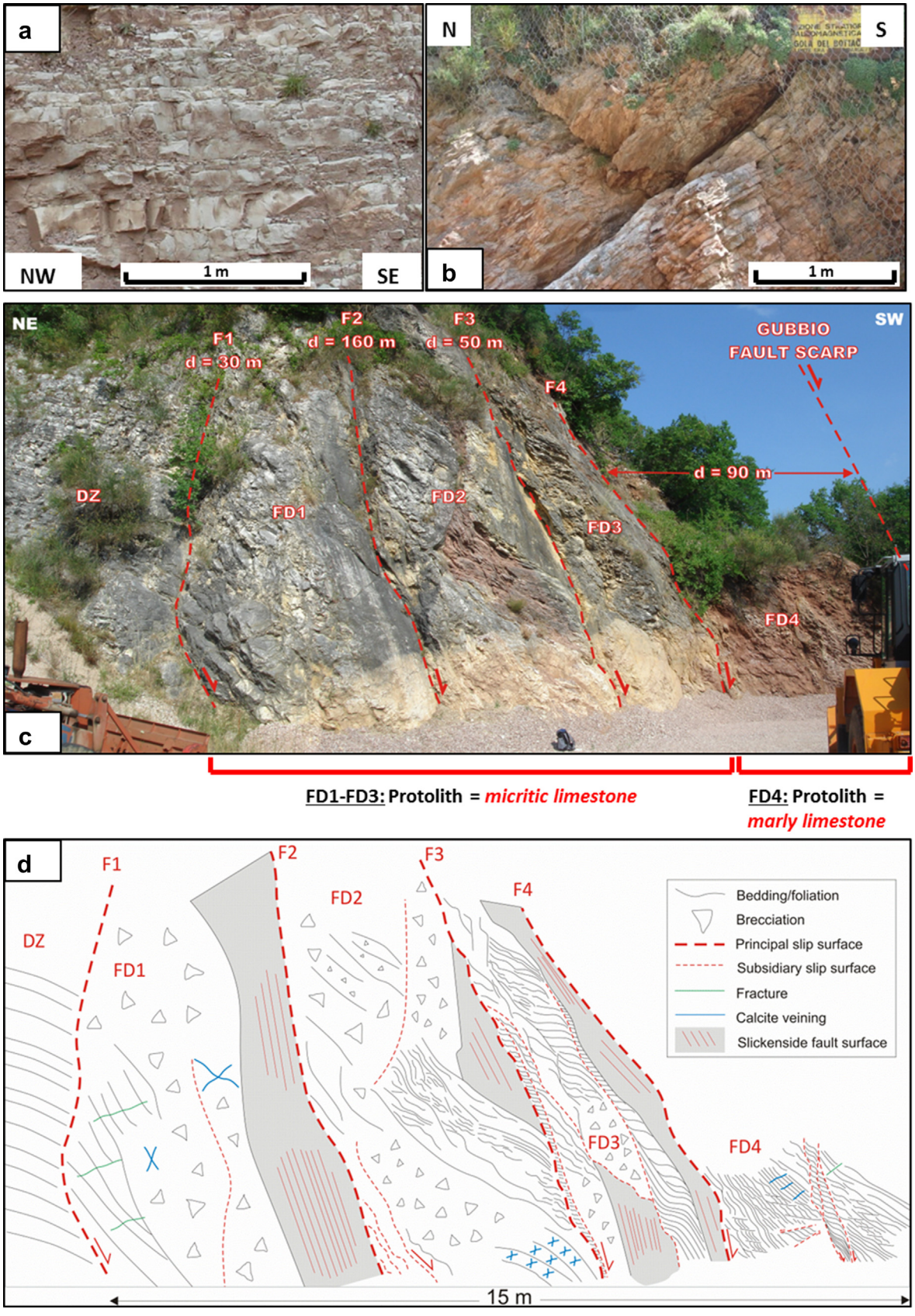

Fig. 3. a–b show photographs of the undeformed rocks of the Scaglia Rossa Formation, which represent the protolith of the rocks deformed in the fault core of the Gubbio fault: a) the micritic limestone member. b) The marly limestone member. c) Photograph of the fault core exposed at Cava Filippi, with PSSs (F1–F4) highlighted and the fault core domains (FD1–FD4) labelled. DZ = damage zone. Estimated fault/intradomain displacements, d (from Bussolotto et al., 2007), are also labelled. Colour variations in the outcrop are due to weathering and leaching rather than compositional differences. d) Schematic sketch of the outcrop shown in c, showing the main structural features. See text for description.

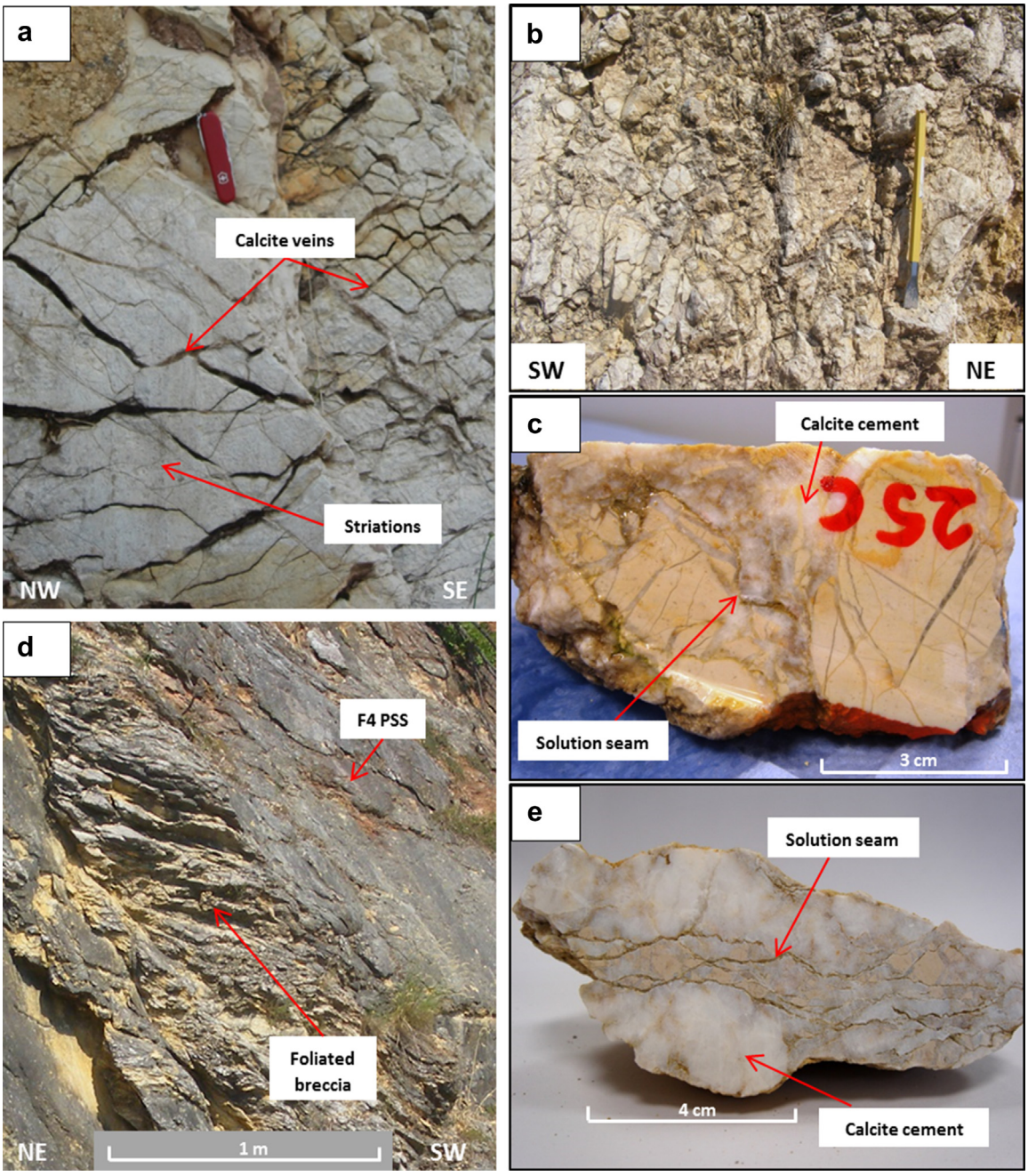

Fig. 4. Typical mesoscale features in domains FD1–FD3. a) FD1: bedding surfaces are striated. They also display several cross-cutting calcite veins, which have curviplanar geometries. b) FD2: pervasive fractures and hydrofractures created breccias and destruction of bedding. c) Mosaic breccia from FD1, although the large clast on the right-hand side displays a crackle breccia texture. Angular clasts of limestone are transected by calcite veins. A solution seam runs across the centre of the sample. d) FD3 is characterised by foliated breccias. e) Chaotic breccia from FD3 with a large proportion of calcite cement. Clay-rich solution seams define a foliation.

(FD1–FD4), delimited by four main slip zones, which are bounded by the PSSs, F1–F4 (Fig. 3c and d). FD1–FD3 are derived from the micritic limestone member of the Scaglia Rossa Formation, whereas FD4 is derived from the marly member, creating a marked lithological heterogeneity within the fault core. Bussolotto et al. (2007) used biostratigraphic controls to estimate the individual fault and intradomain displacements, which are illustrated in Fig. 3c and described in Section 3.4.1. These estimates suggest that each PSS has several tens of metres of displacement, whereas the displacement within the domains (i.e. within FD1, FD2 and FD3) between the faults is negligible. The exception is domain FD4, which, along with F4, is estimated to have accommodated up to 90 m of displacement. In total, the cumulative displacement at the Cava Filippi outcrop is estimated to be 150–230 m, which equates to ~12% of the total estimated throw of the Gubbio fault (Bussolotto et al., 2007), the remainder of the throw being accommodated by the adjacent main Gubbio fault scarp.

3.4.1. Mesostructural observations

3.4.1.1. Domains FD1–FD3 (micritic limestone protolith). FD1 is characterised by highly rotated bedding planes, which are dipping very steeply compared to the shallowly dipping beds in the adjacent damage zone, at angles of up to 75° towards the SW (Figs. 2c and 3d). Some bedding surfaces are striated, in an

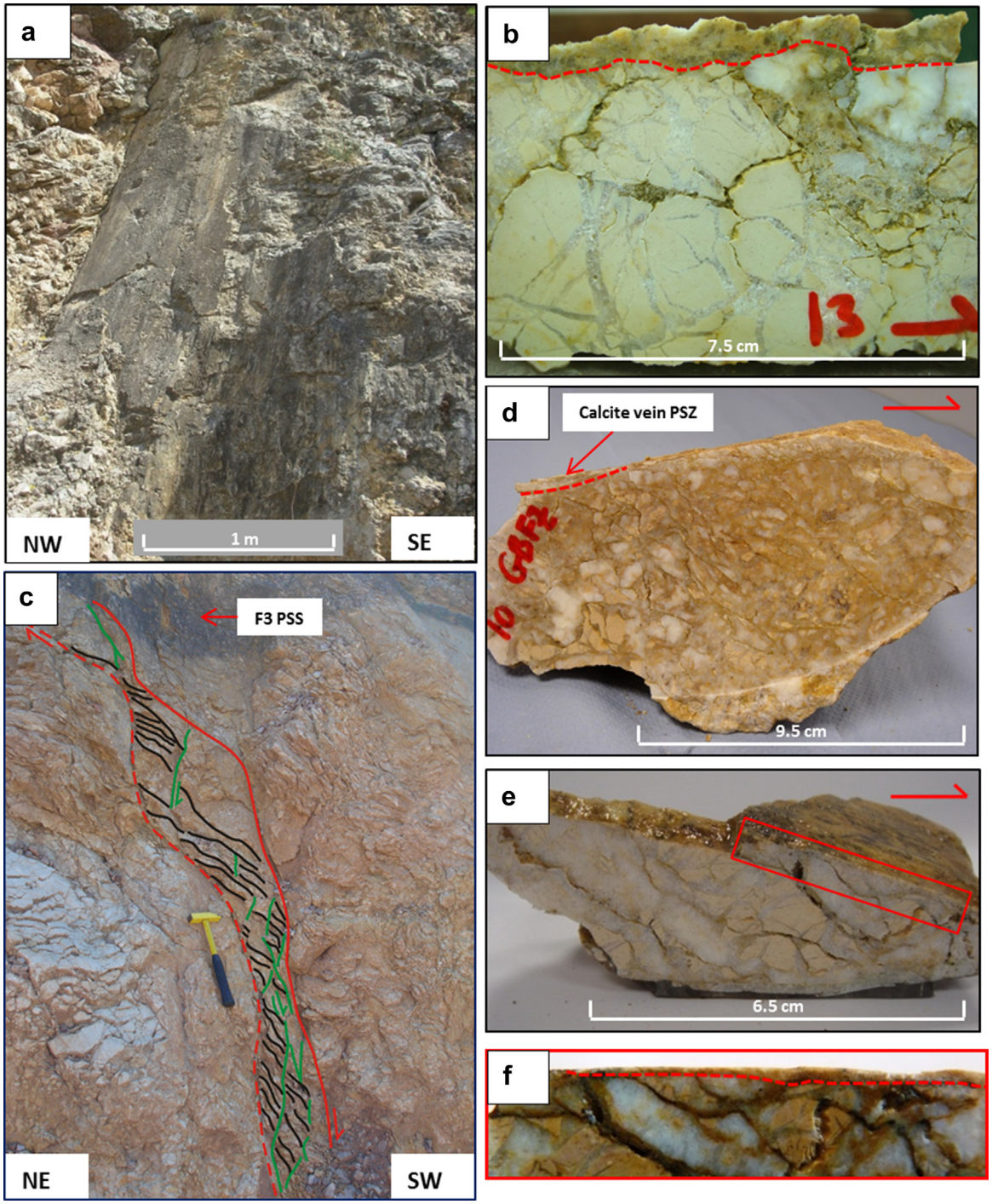

Fig. 5. Mesoscale features associated with the PSSs F1–F4. a) Fault surface of F2. b) A zone of chaotic breccia, up to 1 cm thick, underlies the PSS of F2 (PSS lies at top of sample). A layer of gouge also lay on top of the PSS but was lost during cutting. The remainder of the rock comprises a mosaic breccia. c) The slip zone of F3, which is up to 35 cm wide and displays a foliated S–C fabric (C-planes are shown in green, S-planes in black). d) A chaotic breccia from the slip zone of F3. A PSS lies along the top of the sample, and just beneath is a calcite vein-dominated PSZ, up to 5 mm wide. Clay-rich pressure-solution seams are formed at angles of up to 50° from the dip direction of the PSS and create a foliated fabric. e) Chaotic breccia and PSZ from F4. Boxed area is shown in f, to show the location of the PSZ. The PSZ is up to 1.5 mm wide and consists of ultracataclasite. Note that the pressure-solution seams displayed in d and e have a smoother morphology, and smaller amplitude to wavelength ratios, than observed in domains FD1–FD2 (see Fig. 4).

orientation consistent with slickenlines observed on the PSSs (Fig. 4a), suggesting that they have been locally reactivated as shear planes. Moving towards F2, the limestones are increasingly fractured so that bedding is almost completely destroyed leading to the development of breccias (Fig. 3d). A few relict bedding features remain in FD2. FD2 is characterised by intense fracture and hydrofracture abundance, resulting in heavy brecciation of the rocks (Fig. 4b). The exception is a patch of red, marl-rich material, with dimensions of $\sim 1 \times 2.5$ m (Fig. 3c), which displays characteristics similar to those described for FD4 (Section 3.4.1.3).

We measured fracture densities across the fault core along a 1-D transect. Fracture density in domains FD1–FD2 is ~51 fractures/m, three times greater than observed in the flanking damage zone. Fractures and veins throughout FD1–FD2 are present in two

dominant sets, as in the damage zone. Both strike NW–SE (sub-parallel to the principal slip surfaces), with one set dipping SW whereas the other dips antithetically to the NE (Fig. 2d and f). The veins have a curviplanar geometry, are up to 2 cm wide, and are filled with calcite (Fig. 4a). Several subsidiary slip surfaces occur in FD2 (Fig. 3d), and constraining the displacements for each was not possible, but the lack of any well-developed slip zones and associated gouges or cataclasites suggests that displacements are small, probably less than a few mm.

The breccias in FD1–FD2 range in composition from 30 to 70% limestone clasts, set in a crystalline calcite cement, and range from mosaic to chaotic breccia types (Fig. 4c). Limestone clasts are very angular and randomly oriented, ranging from <1 mm up to 10 cm in diameter. Clasts are commonly transected by several very fine calcite veins, which are typically <1 mm thick. This geometry creates a crackle breccia texture in certain clasts within the host mosaic/chaotic breccias (Fig. 4c). Individual crystals within the calcite cement may be visible with the naked eye and are up to 5 mm in diameter. At the mesoscale, it is difficult to differentiate between what may be clasts of calcite and the calcite cement. Intermittent clay-rich pressure-solution seams are also present, constituting ~5% of the rock volume (Fig. 4c). Where bedding features are still present, the solution seams are sub-parallel and sub-perpendicular to the bedding, consistent with the geometries observed in the protolith. However, where bedding surfaces have been reactivated as shear planes, solution seams are at angles of ~40° to the plane.

Domain FD3 is characterised by coarsely foliated breccias (Fig. 4d). They range from mosaic- to chaotic-type and the foliation is defined by anastomosing pressure-solution seams (Fig. 4e), which dip at angles ranging from ~20 to 40° to the SW, thus creating an angle of 30–50° to the dip of the PSSs (Fig. 4d). Calcite mineralisation in veins and breccia cements represents 25–85% of the rock volume and limestone clasts range from 10 to 65%. Again, clasts are angular and display a wide range of sizes from <1 mm up to 5 cm. The solution seams have a spacing of ~5 cm and locally comprise up to 10% of the bulk rock volume. Solution seams within FD1–FD3 (Fig. 4c and e) typically have lower amplitude to wavelength ratio compared to those in the damage zone, and hence have a smoother, less sutured morphology. They are also noticeably thicker, being up to 3 mm wide, and occasionally contain visible fragments of calcite and limestone (<1 mm in size). Fracture density in FD3 is ~0.3 fractures/m, slightly lower than in domains FD1–FD2.

3.4.1.2. Slip zones and PSSs, F1–F4 (micritic limestone protolith). F1–F4 are discrete shear planes, and >10 m in length based on available exposure, which cut sharply through the outcrop (Fig. 5a). F1 (displacement = 3 ± 27 m, Bussolotto et al., 2007) lacks a well-developed slip zone, but a PSZ is present, consisting of a clay-rich gouge, up to 2 mm thick and containing sub-mm clasts (~25%) of calcite and limestone, coats the slip surface. F2 (displacement = 130 ± 30 m, Bussolotto et al., 2007) also lacks a well-defined slip zone, although in hand specimen, a zone up to 1 cm thick of chaotic breccia is observed immediately underlying the PSS (Fig. 5b). This brecciated zone comprises clasts of chert (20%), limestone (15%) and calcite (10%), averaging 1 mm in size, set in a calcite cement (55%). Again, the PSZ consists of a clay-rich gouge layer up to a few mm thick, which coats the PSS.

F3 (displacement ≤ 50 m, Bussolotto et al., 2007) has a slip zone up to 35 cm wide, which has a foliated S–C fabric (Fig. 5c). The C-planes are defined by shear planes running sub-parallel to F3, and the S-planes are defined by phyllosilicate-rich pressure-solution seams that constitute up to 10% of the rock volume. They form at angles of up to 50° from the dip of F3 and have average spacings of ~1.5 cm (Fig. 5d). Within the lithons bounded by the foliation, the rock is composed of angular clasts of limestone (15%) and calcite (30%) formed from fragmented calcite veins and/or cement, typically <5 mm in size, set in a calcite cement (55%). Given that 30% of the clasts are fragmented veins or cement, then this rock can be classified as a chaotic breccia. F3 has a PSZ up to 1 mm wide, defined by a layer of calcite veining (up to 0.5 mm wide) (Fig. 5d), plus a ~0.5 mm thick gouge layer.

F4 (displacement of 60 ± 30 m along with FD4) also has a slip zone up to 50 cm wide, associated with an S–C foliated chaotic breccia (Fig. 5e). Here, angular limestone and calcite clasts comprise up to 30% each and the calcite cement comprises ~40% by volume. Clasts range from <1 mm to 3.5 cm diameter, averaging ~5 mm in size. Some clasts can still be fitted back together in a jigsaw geometry. The phyllosilicate-rich pressure-solution seams are oriented at angles of up to 30° from the dip of F4 (Fig. 5e), and are often very closely spaced (average spacing ~5 mm). This high density means that the clay seams locally form up to 15% of the rock volume. In addition, the least-weathered parts of the fault exhibit a PSZ up to 1.5 mm wide composed of ultracataclasite (Fig. 5f). The PSSs of F1–F4 are often heavily mineralised, displaying calcite slickenfibres in addition to slickenlines that both indicate predominantly dip-slip fault movement (Figs. 3b and 5a).

3.4.1.3. Domain FD4 (marly protolith). In FD4, which is derived from the marly limestone, the deformation style is very different. Compared to other parts of the fault core, fractures are not abundant and shear localisation along through-going faults is rare. Instead, the deformation is represented by a continuous and pervasive S–C fabric (Fig. 6a). The C-planes have an average strike direction that is sub-parallel to the domain-bounding PSSs (Figs. 2e, f, 6a and b), but they dip at a shallower angle, which is explained by the fact that they appear to have reactivated the pre-existing bedding planes that rotated during deformation. The C-planes are defined by an anastomosing network of clay-rich pressure-solution seams (Fig. 6d). Individual seams are up to a few mm thick. Many C-planes have calcite slickenfibres precipitated on their surfaces (Fig. 6c), which display kinematics consistent with that of the main fault zone, i.e. dip-slip extensional. The S-planes are also defined by seams of pressure-solution, which are generally <1 mm thick (Fig. 6d). They are inferred to have formed perpendicular to the direction of the local maximum principal stress induced by shearing along the C-planes (Fig. 6b). A less well-defined C′-type shear band cleavage locally overprints the primary S–C fabric (Fig. 6a and b). The spacing of the C-foliation ranges from <1 mm up to 2 cm, so that in some places, the clay-rich seams comprise up to 20% of the rock volume. In contrast to the pressure-solution seams in domains FD1–FD3 and in the damage zone, the seams in FD4 have a very smooth, anastomosing morphology (Fig. 6d). This geometry is consistent with the relatively phyllosilicate-rich nature of the marls in FD4, since higher clay content promotes the pressure-solution process (e.g. Rutter, 1976) and favours the development of non-sutured morphologies (Logan and Semeniuk, 1976).

Calcite mineralisation is present but much more sparse than in FD1–FD3. Calcite veins only constitute up to 20% of the rock volume and they tend to be much narrower than those in FD1–FD3, typically <5 mm wide. They are formed predominantly perpendicular to the C-planes (Figs. 6d and 10a). The veins generally have a tabular morphology, although irregular forms are also present (e.g. Fig. 6d). The exception to the predominantly distributed deformation is a localised shear zone that cuts through the centre of FD4 (Fig. 6a). This shear zone, ~25 cm wide, is bounded by two slip surfaces. However, the foliated nature of the rocks within this shear zone does not differ significantly to those seen throughout FD4.

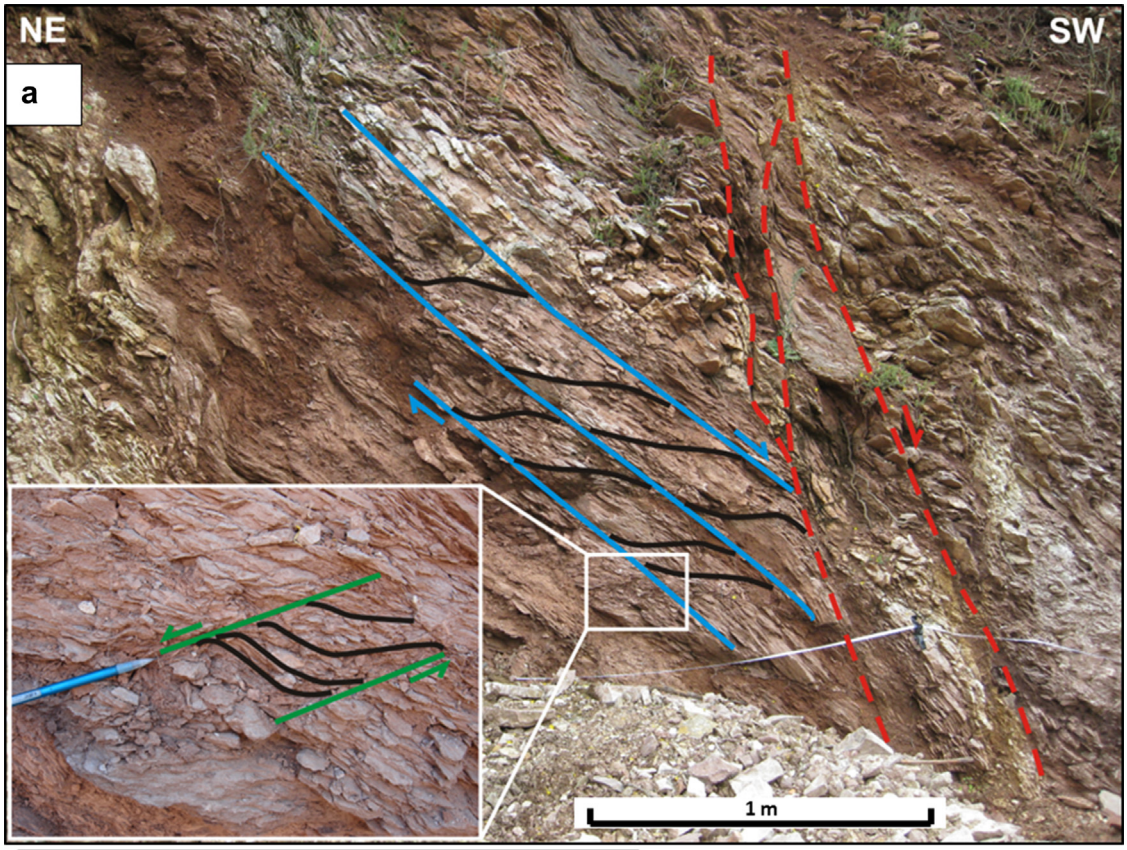
NE
SW
a
1 m

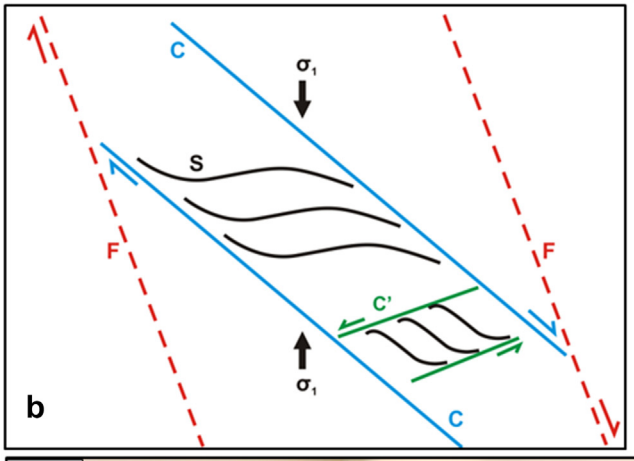
C
σ1
S
F
F
C'
σ1
C
b

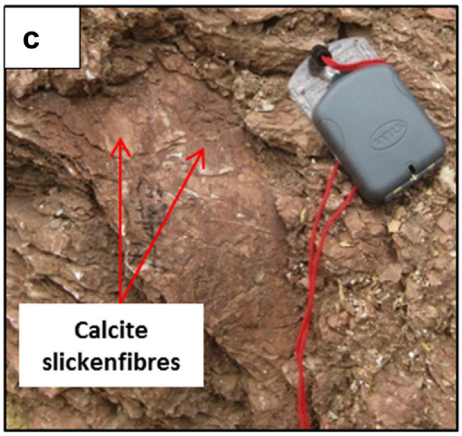
c
Calcite slickenfibres

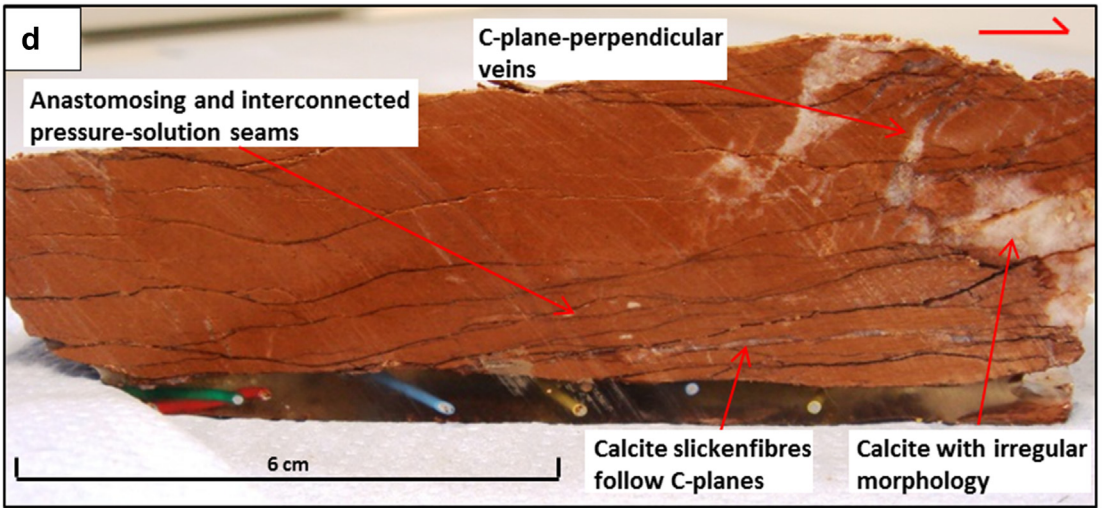
d
C-plane-perpendicular veins
Anastomosing and interconnected pressure-solution seams
6 cm
Calcite slickenfibres follow C-planes
Calcite with irregular morphology

3.4.2. Microstructural observations

3.4.2.1. Domains FD1–FD3 (micritic limestone protolith). Optical microscope analysis shows that the limestone clasts in the breccias have reduced sizes of <100 μm and are always very angular shapes. They are extensively fractured and transected by fine calcite veins ranging from 10 μm up to a few mm wide (e.g. Fig. 7a). Consistent with the observations made at outcrop scale, these veins form conjugate sets. The calcite veins typically have a blocky texture, and occasionally an elongate blocky texture (Fig. 7a). The size of the crystals depends on the width of the vein, but they may be up to 500 μm in diameter in the centre of the widest veins, generally with smaller crystals at the vein boundaries (Fig. 7a). Veins typically have a discontinuous and/or branching geometry (Fig. 7a).

The nature of the calcite crystals within the breccia cement contrasts significantly compared to the vein crystals. Calcite crystals in the cement are mostly anhedral with random orientations (Fig. 7b). They are also highly inequant, ranging from <20 μm up to 5 mm in size. In addition, deformation twins are common within the calcite cement, particularly in the largest crystals, and they may be >1 μm thick and can be curved and taper out within crystals (Fig. 7b). Although several twins correspond to type I deformation twins of Burkhard's (1993) classification, which is consistent with deformation at temperatures < 200 °C, ~50% correspond to type II–type III deformation twins. Typically type II–type III deformation twins are associated with temperatures of deformation in the range 150–250 °C, which is high considering the 2.5–3 km of exhumation for the Gubbio fault. Further, Bussolotto et al. (2007), used palaeothermometric techniques to calculate temperatures of formation of the fault rocks at Cava Filippi of <50 °C. Thus, we infer that the high-strain rates experienced within the fault core enhanced deformation twin morphology (e.g. Rybacki et al., 2013).

Pressure-solution seams average 50 μm to 1 mm wide and are filled with an extremely fine-grained crystal aggregate. EDX analysis with the SEM shows that the seams comprise up to 80% phyllosilicate with the remainder being very fine-grained calcite crystals. Calcite crystals are quite equant, ranging from ~25 to 50 μm in diameter, and are sub-rounded (Fig. 7c). Bearded overgrowths (Fig. 7d) occur in some solution seams in domain FD3, suggesting that pressure-solution creep is likely an active deformation mechanism within this domain. The solution seams typically cross-cut all other structures (i.e., clasts, cement, veins) in the breccias, indicating that they continued to develop after most other structures.

3.4.2.2. PSZs, F1–F4 (micritic limestone protolith). PSSs appear as very sharp, straight boundaries that truncate all features within the host breccias (Fig. 8a). As described in Section 3.1, the PSS bounds a PSZ. The PSZs observed in this study range from ~0.5 to 1.5 mm thick and are one of two types: those defined by zones of ultracataclasite and those defined by PSS-parallel calcite veins.

F4 is an example of an ultracataclasite-dominated PSZ (Fig. 8a) with four well-defined sub-zones. Sub-zone 1, which ranges from 515 to 915 μm wide, consists of ultracataclasite. The ultracataclasite has a random fabric and contains sub-rounded clasts of limestone (10%) and calcite (50%) set in a matrix (40%) of ultrafine-grained calcite and clay (Fig. 8c). Clasts range from 20 to 600 μm in size. Anything less than 20 μm in size is attributed to the matrix. Subzones 2, 3 and 4, which have widths of up to 430 μm, 240 μm and 220 μm, respectively, consist of discontinuous, blocky calcite veins that contain crystals ranging from ~40 to 800 μm in size. Each subzone is bounded by a slip surface. These surfaces are highlighted by the presence of an orange–brown material (Fig. 8d), which at high magnification, and with the SEM, is seen to consist of sub-rounded calcite crystals, <20 μm in size, dispersed within phyllosilicate-rich material. The calcite crystals within this material do not appear to have been particularly fractured or abraded, and many of them have concave boundaries.

SEM investigation of the uppermost slip surface corresponding to the striated F4 plane observed in the field reveals a more complex structure. It shows the presence of an ultrafine-grained, phyllosilicate-rich gouge lining the slip surface (Fig. 9a), and this gouge displays further sub-zones, which we refer to here as "shear localisation zones" (SLZs) 1 and 2. SLZ 1, which is up to 15 μm thick, has a phyllosilicate content of ~50%, in which the phyllosilicates are randomly oriented, and contains sub-angular calcite clasts up to 20 μm in diameter. SLZ 2, which is <5 μm thick, is much finer-grained, containing nano-sized clasts of calcite, which have a smooth and asymmetric shape (Fig. 9a). These clasts are surrounded by finely foliated phyllosilicates, which comprise ~80% of SLZ 2. Also within SLZ 2, several shear surfaces are preserved (Fig. 9a). In some specimens from F4, we observed sub-spherical pores within the SLZs that resemble bubbles, which are surrounded by elongate calcite crystals and a small amount (<20%) of phyllosilicate (Fig. 9c). Other parts of the SLZs preserve "dog-bone" or "H"-shaped calcite crystals (Fig. 9d). SEM analyses have also been performed parallel to the slip surface of F4, i.e. looking down onto the striated fault surface. Here, we observed tightly-packed calcite grains with dimensions ranging from 50 to 150 nm, which sometimes exhibit polygonal boundaries and triple-junction contacts (Fig. 9e and f).

F3 exhibits an example of a calcite vein-dominated PSZ (Fig. 8b). The PSZ contains a number of calcite veins, which are characterised by transitions along their length over distances of <300 μm from a blocky to a fibrous texture (Fig. 8b and d). The areas of blocky calcite are characterised by crystals with an average size of 100 μm that display a crack-seal texture where fluid inclusions are aligned subperpendicular to the slip direction (Fig. 8d). The fibrous veins are characterised by much smaller, euhedral crystals, on average ~15 μm in size with the fibrous texture being created by micron-scale stylolitic surfaces lying sub-parallel to the PSS (Fig. 8e). Similar to F4, the slip surfaces that bound the veins within the PSZ are highlighted by the presence of orange–brown phyllosilicate and have a jagged, stylolitic morphology (Fig. 8d).

3.4.2.3. Domain FD4 (marly protolith). The pressure-solution origin of both the C- and S-planes is evident under the microscope, due to the truncation of micro-fossils (Fig. 10b). The pressure-solution seams that define the C-planes have an anastomosing morphology, creating interconnected, phyllosilicate-rich networks (Fig. 10b). Solution seam spacings range from μm to cm scale (Fig. 10a and b), thus they are much more pervasive than initial field observations suggested, as are the S-planes. The C-planes link up with the S-planes, thus bounding lithons of relatively undeformed limestone.

Fig. 6. Mesoscale features associated with domain FD4. a) Deformation is distributed throughout the domain via a continuous, foliated S–C fabric. Inset shows the detail of a local and less well-defined C′-type shear band cleavage. A localised shear zone cuts through the domain on the right-hand side of the image (red-dashed lines). b) Kinematic summary of the main structures observed in FD4. c) Calcite slickenfibres precipitated on the surface of a C-plane provide evidence for fluid-assisted shearing along the plane. d) Hand sample from FD4, showing the internal structures within a lithon bounded by two S-planes. C-planes, defined by phyllosilicate-rich pressure-solution seams anastomose through the rock, creating interconnected networks. Calcite mineralisation is present, but less so than observed in domains FD1–FD3. Veins are typically perpendicular to the C-planes and have a tabular morphology, but occasional patches of calcite with an irregular morphology are present. Calcite slickenfibres are again present along C-planes. (For interpretation of the references to colour in this figure legend, the reader is referred to the web version of this article.)

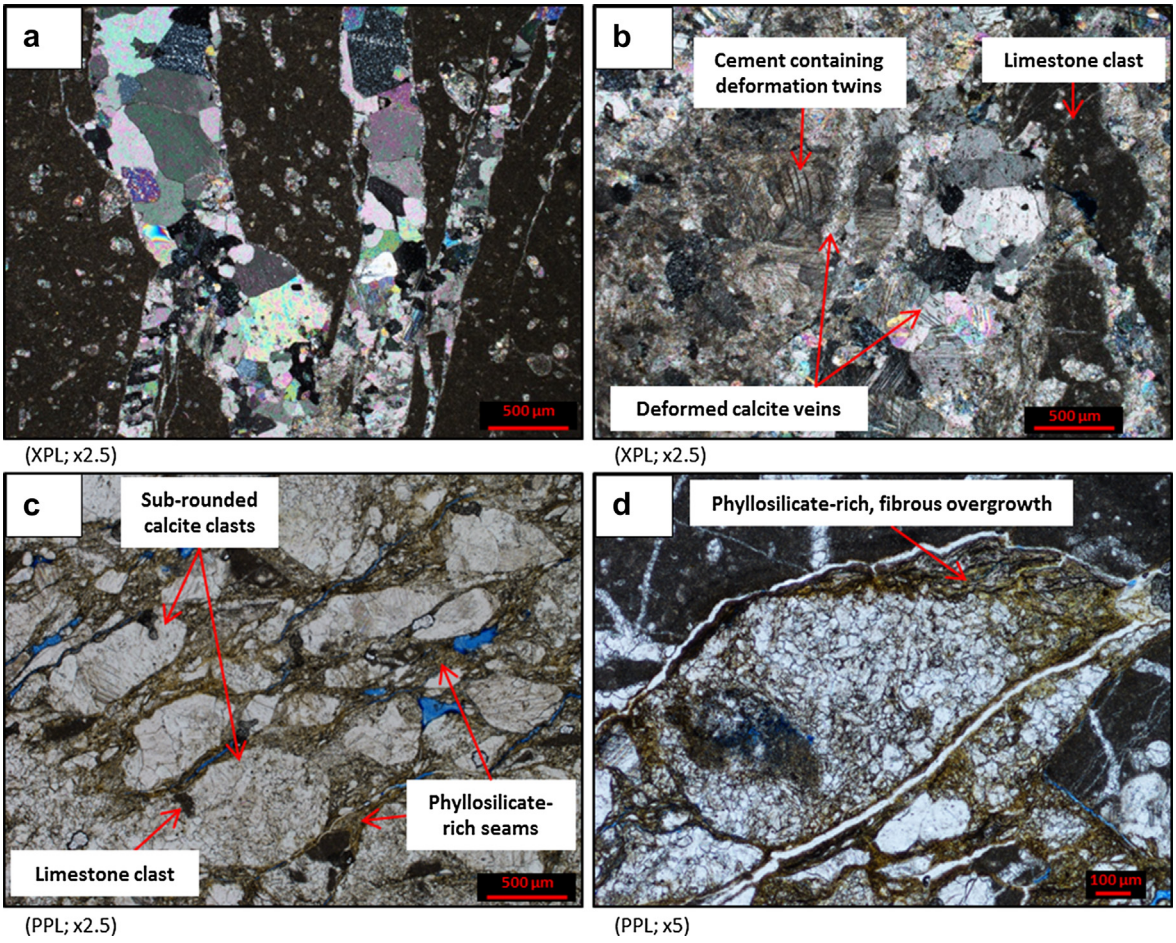

Fig. 7. Typical microscale features in domains FD1–FD3. a) Branching calcite veins, transecting a clast of limestone. They predominantly have a blocky texture, although the bottom left-hand side vein has an elongate blocky texture. Smaller crystals are often concentrated at the limestone-vein boundaries. b) Calcite cement in breccia from FD2. Calcite crystals in the cement appear much more deformed than those in the veins, typically displaying type II/type III deformation twins (Burkhard, 1993). Earlier veins were incorporated into the cement through fracturing and brecciation. c) Anastomosing phyllosilicate-rich solution seams in FD3. The dissolution of clasts of limestone and calcite produced sub-rounded shapes, compared to the typical angular clasts observed in many breccias in FD1–FD2. d) Bearded overgrowth on a clast of calcite within a pressure-solution seam from FD3.

The solution seams that define the S- and C-planes may be up to 100 μm thick. EDX analysis shows that they are filled with ~50% phyllosilicate and 40% calcite with the remaining 10% comprising quartz and diagenetic apatite (Fig. 10d). This material is moderately foliated due to the alignment of phyllosilicate grains (Fig. 10c and d). The clasts within the solution seams have relatively smooth, concave boundaries, typical of dissolution (Fig. 10c), and show little evidence of internal deformation that contrasts with the clasts in the phyllosilicate-rich SLZs of F1–F4, which are highly fractured and have sharp, angular boundaries (Fig. 9b).

Microstructures within the solution seams are inferred to indicate two coeval deformation mechanisms. Firstly, asymmetric delamination features and micro-folds (Fig. 10c) imply foliation-parallel sliding along (001) clay lamellae. And secondly, pressure shadows around clasts (Fig. 10d) indicate the operation of pressure-solution creep. In all cases, the sense of shear interpreted from the asymmetry of these microstructures is consistent with that of the fault zone.

Calcite veins display similar characteristics to those in FD1–FD3. They have a drusy and blocky texture, ranging from <10 μm up to a few mm wide (Fig. 10a). Their consistent orientation orthogonal to the prevailing C-plane foliation is characteristic of deformation by pressure-solution. The veins are also offset by the pressure-solution seams by distances of up to a few cm (Fig. 10a). This geometry may be due to dissolution, or alternatively, some of the larger offsets may be caused by frictional sliding or creep along the solution seams.

4. Mineralogical observations

XRD analyses were performed on the clay fraction present within various parts of the fault zone to constrain what clays are present and to assess what influence clay mineral content may have on the behaviour of the different fault core domains. A total of six samples were analysed: two samples representing the protolith (one from the micritic limestone protolith and one from the marly protolith), two samples representing pressure-solution seams (one from domain FD3 and one from domain FD4), and two samples representing PSZs (one from F3 and one from F4). Sample details and results are summarised in Table 1 and representative XRD traces are shown in Fig. 11.

In the protolith, the clays present are illite, mixed-layered illite-smectite and a very small amount (<1%) of kaolinite. These same clays are present in the pressure-solution seams from both domains FD3 and FD4, although the solution seams show a relative enrichment of kaolinite (up to 25%). However, a significant difference in clay content is observed within the PSZs of F3 and F4. Whilst illite and kaolinite are still present, smectite forms only 2% of the clay fraction within the PSZ of F4 and is completely absent

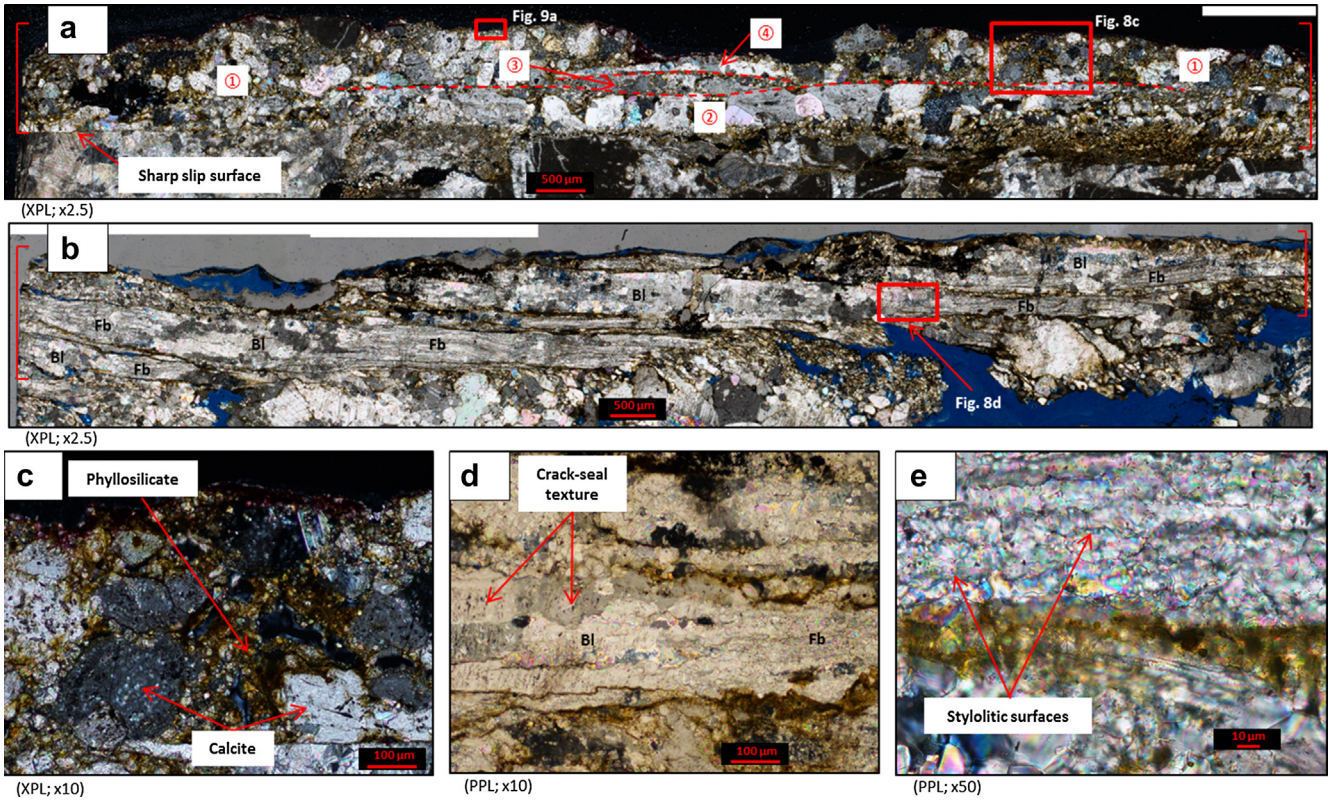

Fig. 8. Typical microscale features associated with the PSSs F1–F4. a) Example of an ultracataclasite-dominated PSZ (bracketed) from F4 (hand sample is shown in Fig. 5e and f). Note the very sharp boundary between the host breccia and the PSZ on the left-hand side of the image. This becomes less sharp towards the right-hand side as the slip surface is overprinted by pressure-solution. This PSZ comprises four sub-zones, labelled 1–4, which are bounded by discontinuous slip surfaces, highlighted in red. Sub-zone 1 is dominant and consists of ultracataclasite (see fig. c). Sub-zones 2–4 are discontinuous and consist of blocky calcite veins. b) Example of a calcite vein-dominated PSZ (bracketed) from F3. A number of calcite veins are present. Veins are characterised by transitions (see fig. d) from a blocky texture to a fibrous texture along their length (labelled Bl = blocky; Fb = fibrous). The blocky calcite veins contain crystals averaging 100 μm in diameter, displaying a crack-seal texture (see fig. d). The fibrous calcite veins contain much smaller, euhedral crystals, averaging 15 μm in diameter (see fig. e). c) Close-up image of the ultracataclasite in the PSZ of F4 (location shown in a). It contains sub-rounded clasts of calcite in a matrix of ultrafine-grained calcite and clay. d) Close-up image of transition between blocky (Bl) and fibrous (Fb) calcite (location shown in b). The alignment of fluid inclusions that creates the crack-seal texture in the blocky calcite can be seen. The orange–brown material is interpreted to be a product of pressure-solution along planes sub-parallel to the PSS/vein boundaries. e) Close up of fibrous vein, showing the jagged stylolitic surfaces that create the fibrous texture. Again, the orange–brown material is inferred to be from pressure-solution between slip surfaces. (For interpretation of the references to colour in this figure legend, the reader is referred to the web version of this article.)

within the PSZ of F3. These results are consistent with the chemical compositions obtained by in-situ EDX analyses of the clay minerals.

5. Discussion

5.1. Deformation styles and mechanisms

Three dominant styles of deformation are recognised within the core of the Gubbio fault. Domains FD1–FD3, derived from the micritic protolith, are characterised by pervasive fractures, veins and chaotic breccias. Other features include intermittent pressure-solution seams and subsidiary slip surfaces. The style of deformation is thus *discontinuous* and *distributed*. The main deformation mechanisms inferred from microstructural observations are fracturing and hydrofracturing, with minor amounts of diffusive mass transfer and local frictional sliding along minor faults.

The slip zones of F1–F4, also derived from the micritic limestone protolith, are up to 50 cm wide, containing chaotic breccias, which can also have a coarsely foliated S–C fabric. They each contain a PSS and an associated PSZ. PSZs are up to 1.5 mm wide, containing variable amounts of ultracataclasite and gouge, together with slip surface-parallel calcite veins. Even narrower SLZs (<5 μm wide) are observed within the PSZs. Thus, the deformation is *discontinuous* and *localised,* with the main inferred deformation mechanisms being cataclasis and frictional sliding. The foliated S–C fabrics within the slip zones and the development of phyllosilicate-rich stylolitic surfaces along some PSSs (e.g. that of F3 described in Section 3.4.2.2) indicate that diffusive mass transfer processes also play a role within the slip zones F1–F4.

In domain FD4, derived from the marly protolith, the style of deformation is very different to that observed in the rest of the fault core. The main deformation product is a pervasive S–C foliation, where the foliation is defined by abundant pressure-solution seams. The style of deformation is thus *continuous* and *distributed*, with the inferred dominant deformation mechanism being pressure-solution.

5.2. Lithological controls on deformation mechanisms and frictional behaviour

Our findings illustrate that marked contrasts in both the deformation styles and dominant deformation mechanisms occur across the fault core, and we correlate these contrasts to changes in lithology across the core. Also, the displacement distribution estimated by Bussolotto et al. (2007) appears to be influenced by lithology because for FD1–FD3 dominated by the micritic limestones, displacement is focused on domain boundaries (i.e. along the PSSs F1–F4), whereas for FD4, significant displacement is accommodated within the domain. Thus, with respect to the

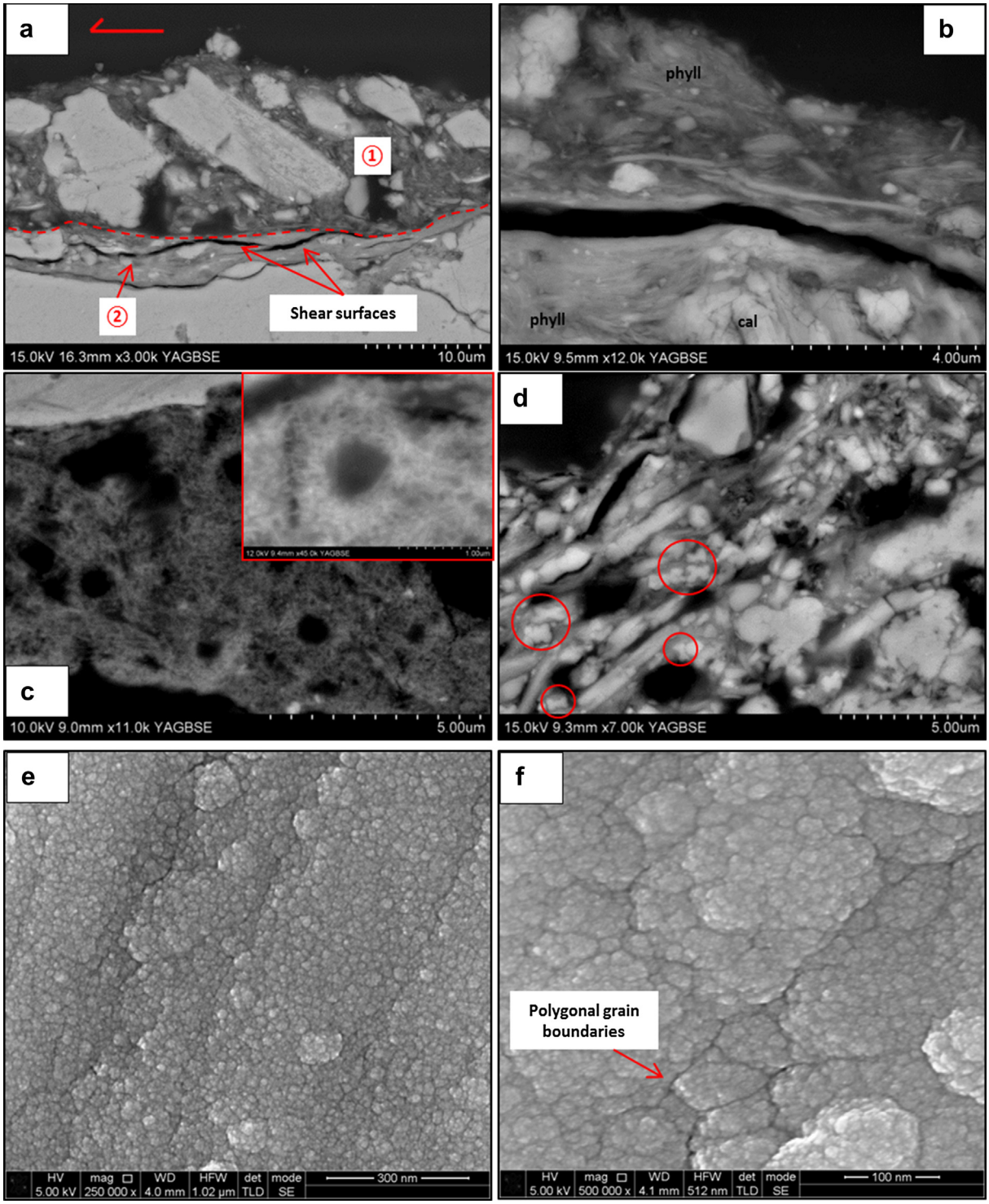

Fig. 9. SEM images of features found along the PSSs F1–F4. a) The gouge that lines the PSS of F4 (see Fig. 8a for location) comprises two SLZs that are numbered in the photograph. b) A close-up image of a SLZ, showing the fractured nature of the calcite clasts and the foliated nature of the phyllosilicates. c) Another SLZ within the PSZ of F4 contains sub-spherical pores, surrounded by a combination of elongate calcite crystals and phyllosilicate. Inset shows a close-up image of one of these pores. d) "Dog-bone"/"H"-shaped calcite crystals (highlighted by red circles). e) Image taken parallel to the PSS of F4 showing striations on the slip surface from the top right-hand side to the bottom left-hand side of the image. The grooves and ridges between striations are composed of nanoparticles of calcite. f) Close-up image of the nanoparticles that form the slip surface in e. The particles, which have dimensions ranging from 50 to 150 nm, are tightly packed with sub-polygonal boundaries and triple-junction contacts. The smaller 10–20 nm grains are an artefact of the coating applied to the sample prior to analysis. (For interpretation of the references to colour in this figure legend, the reader is referred to the web version of this article.)

behaviour of the Gubbio fault during the seismic cycle, we now focus our discussion on those parts of the fault core where most of the displacements appear to be concentrated, i.e. F1–F4 and FD4. Although the total displacement accrued at the Cava Filippi outcrop only amounts to ~12% of the total displacement of the Gubbio fault, the structures here are considered analogues for what may be encountered either along-strike or down-dip of the main Gubbio fault scarp as it traverses lithological heterogeneities in the

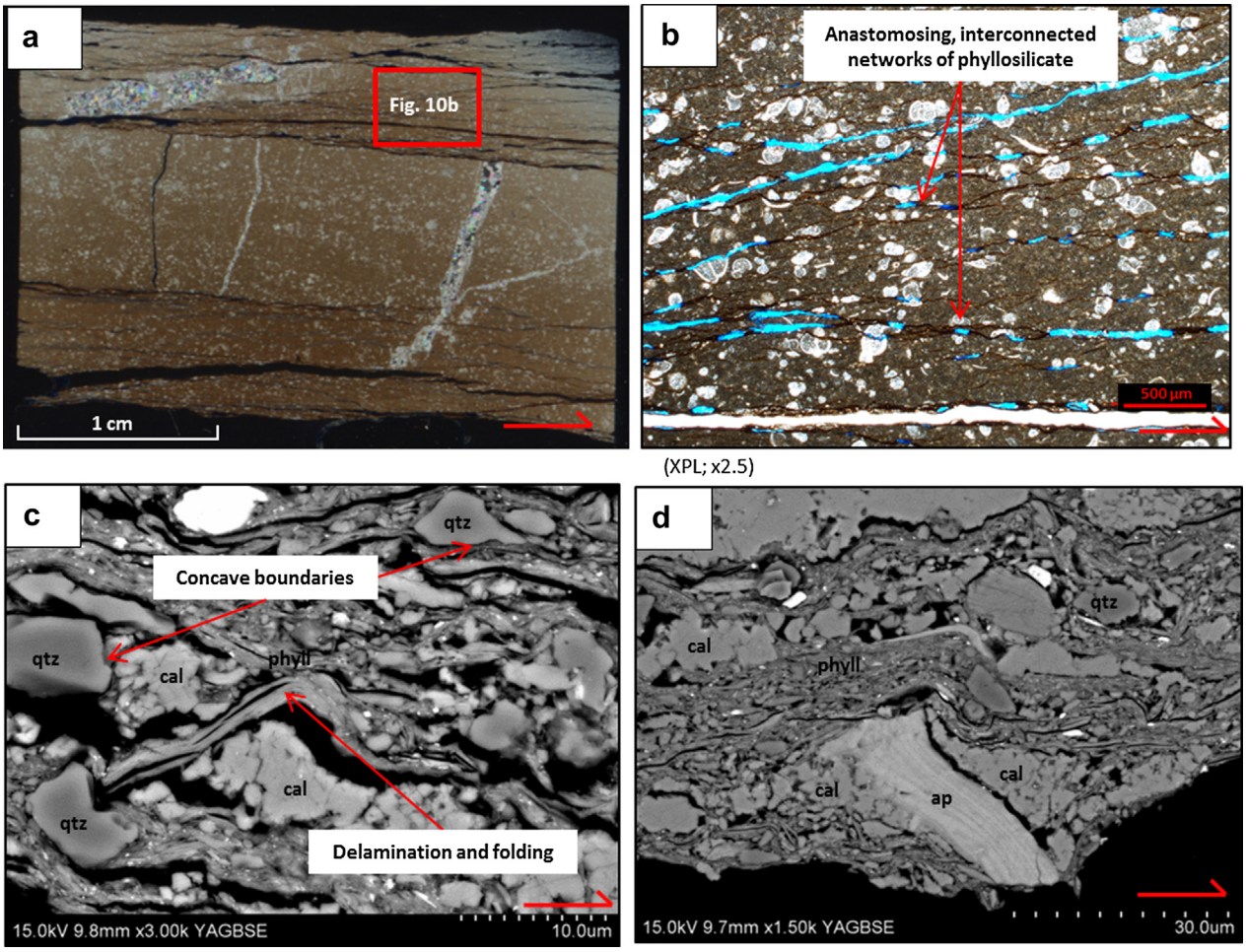

Fig. 10. Typical microscale features in domain FD4. a) Thin section scan (crossed polars) of foliated marly limestone from within a lithon bounded by S-planes. Calcite veins trend predominantly sub-perpendicular to the C-planes and are offset by up to a few mm due to pressure-solution along the C-planes. b) Optical microscope image of the foliated marly limestone (see fig. a for location). Truncation of fossils is observed adjacent to solution seams. The pressure-solution seams anastomose, bounding lithons of relatively undeformed limestone. c) SEM image of typical microstructures within the pressure-solution seams. Phyllosilicates exhibit delamination and folds/kinks, and quartz grains display smooth concave boundaries. d) SEM image showing a pressure shadow around a grain of apatite within a pressure-solution seam. The shadows on either side are composed of calcite. The alignment of phyllosilicates within the seams is the foliation. (ap = apatite; cal = calcite; phyll = phyllosilicate; qtz = quartz).

host rock. To better understand the possible behaviour of the Gubbio fault during the seismic cycle, we compare our field, microstructural and mineralogical observations with previous studies of active faults and with experimental studies for deformation of rock types similar to those at Gubbio.

The displacements accommodated along F1–F4 are concentrated mostly along the PSSs themselves and also within the PSZs. The presence of fractured, sub-rounded clasts and ultrafine-grained gouge material suggests that cataclastic deformation occurred within the PSZs. The presence of SLZs < 20 µm wide, which themselves contain further shear surfaces and an increasing proportion of phyllosilicates, suggests that shear becomes progressively localised into narrower zones during slip evolution. Similar styles of shear localisation are observed in a number of experimental studies and associated with a transition from stable sliding (velocity-strengthening) to unstable, stick-slip (velocity-weakening) behaviour (e.g. Engelder et al., 1975; Moore et al., 1988; Logan et al., 1992; Beeler et al., 1996; Collettini et al., 2011; Ikari et al., 2011). These experiments were performed on a wide range of crustal rock types (quartz, calcite, quartzo-feldspathic and phyllosilicate gouges) and under a broad spectrum of experimental conditions. On this evidence, it seems possible that the PSSs F1–F4 have behaved in a velocity- and/or slip-weakening manner. This interpretation would be consistent with the fact that they are derived from the micritic limestone protolith, since carbonate rocks do experimentally exhibit both velocity- and slip-weakening behaviour under certain conditions. For example, Verberne et al. (2010) recorded a change from velocity-strengthening to velocity-weakening in limestone gouge at temperatures between 100 and 150 °C; Collettini et al. (2011) observed an evolution from velocity-strengthening to velocity-weakening with increasing sliding velocity; and Logan et al. (1992) observed this transition at confining pressures > 50 MPa.

In FD4, displacement is distributed throughout the domain with movement accommodated along pressure-solution seams in the S–C fabric. The common occurrence of slickenfibres on C-plane surfaces suggests that the shearing within this domain is fluid-assisted. The microstructures observed within the pressure-solution seams, such as folds and kinks of the phyllosilicates and pressure shadows around clasts, are indicative of bulk ductile flow by diffusive mass transfer. They are very similar to those reported by Holdsworth et al. (2011) and Hadizadeh et al. (2012) in the phyllosilicate-rich, actively creeping zone of the San Andreas fault, i.e. they are more typical of creeping deformation than seismic slip. Interpreting the structures in FD4 to be of aseismic origin would be consistent with their phyllosilicate-rich composition due

to the marly protolith, because phyllosilicates have been shown experimentally to be almost exclusively velocity-strengthening (e.g. Morrow et al., 2007; Tembe et al., 2010; Ikari et al., 2011 and references therein). The proportion of phyllosilicates within the solution seams is >50%, which experimental evidence suggests is enough for the frictional behaviour to be controlled by the weak phyllosilicates rather than by the stronger carbonate phases (e.g. Tesei et al., 2012), due to the formation of an interconnected clay network (e.g. Schleicher et al., 2010; Tembe et al., 2010). Although phyllosilicates comprise <20% of the rock volume in FD4, the fact that they are concentrated along the solution seams means that shear strain can preferentially be focused along these pre-existing zones of weakness (Collettini et al., 2009; Behnsen and Faulkner, 2012), so that ultimately, the strength and frictional behaviour of FD4 is likely dominated by the weak phyllosilicate-rich seams. Thus, we hypothesise that FD4 deforms predominantly in a velocity-strengthening, aseismic manner, with the potential to act as a barrier to rupture propagation (e.g. Boatwright and Cocco, 1996; Kaneko et al., 2010). Consequently, earthquake ruptures might tend to bypass FD4, and concentrate displacement along the PSSs F1–F4, which lie within the velocity-weakening, micritic limestone part of the fault core.

5.3. Coseismic slip indicators

As well as having the potential to exhibit velocity-weakening behaviour, carbonate rocks are also widely shown to demonstrate strong dynamic-weakening behaviour at seismic slip rates (>1 m/s), when the frictional strength of carbonate faults reduces dramatically from Byerlee values ($\mu = 0.6–0.85$) to values as low as 0.1 (Han et al., 2007, 2010, 2011; De Paola et al., 2011a; 2011b). The weakening mechanisms are thought to be thermally activated due to the frictional heat generated along highly localised slip surfaces during rapid seismic slip (Di Toro et al., 2011).

Temperatures attained within micron-scale width slip zones at seismic slip rates may be on the order of several hundreds of degrees Celsius and that would be sufficient to trigger physical and chemical modifications to the fault rocks and slip-zone materials. For example, in carbonates, these conditions can trigger decarbonation reactions, releasing CO_2 gas into the slip zone and producing a thin layer of sub-rounded and spherical nanoparticles of lime (CaO) within the slip zone. These nanoparticles may be able to undergo rolling along the slip surface, leading to fault lubrication (Han et al., 2010, 2011; De Paola et al., 2011a).

As described in Section 3.4.2, within one of the SLZs present within the PSZ of F4, we observed bubble-like features set within a matrix of elongate calcite crystals and phyllosilicate, together with some unusual “dog-bone” or “H”-shaped calcite crystals. These microstructures are strikingly similar to those observed by Collettini et al. (2013) within the PSZ of the Spoleto thrust in central Italy. Collettini et al. (2013) performed transmission electron microscope analyses on the matrix material within the PSZ and found the presence of amorphous silicate. The fault rocks at Spoleto are derived from the Scaglia Rossa Formation, so they are formed from the same protolith as the fault rocks at Gubbio and also formed at similar depths of 2–3 km. Collettini et al. (2013) suggested that the observed microstructures are produced by thermally-triggered reactions in the PSZ as a result of rapid heating during earthquake slip. They propose that dehydroxylation of clays has resulted in amorphisation, and that the skeletal habit of calcite is a result of disequilibrium crystallisation under rapid cooling conditions (e.g. Faure et al., 2003) following carbonate dissociation. The fact that we can make a direct comparison between the microstructures observed along F4 and those described above of Collettini et al. (2013) leads to the conclusion that F4 has slipped coseismically.

The absence of smectite in the PSZs of F1–F4, as revealed by XRD analyses, may also be due to frictional heating associated with seismic slip, since smectite becomes unstable at temperatures between 120 and 150 °C and collapses to an illite-type structure (e.g. Pytte and Reynolds, 1989). The exact mechanism of this smectite-illite transformation has not been well constrained, but it is often associated with the loss of interlayer water (due to dehydration) (Colten-Bradley, 1987).

With knowledge of the thickness of the PSZ, the thermal properties of the PSZ constituents, plus the slip rates and displacements experienced during a seismic event of a given magnitude, it is possible to estimate the average temperature attained within the PSZ during the propagation of an earthquake. Given that the SLZs present within the PSZs are on the order of <20 μm wide, we can simplify our analysis to assume that slip occurred within a zone of zero thickness (Rice, 2006), making it possible to use the equation of Carslaw and Jaeger (1959) to estimate the temperature rise:

$$T_{Av} = \frac{\tau_{av}\sqrt{Dv}}{\rho c_p \sqrt{\pi k}} \quad (1)$$

where D = displacement (using values of earthquake slip for a given magnitude as presented by Sibson, 1989), τ_{av} = the shear strength of the fault for a hydrostatic fluid pressure of $\lambda = 0.4$, v = slip velocity, and ρ, c_p and κ are the density, specific heat capacity and thermal diffusivity, respectively, of the slip zone materials. We use values for calcite of $\rho = 2710\ \mathrm{kg\,m^{-3}}$, $c_p = 820\ \mathrm{J\,kg^{-1}\,K^{-1}}$ and $\kappa = 1.62 \times 10^{-6}\ \mathrm{m^2\,s^{-1}}$ (Wangen, 2010), values for smectite of $\rho = 2608\ \mathrm{kg\,m^{-3}}$, $c_p = 795\ \mathrm{J\,kg^{-1}\,K^{-1}}$ and $\kappa = 0.91 \times 10^{-6}\ \mathrm{m^2\,s^{-1}}$ (Wangen, 2010) and values for illite of $\rho = 2660\ \mathrm{kg\,m^{-3}}$, $c_p = 808\ \mathrm{J\,kg^{-1}\,K^{-1}}$ and $\kappa = 0.86 \times 10^{-6}\ \mathrm{m^2\,s^{-1}}$ (Wangen, 2010). Considering a depth of faulting of 2.5 km, this equation yields temperatures adequate for calcite decarbonation, which initiates at a temperature of ~720 °C (Sharp et al., 2003), for earthquakes with $M > 3$, in the case of a strong fault ($\mu = 0.85$), or $M > 6$, in the case of a weak fault ($\mu = 0.2$). Dehydroxylation of smectite and illite initiate at temperatures of approximately 600 °C (Shoval, 2003) and 900 °C (Jordán et al., 1999) respectively. This behaviour would correspond to an $M > 3$ earthquake in the case of a strong fault, and an $M > 5$ earthquake in the case of a weak fault. Thus, the historical normal-faulting earthquakes that have occurred throughout the Apennines, which typically have $M \approx 5–6$, could easily trigger thermal decomposition reactions and leave behind recrystallised calcite textures and clay transformations as signatures of seismic slip.

We have also observed nanoparticles coating the slip surfaces of F1–F4 (Section 3.4.2.2; Fig. 9e and f), providing further evidence that the thermal dissociation of carbonate may have occurred and that dynamic weakening was operative along these faults. In fact, their tightly-packed geometries and polygonal boundaries resemble those produced experimentally by Smith et al. (2013), who suggested that they result from dynamic recrystallisation due to intense frictional heating. Thus, there are several lines of evidence to suggest that seismic slip has occurred along the PSSs F1–F4, but we have been unable to identify any seismic signatures

Table 1
Summary of clay fraction XRD results. Percentages are estimates based on peak area.

Sample #	Description	Illite	Smectite	Kaolinite
2	Protolith (micritic limestone)	6.15%	93.20%	0.64%
28	Protolith (marly limestone)	11.70%	87.60%	0.70%
21a	Solution seam (FD3)	79.60%	15.80%	4.60%
28 (2010)	Solution seam (FD4)	45.54%	28.60%	25.85%
10	PSZ (F3)	92.60%	0.00%	7.40%
21b	PSZ (F4)	84.60%	2.00%	13.40%

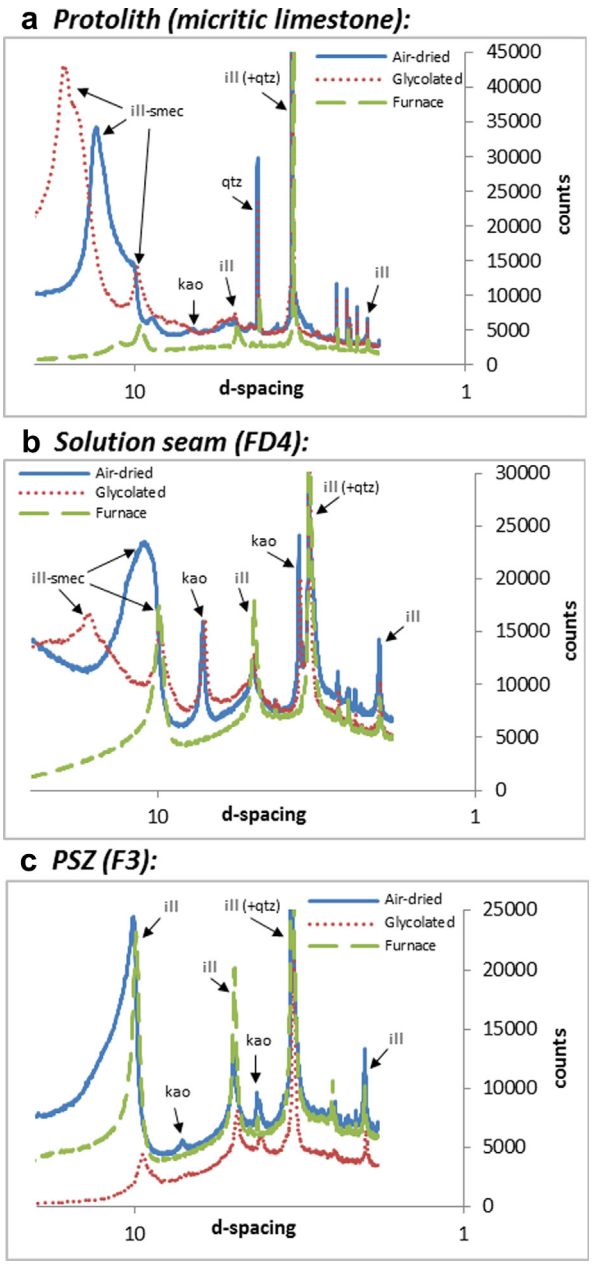

Fig. 11. Representative XRD traces of the clay fraction present in different parts of the fault zone: a) The micritic limestone protolith. b) A pressure-solution seam from FD4. c) A PSZ from F3. See Table 1 for a summary of the results and see text for discussion. (ill-smec = mixed-layer illite-smectite; kao = kaolinite; ill = illite; qtz = quartz).

within domain FD4, further supporting our hypothesis that FD4 behaves predominantly aseismically.

5.4. Seismic vs. aseismic behaviour during the seismic cycle

While it would be useful if our hypothesis fully described the deformation behaviour of the fault core, evidence suggests that the simple seismic vs. aseismic differentiation between the PSSs F1–F4 and domain FD4 is unlikely. Firstly, carbonate rocks do not behave exclusively in a velocity-weakening manner (Logan et al., 1992; Verberne et al., 2010; Collettini et al., 2011) and shear localisation is not always associated with stick-slip behaviour (e.g. Logan et al., 1979; Marone et al., 1990; Rathbun and Marone, 2010). Similarly, phyllosilicates do not behave exclusively in a velocity-strengthening manner (e.g. Saffer and Marone, 2003; Ikari et al., 2007; Niemeijer et al., 2012). Frictional behaviour is dependent on a number of factors, including the ambient conditions (normal stress, temperature and pore fluid pressure), the imposed rupture velocity, pre-existing structures within the slip zone, and the composition and distribution of mineral phases within the slip zone.

Secondly, Kaneko et al. (2010) showed that under certain conditions, velocity-strengthening fault patches can host earthquake ruptures, for example, if the earthquake is of large-enough magnitude to overcome the negative stress drop encountered within the velocity-strengthening material, or because of high pre-stress in the velocity-strengthening patch as a consequence of it not being ruptured during previous seismic events. This would explain the occurrence of a localised zone of shearing in the centre of FD4. Indeed, once transected, seismic ruptures may exploit this localised zone in FD4 by reactivation.

A complex interplay between seismic and aseismic behaviour is also evident from our microstructural observations. For example, we have observed that many slip surfaces associated with F1–F4 have stylolitic morphologies, highlighted by the presence of phyllosilicate (Section 3.4.2; Fig. 8e and d). We have also observed SLZs that are enriched in phyllosilicates (up to 80%; Fig. 9a). The concentration of phyllosilicates within PSZs is likely to be a result of pressure-solution processes operating along the PSSs during the interseismic period. And thus at certain times during the seismic cycle, diffusive mass transfer processes dominate over cataclasis and frictional sliding within the PSZs. In fact, grain-size reduction by cataclasis will promote diffusive mass transfer processes and may lead to a transition from frictional to frictional-viscous behaviour (Bos and Spiers, 2001), therefore promoting fault creep. Conversely, the dissolution of the asperities along a fault surface may reduce their strength, causing them to break successively and trigger fracturing of the fault plane (Gratier and Gamond, 1990).

Finally, the variations in calcite vein textures observed within the PSZ of F3 (Section 3.4.2.2; Fig. 8b and d) further point to variations in the seismic history of the fault. As proposed by Gratier and Gamond (1990), a crack-seal texture (Ramsay, 1980) may reflect sliding occurring at a very slow rate, during which successive microcracks are healed. The presence of small euhedral crystals, on the other hand, may reflect precipitation of calcite into larger fluid-filled cavities created during more rapid displacement events (Gratier and Gamond, 1990), whilst the PSS-parallel stylolites are indicative of fault healing by pressure-solution welding (e.g. Yasuhara et al., 2005).

Despite these complexities, we propose a simplified conceptual model, which summarises possible scenarios for the mechanical behaviour of the Gubbio fault (Fig. 12). During an earthquake, the micritic limestone-dominated portions of the fault core accommodate the coseismic displacements along the localised PSSs F1–F4. This localisation is accompanied by fracturing and/or hydrofracturing within domains FD1–FD3. At these times, domain FD4, which does not accommodate either of these modes of deformation, remains loaded, and this residual stress is then relaxed during the post-seismic period by slow, creeping afterslip deformation concentrated in the marly sections of the fault core. Alternatively, it may be that domain FD4 and certain parts of domains FD1–FD3, i.e. the pressure-solution seams, and certain portions of the PSZs of F1–F4, creep continuously during the interseismic period, whilst the other parts of the fault core remain locked. This behaviour will increase the stresses in the locked parts of the fault core until they fail seismogenically. In addition, Sagi (2012) found that the marl-rich units of the Scaglia Rossa Formation act as fault seals, inhibiting fluid flow. This behaviour is consistent with the observation that calcite veining in FD4 occurs to a much lesser extent than in domains FD1–FD3. It

is possible that the fluids involved in the pressure-solution processes in FD4, transport material away from FD4 to be deposited in the veins within FD1–FD3. Either way, the preferential transport of fluids away from FD4 and towards FD1–FD3 will generate a fluid overpressure and result in the hydrofracturing and hydraulic brecciation that we observe in domains FD1–FD3. This fluid overpressure can also trigger seismic slip along the PSSs F1–F4, which would be consistent with the fact that some PSZs are characterised by calcite veining (e.g. Fig. 5d) and chaotic breccias (e.g. Fig. 5b). A similar mixed-mode fault slip behaviour has been proposed, and supported experimentally, by Collettini et al. (2011) for the Zuccale fault zone, which similarly consists of domains of competent carbonate material surrounded by foliated, phyllosilicate-rich horizons (Collettini and Holdsworth, 2004; Collettini et al., 2011).

Although there is no recorded evidence of afterslip deformation occurring at Gubbio specifically, one of the best-documented examples of afterslip deformation comes from L'Aquila, ~130 km south of Gubbio, after the 2009 Mw 6.1 earthquake, where post-seismic deformation may have amounted to as much as 50% of the coseismic slip (Wilkinson et al., 2010; D'Agostino et al., 2012). Evidence of interseismic creep in the Apennines is also limited, but D'Agostino et al. (2009) identified, through the study of GPS velocity fields, a significant deficit in seismic release in the Umbria–Marche Apennines, which makes aseismic activity a real possibility. The one place where interseismic creep is documented in the northern Apennines is along the Alto-Tiberina low-angle normal fault, of which the Gubbio fault is an antithetic splay (Chiaraluce et al., 2007; Hreinsdóttir and Bennett, 2009). These observations show that the lithologies through which the Gubbio fault penetrates are able to accommodate aseismic creep. The driving forces and mechanisms by which afterslip and interseismic creep occur are not yet fully understood, but a number of recent studies show a coincidence between the operation of pressure-solution creep and the aseismic sliding of active faults (Gratier et al., 2011, 2013; Holdsworth et al., 2011; Hadizadeh et al., 2012).

Other factors besides lithology can control the distribution of seismicity within a fault zone such as geometric complexities,

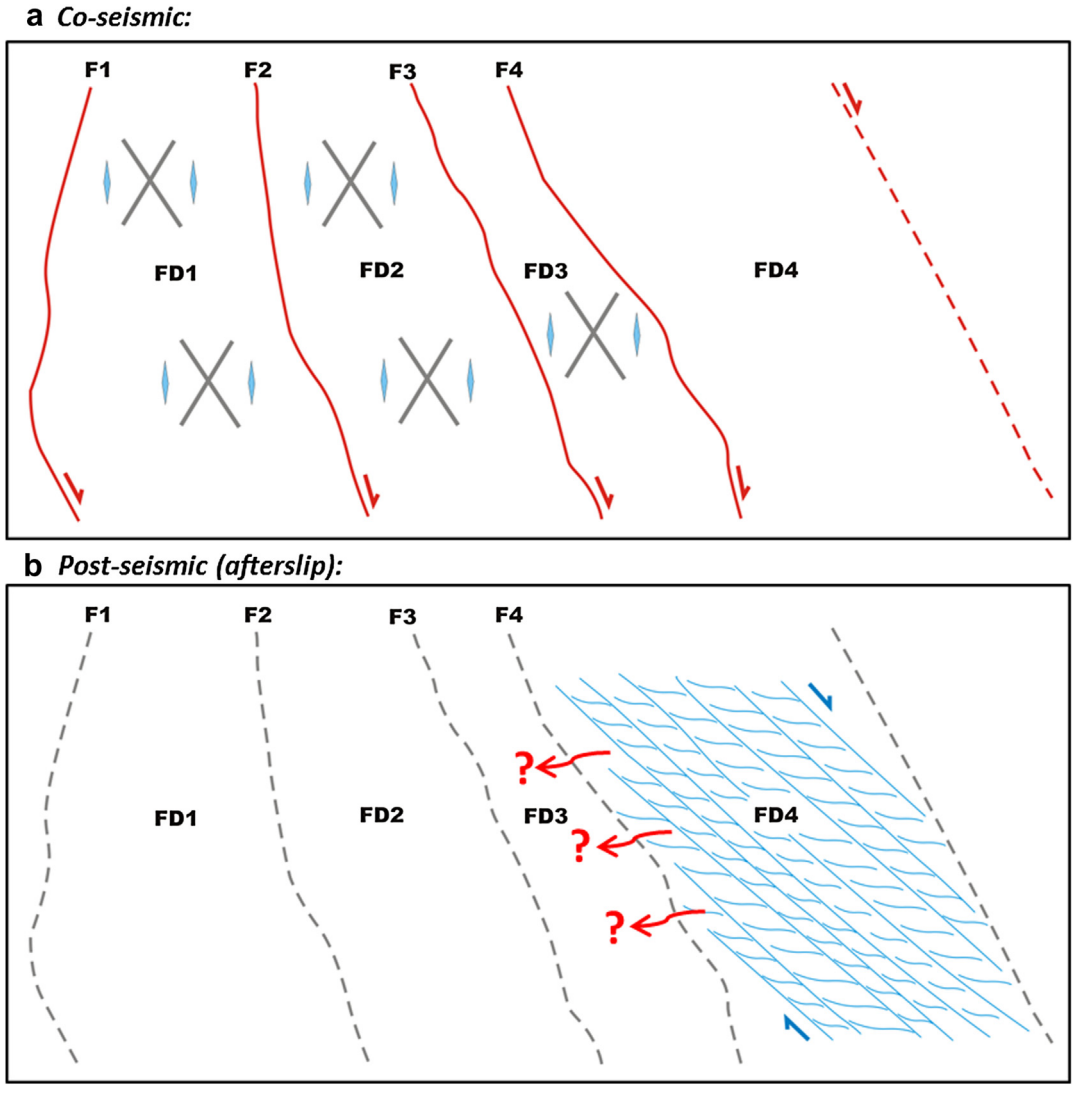

Fig. 12. A conceptual model summarising our proposed behaviour of the Gubbio fault over the course of the seismic cycle. a) During the coseismic period, activity is concentrated within the micritic limestone-hosted parts of the fault core. Coseismic displacements are localised along the PSSs F1–F4 and seismic energy dissipated through domains FD1–FD3 produces fractures/hydrofractures, resulting in extensive brecciation over time within these domains. FD4 remains locked during the coseismic period due to its velocity-strengthening nature, resulting in stress accumulation within the domain. b) During the post-seismic period, the accumulated stress in FD4 is relaxed by slow, creeping afterslip deformation. If FD4 creeps continuously during the interseismic period, stress in the locked domains FD1–FD3 will increase, until they fail seismogenically. The possible transfer of fluids away from FD4, as shown by the red arrows, may further enhance stress accumulation in domains FD1–FD3.

which can induce different strain rates within a fault zone (e.g. Tesei et al., 2013), and the location of the mainshock rupture patch, since post-seismic strains will preferentially occur in the areas surrounding the location of the mainshock (e.g. Johnson et al., 2006; Ozawa et al., 2011; D'Agostino et al., 2012). But still, playing down the importance of lithology is hard in these cases. Geometric complexities within fault zones are often a result of lithological heterogeneities within the sequences through which a fault traverses (e.g. Bonson et al., 2007; Nemser and Cowan, 2009; Tesei et al., 2013). Also, lithology can control the location of earthquake rupture patches, since, as discussed in Section 5.2, earthquakes will only nucleate in materials that are velocity-weakening.

6. Conclusion

The majority of displacement at the Cava Filippi outcrop is accommodated along the PSSs F1–F4 and in domain FD4. Along F1–F4, the dominant deformation mechanisms are cataclasis and frictional sliding. The resulting microstructures and localised deformation features are similar to those observed in both natural and experimental examples of major earthquake-hosting faults. We therefore propose that earthquake nucleation and propagation are favoured along F1–F4, which are hosted in micritic limestones. Domain FD4 is characterised by continuous, distributed deformation with the dominant deformation mechanism being pressure-solution. The structures observed in FD4 are comparable to those observed in natural and experimental examples of creeping faults. Thus, we propose that domain FD4 behaves in an aseismic manner and we attribute this behaviour to its phyllosilicate-rich host rock. The behaviour of the Gubbio fault over the course of the seismic cycle is therefore likely to be complex, with a lithologically-controlled interplay between localised earthquake nucleation and propagation, and distributed interseismic and post-seismic deformation. Combined field, microstructural, geodetic and experimental studies of faults in varying lithologies, and under a range of conditions, will help us to better constrain the role of lithology in controlling fault behaviour, so that lithological variations along or across a fault may be considered when assessing the past seismicity and future seismic hazard of a fault.

Acknowledgements

We thank Cristiano Collettini and an anonymous reviewer for thoughtful comments which helped to improve the manuscript. Thanks also go to the Editor, William Dunne, for further constructive revisions. This work was funded by the Natural Environment Research Council through a NERC PhD studentship NE/J500215/1 awarded to RJB, and a NERC Standard Grant NE/H021744/1 awarded to NDP. L. Bowen (G.J. Russell Microscopy Facility, Durham University, UK) provided assistance during SEM analyses. We thank also E. Dempsey and I. Faoro for assistance in the field. Enquiries regarding access to research materials should be directed towards the corresponding author.

References

Agosta, F., Aydin, A., 2006. Architecture and deformation mechanism of a basin-bounding normal fault in Mesozoic platform carbonates, central Italy. J. Struct. Geol. 28, 1445–1467.

Amato, A., Azzara, R., Chiarabba, C., Cimini, G., Cocco, M., Di Bona, M., Margheriti, L., Mazza, S., Mele, F., Selvaggi, G., 1998. The 1997 Umbria–Marche, Italy, earthquake sequence: a first look at the main shocks and aftershocks. Geophys. Res. Lett. 25, 2861–2864.

Barchi, M., DeFeyter, A., Magnani, M., Minelli, G., Pialli, G., Sotera, B., 1998a. Extensional tectonics in the northern Apennines (Italy): evidence from the CROP03 deep seismic reflection line. Mem. Soc. Geol. Ital. 52, 528–538.

Barchi, M., DeFeyter, A., Magnani, M., Minelli, G., Pialli, G., Sotera, B., 1998b. The structural style of the Umbria–Marche fold and thrust belt. Mem. Soc. Geol. Ital. 52, 557–578.

Barchi, M., Pucci, S., Collettini, C., Mirabella, F., Massoli, D., Guzzetti, F., Reichenbach, P., Cardinali, M., Vergoni, N., Troiani, E., Chiraz, P., Giombini, L., 2001. A geologic map of the Colfiorito area. Geoitalia, 333–334, 3° forum first poster session.

Bastesen, E., Braathen, A., 2010. Extensional faults in fine grained carbonates – analysis of fault core lithology and thickness–displacement relationships. J. Struct. Geol. 32, 1609–1628.

Beeler, N., Tullis, T., Blanpied, M., Weeks, J., 1996. Frictional behavior of large displacement experimental faults. J. Geophys. Res. 101, 8697–8715.

Behnsen, J., Faulkner, D.R., 2012. The effect of mineralogy and effective normal stress on frictional strength of sheet silicates. J. Struct. Geol. 42, 49–61.

Boatwright, J., Cocco, M., 1996. Frictional constraints on crustal faulting. J. Geophys. Res.: Solid Earth 101, 13895–13909.

Boncio, P., Brozzetti, F., Ponziani, F., Barchi, M., Lavecchia, G., Pialli, G., 1998. Seismicity and extensional tectonics in the northern Umbria–Marche Apennines. Mem. Geol. Soc. Italy 52, 539–555.

Boncio, P., Lavecchia, G., 2000. A structural model for active extension in central Italy. J. Geodyn. 29, 233–244.

Bonson, C.G., Childs, C., Walsh, J.J., Schöpfer, M.P., Carboni, V., 2007. Geometric and kinematic controls on the internal structure of a large normal fault in massive limestones: the Maghlaq Fault, Malta. J. Struct. Geol. 29, 336–354.

Bortolotti, V., Passerini, P., Sagri, M., Sestini, G., 1970. The miogeosynclinal sequences. Sediment. Geol. 4, 341–444.

Bos, B., Spiers, C., 2001. Experimental investigation into the microstructural and mechanical evolution of phyllosilicate-bearing fault rock under conditions favouring pressure solution. J. Struct. Geol. 23, 1187–1202.

Burkhard, M., 1993. Calcite twins, their geometry, appearance and significance as stress-strain markers and indicators of tectonic regime: a review. J. Struct. Geol. 15, 351–368.

Bussolotto, M., Benedicto, A., Invernizzi, C., Micarelli, L., Plagnes, V., Deiana, G., 2007. Deformation features within an active normal fault zone in carbonate rocks: the Gubbio fault (Central Apennines, Italy). J. Struct. Geol. 29, 2017–2037.

Byerlee, J., 1978. Friction of rocks. Pure Appl. Geophys. 116, 615–626.

Carslaw, H., Jaeger, J., 1959. Conduction of Heat in Solids, second ed. Oxford University Press, New York.

Carpenter, B., Marone, C., Saffer, D., 2011. Weakness of the San Andreas Fault revealed by samples from the active fault zone. Nature Geoscience 4, 251–254.

Chester, F., Logan, J., 1986. Implications for mechanical properties of brittle faults from observations of the Punchbowl fault zone, California. Pure Appl. Geophys. 124, 79–106.

Chester, F.M., Evans, J.P., Biegel, R.L., 1993. Internal structure and weakening mechanisms of the San Andreas Fault. J. Geophys. Res. 98, 771–786.

Chester, F.M., Chester, J.S., 1998. Ultracataclasite structure and friction processes of the Punchbowl fault, San Andreas system, California. Tectonophysics 295, 199–221.

Chiarabba, C., et al., 2009. The 2009 L'Aquila (central Italy) Mw6. 3 earthquake: main shock and aftershocks. Geophys. Res. Lett. 36, L18308. http://dx.doi.org/10.1029/2009GL039627.

Chiaraluce, L., 2012. Unravelling the complexity of Apenninic extensional fault systems: a review of the 2009 L'Aquila earthquake (Central Apennines, Italy). J. Struct. Geol. 42, 2–18.

Chiaraluce, L., Chiarabba, C., Collettini, C., Piccinini, D., Cocco, M., 2007. Architecture and mechanics of an active low-angle normal fault: Alto Tiberina Fault, northern Apennines, Italy. J. Geophys. Res. 112, B10310. http://dx.doi.org/10.1029/2007JB005015.

Collettini, C., Barchi, M., Chiaraluce, L., Mirabella, F., Pucci, S., 2003. The Gubbio fault: can different methods give pictures of the same object? J. Geodyn. 36, 51–66.

Collettini, C., Holdsworth, R., 2004. Fault zone weakening and character of slip along low-angle normal faults: insights from the Zuccale fault, Elba, Italy. J. Geol. Soc. 161, 1039–1051.

Collettini, C., Niemeijer, A., Viti, C., Marone, C., 2009. Fault zone fabric and fault weakness. Nature 462, 907–910.

Collettini, C., Niemeijer, A., Viti, C., Smith, S.A.F., Marone, C., 2011. Fault structure, frictional properties and mixed-mode fault slip behavior. Earth Planet. Sci. Lett. 311, 316–327.

Collettini, C., Viti, C., Tesei, T., Mollo, S., 2013. Thermal decomposition along natural carbonate faults during earthquakes. Geology 41, 927–930.

Colten-Bradley, V.A., 1987. Role of pressure in smectite dehydration – effects on geopressure and smectite-to-illite transformation. AAPG Bull. 71, 1414–1427.

D'Agostino, N., Cheloni, D., Fornaro, G., Giuliani, R., Reale, D., 2012. Space-time distribution of afterslip following the 2009 L'Aquila earthquake. J. Geophys. Res. 117, B02402. http://dx.doi.org/10.1029/2011JB008523.

D'Agostino, N., Mantenuto, S., D'Anastasio, E., Avallone, A., Barchi, M., Collettini, C., Radicioni, F., Stoppini, A., Fastellini, G., 2009. Contemporary crustal extension in the Umbria–Marche Apennines from regional CGPS networks and comparison between geodetic and seismic deformation. Tectonophysics 476, 3–12.

De Paola, N., Chiodini, G., Hirose, T., Cardellini, C., Caliro, S., Shimamoto, T., 2011a. The geochemical signature caused by earthquake propagation in carbonate-hosted faults. Earth Planet. Sci. Lett. 310, 225–232.

De Paola, N., Collettini, C., Faulkner, D., Trippetta, F., 2008. Fault zone architecture and deformation processes within evaporitic rocks in the upper crust. Tectonics 27, TC4017. http://dx.doi.org/10.1029/2007TC002230.
De Paola, N., Hirose, T., Mitchell, T., Di Toro, G., Viti, C., Shimamoto, T., 2011b. Fault lubrication and earthquake propagation in thermally unstable rocks. Geology 39, 35–38.
De Paola, N., Mirabella, F., Barchi, M., Burchielli, F., 2006. Early orogenic normal faults and their reactivation during thrust belt evolution: the Gubbio fault case study, Umbria–Marche Apennines (Italy). J. Struct. Geol. 28, 1948–1957.
Deschamps, A., Iannaccone, G., Scarpa, R., 1984. The Umbrian earthquake (Italy) of 19 September 1979. Ann. Geophys. 2, 29–36.
Di Toro, G., Han, R., Hirose, T., De Paola, N., Nielsen, S., Mizoguchi, K., Ferri, F., Cocco, M., Shimamoto, T., 2011. Fault lubrication during earthquakes. Nature 471, 494–498.
Dieterich, J.H., Kilgore, B.D., 1994. Direct observation of frictional contacts: new insights for state-dependent properties. Pure Appl. Geophys. 143, 283–302.
Dziewonski, A., Franzen, J., Woodhouse, J., 1985. Centroid-moment tensor solutions for April–June, 1984. Phys. Earth Planet. Inter. 37, 87–96.
Ekström, G., Morelli, A., Boschi, E., Dziewonski, A.M., 1998. Moment tensor analysis of the central Italy earthquake sequence of September–October 1997. Geophys. Res. Lett. 25, 1971–1974.
Engelder, J.T., Logan, J.M., Handin, J., 1975. The sliding characteristics of sandstone on quartz fault-gouge. Pure Appl. Geophys. 113, 69–86.
Fagereng, Å., Sibson, R.H., 2010. Melange rheology and seismic style. Geology 38, 751–754.
Faulkner, D., Lewis, A., Rutter, E., 2003. On the internal structure and mechanics of large strike-slip fault zones: field observations of the Carboneras fault in southeastern Spain. Tectonophysics 367, 235–251.
Faulkner, D., Jackson, C., Lunn, R., Schlische, R., Shipton, Z., Wibberley, C., Withjack, M., 2010. A review of recent developments concerning the structure, mechanics and fluid flow properties of fault zones. J. Struct. Geol. 32, 1557–1575.
Faure, F., Trolliard, G., Nicollet, C., Montel, J.-M., 2003. A developmental model of olivine morphology as a function of the cooling rate and the degree of undercooling. Contrib. Mineral. Petrol. 145, 251–263.
Fondriest, M., Smith, S.A.F., Di Toro, G., Zampieri, D., Mittempergher, S., 2012. Fault zone structure and seismic slip localization in dolostones, an example from the Southern Alps, Italy. J. Struct. Geol. 45, 52–67.
GE.MI.NA, 1963. Ligniti e torbe dell'Italia Centrale. GE.MI.NA., Geomineraria Nazionale, Torino.
Gratier, J., Gamond, J., 1990. Transition between seismic and aseismic deformation in the upper crust. Geol. Soc., Lond., Spec. Publ. 54, 461–473.
Gratier, J.-P., Richard, J., Renard, F., Mittempergher, S., Doan, M.-L., Di Toro, G., Hadizadeh, J., Boullier, A.-M., 2011. Aseismic sliding of active faults by pressure solution creep: evidence from the San Andreas Fault Observatory at Depth. Geology 39, 1131–1134.
Gratier, J.P., Thouvenot, F., Jenatton, L., Tourette, A., Doan, M.L., Renard, F., 2013. Geological control of the partitioning between seismic and aseismic sliding behaviours in active faults: evidence from the Western Alps, France. Tectonophysics 600, 226–242.
Gu, Y., Wong, T., 1994. Development of shear localization in simulated quartz gouge: effect of cumulative slip and gouge particle size. Pure Appl. Geophys. 143, 387–423.
Hadizadeh, J., Mittempergher, S., Gratier, J.P., Renard, F., Di Toro, G., Richard, J., Babaie, H.A., 2012. A microstructural study of fault rocks from the SAFOD: implications for the deformation mechanisms and strength of the creeping segment of the San Andreas Fault. J. Struct. Geol. 42, 246–260.
Haessler, H., Gaulon, R., Rivera, L., Console, R., Frogneux, M., Gasparini, G., Martel, L., Patau, G., Siciliano, M., Cisternas, A., 1988. The Perugia (Italy) earthquake of 29, April 1984: a microearthquake survey. Bull. Seismol. Soc. Am. 78, 1948–1964.
Han, R., Hirose, T., Shimamoto, T., 2010. Strong velocity weakening and powder lubrication of simulated carbonate faults at seismic slip rates. J. Geophys. Res. 115, B03412. http://dx.doi.org/10.1029/2008JB006136.
Han, R., Hirose, T., Shimamoto, T., Lee, Y., Ando, J., 2011. Granular nanoparticles lubricate faults during seismic slip. Geology 39, 599–602.
Han, R., Shimamoto, T., Hirose, T., Ree, J.H., Ando, J., 2007. Ultralow friction of carbonate faults caused by thermal decomposition. Science 316, 878–881.
Holdsworth, R., Van Diggelen, E., Spiers, C., De Bresser, J., Walker, R., Bowen, L., 2011. Fault rocks from the SAFOD core samples: implications for weakening at shallow depths along the San Andreas Fault, California. J. Struct. Geol. 33, 132–144.
Hreinsdóttir, S., Bennett, R.A., 2009. Active aseismic creep on the Alto Tiberina low-angle normal fault, Italy. Geology 37, 683–686.
Ikari, M.J., Marone, C., Saffer, D.M., 2011. On the relation between fault strength and frictional stability. Geology 39, 83–86.
Ikari, M.J., Saffer, D.M., Marone, C., 2007. Effect of hydration state on the frictional properties of montmorillonite-based fault gouge. J. Geophys. Res. 112, B06423. http://dx.doi.org/10.1029/2006JB004748.
Ikari, M.J., Saffer, D.M., Marone, C., 2009. Frictional and hydrologic properties of clay-rich fault gouge. J. Geophys. Res. 114, B05409. http://dx.doi.org/10.1029/2008JB006089.
ISC, 2001. On-line Bulletin. International Seismological Centre, Thatcham, United Kingdom. http://www.isc.ac.uk, 2011.
Jefferies, S.P., Holdsworth, R.E., Wibberley, C.A.J., Shimamoto, T., Spiers, C.J., Niemeijer, A.R., Lloyd, G.E., 2006. The nature and importance of phyllonite development in crustal-scale fault cores: an example from the Median Tectonic Line, Japan. J. Struct. Geol. 28, 220–235.
Johnson, K.M., Bürgmann, R., Larson, K., 2006. Frictional properties on the San Andreas Fault near Parkfield, California, inferred from models of afterslip following the 2004 earthquake. Bull. Seismol. Soc. Am. 96, S321–S338.
Jordán, M.M., Boix, A., Sanfeliu, T., de la Fuente, C., 1999. Firing transformations of cretaceous clays used in the manufacturing of ceramic tiles. Appl. Clay Sci. 14, 225–234.
Kaneko, Y., Avouac, J.-P., Lapusta, N., 2010. Towards inferring earthquake patterns from geodetic observations of interseismic coupling. Nat. Geosci. 3, 363–369.
Kuo, L.-W., Hsiao, H.-C., Song, S.-R., Sheu, H.-S., Suppe, J., 2013. Coseismic thickness of principal slip zone from the Taiwan Chelungpu fault Drilling Project-A (TCDP-A) and correlated fracture energy. Tectonophysics in press.
Li, H., Wang, H., Xu, Z., Si, J., Pei, J., Li, T., Huang, Y., Song, S.-R., Kuo, L.-W., Sun, Z., 2013. Characteristics of the fault-related rocks, fault zones and the principal slip zone in the Wenchuan Earthquake Fault Scientific Drilling Project Hole-1 (WFSD-1). Tectonophysics 584, 23–42.
Lockner, D.A., Morrow, C., Moore, D., Hickman, S., 2011. Low strength of deep San Andreas Fault gouge from SAFOD core. Nature 472, 82–85.
Logan, B.W., Semeniuk, V., 1976. Dynamic Metamorphism: Processes and Products in Devonian Carbonate Rocks, Canning Basin, Western Australia. Geological Society of Australia.
Logan, J., Friedman, M., Higgs, N., Dengo, C., Shimamoto, T., 1979. Experimental Studies of Simulated Gouge and Their Application to Studies of Natural Fault Zones: Analyses of Actual Fault Zones in Bedrock. United States geological survey open file report 1239, pp. 305–343.
Logan, J., Dengo, C., Higgs, N., Wang, Z., 1992. Fabrics of experimental fault zones: their development and relationship to mechanical behavior. Int. Geophys. Ser. 51, 33.
Marone, C., 1998. Laboratory-derived friction laws and their application to seismic faulting. Annu. Rev. Earth Planet. Sci. 26, 643–696.
Marone, C., Raleigh, C.B., Scholz, C., 1990. Frictional behavior and constitutive modeling of simulated fault gouge. J. Geophys. Res. 95, 7007–7025.
Micarelli, L., Benedicto, A., Wibberley, C., 2006. Structural evolution and permeability of normal fault zones in highly porous carbonate rocks. J. Struct. Geol. 28, 1214–1227.
Mirabella, F., Ciaccio, M., Barchi, M., Merlini, S., 2004. The Gubbio normal fault (central Italy): geometry, displacement distribution and tectonic evolution. J. Struct. Geol. 26, 2233–2249.
Molli, G., Cortecci, G., Vaselli, L., Ottria, G., Cortopassi, A., Dinelli, E., Mussi, M., Barbieri, M., 2010. Fault zone structure and fluid–rock interaction of a high angle normal fault in Carrara marble (NW Tuscany, Italy). J. Struct. Geol. 32, 1334–1348.
Moore, D., Summers, R., Byerlee, J., 1988. Relationship between textures and sliding motion of experimentally deformed fault gouge: application to fault zone behavior. In: The 29th US Symposium on Rock Mechanics (USRMS).
Moore, D.E., Lockner, D.A., 2004. Crystallographic controls on the frictional behavior of dry and water-saturated sheet structure minerals. J. Geophys. Res. 109, B03401. http://dx.doi.org/10.1029/2003JB002582.
Moore, D.E., Lockner, D.A., 2011. Frictional strengths of talc-serpentine and talc-quartz mixtures. J. Geophys. Res. 116, B01403. http://dx.doi.org/10.1029/2010JB007881.
Morrow, C., Solum, J., Tembe, S., Lockner, D., Wong, T.F., 2007. Using drill cutting separates to estimate the strength of narrow shear zones at SAFOD. Geophys. Res. Lett. 34, L11301. http://dx.doi.org/10.1029/2007GL029665.
Nemser, E.S., Cowan, D.S., 2009. Downdip segmentation of strike-slip fault zones in the brittle crust. Geology 37, 419–422.
Niemeijer, A., Collettini, C., Smith, S.A.F., Spiers, C.J., 2012. Frictional properties of Zuccale fault rocks from room temperature to in-situ conditions: results from high strain rotary shear experiments. Geophys. Res. Abstr. 14. EGU2012-8001.
Otsuki, K., Monzawa, N., Nagase, T., 2003. Fluidization and melting of fault gouge during seismic slip: identification in the Nojima fault zone and implications for focal earthquake mechanisms. J. Geophys. Res. 108 (B4), 2192. http://dx.doi.org/10.1029/2001JB001711.
Ozawa, S., Nishimura, T., Suito, H., Kobayashi, T., Tobita, M., Imakiire, T., 2011. Coseismic and postseismic slip of the 2011 magnitude-9 Tohoku-Oki earthquake. Nature 475, 373–376.
Piccinini, D., Cattaneo, M., Chiarabba, C., Chiaraluce, L., De Martin, M., Di Bona, M., Moretti, M., Selvaggi, G., Augliera, P., Spallarossa, D., 2003. A microseismic study in a low seismicity area of Italy: the Città di Castello 2000–2001 experiment. Ann. Geophys. 46, 1315–1324.
Pucci, S., De Martini, P.M., Pantosti, D., Valensise, G., 2003. Geomorphology of the Gubbio basin (central Italy): understanding the active tectonics and earthquake potential. Ann. Geophys. 46, 837–864.
Power, W.L., Tullis, T.E., 1989. The relationship between slickenside surfaces in fine-grained quartz and the seismic cycle. J. Struct. Geol. 11, 879–893.
Pytte, A., Reynolds, R., 1989. The thermal transformation of smectite to illite. Therm. Hist. Sediment. Basins: Methods Case Hist., 133–140.
Ramsay, J.G., 1980. The crack-seal mechanism of rock deformation. Nature 284, 135–139.
Rathbun, A.P., Marone, C., 2010. Effect of strain localization on frictional behavior of sheared granular materials. J. Geophys. Res. 115, B01204. http://dx.doi.org/10.1029/2009JB006466.

Rice, J.R., 2006. Heating and weakening of faults during earthquake slip. J. Geophys. Res. 111, B05311. http://dx.doi.org/10.1029/2005JB004006.
Rutter, E., 1976. The kinetics of rock deformation by pressure solution. Philos. Trans. R. Soc. Lond. Ser. A, Math. Phys. Sci. 283, 203–219.
Rutter, E., Maddock, R., Hall, S., White, S., 1986. Comparative microstructures of natural and experimentally produced clay-bearing fault gouges. Pure Appl. Geophys. 124, 3–30.
Rutter, E., Faulkner, D., Burgess, R., 2012. Structure and geological history of the Carboneras fault zone, SE Spain: part of a stretching transform fault system. J. Struct. Geol. 45, 68–86.
Rybacki, E., Evans, B., Janssen, C., Wirth, R., Dresen, G., 2013. Influence of stress, temperature, and strain on calcite twins constrained by deformation experiments. Tectonophysics 601, 20–36.
Saffer, D.M., Frye, K.M., Marone, C., Mair, K., 2001. Laboratory results indicating complex and potentially unstable frictional behavior of smectite clay. Geophys. Res. Lett. 28, 2297–2300. http://dx.doi.org/10.1029/2001GL012869.
Saffer, D.M., Marone, C., 2003. Comparison of smectite-and illite-rich gouge frictional properties: application to the updip limit of the seismogenic zone along subduction megathrusts. Earth Planet. Sci. Lett. 215, 219–235.
Sagi, D.A., 2012. Characterisation of the 2D and 3D Density and Connectivity Attributes of Fracture Systems in Carbonate Reservoir Analogues: Implications for Fluid Flow (Ph.D. thesis). University of Durham, UK.
Schleicher, A., van der Pluijm, B., Warr, L., 2010. Nanocoatings of clay and creep of the San Andreas Fault at Parkfield, California. Geology 38, 667–670.
Scholz, C.H., 1998. Earthquakes and friction laws. Nature 391, 37–42.
Sharp, Z., Papike, J., Durakiewicz, T., 2003. The effect of thermal decarbonation on stable isotope compositions of carbonates. Am. Mineral. 88, 87–92.
Shipton, Z.K., Soden, A.M., Kirkpatrick, J.D., Bright, A.M., Lunn, R.J., 2006. How thick is a fault? Fault displacement–thickness scaling revisited. Geophys. Monogr. Ser. 170, 193–198.
Shoval, S., 2003. Using FT-IR spectroscopy for study of calcareous ancient ceramics. Optic. Mater. 24, 117–122.
Sibson, R., 1977. Fault rocks and fault mechanisms. J. Geol. Soc. 133, 191–213.
Sibson, R.H., 1989. Earthquake faulting as a structural process. J. Struct. Geol. 11, 1–14.
Sibson, R.H., 2003. Thickness of the seismic slip zone. Bull. Seismol. Soc. Am. 93, 1169–1178.
Smith, S.A.F., Billi, A., Toro, G.D., Spiess, R., 2011a. Principal slip zones in limestone: microstructural characterization and implications for the seismic cycle (Tre Monti Fault, Central Apennines, Italy). Pure Appl. Geophys. 168, 2365–2393.
Smith, S.A.F., Holdsworth, R.E., Collettini, C., Pearce, M.A., 2011b. The microstructural character and mechanical significance of fault rocks associated with a continental low-angle normal fault: the Zuccale fault, Elba Island, Italy. Geol. Soc., Lond., Spec. Publ. 359, 97–113.
Smith, S., Di Toro, G., Kim, S., Ree, J.H., Nielsen, S., Billi, A., Spiess, R., 2013. Coseismic recrystallization during shallow earthquake slip. Geology 41, 63–66.
Sone, H., Shimamoto, T., Moore, D.E., 2012. Frictional properties of saponite-rich gouge from a serpentinite-bearing fault zone along the Gokasho-Arashima Tectonic Line, central Japan. J. Struct. Geol. 38, 172–182.
Tembe, S., Lockner, D.A., Wong, T.F., 2010. Effect of clay content and mineralogy on frictional sliding behavior of simulated gouges: binary and ternary mixtures of quartz, illite, and montmorillonite. J. Geophys. Res. 115, B03416. http://dx.doi.org/10.1029/2009JB006383.
Tesei, T., Collettini, C., Carpenter, B.M., Viti, C., Marone, C., 2012. Frictional strength and healing behavior of phyllosilicate-rich faults. J. Geophys. Res. 117, B09402. http://dx.doi.org/10.1029/2012JB009204.
Tesei, T., Collettini, C., Viti, C., Barchi, M.R., 2013. Fault architecture and deformation mechanisms in exhumed analogues of seismogenic carbonate-bearing thrusts. J. Struct. Geol. 55, 167–181.
Trabucho-Alexandre, J., Negri, A., de Boer, P.L., 2011. Early Turonian pelagic sedimentation at Moria (Umbria–Marche, Italy): primary and diagenetic controls on lithological oscillations. Palaeogeogr. Palaeoclimatol. Palaeoecol. 311, 200–214.
Verberne, B.A., He, C., Spiers, C.J., 2010. Frictional properties of sedimentary rocks and natural fault gouge from the Longmen Shan fault zone, Sichuan, China. Bull. Seismol. Soc. Am. 100, 2767–2790.
Walker, R.J., Holdsworth, R.E., Armitage, P.J., Faulkner, D.R., 2013. Fault zone permeability structure evolution in basalts. Geology 41, 59–62.
Wangen, M., 2010. Physical Principles of Sedimentary Basin Analysis. Cambridge University Press, Cambridge.
Westaway, R., Gawthorpe, R., Tozzi, M., 1989. Seismological and field observations of the 1984 Lazio-Abruzzo earthquakes: implications for the active tectonics of Italy. Geophys. J. Int. 98, 489–514.
Wibberley, C.A.J., Shimamoto, T., 2003. Internal structure and permeability of major strike-slip fault zones: the Median Tectonic Line in Mie Prefecture, Southwest Japan. J. Struct. Geol. 25, 59–78.
Wilkinson, M., McCaffrey, K., Roberts, G., Cowie, P., Phillips, R., Michetti, A.M., Vittori, E., Guerrieri, L., Blumetti, A., Bubeck, A., 2010. Partitioned postseismic deformation associated with the 2009 Mw 6.3 L'Aquila earthquake surface rupture measured using a terrestrial laser scanner. Geophys. Res. Lett. 37, L10309. http://dx.doi.org/10.1029/2010GL043099.
Woodcock, N., Mort, K., 2008. Classification of fault breccias and related fault rocks. Geol. Mag. 145, 435–440.
Yasuhara, H., Marone, C., Elsworth, D., 2005. Fault zone restrengthening and frictional healing: the role of pressure solution. J. Geophys. Res. 110, B06310. http://dx.doi.org/10.1029/2004JB003327.
Zoback, M., Hickman, S., Ellsworth, W., 2010. Scientific drilling into the San Andreas Fault zone. Eos, Trans. Am. Geophys. Union 91, 197–199.

Appendix 4

Published version of Chapter 3

AGU PUBLICATIONS

JGR

Journal of Geophysical Research: Solid Earth

RESEARCH ARTICLE
10.1002/2015JB011914

Key Points:
- Ten percent of clay in water-saturated calcite gouges can facilitate surface faulting
- It also inhibits the development of microstructures associated with seismic slip
- The weakness of wet clay-bearing gouges is explained via a microphysical model

Supporting Information:
- Texts S1–S7

Correspondence to:
R. J. Bullock,
r.j.bullock@durham.ac.uk

Citation:
Bullock, R. J., N. De Paola, and R. E. Holdsworth (2015), An experimental investigation into the role of phyllosilicate content on earthquake propagation during seismic slip in carbonate faults, *J. Geophys. Res. Solid Earth*, *120*, doi:10.1002/2015JB011914.

Received 5 FEB 2015
Accepted 29 APR 2015
Accepted article online 4 MAY 2015

An experimental investigation into the role of phyllosilicate content on earthquake propagation during seismic slip in carbonate faults

Rachael J. Bullock[1], Nicola De Paola[1], and Robert E. Holdsworth[1]

[1]Rock Mechanics Laboratory, Department of Earth Sciences, University of Durham, Durham, UK

Abstract Carbonate faults commonly contain small amounts of phyllosilicate in their slip zones, due to pressure solution and/or clay smear. To assess the effect of phyllosilicate content on earthquake propagation in carbonate faults, friction experiments were performed at 1.3 m/s on end-members and mixtures of calcite, illite-smectite, and smectite gouge. Experiments were performed at 9 MPa normal load, under room humidity and water-saturated conditions. All dry gouges show initial friction values (μ_i) of 0.51–0.58, followed by slip hardening to peak values of 0.61–0.76. Slip weakening then ensues, with friction decreasing to steady state values (μ_{ss}) of 0.19–0.33 within 0.17–0.58 m of slip. Contrastingly, wet gouges containing 10–50 wt % phyllosilicate exhibit μ_i values between 0.07 and 0.52 followed by negligible or no slip hardening; rather, steady state sliding ($\mu_{ss} \ll 0.2$) is attained almost immediately. Microstructurally, dry gouges show intense cataclasis and wear within localized principal slip zones, plus evidence for thermal decomposition of calcite. Wet gouges exhibit distributed deformation, less intense cataclasis, and no evidence of thermal decomposition. It is proposed that in wet gouges, slip is distributed across a network of weak phyllosilicate formed during axial loading compaction prior to shear. This explains the (1) subdued cataclasis and associated lack of slip hardening, (2) distributed nature of deformation, and (3) lack of evidence for thermal decomposition, due to low friction and lack of slip localization. These findings imply that just 10% phyllosilicate in the slip zone of fluid-saturated carbonate faults can (1) dramatically change their frictional behavior, facilitating rupture propagation to the surface, and (2) significantly lower frictional heating, preventing development of microscale seismic markers.

1. Introduction

Phyllosilicates are traditionally viewed as having a stabilizing influence on the behavior of upper crustal fault zones. Experimental studies have shown that most phyllosilicates behave in a predominantly velocity-strengthening manner when deformed at subseismic slip rates (<1 cm/s) [*Saffer and Marone*, 2003; *Ikari et al.*, 2009; *Tembe et al.*, 2010; *Moore and Lockner*, 2011; *Behnsen and Faulkner*, 2012; *Sone et al.*, 2012; *Tesei et al.*, 2012]. Therefore, earthquakes are unable to nucleate in upper crustal fault zones that are rich in phyllosilicates. Instead, phyllosilicate-rich fault zones are widely believed to deform predominantly aseismically by fault creep [*Marone*, 1998; *Scholz*, 1998]. For example, the creeping behavior of the Parkfield segment of the San Andreas Fault is attributed to the presence of smectitic phyllosilicates in fault gouges [e.g., *Carpenter et al.*, 2011; *Holdsworth et al.*, 2011; *Lockner et al.*, 2011]. In addition, crustal regions containing a significant proportion of such velocity-strengthening materials, such as poorly lithified, clay-rich fault gouges, are viewed as energy sinks, due to a negative stress drop, with the potential to attenuate, or even arrest, an earthquake rupture as it propagates toward the surface [*Scholz*, 1998].

The frictional behavior of phyllosilicates at seismic slip rates is quite different to that observed at subseismic slip rates. When subject to slip velocities in excess of 1 cm/s, phyllosilicates can undergo dynamic weakening; after attaining a peak in friction at the onset of slip, they undergo an exponential decay in frictional strength, of up to 90% [e.g., *Boutareaud et al.*, 2008; *Brantut et al.*, 2008; *Ferri et al.*, 2010; *Ujiie and Tsutsumi*, 2010; *Faulkner et al.*, 2011]. This is a phenomenon observed for a wide range of rock types and has been attributed to mechanically and thermally activated reactions which weaken the fault during fast, localized slip [see *Di Toro et al.*, 2011].

Wet phyllosilicates subject to seismic slip again show a different frictional behavior; they do not attain a peak in friction and instead attain steady state sliding immediately at the onset of slip [*Ferri et al*., 2010; *Ujiie and Tsutsumi*, 2010; *Faulkner et al*., 2011; *Ferri et al*., 2011; *Ujiie et al*., 2011, 2013]. These results from high-velocity friction experiments suggest that particularly when wet, velocity-strengthening phyllosilicates may offer less resistance to seismic slip than other rock types, provided that dynamic stresses continue to produce a large enough velocity jump to trigger dynamic weakening. The reasons saturated clay-rich gouges are so weak when subject to seismic slip velocities are not well understood. Suggestions have included rapid thermal pressurization at the onset of slip [*Faulkner et al*., 2011] and pore fluid pressurization due to a combination of shear-enhanced compaction and frictional heating [*Ujiie and Tsutsumi*, 2010]. Alternatively, *Ferri et al*. [2010] proposed that the low friction coefficients associated with water-saturated clays may be due either to water molecules bonding to the surfaces of clay grains, forming thin, lubricating films (as per *Moore and Lockner* [2004]), or to water being extruded from the gouge layer during compaction and localizing at the gouge-wall rock interface so that friction is controlled by a lubricating film of water. However, these theories lack robust experimental evidence.

The complex range of frictional behaviors observed in the lab presents us with the challenge of trying to understand what role phyllosilicates may play in the behavior of natural fault zones. Phyllosilicates are widely recognized to be prevalent within clay-rich fault gouges of upper crustal faults [e.g., *Wu et al*., 1975; *Vrolijk and van der Pluijm*, 1999; *Faulkner et al*., 2003; *Holdsworth*, 2004], and within accretionary wedges at subduction zones, which frequently host tsunamigenic earthquakes [e.g., *Lay et al*., 2005; *Ide et al*., 2011; *Chester et al*., 2013]. But they are also common constituents of carbonate fault zones, for example, if the protolith is a marly limestone, or a limestone formation with marl interbeds [e.g., *Gratier et al*., 2013; *Tesei et al*., 2013; *Bullock et al*., 2014]. Several recent studies have documented the influence of phyllosilicates on the architecture and frictional behavior of carbonate fault zones. These studies include examples of strike-slip faults, e.g., the active Vuache fault in the French Alps [*Gratier et al*., 2013]; thrust faults, e.g., within the exhumed Northern Apennines fold-thrust belt in Italy (Figure 1) [*Tesei et al*., 2013]; and normal faults, e.g., the active Gubbio fault in the Northern Apennines (Figure 1) [*Bullock et al*., 2014] and the active Clansayes fault system in the French Alps [*Gratier et al*., 2013]. These studies have concluded, through a combination of geological, laboratory, and seismological observations, that marl- or phyllosilicate-rich fault domains host predominantly distributed deformation and aseismic slip, while limestone-dominated fault domains tend to host localized, brittle deformation and seismic rupture. This is attributed to the fact that pressure solution processes, and associated creep, are more efficient in polymineralic marls than in monomineralic limestone [*Gratier et al*., 2013] and that the phyllosilicates present within marls are almost exclusively velocity strengthening [e.g., *Morrow et al*., 2007; *Tembe et al*., 2010; *Ikari et al*., 2011], whereas limestone, under certain conditions, can behave in an unstable, velocity-weakening manner [*Logan et al*., 1992; *Verberne et al*., 2010; *Collettini et al*., 2011; *Verberne et al*., 2014].

As well as being associated with zones of distributed deformation within carbonate faults, phyllosilicates are also observed to be concentrated within the principal slip zones (PSZs) of many carbonate faults (Figures 1b–1e; see also Text S1 in the supporting information) [*Collettini et al*., 2013; *Tesei et al*., 2013; *Bullock et al*., 2014]. These phyllosilicates may have become concentrated in the PSZs either by smearing of clay interbeds along the fault during slip or by pressure solution acting on the fault planes or within the slip zones, preferentially removing the soluble carbonate phases and leaving behind the insoluble phyllosilicates. The phyllosilicate content within the PSZs may be as high as 50%, and often these minerals form interconnected networks of strongly aligned grains oriented subparallel to the PSZs [e.g., *Bullock et al*., 2014, Figure 9a]. In many cases, there is evidence that the phyllosilicate-enriched carbonate PSZs have hosted past seismic events [*Collettini et al*., 2013; *Tesei et al*., 2013; *Bullock et al*., 2014]. The effect that phyllosilicate content may have on the frictional behavior of carbonate faults during seismic slip represents a subject of critical importance, particularly since earthquakes within the Italian Apennines, one of the most seismically active zones in Europe (Figure 1a) [e.g., *Lavecchia et al*., 2003; *D'Agostino et al*., 2009; *Chiaraluce*, 2012; *Ventura and Di Giovambattista*, 2013], all nucleate within and propagate through a carbonate multilayer sequence comprising interbedded limestones and marls [e.g., *Barchi et al*., 1998]. Thus, in order to assess the effect of variable phyllosilicate content on the frictional behavior of phyllosilicate-bearing carbonate faults during seismic slip, we present the results from a set of high-velocity friction experiments carried out on gouges containing different proportions of calcite and phyllosilicate, under dry and water-saturated

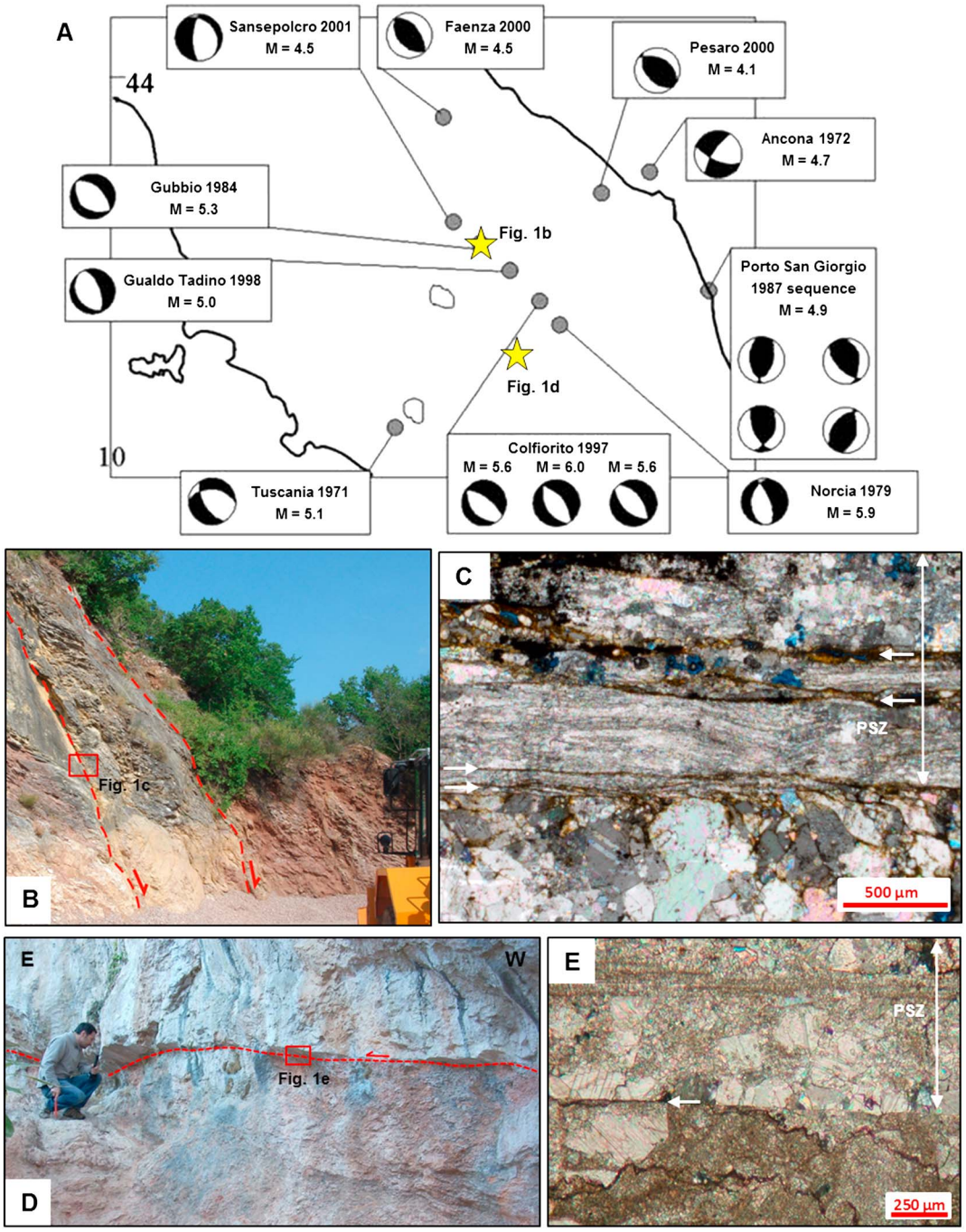

Figure 1. (a) Focal mechanism distribution within the Northern Apennines seismic belt in central Italy. Figure taken from *Collettini et al*. [2006]. (b) The active Gubbio normal fault (see Figure 1a for location), which deforms a mixture of Jurassic-Oligocene micritic limestone (yellow in color) and marly limestone (red in color). (c) Optical microscope image of a PSZ within the core of the Gubbio fault (see Figure 1b for sample location). The PSZ contains numerous slip surfaces (indicated by arrows), which are highlighted by the presence of dark brown phyllosilicate. The rest of the PSZ is dominated by calcite veining. Additional examples of phyllosilicate-enriched PSZs from the Northern Apennines are presented in Text S1. (d) The exhumed Spoleto thrust fault (see Figure 1a for location), which brings Lower Jurassic massive limestones in the HW on top of Cretaceous layered limestones in the FW. (e) Optical microscope image of the PSZ of the Spoleto fault (see Figure 1d for sample location). Again, the PSZ is dominated by calcite veining, and the PSS is contaminated by brown phyllosilicate (indicated by arrow) from pressure solution. Figures 1d and 1e are courtesy of Telemaco Tesei.

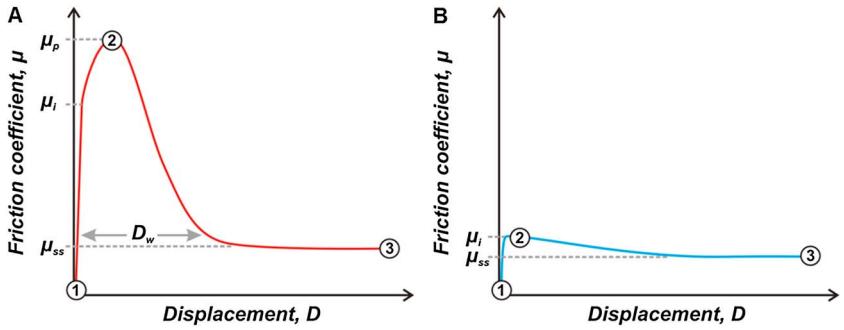

Figure 2. Schematic representation of frictional evolution during the experiments. (a) The case for gouges which exhibit a peak in friction during the experiments and (b) the case for gouges which do not exhibit a peak in friction. Numbering refers to the three stages at which samples were recovered for inspection. See text for explanation.

conditions. The mechanical data from our experiments are accompanied by microstructural observations of the deformed gouges, which we use to devise a micromechanical model that can be used to explain their frictional behavior.

2. Experimental Setup and Procedure

Friction experiments were performed using the Low to High Velocity Rotary Shear Apparatus at Durham University (Text S2). We deformed end-member gouges of calcite, mixed-layer illite-smectite, and smectite, as well as 50:50, 80:20, and 90:10 mixtures of calcite + illite-smectite and calcite + smectite. These are representative of the PSZ compositions observed in the Northern Apennines [*Collettini et al*., 2013; *Bullock et al*., 2014]. The calcite gouges were prepared from undeformed samples of the Scaglia Rossa limestone (~95% calcite), which were collected from field locations close to the exposure of the Gubbio fault [see *Bullock et al*., 2014]. The mixed-layer illite-smectite clay (90–98% purity) was obtained from the Clay Minerals Society Special Clays Repository, and the smectite was obtained as Na montmorillonite (90–100% purity) from the Clay Minerals Society Source Clays Repository. All samples were crushed by hand using a fly press and were subsequently ground to a fine powder using a pestle and mortar. These powders were then sieved to create synthetic gouges with a grain size range of 180–250 μm.

The samples were assembled for testing by sandwiching 1.5 g of gouge (or 1.2 g of gouge for wet experiments, to allow for volume increase when swelling clays were saturated) between two steel cylinders of 25 mm diameter. The surfaces of the steel cylinders are radially grooved to depths of 500 μm in order to ensure that slip localization occurs within the gouge layer rather than along the boundaries between the cylinders and the gouge. The gouge is confined by fixing a Teflon ring around the sample assembly [*Mizoguchi et al*., 2007] (Figure 2 of Text S2). The sample is then set within a vertical loading frame in which the lower cylinder remains stationary while the upper cylinder is rotated by a servomotor. An axial load is applied from the base of the loading frame via a pneumatic Bellofram cylinder. Friction during the experiments is measured using compression load cells attached to a high-precision arm-type torque meter, and output values were recorded by a data logger at a sampling frequency of 1 KHz.

Experiments were conducted at room temperature, and each sample was run both at room humidity ("dry") and under water-saturated ("wet") conditions. Prior to the room humidity experiments, the clays were oven dried overnight at 105°C to remove adsorbed water. For water-saturated experiments, ~0.27 mL of deionized water was applied to the gouge layer to achieve saturation. After application of normal load, samples were held for 3 min prior to shearing to allow for an initial phase of compaction. The experiments were then run at an equivalent velocity [*Shimamoto and Tsutsumi*, 1994] (Text S2) of 1.3 m/s, representative of seismic slip, and a normal load of 9 MPa (with the exception of experiment 416, which had to be run at 1.2 MPa due to the excessive mobilization of saturated montmorillonite gouge at higher normal loads).

Experiments were terminated at three different stages for sampling of deformed gouges. These stages were (Figure 2) (1) after application of normal load for 3 min, prior to shearing; (2) on attainment of peak friction, before slip weakening has occurred (or during the very early stages of slip in the case of gouges that do not

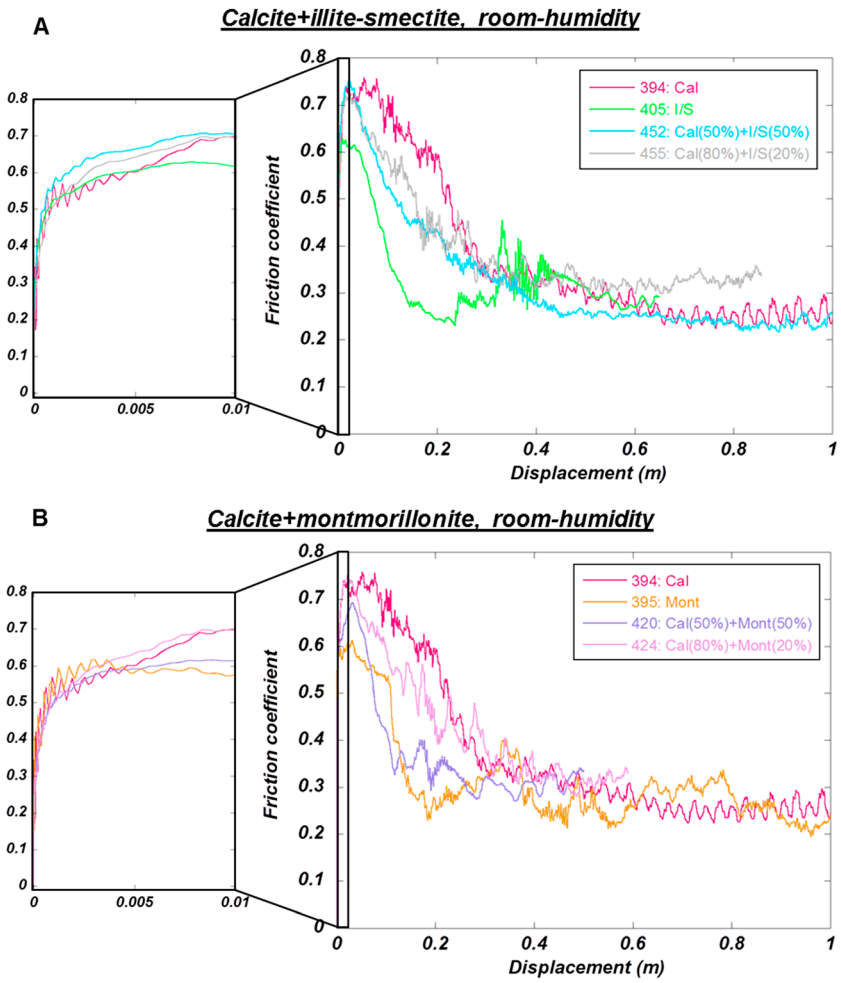

Figure 3. Experimental results for dry gouges sheared until the attainment of steady state sliding. The magnified section of the curve shows the initial slip-hardening phase during which the initial value of friction attained at the very start of the experiment increases toward a peak value. (a) Calcite and illite-smectite end-members and mixtures. (b) Calcite and montmorillonite end-members and mixtures.

exhibit a peak in friction); and (3) on attainment of steady state friction, subsequent to weakening. This systematic sampling enables observation of microstructural evolution during slip and an assessment of how grain- and aggregate-scale deformation mechanisms may influence frictional behavior.

The experimental configuration does not enable us to measure variations in pore fluid pressure, temperature, or gas emissions during our experiments. Therefore, in this manuscript we do not attempt to speculate on the dynamic weakening mechanisms that may be in operation during our experiments. We rely on microstructural observations of the deformed gouges to explain differences in mechanical behavior. In addition, since we cannot monitor pore pressure during the experiments, values of the friction coefficient are calculated as the measured shear stress divided by the applied normal load, rather than the effective normal stress. Our friction coefficient values may therefore be considered as apparent values, which neglect the effects of pore fluid pressurization due to decarbonation/dehydration reactions, shear heating of pore fluids, and compaction-driven pressurization. However, it is preferable to present the data in terms of friction coefficient, rather than shear stress, as it allows for easier comparison of data with previous studies, which have been performed at different normal loads. The inability to monitor pore fluid pressure is a common technical limitation during high-velocity friction experiments, which has only recently been overcome [*Violay et al.*, 2013]. Therefore, presenting our data in terms of apparent rather than true friction coefficient is in line with the majority of published results from high-velocity friction experiments.

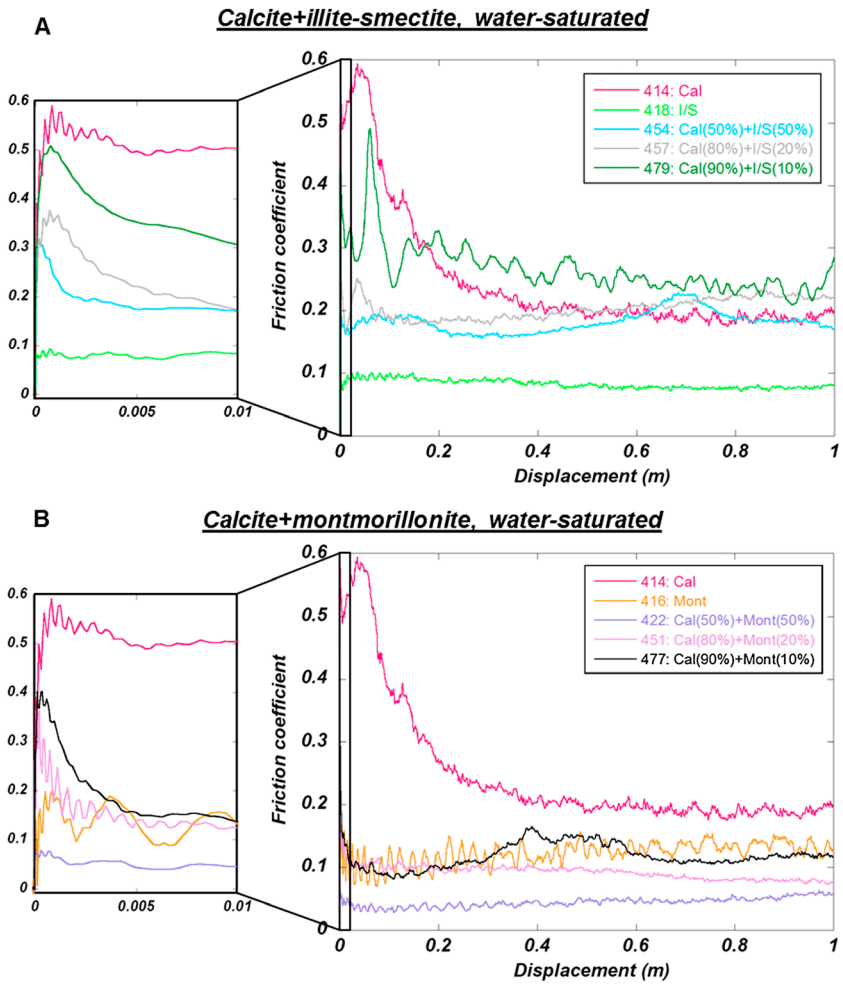

Figure 4. Experimental results for wet gouges sheared until the attainment of steady state sliding. The magnified section of the curve shows the initial slip-weakening phase during which the initial value of friction attained at the very start of the experiment decreases before either (1) restrengthening toward a peak value (in the case of experiments 414, 457, and 479) or (2) attaining steady state sliding without undergoing any slip hardening. (a) Calcite and illite-smectite end-members and mixtures. (b) Calcite and montmorillonite end-members and mixtures.

3. Results

3.1. Mechanical Data

3.1.1. Dry Gouges

Plots of friction coefficient against displacement for all experiments run until steady state are shown in Figures 3 and 4. These results are also summarized in Table 1 and Figure 5. Results of experiments terminated at peak friction are shown in Text S3. All of the experiments exhibit an initial phase of linear-elastic deformation prior to yielding. The yield point, at which the friction curve deviates from being linear, gives us the initial frictional strength of the gouge, μ_i (Figure 2; see also Text S4). For the dry end-member gouges, μ_i values are all similar, falling within the range 0.53–0.58 (Figures 3 and 5a). Within the first ~0.1 m of slip, μ_i is followed by a slip-hardening phase, during which friction evolves to a peak value, μ_p (Figure 3). The end-member calcite gouge has a μ_p value of 0.75 (Figures 3 and 5b), which is slightly higher than that of the clay end-members, which have μ_p values of 0.63 for illite-smectite (Figures 3a and 5b) and 0.61 for montmorillonite (Figures 3b and 5b). The peak in friction is followed by a dramatic decrease in frictional strength, over a slip-weakening distance, D_w, to steady-state values (μ_{ss}), which for all dry end-member gouges lies in the range 0.25–0.26 (Figures 3 and 5c). The slip-weakening distance is defined as the displacement at which $(\mu_p - \mu_{ss})$ reduces to 5% of $(\mu_p - \mu_{ss})$ (Figure 2) [*Mizoguchi et al.*, 2007]. The end-

Table 1. Summary of Experiments Run Until Steady State and Frictional Parameters Obtained

Experiment No.	wt % Calcite	wt % Clay	μ_i	μ_p	μ_{ss}	D_w	Total Displacement (m)	Experiment No.	wt % Calcite	wt % Clay	μ_i	μ_p	μ_{ss}	D_w	Total Displacement (m)
Calcite + Illite-Smectite								Calcite + Montmorillonite							
Dry Gouges															
394	100	0	0.53	0.75	0.25	0.58	7.05	394	100	0	0.53	0.75	0.25	0.58	7.05
455	80	20	0.54	0.72	0.33	0.29	0.92	424	80	20	0.51	0.75	0.33	0.36	0.62
452	50	50	0.56	0.76	0.23	0.44	1.92	420	50	50	0.55	0.69	0.31	0.19	0.54
405	0	100	0.54	0.63	0.25	0.17	0.73	395	0	100	0.58	0.61	0.26	0.2	1.04
Wet Gouges															
414	100	0	0.56	0.6	0.19	0.36	1.6	414	100	0	0.56	0.6	0.19	0.36	1.6
479	90	10	0.52	0.49	0.26	0.34	1.06	477	90	10	0.38	0.38	0.09	-	1.36
457	80	20	0.37	0.25	0.18	-	1.42	451	80	20	0.16	-	0.09	-	1.57
454	50	50	0.31	-	0.16	-	1.44	422	50	50	0.07	-	0.05	-	1.97
418	0	100	0.09	-	0.08	-	1.48	416	0	100	0.17	-	0.13	-	3.13

member calcite gouge displays a slip-weakening distance of 0.58 m, whereas the clay end-members become weaker over shorter distances of 0.17 m and 0.2 m for the illite-smectite and montmorillonite gouges, respectively (Figures 3 and 5d).

As would be expected, the curves for the gouges of mixed composition plot in positions intermediate between those of the end-members, although their overall trend is the same (Figure 3). Initial friction values again show little variation, ranging from 0.51 to 0.56 (Figure 5a), but μ_p decreases systematically as clay content increases, in both the calcite + illite-smectite and calcite + montmorillonite gouges (Figure 5b), as does D_w (Figure 5d).

3.1.2. Wet Gouges

The 100 wt % wet calcite gouge displays a slip-weakening curve similar to that of its dry equivalent (Figure 4), although values of μ_p, μ_{ss}, and D_w are slightly reduced (0.6, 0.19, and 0.36 m, respectively) (Figure 5). The other difference observed between the dry and wet calcite gouges is that whereas the dry gouge undergoes an immediate slip-hardening phase toward μ_p following the attainment of μ_i, the wet calcite gouge undergoes a brief slip-weakening phase, over a distance of just a few millimeters, before restrengthening and evolving toward μ_p (Figure 4).

Wet gouges containing 100% illite-smectite (Figure 4a) and 100% montmorillonite (Figure 4b), on the other hand, exhibit friction evolution curves that are markedly different to their dry equivalents. First, they display a significantly reduced μ_i of 0.09 for illite-smectite and 0.17 for montmorillonite (Figure 5a). Then, as for the wet calcite gouge, μ_i is followed by an immediate slip-weakening phase. The difference is that as slip proceeds, slip hardening does not occur at any stage in the wet clay gouges, and consequently, a peak in friction is never attained. Instead, friction evolves toward steady state values almost immediately at the onset of slip (Figure 4). Furthermore, the μ_{ss} values are very low: 0.08 for the illite-smectite end-member and 0.13 for the montmorillonite end-member (Figure 5c). Considering that these gouges are weak from the onset of slip, we do not assign them a slip-weakening distance.

The behavior of the mixtures of calcite + phyllosilicate is very much dependent on the phyllosilicate composition and content. In calcite + illite-smectite gouges (Figure 4a), there is a systematic decrease in frictional strength as the clay content is increased (Figures 5a–5c). At 10% clay, there is still a peak in friction, but its attainment is delayed; as in the wet calcite gouge, after the attainment of μ_i, the gouge undergoes slip weakening, followed by a brief restrengthening phase to a peak value of 0.49, before again undergoing slip weakening to steady state sliding. A similar friction evolution is observed at 20% illite-smectite, but the peak in friction is drastically reduced to just 0.25, which may be considered negligible. At 50 wt % illite-smectite, the peak in friction is eradicated altogether. Steady-state friction values also decrease with increasing clay content, falling from 0.26 at 10% illite-smectite, to 0.16 at 50%.

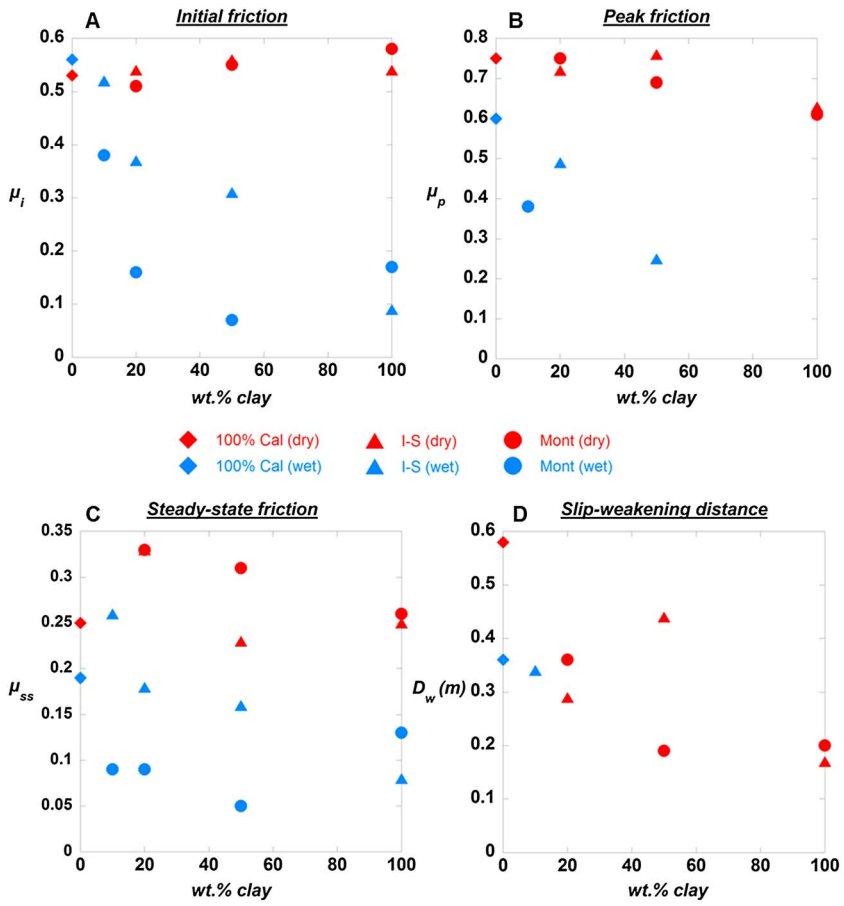

Figure 5. Summary plots showing evolution of frictional parameters as a function of increasing clay content. A key for all the plots is shown in the center of the figure. (a) Initial friction values are relatively constant for dry gouges but decrease with increasing clay content for wet gouges. (b) Peak friction values decrease slightly with increasing clay content for dry gouges, but this trend is much more enhanced for the wet gouges, to the extent that a peak in friction is absent for the most clay-rich gouges. (c) Steady state friction values show an overall decrease with increasing clay content for both dry and wet gouges. (d) D_w values again show an overall decreasing trend with increasing clay content, although in the case of wet clay-bearing gouges that do not exhibit a peak in friction, a slip-weakening distance is not applicable.

In the calcite + montmorillonite gouges under wet conditions (Figure 4b), μ_i values decrease as clay content increases (Figure 5a), but during subsequent slip, they display very similar strengths, regardless of clay content (Figure 5c). The exception is the 50 wt % montmorillonite gouge, which has a μ_i value of just 0.07, less than half that of the montmorillonite end-member, and it remains anomalously weak throughout the experiment. It should, however, be remembered that the 100% montmorillonite gouge was deformed under a lower normal load of 1.2 MPa, which could explain why it displays greater strength than the 50% montmorillonite gouge. Despite these subtle anomalies, all of the montmorillonite-bearing gouges exhibit the same frictional evolution during the experiments, in that none of them display a peak in friction, even when clay content is just 10 wt %. All of the mixtures evolve to steady state sliding, at values of μ_{ss} between 0.05 and 0.09, as soon as slip initiates. It should also be noted that for ≥20 wt % montmorillonite, the μ_i value is less than the yield strength of the gouge (Figures 4b and 6 of Text S4); this further illustrates just how weak these gouges are right from the onset of slip.

3.2. Microstructural Observations

Thin sections were analyzed using a field emission scanning electron microscope. Unsheared gouges were prepared by sectioning gouges that had been held under 9 MPa of normal load for 3 min, allowing examination of the initial microstructure of the gouge prior to shearing. Deformed gouges were prepared by sectioning the sheared gouges in an orientation normal to the shear plane and tangential to the direction of rotary shear. We refer to the entire width of the deformed gouge as the "slip zone" produced

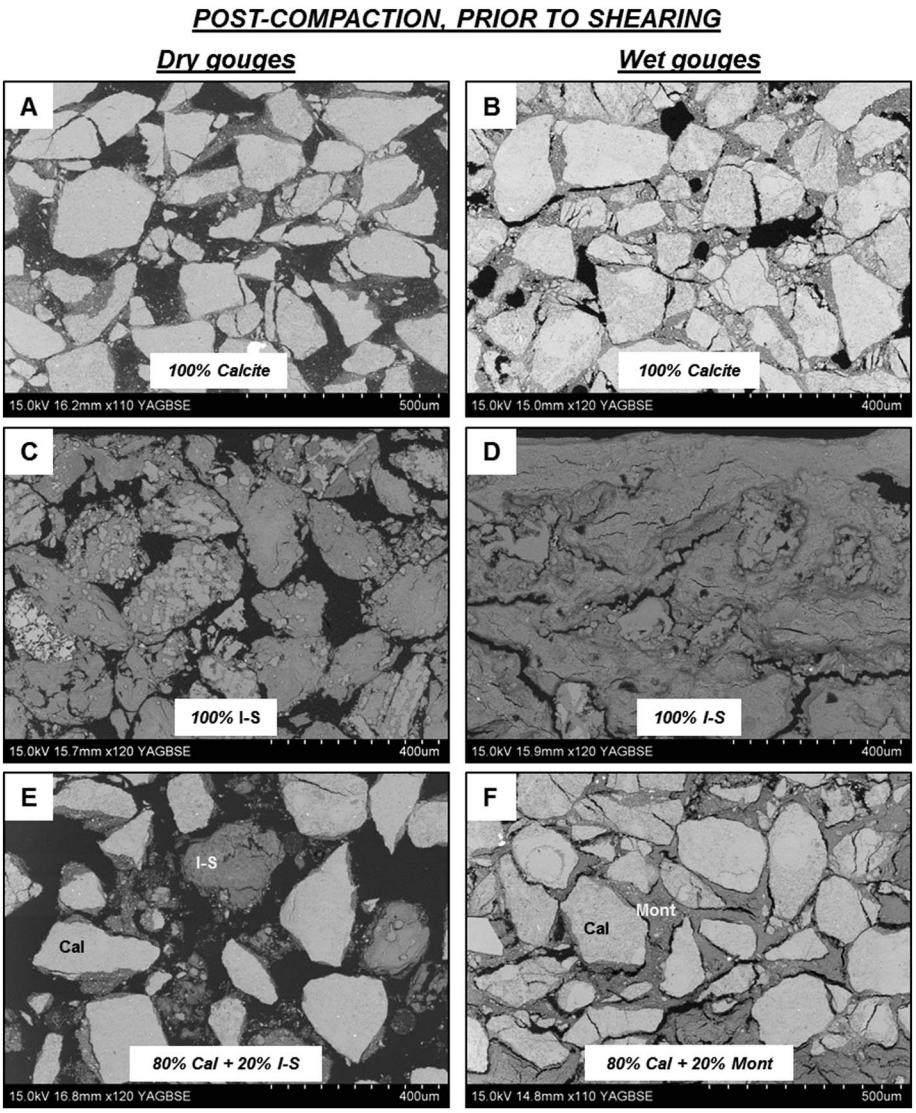

Figure 6. Initial microstructure of the gouges recovered after being held under 9 MPa normal load for 3 min, prior to shearing. See main text for full description. (a) 100% calcite, dry. (b) 100% calcite, wet. (c) 100% illite-smectite, dry. (d) 100% illite-smectite, wet. (e) 80% calcite + 20% illite-smectite, dry. (f) 80% calcite + 20% montmorillonite, wet.

during the experiment. Each slip zone contains a principal slip surface (PSS), where the majority of the rotary shear displacement is accommodated. The sample typically splits along the PSS on removal from the apparatus. In some experiments, slip appears to localize into a narrow zone adjacent to the PSS and this region is referred to as the principal slip zone (PSZ). Alongside the images presented in Figures 6–9, we present supporting images in Texts S5–S7.

3.2.1. Unsheared Gouges (Postcompaction)

The initial microstructure of the 100 wt % calcite gouge under dry conditions comprises discrete, angular grains of calcite (Figure 6a). The gouges were sieved to obtain an average starting grain size $< 250\ \mu m$. Many of the calcite grains are rimmed by a much finer powder of calcite grains averaging ~1 μm diameter (Figure 6a). These finer grains were likely produced during crushing and sieving of the gouges and adhered to the larger grains due to electrostatic charges and/or moisture on grain surfaces. The appearance of the 100 wt % calcite gouge under wet conditions is very similar to its dry equivalent, except that there is a greater amount of the fine calcite powder surrounding and in between the larger calcite grains (Figure 6b). This is likely due to the wet gouge being more cohesive and therefore the powder being more easily retained during thin-section preparation.

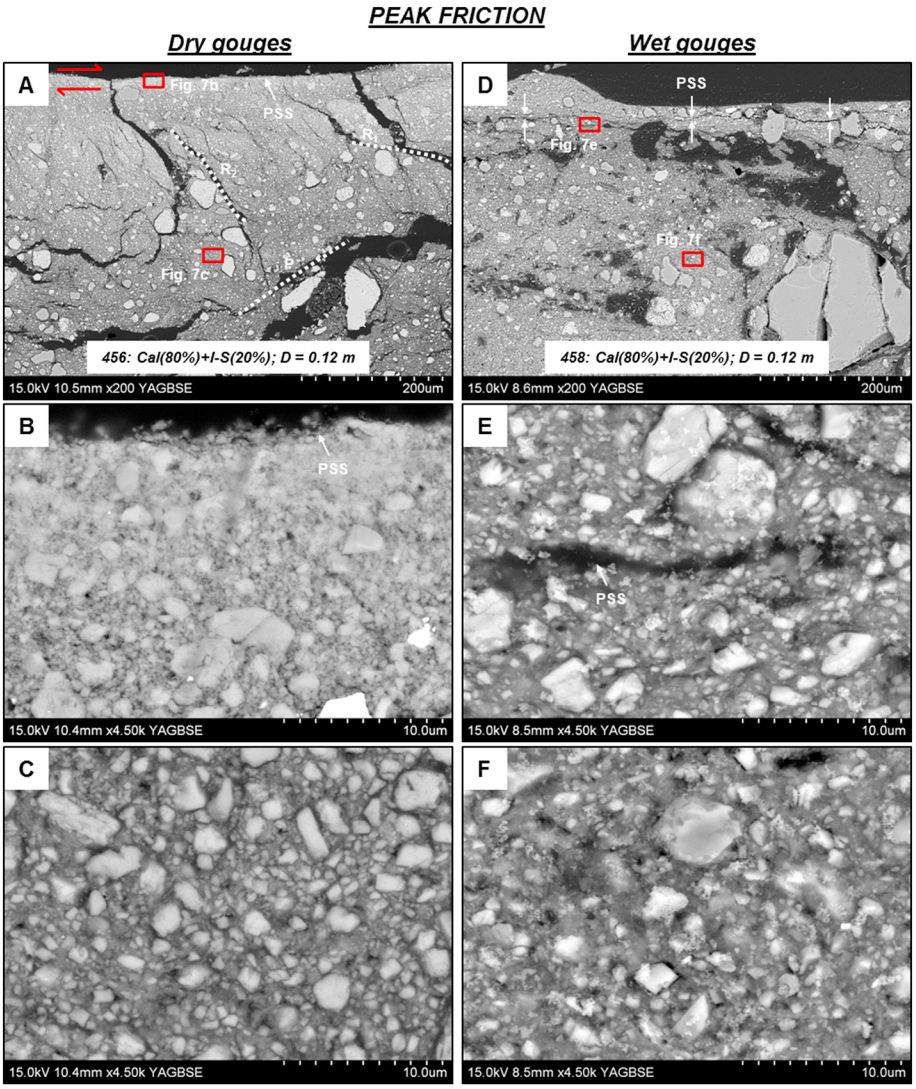

Figure 7. Deformed microstructures after recovery of gouges at peak friction. See main text for full description. (a) 80% calcite + 20% illite-smectite, dry. Overview of slip zone showing location of PSS. Examples of Riedel shear structures are labeled and the sense of shear inferred. R_2 shears dominate the fabric in the upper part of the slip zone, and *P* shears dominate the fabric in the central part of the slip zone in the lower portion of the image. (b) Zoomed in image of PSS and adjacent region in Figure 7a. (c) Zoomed in image of matrix within central slip zone of Figure 7a. (d) 80% calcite + 20% illite-smectite, wet. Overview of slip zone showing location of a very vague and undulating PSS. (e) Zoomed in image of PSS and adjacent region shown in Figure 7d. (f) Zoomed in image of matrix within central slip zone of Figure 7d.

The initial microstructure of the 100 wt % clay gouges under dry conditions comprises discrete agglomerates of clay particles, which have random shapes and orientations (Figure 6c); no fabric is developed. The initial microstructure of the 100 wt % clay gouges under wet conditions is rather different. Discrete agglomerates no longer exist; instead, when wet, the agglomerates appear to merge together upon compaction to form a mass of interconnected clay material, although still no fabric is formed (Figure 6d).

For the mixed calcite + phyllosilicate gouges, the initial microstructure when dry again comprises discrete grains of calcite and agglomerates of clay (Figure 6e). However, when wet, the clays once again merge together upon compaction and disperse throughout the gouge, forming a network of interconnected clay surrounding the calcite grains (Figure 6f).

3.2.2. Sheared Gouges: Peak Friction

The microstructure of dry gouges sheared until peak friction is characterized by the formation of a sharp, but sometimes wavy, PSS (Figures 7a and 7b; see also Figures 1–4 of Text S6). R_1 shears are already well

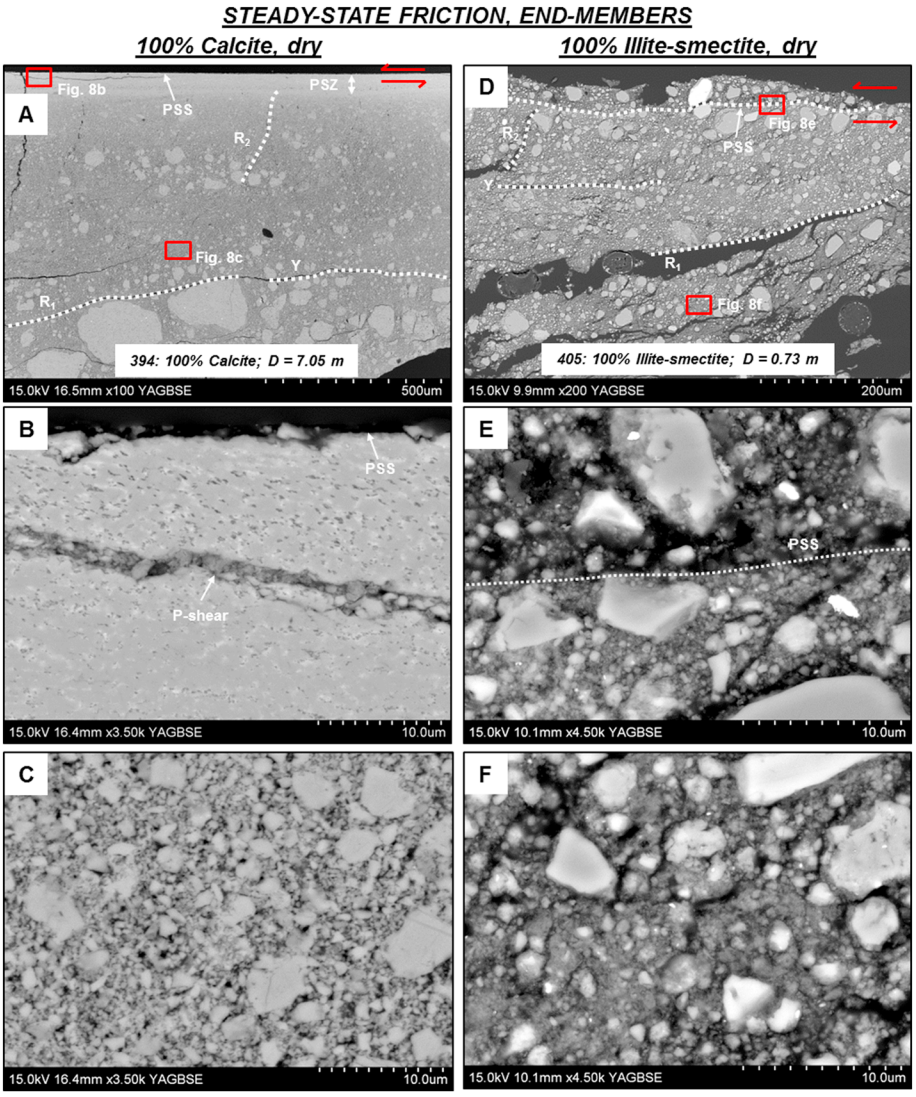

Figure 8. Deformed microstructures of dry end-member gouges after recovery during steady state sliding. See main text for full description. (a) 100% calcite, dry. Overview of slip zone showing location of PSS and PSZ. Examples of Riedel shear structures are labeled and the sense of shear inferred. R_1 shears dominate the fabric in the lower part of the slip zone, while higher-angle R_2 shears dominate the fabric in the upper part of the slip zone. (b) Zoomed in image of region adjacent to PSS and PSZ shown in Figure 8a. A *P* shear transects the center of the image. The dark spots scattered throughout the PSZ are holes, inferred to be the result of degassing as a consequence of thermal decomposition of calcite. (c) Zoomed in image of matrix within central slip zone of Figure 8a. (d) 100% illite-smectite, dry. Overview of slip zone showing location of PSS. Examples of Riedel shear structures are labeled and the sense of shear inferred. (e) Zoomed in image of PSS and adjacent region shown in Figure 8d. (f) Zoomed in image of matrix within central slip zone of Figure 8d.

developed within the slip zone at this stage, and R_2, *P*, and *Y* shears are present in some but not all cases (Figure 7a). Significant grain size reduction is evident throughout the gouge layers recovered at peak friction (Figures 7a–7c), when compared with the initial starting material (Figures 6a, 6c, and 6e). Grain size reduction is more intense in close proximity to the PSS (Figure 7b) than it is in the lower parts of the slip zone (Figure 7c), in some cases producing nanoparticle-sized material adjacent to the PSS (Figure 7b).

The wet gouges display quite a different microstructure when sheared until peak friction. There is no well-defined PSS in the wet gouges but instead just a poorly defined wavy surface, which likely corresponds to the PSS (Figures 7d and 7e). Unlike the dry gouges, there is no Riedel shear development within the slip zone. Significant grain size reduction has occurred, but it is not as intense as in the dry gouges. This is particularly evident when examining the region adjacent to the PSS (Figure 7e), where grain size appears

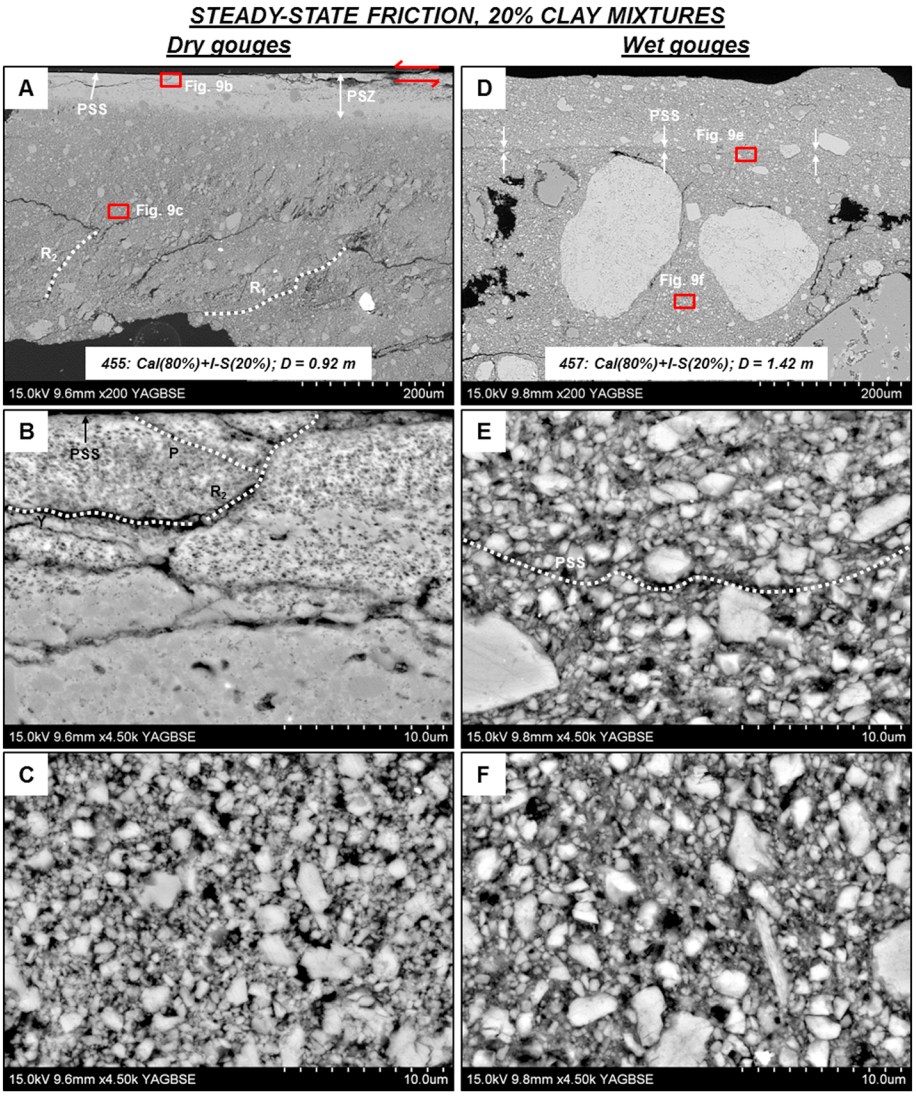

Figure 9. Deformed microstructures after recovery of gouges containing 20 wt % clay during steady state sliding. See main text for full description. (a) 80% calcite + 20% illite-smectite, dry. Overview of slip zone showing location of PSS and PSZ. Examples of Riedel shear structures are labeled and the sense of shear inferred. Fabric within the slip zone is dominated by R_1 shears. (b) Zoomed in image of PSZ shown in Figure 9a. R_1, *P*, and *Y* shears are present within the PSZ. The black spots scattered throughout the PSZ are holes, inferred to be degassing bubbles as a consequence of calcite decarbonation. (c) Zoomed in image of matrix within central slip zone of Figure 9a. (d) 80% calcite + 20% illite-smectite, wet. Overview of slip zone showing location of PSS. (e) Zoomed in image of PSS and adjacent region shown in Figure 9d. (f) Zoomed in image of matrix within central slip zone of Figure 9d.

very similar to that observed away from the PSS (Figure 7f). In addition, large grains up to 200 μm diameter, which appear to have undergone minimal deformation, remain in the slip zone (Figure 7d).

3.2.3. Sheared Gouges: Steady State

The microstructure of the dry gouges deformed until steady state friction varies slightly depending on gouge composition. In the 100% dry calcite gouge, the PSS (Figures 8a and 8b) is much sharper and straighter than it was at peak friction (see Figure 1 of Text S6). As at peak friction, there is a marked reduction in grain size toward the PSS. In addition, a PSZ, up to 60 μm wide, is formed adjacent to the PSS. The PSZ comprises highly compacted, ultrafine-grained calcite, which is scattered with bubbles (Figure 8b). The grain size in the bulk of the gouge, i.e., away from the PSZ, does not differ greatly to that observed at peak friction (compare Figures 8c and Figure 1c of Text S6). R_1 shears are extensive in the lower part of the slip zone

and are sometimes rotated into a *Y* orientation (Figure 8a). R_2 shears are also common, more so toward the upper part of the slip zone. Smaller-scale R_1, *Y*, and *P* shears are also common within the PSZ (Figure 8b).

In the 100% dry clay gouges (Figures 8d–8f and Figure 1 of Text S7), the PSSs are not as sharp and straight as in the 100% calcite sample (Figures 8a and 8b). It should be noted that the 100% illite-smectite and 100% montmorillonite gouges have experienced smaller displacements (0.73 m and 1.04 m total displacement, respectively) than the 100% calcite gouge (7.05 m total displacement). However, we see that in other calcite-rich gouges deformed to similar displacements as the clay end-members, the PSSs are still very sharp and straight compared to those in the clay gouges (e.g., Figures 9a, 9b, 10a, and 10b, plus Figures 2 and 3 of Text S7). Thus, it appears that a wispy, undulating PSS is a feature unique to the 100% clay gouges, regardless of displacement. In addition, grain size reduction adjacent to the PSS (Figure 8e) is not as intense in the clay end-member gouges as in the 100% calcite gouge; grain size is more uniform over the whole slip zone (compare Figures 8e and 8f), and subsequently, no PSZ is present. However, there are Riedel shears developed throughout the slip zone (Figure 8d).

In the dry gouges of mixed composition (Figures 9a–9c and 10a–10c), the microstructure at steady state is somewhat intermediate between those of the end-members described above. In the presence of 20 wt % clay, microstructures are comparable to those in the calcite end-member. PSSs are very sharp and straight, and intense grain size reduction has occurred toward these surfaces (Figures 9a and 9b; see also Figure 2 of Text S7). In the 20 wt % illite-smectite gouge, there is a very well developed, continuous PSZ up to 65 μm wide (Figures 9a and 9b), whereas in the 20 wt % montmorillonite gouge, the PSZ is highly variable in width, being only a few microns in some places but up to 35 μm in others (Figure 2 of Text S7). Despite differences in development, the PSZs in the illite-smectite- and montmorillonite-bearing gouges are of similar nature: they comprise a matrix of highly compacted, ultrafine-grained calcite + clay, and both contain bubbles, replicating the PSZ microstructure observed in the 100% calcite gouge (Figure 9b and Figure 2b of Text S7). As in the 100% calcite gouge, the slip zone has a fabric characterized by R_1, R_2, and *Y* shears (Figure 9a and Figure 2a of Text S7), and the grain size out width of the PSZ does not vary greatly from peak friction to steady state (compare Figures 7c and 9c).

In the presence of 50 wt % clay, the microstructures are different for the illite-smectite-bearing and the montmorillonite-bearing gouge. The 50 wt % illite-smectite gouge has a microstructure unlike any of the other gouges in that there is quite a distinct partitioning of strain across the slip zone, with different domains separated by *Y* shears (Figure 3a of Text S7). Despite this, it still has a sharp PSS as in all the other dry gouges, but it is relatively rough in comparison (Figure 3b of Text S7). Increased grain size reduction is also observed in areas adjacent to the PSS (Figure 3b of Text S7). There is not a well-developed PSZ, but the compacted, ultrafine-grained material associated with PSZs in the 20 wt % clay samples is present in localized patches along the PSS (Figure 3b of Text S7). Where this compacted ultrafine-grained material is not present, the material adjacent to the PSS is characterized by predominantly submicron sized, subangular to subrounded clasts of calcite and flakes of phyllosilicate (Figure 3b of Text S7).

The 50 wt % montmorillonite gouge is similar to the 20 wt % montmorillonite gouge, in that it has a sharp, smooth PSS and a variably developed PSZ (up to 30 μm wide) (Figures 10a and 10b). Plus it has a pervasive fabric dominated by R_1 shears (plus some R_2 and *P* shears present within the PSZ) (Figures 10a and 10b). Once again, the PSZ (Figure 10b) is characterized by a matrix of compacted, ultrafine-grained calcite + clay and, in places, contains bubbles, although the bubbles are not as ubiquitous as in the gouges containing just 20 wt % clay (Figure 9b).

We were not able to recover any wet clay end-member gouges for thin sectioning; the swelling nature of the clays causes them to be easily extruded from the sample assembly during the experiments. Thus, we only describe here the observations made for gouges of mixed calcite + phyllosilicate composition. The wet clay-bearing gouges recovered after steady state sliding have a more fully developed, throughgoing PSS (Figures 9d and 10d; see also Figures 4 and 5 of Text S7) than those recovered at peak friction (Figure 7d). However, the PSS is still quite a vague and undulating feature (Figures 9e and 10e) and not as sharp and straight as in the dry gouges (Figures 9b and 10b). The PSS does not appear to be defined by anything in particular; e.g., we do not observe any alignment of phyllosilicates along the PSS. Several large, subrounded grains, up to 230 μm in diameter, remain within the central portion of the slip zone (Figures 9d and 10d). This is more than twice the size of the largest grains in the central slip zone of their

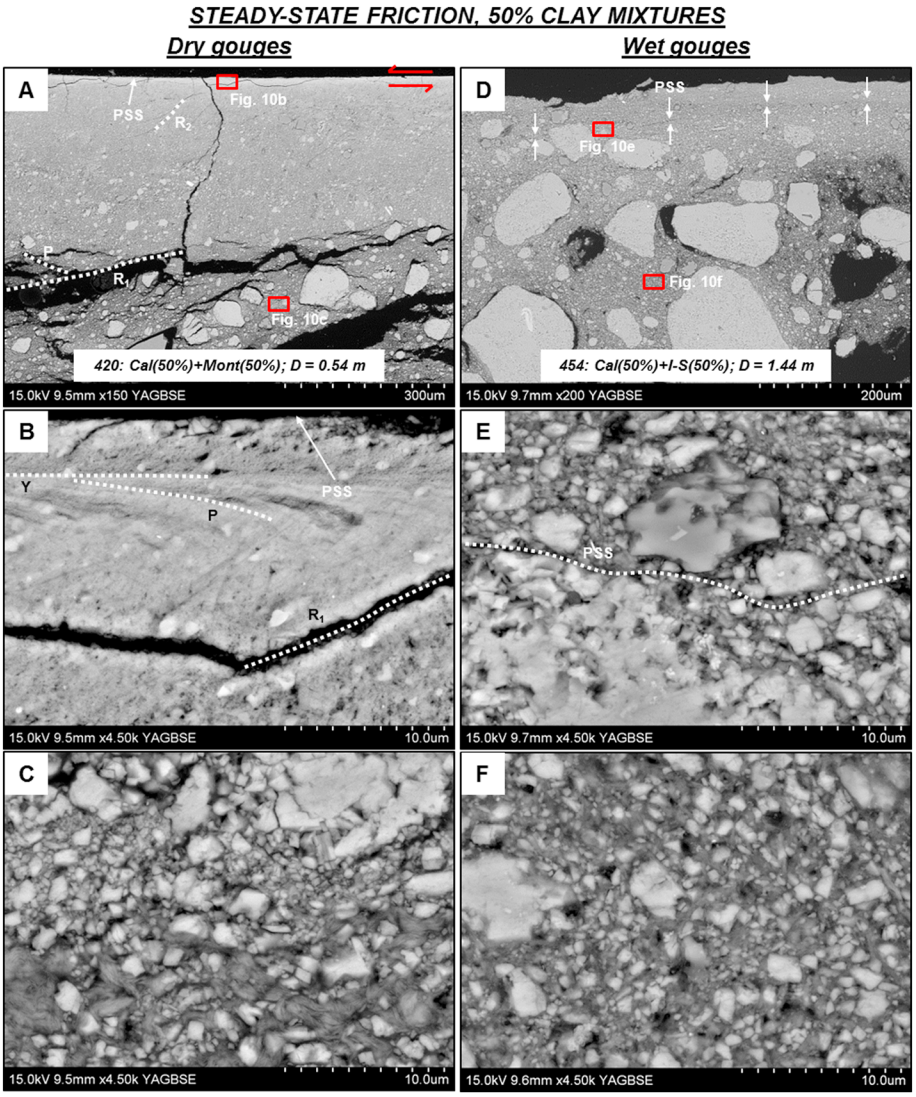

Figure 10. Deformed microstructures after recovery of gouges containing 50 wt % clay during steady state sliding. See main text for full description. (a) 50% calcite + 50% montmorillonite, dry. Overview of slip zone showing location of PSS. Examples of Riedel shear structures are labeled and the sense of shear inferred. R_1 shears dominate the fabric within the slip zone. A PSZ up to 30 μm wide is formed adjacent to the PSS (see Figure 10b) but is unresolvable at the scale of the image. (b) Zoomed in image of PSS and PSZ shown in Figure 10a. The 5 μm wide zone right at the top of the image, delimited from the rest of the PSZ by a subhorizontal *Y* shear, contains rounded to elongate black spots, which we interpret to be degassing bubbles as a result of calcite decarbonation. Several very fine *P* shears are visible just beneath this zone as well as the intersecting *P* and R_1 shears in the lower part of the image. (c) Zoomed in image of matrix within central slip zone of Figure 10a. (d) 50% calcite + 50% illite-smectite, wet. Overview of slip zone showing location of PSS, which is very vague and almost unresolvable at the scale of the image. (e) Zoomed in image of PSS and adjacent region in Figure 10d. (f) Zoomed in image of matrix within central slip zone of Figure 10d.

dry equivalents, which are also more subangular in nature (Figures 9a and 10a). In addition, no PSZ is developed; the matrix grain size adjacent to the PSS (Figures 9d and 10d) is comparable to that in the lower parts of the slip zone (Figures 9f and 10f) and is certainly much coarser than in the dry gouge equivalents (Figures 9b and 10b). Finally, none of the PSZ characteristics observed in the dry gouges sheared until steady state, i.e., the presence of highly compacted ultrafine-grained material or bubbles, are observed in the wet gouges. Fabric development in the slip zone, in the form of Riedel shears, is also absent. These microstructures are consistent for all wet clay-bearing gouges, the only difference being that in the gouges containing just 10 wt % clay (Figures 4 and 5 of Text S7), the large grains in the central portion of the slip zone are more angular than in the gouges that have higher clay contents.

4. Discussion

4.1. Frictional Evolution of Dry Versus Wet Clay-Bearing Gouges

Our experimental results show a dramatic contrast in frictional behavior between dry and wet clay-bearing carbonate gouges. The dry clay-bearing gouges display typical high-velocity friction evolution curves that have been produced in numerous experiments on a wide range of materials [*Di Toro et al*., 2011]. The wet clay-bearing gouges, on the other hand, do not conform to a typical high-velocity frictional evolution, in that they undergo little or no slip hardening after the attainment of the initial friction value and thus do not attain a peak in friction during the experiments. This behavior replicates that observed during previous high-velocity friction experiments on saturated clay-bearing gouges [*Ferri et al*., 2010; *Ujiie and Tsutsumi*, 2010; *Faulkner et al*., 2011; *Ferri et al*., 2011; *Ujiie et al*., 2011, 2013]. However, these previous studies used natural gouges, in most cases with >50% clay. What we are able to show here by systematically varying the clay content in synthetic gouges is that just 10 wt % clay (in the case of montmorillonite) or 20 wt % clay (in the case of mixed-layer illite-smectite) is required to produce the same weakening behavior that is observed in clay-dominated gouges.

4.2. Microstructural Evolution of Dry Versus Wet Clay-Bearing Gouges

The contrasting frictional behaviors of the dry versus wet clay-bearing gouges are accompanied by starkly contrasting microstructures. The dry clay-bearing gouges are characterized by localized slip, which is accommodated along a very sharp, smooth PSS and within a variably developed PSZ. The PSS and PSZ have undergone intense cataclasis and wear and show evidence for frictional heating in excess of ~700°C, in the form of degassing bubbles within PSZs, which we infer to be a result of calcite decarbonation. The wet clay-bearing gouges, on the other hand, are characterized by a much more distributed style of deformation, whereby they lack a sharp PSS and a PSZ, and cataclasis appears to have been less intense. Additionally, none of the wet clay-bearing gouges show any evidence for calcite decarbonation, suggesting significantly lower amounts of frictional heating than in their dry equivalents. The observation of contrasting microstructures between dry and wet clay-bearing gouges sheared at seismic velocity is consistent with observations made in previous studies [e.g., *Ferri et al*., 2011; *Ujiie et al*., 2011; *French et al*., 2014]. A direct comparison would not be appropriate, due to the fact that these previous studies were conducted at much lower normal load (~1 MPa) than in our experiments, but it seems that wet clay-bearing gouges typically experience a less intense grain size reduction and shear fabric or foliation development than their dry counterparts.

The contrasting microstructures observed in the dry versus wet clay-bearing gouges suggest that it may be possible to explain their contrasting frictional behaviors through micromechanical processes. We propose a micromechanical model as follows. In the dry clay-bearing gouges, the initial microstructure comprises discrete clasts of calcite and agglomerates of clay (Figure 11a, panel 1). When slip initiates in these gouges, it is necessary for pervasive cataclasis to occur before slip can localize along a throughgoing PSS (Figure 11a, panel 2). Once the PSS has formed, then a large amount of wear must also occur in order to produce the smooth surfaces observed in the microstructures (Figures 9b and 10b). These processes explain the slip-hardening phase at the start of the dry experiments [e.g., *Biegel et al*., 1992, and references therein]. Once a PSS is well established, then slip localizes here and a PSZ forms adjacent to it (Figure 11a, panel 3). Because strain is concentrated along the PSS and within the PSZ, grain size in the remainder of the slip zone does not change significantly from peak friction to steady state sliding. The localization of slip results in intense frictional heating along the PSS and within the PSZ, enough to trigger calcite decarbonation (and perhaps implying that clay dehydration has also taken place, although microstructural evidence of this is not obvious). Mechanical wear and thermal decomposition processes also result in the production of nanoparticles within the PSZ and coating the PSS. A combination of thermal pressurization, dynamic recrystallization, and nanoparticle lubrication are likely responsible for the dynamic weakening behavior of the dry gouges, as invoked by previous studies [*Han et al*., 2007; *De Paola et al*., 2011a, 2011b; *Han et al*., 2011; *Smith et al*., 2013; *De Paola et al*., 2014].

In the wet clay-bearing gouges, on the other hand, the initial microstructure comprises an interconnected matrix of wet clay surrounding calcite grains (Figure 11b, panel 1). Saturated clays have been shown to be inherently weak, even at low slip velocities. The average coefficient of friction reported in the literature for wet montmorillonite is 0.18 [*Saffer et al*., 2001; *Saffer and Marone*, 2003; *Ikari et al*., 2007; *Moore and Lockner*, 2007;

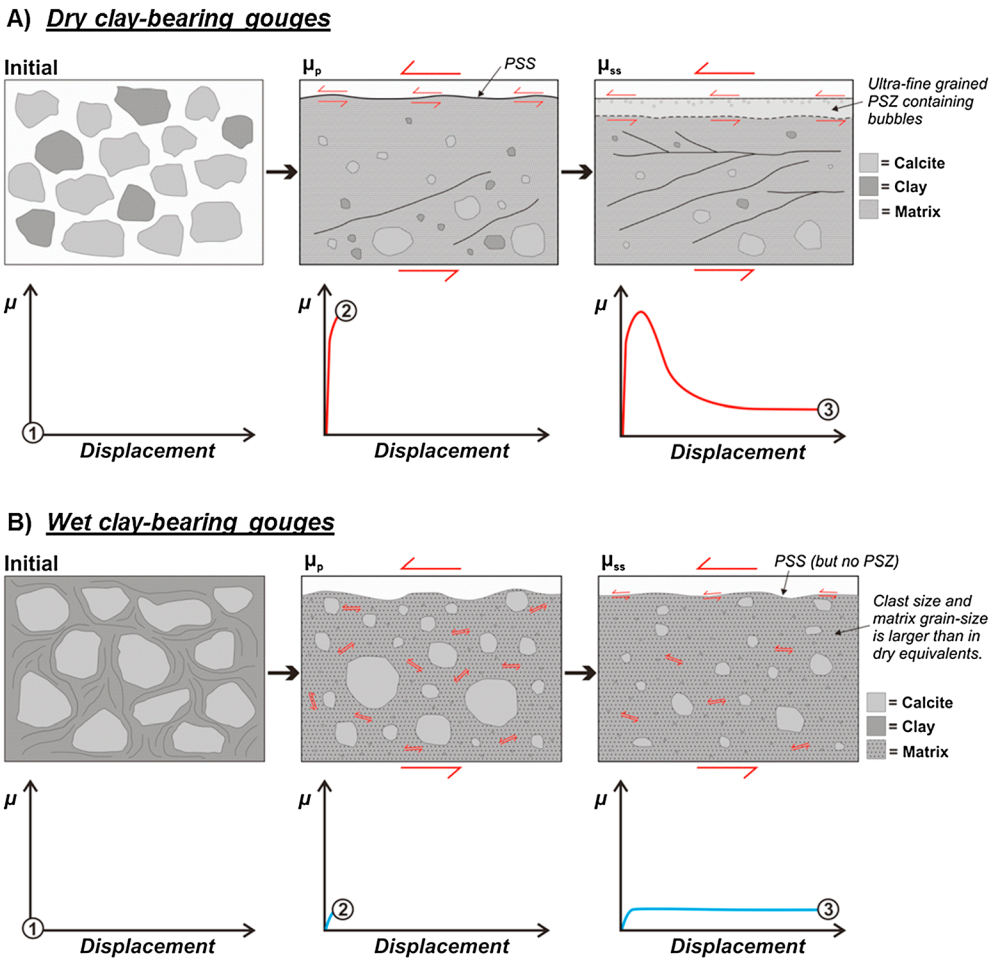

Figure 11. Proposed micromechanical model, based on microstructural observations, to explain the contrasting mechanical behavior, also depicted, of (a) dry clay-bearing gouges and (b) wet clay-bearing gouges. Panels show microstructural evolution from the initial starting material through to peak friction and steady state sliding. See main text for explanation.

Tembe et al., 2010; *Behnsen and Faulkner*, 2012] and for wet illite is 0.37 [*Morrow et al.*, 1992; *Saffer and Marone*, 2003; *Ikari et al.*, 2009; *Tembe et al.*, 2010; *Behnsen and Faulkner*, 2012]. Thus, when slip initiates, it preferentially occurs on the preexisting, weak clay lamellae, which are distributed throughout the gouge (Figure 11b, panel 2). This reduces the need for pervasive cataclasis to occur before slip is able to localize and explains the lack of slip hardening in the wet clay-bearing gouges. This theory is supported by the distributed style of deformation observed in the wet gouges, including the absence of a PSZ (Figure 11b, panel 3), plus the larger grain sizes in the deformed wet clay-bearing gouges in comparison to their dry equivalents. The fact that slip is not localized within a narrow zone, plus the low values of friction, would result in a far lesser amount of frictional heating in the wet gouges than in the dry ones. This would explain why there is no microstructural evidence for thermal decomposition of calcite having occurred in the wet clay-bearing gouges.

A PSS still forms in the wet gouges, and so it is evident that slip does attempt to localize. However, the mechanical processes involved during slip localization are different. In the dry clay-bearing gouges, slip localization is driven by cataclasis and wear, whereas in the wet clay-bearing gouges, it is likely driven by sliding on weak, water-saturated clay lamellae [*Moore and Lockner*, 2004, 2007]. This is reflected in the nature of the PSSs in the wet gouges, which are rather undulating (Figures 9e and 10e), suggesting that they are located where weak clay horizons are most readily available, as opposed to on a sharp slip plane where asperities have been broken and worn down by shearing. Given that we do not observe a throughgoing layer of aligned phyllosilicates along the PSS for slip to occur on, we would not rule out the

possibility that slip may actually occur on a thin film of water, which has been expelled from the gouge and become trapped along the PSS, as suggested by *Ferri et al*. [2010]. Alternatively, it may be that a throughgoing layer of aligned phyllosilicates is formed along the PSS, but it is so localized and narrow that it cannot be resolved with the scanning electron microscope. Or such a layer may be obscured by the sinking of calcite clasts into the layer as the sample relaxes postdeformation.

The slight difference in behavior between the wet illite-smectite bearing gouges and the wet montmorillonite-bearing gouges can be explained through the expansive capabilities of smectite clays. Upon saturation, smectite group clays allow water into their interlayer structure. It has been suggested that the extreme weakness of smectites may be due to sliding occurring on thin lubricating films of water located between clay interlayers [e.g., *Moore and Lockner*, 2004]. If this is the case, then it is not surprising that the mixed-layer illite-smectite clay should be stronger, because the illite component of the clay does not have the same expansive capability. Thus, the delayed peak in friction in experiments 479 and 457, containing 10 wt % and 20 wt % of illite-smectite, respectively, may be due to water-saturated smectite horizons within the gouge being consumed through comminution, before slip has fully localized. Thus, in order for slip to localize and proceed, some cataclasis is still necessary, hence the delayed slip-hardening phase.

As well as the saturated clays being inherently weak, the impermeable nature of the starting material created by the interconnected clay network (Figures 6d and 6f) would enhance pore fluid pressurization generated by shear-induced compaction, which would further reduce the strength of the gouge [e.g., *Blanpied et al*., 1992]. Gouge dilatancy triggered by pore fluid pressurization may also inhibit the localization of shear [e.g. *Rice et al*., 2014], consistent with our observation of a distributed style of deformation in the wet clay-bearing gouges. The initial weakening phase observed during experiments 457 and 479, and also during experiment 414 on the water-saturated 100% calcite gouge (Figure 4a), before they undergo slip hardening to attain their peak friction, is most likely due to a sudden pore fluid overpressure generated at the onset of slip.

4.3. Implications

4.3.1. Rupture Propagation in Clay-Bearing Carbonate Faults

Our results show that the presence of clay in fault gouge alone does not significantly affect the frictional behavior of a fault during earthquake propagation. However, if water is present within gouges containing as little as 10–20% clay, then they can become very weak and resistance to earthquake propagation is significantly reduced. As highlighted by *Faulkner et al*. [2011], the negligible fracture energy associated with saturated clay-bearing gouges means that very little energy is required to maintain rupture propagation, and so it would be energetically more feasible for a rupture to propagate all the way to the surface. Thus, while wide, phyllosilicate-rich zones in the shallow portions of faults may promote stable fault slip due to their velocity-strengthening properties [e.g., *Hsu et al*., 2006; *Holdsworth et al*., 2011], if these phyllosilicates become concentrated within narrow PSZs, they will likely facilitate earthquake propagation. The results have significant implications for seismic hazard assessment, particularly in the Northern Apennines of Italy, which has experienced a number of large earthquakes in recent years [e.g., *D'Agostino et al*., 2009]. This is an area where clays are sometimes present within the PSZs of earthquake-hosting carbonate faults (e.g., Figure 1) [*Collettini et al*., 2013; *Tesei et al*., 2013; *Bullock et al*., 2014; *Collettini et al*., 2014]. These natural gouges often display a foliated fabric as a result of previous slip events and/or aseismic creep during the interseismic period (e.g., Figure 9 of *Bullock et al*. [2014] and Figures 1–3 of Text S1). Rock/gouge samples with a preexisting fabric have been shown experimentally to have significantly lower strength than powdered gouge samples with no fabric [e.g., *Collettini et al*., 2009; *Niemeijer et al*., 2010]. It is therefore plausible that natural clay-bearing fault gouges could be even weaker than the results we have presented here for experiments on powdered gouges with no preexisting fabric. In addition, seismological models have invoked fluids as playing an important role in active seismicity in the Northern Apennines [e.g., *Miller et al*., 2004; *Di Luccio et al*., 2010; *Malagnini et al*., 2012]. The presence of fluids is supported by geological observations documenting pervasive calcite mineralization within and adjacent to PSZs, in the form of both veins (e.g., Figures 1c and 1e) and hydraulic breccias [*Tesei et al*., 2013; *Bullock et al*., 2014; *Collettini et al*., 2014]. The clays within the PSZs likely act as seals and promote the generation of high fluid pressures along faults [*Blanpied et al*., 1992].

The evident interaction of fluids with clay-bearing carbonate fault gouges may be a contributing factor toward the common occurrence of surface-breaking scarps in the Northern Apennines [e.g., *Vittori et al*., 2000; *Guerrieri et al*., 2009].

So far, such results concerning the extreme weakness of saturated clay gouges at seismic slip velocities have been considered with relation to subduction zone earthquakes [*Ujiie and Tsutsumi*, 2010; *Faulkner et al*., 2011; *Ujiie et al*., 2013], which appear to propagate through the clay-rich sediments of accretionary wedges with relative ease [e.g., *Ide et al*., 2011]. However, clays are a common feature of many upper crustal earthquake-hosting faults [e.g., *Wu et al*., 1975; *Vrolijk and van der Pluijm*, 1999; *Holdsworth*, 2004], where fluids are often invoked to play a major role during faulting [e.g., *Sibson*, 1981]. Thus, these results are relevant for assessing the behavior and potential capability of any clay-bearing seismogenic fault, regardless of its tectonic setting.

4.3.2. Seismic Markers in Clay-Bearing Carbonate Faults

In recent years, it has become increasingly common for structural geologists to try and distinguish indicators of seismic versus aseismic slip, both from laboratory and field observations. A growing range of so-called "coseismic slip indicators" have been documented, for example, pseudotachylytes [*Sibson*, 1975], dynamically recrystallized calcite [*Smith et al*., 2013; *De Paola et al*., 2014], fault mirrors [*Fondriest et al*., 2013; *Siman-Tov et al*., 2013], clay mineral transformations [*Yamaguchi et al*., 2011; *Bullock et al*., 2014], biomarkers [*Savage et al*., 2014], degassing bubbles, and "quenched" calcite crystals [*Collettini et al*., 2013; *Bullock et al*., 2014]. All of these coseismic signatures are associated with localized slip and frictional heating. In contrast, fault gouges exhibiting distributed deformation, particularly those rich in velocity-strengthening phyllosilicates, are generally interpreted as representing aseismic portions of faults [e.g., *Faulkner et al*., 2003; *Holdsworth et al*., 2011]. The fault gouges such as those produced during our high-velocity experiments on water-saturated clay-bearing gouges do not contain any seismic markers and exhibit distributed deformation. Thus, they may be overlooked as seismogenic faults if observed in nature, when, in fact, they have the potential to allow capable faulting and the production of devastating surface ruptures. In addition, the fact that phyllosilicates are prone to creep makes it likely that even seismic markers such as those produced during our dry run experiments, e.g., localized PSZs containing signatures of thermal decomposition, would be overprinted during the interseismic period. Therefore, clay-bearing carbonate gouges should be approached with a high degree of caution when considering the seismic history and potential of a natural fault zone.

5. Conclusions

High-velocity friction experiments performed on mixtures of calcite + illite-smectite and calcite + montmorillonite produce very different results depending on whether the gouges are deformed under room humidity (dry) or water-saturated (wet) conditions. Dry clay-bearing gouges display a friction evolution curve that is typical of those associated with high-velocity friction experiments on a wide range of rock types. The wet clay-bearing gouges, on the other hand, do not exhibit a typical frictional evolution, in that they undergo little or no slip hardening, and therefore do not attain a peak in friction. Instead, they attain steady state frictional sliding almost immediately at the onset of slip, at values of $\mu_{ss} \ll 0.2$. This behavior is observed even when the clay content is just 10 wt %, in the case of montmorillonite, and 20 wt %, in the case of illite-smectite. These results have significant implications for seismic hazard assessment, as they show that calcite gouges containing small amounts of wet clay will potentially present very little resistance to seismic rupture propagation, enhancing the potential for surface-rupturing capable faulting in a variety of tectonic settings.

In our experiments we attribute the observed weak behavior of the wet clay-bearing gouges to their initial microstructure prior to shearing, which consists of an interconnected network of wet clay surrounding the calcite grains. Thus, as slip initiates, it preferentially occurs on the clay horizons distributed throughout the gouge, which are inherently weak. In the dry gouges, cataclasis must occur before slip can localize and trigger dynamic weakening, and thus, they present a much greater resistance to frictional sliding. The lack of slip localization and the low friction values in the wet clay-bearing gouges significantly reduce the amount of frictional heating generated. This means that natural seismogenic fault gouges containing small amounts of wet clay will not necessarily exhibit the signatures that are so commonly thought to be associated with seismic slip.

Acknowledgments
Brett Carpenter and Cristiano Collettini are thanked for their constructive reviews which helped to clarify and strengthen the manuscript. This work was funded by the Natural Environment Research Council through a NERC PhD studentship NE/J500215/1 awarded to R.J.B. and a NERC standard grant NE/H021744/1 awarded to N.D.P. The raw data presented in this paper are available upon request from the corresponding author.

References

Barchi, M., G. Minelli, and G. Pialli (1998), The CROP 03 profile: A synthesis of results on deep structures of the Northern Apennines, *Mem. Soc. Geol. Ital.*, *52*, 383–400.

Behnsen, J., and D. R. Faulkner (2012), The effect of mineralogy and effective normal stress on frictional strength of sheet silicates, *J. Struct. Geol.*, *42*, 49–61.

Biegel, R. L., W. Wang, C. H. Scholz, G. N. Boitnott, and N. Yoshioka (1992), Micromechanics of rock friction: 1. Effects of surface roughness on initial friction and slip hardening in westerly granite, *J. Geophys. Res.*, *97*(B6), 8951–8964, doi:10.1029/92JB00042.

Blanpied, M. L., D. A. Lockner, and J. D. Byerlee (1992), An earthquake mechanism based on rapid sealing of faults, *Nature*, *358*(6387), 574–576.

Boutareaud, S., D.-G. Calugaru, R. Han, O. Fabbri, K. Mizoguchi, A. Tsutsumi, and T. Shimamoto (2008), Clay-clast aggregates: A new textural evidence for seismic fault sliding?, *Geophys. Res. Lett.*, *35*, L05302, doi:10.1029/2007GL032554.

Brantut, N., A. Schubnel, J. N. Rouzaud, F. Brunet, and T. Shimamoto (2008), High-velocity frictional properties of a clay-bearing fault gouge and implications for earthquake mechanics, *J. Geophys. Res.*, *113*, B10401, doi:10.1029/2007JB005551.

Bullock, R. J., N. De Paola, R. E. Holdsworth, and J. Trabucho-Alexandre (2014), Lithological controls on the deformation mechanisms operating within carbonate-hosted faults during the seismic cycle, *J. Struct. Geol.*, *58*, 22–42, doi:10.1016/j.jsg.2013.10.008.

Carpenter, B., C. Marone, and D. Saffer (2011), Weakness of the San Andreas Fault revealed by samples from the active fault zone, *Nat. Geosci.*, *4*(4), 251–254.

Chester, F. M., et al. (2013), Structure and composition of the plate-boundary slip zone for the 2011 Tohoku-Oki earthquake, *Science*, *342*(6163), 1208–1211, doi:10.1126/science.1243719.

Chiaraluce, L. (2012), Unravelling the complexity of Apenninic extensional fault systems: A review of the 2009 L'Aquila earthquake (Central Apennines, Italy), *J. Struct. Geol.*, *42*, 2–18, doi:10.1016/j.jsg.2012.06.007.

Collettini, C., N. De Paola, R. Holdsworth, and M. Barchi (2006), The development and behaviour of low-angle normal faults during Cenozoic asymmetric extension in the Northern Apennines, Italy, *J. Struct. Geol.*, *28*(2), 333–352.

Collettini, C., A. Niemeijer, C. Viti, and C. Marone (2009), Fault zone fabric and fault weakness, *Nature*, *462*(7275), 907–910. [Available at http://www.nature.com/nature/journal/v462/n7275/suppinfo/nature08585_S1.html.]

Collettini, C., A. Niemeijer, C. Viti, S. A. F. Smith, and C. Marone (2011), Fault structure, frictional properties and mixed-mode fault slip behavior, *Earth Planet. Sci. Lett.*, *311*(3), 316–327.

Collettini, C., C. Viti, T. Tesei, and S. Mollo (2013), Thermal decomposition along natural carbonate faults during earthquakes, *Geology*, *41*(8), 927–930, doi:10.1130/g34421.1.

Collettini, C., B. M. Carpenter, C. Viti, F. Cruciani, S. Mollo, T. Tesei, F. Trippetta, L. Valoroso, and L. Chiaraluce (2014), Fault structure and slip localization in carbonate-bearing normal faults: An example from the Northern Apennines of Italy, *J. Struct. Geol.*, *67*, 154–166, doi:10.1016/j.jsg.2014.07.017.

D'Agostino, N., S. Mantenuto, E. D'Anastasio, A. Avallone, M. Barchi, C. Collettini, F. Radicioni, A. Stoppini, and G. Fastellini (2009), Contemporary crustal extension in the Umbria–Marche Apennines from regional CGPS networks and comparison between geodetic and seismic deformation, *Tectonophysics*, *476*(1–2), 3–12, doi:10.1016/j.tecto.2008.09.033.

De Paola, N., G. Chiodini, T. Hirose, C. Cardellini, S. Caliro, and T. Shimamoto (2011a), The geochemical signature caused by earthquake propagation in carbonate-hosted faults, *Earth Planet. Sci. Lett.*, *310*(3), 225–232.

De Paola, N., T. Hirose, T. Mitchell, G. Di Toro, C. Viti, and T. Shimamoto (2011b), Fault lubrication and earthquake propagation in thermally unstable rocks, *Geology*, *39*(1), 35–38.

De Paola, N., R. E. Holdsworth, C. Viti, C. Collettini, I. Faoro, and R. J. Bullock (2014), Can grain size sensitive creep lubricate faults during earthquake propagation?, paper presented at AGU Fall meeting, San Francisco, Calif.

Di Luccio, F., G. Ventura, R. Di Giovambattista, A. Piscini, and F. Cinti (2010), Normal faults and thrusts reactivated by deep fluids: The 6 April 2009 M_w 6.3 L'Aquila earthquake, central Italy, *J. Geophys. Res.*, *115*, B06315, doi:10.1029/2009JB007190.

Di Toro, G., R. Han, T. Hirose, N. De Paola, S. Nielsen, K. Mizoguchi, F. Ferri, M. Cocco, and T. Shimamoto (2011), Fault lubrication during earthquakes, *Nature*, *471*(7339), 494–498.

Faulkner, D. R., T. M. Mitchell, J. Behnsen, T. Hirose, and T. Shimamoto (2011), Stuck in the mud? Earthquake nucleation and propagation through accretionary forearcs, *Geophys. Res. Lett.*, *38*, L18303, doi:10.1029/2011GL048552.

Faulkner, D., A. Lewis, and E. Rutter (2003), On the internal structure and mechanics of large strike-slip fault zones: Field observations of the Carboneras fault in southeastern Spain, *Tectonophysics*, *367*(3), 235–251.

Ferri, F., G. Di Toro, T. Hirose, and T. Shimamoto (2010), Evidence of thermal pressurization in high-velocity friction experiments on smectite-rich gouges, *Terra Nova*, *22*(5), 347–353, doi:10.1111/j.1365-3121.2010.00955.x.

Ferri, F., G. Di Toro, T. Hirose, R. Han, H. Noda, T. Shimamoto, M. Quaresimin, and N. de Rossi (2011), Low-to high-velocity frictional properties of the clay-rich gouges from the slipping zone of the 1963 Vaiont slide, northern Italy, *J. Geophys. Res.*, *116*, B09208, doi:10.1029/2011JB008338.

Fondriest, M., S. A. Smith, T. Candela, S. B. Nielsen, K. Mair, and G. Di Toro (2013), Mirror-like faults and power dissipation during earthquakes, *Geology*, *41*(11), 1175–1178.

French, M. E., H. Kitajima, J. S. Chester, F. M. Chester, and T. Hirose (2014), Displacement and dynamic weakening processes in smectite-rich gouge from the Central Deforming Zone of the San Andreas Fault, *J. Geophys. Res. Solid Earth*, *119*, 1777–1802, doi:10.1002/2013JB010757.

Gratier, J. P., F. Thouvenot, L. Jenatton, A. Tourette, M. L. Doan, and F. Renard (2013), Geological control of the partitioning between seismic and aseismic sliding behaviours in active faults: Evidence from the Western Alps, France, *Tectonophysics*, *600*, 226–242, doi:10.1016/j.tecto.2013.02.013.

Guerrieri, L., A. Blumetti, E. Esposito, A. Michetti, S. Porfido, L. Serva, E. Tondi, and E. Vittori (2009), Capable faulting, environmental effects and seismic landscape in the area affected by the 1997 Umbria–Marche (Central Italy) seismic sequence, *Tectonophysics*, *476*(1), 269–281.

Han, R., T. Shimamoto, T. Hirose, J. H. Ree, and J. Ando (2007), Ultralow friction of carbonate faults caused by thermal decomposition, *Science*, *316*(5826), 878–881.

Han, R., T. Hirose, T. Shimamoto, Y. Lee, and J. Ando (2011), Granular nanoparticles lubricate faults during seismic slip, *Geology*, *39*(6), 599–602.

Holdsworth, R. E. (2004), Weak faults—Rotten cores, *Science*, *303*(5655), 181–182, doi:10.1126/science.1092491.

Holdsworth, R., E. Van Diggelen, C. Spiers, J. De Bresser, R. Walker, and L. Bowen (2011), Fault rocks from the SAFOD core samples: Implications for weakening at shallow depths along the San Andreas Fault, California, *J. Struct. Geol.*, *33*(2), 132–144.

Hsu, Y.-J., M. Simons, J.-P. Avouac, J. Galetzka, K. Sieh, M. Chlieh, D. Natawidjaja, L. Prawirodirdjo, and Y. Bock (2006), Frictional afterslip following the 2005 Nias-Simeulue earthquake, Sumatra, *Science*, *312*(5782), 1921–1926, doi:10.1126/science.1126960.

Ide, S., A. Baltay, and G. C. Beroza (2011), Shallow dynamic overshoot and energetic deep rupture in the 2011 M_w 9.0, Tohoku-Oki earthquake, *Science*, *332*(6036), 1426–1429, doi:10.1126/science.1207020.

Ikari, M. J., D. M. Saffer, and C. Marone (2007), Effect of hydration state on the frictional properties of montmorillonite-based fault gouge, *J. Geophys. Res.*, *112*, B06423, doi:10.1029/2006JB004748.

Ikari, M. J., D. M. Saffer, and C. Marone (2009), Frictional and hydrologic properties of clay-rich fault gouge, *J. Geophys. Res.*, *114*, B05409, doi:10.1029/2008JB006089.

Ikari, M. J., C. Marone, and D. M. Saffer (2011), On the relation between fault strength and frictional stability, *Geology*, *39*(1), 83–86.

Lavecchia, G., P. Boncio, and N. Creati (2003), A lithospheric-scale seismogenic thrust in central Italy, *J. Geodyn.*, *36*(1–2), 79–94, doi:10.1016/S0264-3707(03)00040-1.

Lay, T., et al. (2005), The Great Sumatra-Andaman earthquake of 26 December 2004, *Science*, *308*(5725), 1127–1133, doi:10.1126/science.1112250.

Lockner, D. A., C. Morrow, D. Moore, and S. Hickman (2011), Low strength of deep San Andreas Fault gouge from SAFOD core, *Nature*, *472*(7341), 82–85.

Logan, J., C. Dengo, N. Higgs, and Z. Wang (1992), Fabrics of experimental fault zones: Their development and relationship to mechanical behavior, *Int. Geophys.*, *51*, 33–67.

Malagnini, L., F. P. Lucente, P. De Gori, and A. Akinci (2012), Control of pore fluid pressure diffusion on fault failure mode: Insights from the 2009 L'Aquila seismic sequence, *J. Geophys. Res.*, *117*, B05302, doi:10.1029/2011JB008911.

Marone, C. (1998), Laboratory-derived friction laws and their application to seismic faulting, *Annu. Rev. Earth Planet. Sci.*, *26*(1), 643–696.

Miller, S. A., C. Collettini, L. Chiaraluce, M. Cocco, M. Barchi, and B. J. Kaus (2004), Aftershocks driven by a high-pressure CO_2 source at depth, *Nature*, *427*(6976), 724–727.

Mizoguchi, K., T. Hirose, T. Shimamoto, and E. Fukuyama (2007), Reconstruction of seismic faulting by high-velocity friction experiments: An example of the 1995 Kobe earthquake, *Geophys. Res. Lett.*, *34*, L01308, doi:10.1029/2006GL027931.

Moore, D. E., and D. A. Lockner (2004), Crystallographic controls on the frictional behavior of dry and water-saturated sheet structure minerals, *J. Geophys. Res.*, *109*(B3), B03401, doi:10.1029/2003JB002582.

Moore, D. E., and D. A. Lockner (2007), Friction of the smectite clay montmorillonite: A review and interpretation of data, in *The Seismogenic Zone of Subduction Thrust Faults, MARGINS Theor. Exp. Earth Sci. Ser.*, vol. 2, edited by T. H. Dixon and J. C. Moore, pp. 317–345, Columbia Univ. Press, New York.

Moore, D. E., and D. A. Lockner (2011), Frictional strengths of talc-serpentine and talc-quartz mixtures, *J. Geophys. Res.*, *116*, B01403, doi:10.1029/2010JB007881.

Morrow, C. A., B. Radney, and J. D. Byerlee (1992), Frictional strength and the effective pressure law of montmorillonite and illite clays, in *Fault Mechanics and Transport Properties of Rocks*, edited by B. Evans, and T.-F. Wong, pp. 69–88, Academic, San Diego, Calif.

Morrow, C., J. Solum, S. Tembe, D. Lockner, and T. F. Wong (2007), Using drill cutting separates to estimate the strength of narrow shear zones at SAFOD, *Geophys. Res. Lett.*, *34*, L11301, doi:10.1029/2007GL029665.

Niemeijer, A., C. Marone, and D. Elsworth (2010), Fabric induced weakness of tectonic faults, *Geophys. Res. Lett.*, *37*, L03304, doi:10.1029/2009GL041689.

Rice, J. R., J. W. Rudnicki, and J. D. Platt (2014), Stability and localization of rapid shear in fluid-saturated fault gouge: 1. Linearized stability analysis, *J. Geophys. Res. Solid Earth*, *119*, 4311–4333.

Saffer, D. M., and C. Marone (2003), Comparison of smectite-and illite-rich gouge frictional properties: Application to the updip limit of the seismogenic zone along subduction megathrusts, *Earth Planet. Sci. Lett.*, *215*(1), 219–235.

Saffer, D. M., K. M. Frye, C. Marone, and K. Mair (2001), Laboratory results indicating complex and potentially unstable frictional behavior of smectite clay, *Geophys. Res. Lett.*, *28*(12), 2297–2300, doi:10.1029/2001GL012869.

Savage, H. M., P. J. Polissar, R. Sheppard, C. D. Rowe, and E. E. Brodsky (2014), Biomarkers heat up during earthquakes: New evidence of seismic slip in the rock record, *Geology*, *42*(2), 99–102.

Scholz, C. H. (1998), Earthquakes and friction laws, *Nature*, *391*(6662), 37–42.

Shimamoto, T., and A. Tsutsumi (1994), A new rotary-shear high-speed frictional testing machine: Its basic design and scope of research [in Japanese with English abstract], *J. Tectonic Res. Group Jpn*, *39*, 65–78.

Sibson, R. H. (1975), Generation of pseudotachylyte by ancient seismic faulting, *Geophys. J. Int.*, *43*(3), 775–794, doi:10.1111/j.1365-246X.1975.tb06195.x.

Sibson, R. H. (1981), Fluid flow accompanying faulting: Field evidence and models, in *Earthquake Prediction*, pp. 593–603, AGU, Washington, D. C.

Siman-Tov, S., E. Aharonov, A. Sagy, and S. Emmanuel (2013), Nanograins form carbonate fault mirrors, *Geology*, *41*(6), 703–706.

Smith, S., G. Di Toro, S. Kim, J. H. Ree, S. Nielsen, A. Billi, and R. Spiess (2013), Coseismic recrystallization during shallow earthquake slip, *Geology*, *41*(1), 63–66.

Sone, H., T. Shimamoto, and D. E. Moore (2012), Frictional properties of saponite-rich gouge from a serpentinite-bearing fault zone along the Gokasho-Arashima Tectonic Line, central Japan, *J. Struct. Geol.*, *38*, 172–182.

Tembe, S., D. A. Lockner, and T. F. Wong (2010), Effect of clay content and mineralogy on frictional sliding behavior of simulated gouges: Binary and ternary mixtures of quartz, illite, and montmorillonite, *J. Geophys. Res.*, *115*, B03416, doi:10.1029/2009JB006383.

Tesei, T., C. Collettini, B. M. Carpenter, C. Viti, and C. Marone (2012), Frictional strength and healing behavior of phyllosilicate-rich faults, *J. Geophys. Res.*, *117*, B09402, doi:10.1029/2012JB009204.

Tesei, T., C. Collettini, C. Viti, and M. R. Barchi (2013), Fault architecture and deformation mechanisms in exhumed analogues of seismogenic carbonate-bearing thrusts, *J. Struct. Geol.*, *55*, 167–181.

Ujiie, K., and A. Tsutsumi (2010), High-velocity frictional properties of clay-rich fault gouge in a megasplay fault zone, Nankai subduction zone, *Geophys. Res. Lett.*, *37*, L24310, doi:10.1029/2010GL046002.

Ujiie, K., A. Tsutsumi, and J. Kameda (2011), Reproduction of thermal pressurization and fluidization of clay-rich fault gouges by high-velocity friction experiments and implications for seismic slip in natural faults, *Geol. Soc., London Spec. Publ.*, *359*(1), 267–285.

Ujiie, K., et al. (2013), Low coseismic shear stress on the Tohoku-Oki megathrust determined from laboratory experiments, *Science*, *342*(6163), 1211–1214, doi:10.1126/science.1243485.

Ventura, G., and R. Di Giovambattista (2013), Fluid pressure, stress field and propagation style of coalescing thrusts from the analysis of the 20 May 2012 M_L 5.9 Emilia earthquake (Northern Apennines, Italy), *Terra Nova*, *25*(1), 72–78, doi:10.1111/ter.12007.

Verberne, B. A., C. He, and C. J. Spiers (2010), Frictional properties of sedimentary rocks and natural fault gouge from the Longmen Shan fault zone, Sichuan, China, *Bull. Seismol. Soc. Am.*, *100*(5B), 2767–2790.

Verberne, B. A., C. J. Spiers, A. R. Niemeijer, J. H. P. De Bresser, D. A. M. De Winter, and O. Plümper (2014), Frictional properties and microstructure of calcite-rich fault gouges sheared at sub-seismic sliding velocities, *Pure Appl. Geophys.*, *171*(10), 2617–2640, doi:10.1007/s00024-013-0760-0.

Violay, M., S. Nielsen, E. Spagnuolo, D. Cinti, G. Di Toro, and G. Di Stefano (2013), Pore fluid in experimental calcite-bearing faults: Abrupt weakening and geochemical signature of co-seismic processes, *Earth Planet. Sci. Lett.*, *361*, 74–84, doi:10.1016/j.epsl.2012.11.021.

Vittori, E., G. Deiana, E. Esposito, L. Ferreli, L. Marchegiani, G. Mastrolorenzo, A. Michetti, S. Porfido, L. Serva, and A. Simonelli (2000), Ground effects and surface faulting in the September–October 1997 Umbria–Marche (Central Italy) seismic sequence, *J. Geodyn.*, *29*(3), 535–564.

Vrolijk, P., and B. A. van der Pluijm (1999), Clay gouge, *J. Struct. Geol.*, *21*(8), 1039–1048.

Wu, F. T., L. Blatter, and H. Roberson (1975), Clay gouges in the San Andreas Fault system and their possible implications, *Pure Appl. Geophys.*, *113*(1), 87–95, doi:10.1007/BF01592901.

Yamaguchi, A., A. Sakaguchi, T. Sakamoto, K. Iijima, J. Kameda, G. Kimura, K. Ujiie, F. M. Chester, O. Fabbri, and D. Goldsby (2011), Progressive illitization in fault gouge caused by seismic slip propagation along a megasplay fault in the Nankai Trough, *Geology*, *39*(11), 995–998.

Appendix 5

Paper on which I am a co-author

Earth and Planetary Science Letters 431 (2015) 48–58

Contents lists available at ScienceDirect

Earth and Planetary Science Letters

www.elsevier.com/locate/epsl

Can grain size sensitive flow lubricate faults during the initial stages of earthquake propagation?

Nicola De Paola [a,*], Robert E. Holdsworth [a], Cecilia Viti [b], Cristiano Collettini [c,d], Rachael Bullock [a]

[a] Rock Mechanics Laboratory, Earth Sciences Department, Durham University, South Road, Durham, DH1 3LE, UK
[b] Dipartimento di Scienze Fisiche, della Terra e dell'Ambiente, Siena University, Via Laterina 8, 53100 Siena, Italy
[c] Dipartimento di Scienze della Terra, Sapienza Università di Roma, Piazzale Aldo Moro, 5, 00185 Rome, Italy
[d] Istituto Nazionale di Geofisica e Vulcanologia, Sezione Roma 1, Via Vigna Murata 605, I-00143 Rome, Italy

ARTICLE INFO

Article history:
Received 21 April 2015
Received in revised form 29 August 2015
Accepted 1 September 2015
Available online 24 September 2015
Editor: P. Shearer

Keywords:
earthquake
grain boundary sliding
superplasticity
friction
viscous flow
dynamic weakening

ABSTRACT

Recent friction experiments carried out under upper crustal P–T conditions have shown that microstructures typical of high temperature creep develop in the slip zone of experimental faults. These mechanisms are more commonly thought to control aseismic viscous flow and shear zone strength in the lower crust/upper mantle. In this study, displacement-controlled experiments have been performed on carbonate gouges at seismic slip rates (1 m s^{-1}), to investigate whether they may also control the frictional strength of seismic faults at the higher strain rates attained in the brittle crust. At relatively low displacements (<1 cm) and temperatures (≤100 °C), brittle fracturing and cataclasis produce shear localisation and grain size reduction in a thin slip zone (150 μm). With increasing displacement (up to 15 cm) and temperatures (T up to 600 °C), due to frictional heating, intracrystalline plasticity mechanisms start to accommodate intragranular strain in the slip zone, and play a key role in producing nanoscale subgrains (≤100 nm). With further displacement and temperature rise, the onset of weakening coincides with the formation in the slip zone of equiaxial, nanograin aggregates exhibiting polygonal grain boundaries, no shape or crystal preferred orientation and low dislocation densities, possibly due to high temperature (>900 °C) grain boundary sliding (GBS) deformation mechanisms. The observed micro-textures are strikingly similar to those predicted by theoretical studies, and those observed during experiments on metals and fine-grained carbonates, where superplastic behaviour has been inferred. To a first approximation, the measured drop in strength is in agreement with our flow stress calculations, suggesting that strain could be accommodated more efficiently by these mechanisms within the weaker bulk slip zone, rather than by frictional sliding along the main slip surfaces in the slip zone. Frictionally induced, grainsize-sensitive GBS deformation mechanisms can thus account for the self-lubrication and dynamic weakening of carbonate faults during earthquake propagation in nature.

1. Introduction

Earthquakes are typically hosted in the shallower portion of crustal fault zones (≤15 km depth and ambient $T \leq 300$ °C), where fracturing and cataclasis are traditionally thought to be the dominant processes during frictional sliding (Kohlstedt et al., 1995; Scholz, 1998; Sibson, 1977). At greater depths and temperatures, in the lower crust/upper mantle, viscous flow, potentially associated with superplastic behaviour (Ashby and Verrall, 1973; Boullier and Gueguen, 1975; Hiraga et al., 2010; Rutter et al., 1994; Schmid et al., 1977; Walker et al., 1990), is inferred to facilitate aseismic creep along shear zones, based on experimental data and microstructural observations (Ashby and Verrall, 1977; Kohlstedt et al., 1995; Passchier and Trouw, 2005; Poirier, 1985; Rutter, 1995, 1999). Grain boundary sliding (GBS) diffusion creep, associated with superplastic behaviour, i.e., the ability of materials to achieve unusually high elongations (>100%) before failure, has been observed at high strain rates (>10^2 s^{-1}) for a range of nano-phase alloys (Chandra, 2002) and ceramics (Lankford, 1996). These mechanisms could potentially occur in ultrafine-grained (nano-scale) geological materials deformed at higher strain rates and temperatures appropriate for seismic slip or slow earthquakes (Green et al., 2015; Rutter and Brodie, 1988; Schubnel et al., 2013; Verberne et al., 2014).

* Corresponding author. Tel.: +44 (0)191 3342333.
E-mail address: nicola.de-paola@durham.ac.uk (N. De Paola).

http://dx.doi.org/10.1016/j.epsl.2015.09.002
0012-821X/

Recent laboratory experiments, performed using rotary shear apparatuses, show that when sliding at seismic velocities ($\geq$0.5 m s^{-1}) the frictional strength of faults, μ, is significantly lower ($\mu = 0.1$–0.3) (Di Toro et al., 2011; Goldsby and Tullis, 2011; Hirose and Shimamoto, 2005; Reches and Lockner, 2010) than when sliding at low (<1 mm s^{-1}), sub-seismic speeds ($\mu =$ 0.6–0.85) (Byerlee, 1978). Understanding the processes controlling the evolution of fault strength as seismic slip rates are approached is of paramount importance. Strength cannot be measured directly using seismological data, yet it affects the magnitude of the stress drop, the heat flow signature of seismogenic faults, and the relative partitioning of the earthquake energy budget (i.e., the proportion of energy dissipated as seismic waves that can travel to the Earth's surface and cause damaging earthquakes). It has been proposed that slip weakening of experimental and natural seismic faults is caused by thermally-activated processes triggered by localised frictional heating and high temperatures attained in the slip zone (Rice, 2006). Furthermore, recent studies show that cohesive slip zones (SZs), in natural (Siman-Tov et al., 2013) and experimental carbonate seismic faults (De Paola et al., 2011a, 2011b; Fondriest et al., 2013; Green et al., 2015; Ree et al., 2014; Smith et al., 2013; Verberne et al., 2014), are composed of striated and mirrored slip surfaces (SSs). Microstructural analyses show that the SSs and the adjacent SZ material are made of calcite nanograin ($D < 1$ µm) aggregates with a polygonal texture, a microstructure consistent with deformation by creep deformation mechanisms. The use of mirror SSs and nano-granular SZ textures as indicators of seismic slip on faults in carbonates (e.g. Ree et al., 2014; Smith et al., 2013) has been questioned by Verberne et al. (2013, 2014) who have shown that similar features can develop during low velocity (1 µm s^{-1}) friction experiments performed on simulated calcite gouge at upper crustal P–T conditions. However, the grain-scale processes suggested to account for the observed weakening of rocks deformed in the laboratory at seismic velocities are still debated (De Paola et al., 2011a, 2011b; De Paola, 2013; Han et al., 2010; Tisato et al., 2012), as is their occurrence along natural faults during earthquake propagation. Verberne et al. (2014) performed microstructural analyses on experimentally deformed samples at sub-seismic slip rates (1 µm s^{-1}) and low temperatures (<140 °C). They show that nanofibre formation during nanogranular flow with diffusive mass transfer can promote velocity-weakening behaviour and earthquake nucleation in carbonate rocks. Green et al. (2015) integrated microstructural observations and experimental work to show that mineral phase transformation in carbonate rocks, occurring at the high temperatures produced by frictional heating, can generate nanometric materials which are weak at seismic slip rates ($\approx$1 m s^{-1}) and flow by grain-boundary sliding mechanisms.

Here we study the evolution of deformation mechanisms, and their control on the frictional strength of slip zones developed in simulated, carbonate gouges during accelerating sliding to seismic slip rates ($v = 1$ m s^{-1}). To do so we combine results from new laboratory friction experiments with microstructural observations on samples sheared up to the attainment of dynamic weakening, but *prior* to the onset of phase transformation. Flow stress calculations are performed to investigate whether grainsize-sensitive creep deformation mechanisms, potentially associated with superplastic behaviour, can effectively weaken faults and facilitate earthquake propagation in the shallow crust. To illustrate the relevance of our findings to natural faults, we also carried out microstructural observations on the principal slip zone material extracted from natural, seismically active faults in carbonates.

2. Experimental settings

Friction experiments were performed in the Rock Mechanics Laboratory, at Durham University (UK), using a low to high velocity rotary shear apparatus (details in Supplementary Information 1 – Fig. SI1) built by the Marui and Co., Ltd Company (Osaka, Japan). We performed a set of eight displacement-controlled experiments at room temperature and humidity conditions on fine-grained ($63 < D < 93$ µm), carbonate gouges at target slip rates $v = 1$ m s^{-1} and normal stresses $\sigma_n = 12$–18 MPa (Supplementary Information Table 1). During displacement-controlled experiments, arrested at pre-determined displacements, the electric servomotor of the apparatus was controlled in the digital mode, using a signal generator DF1906 (NF corporation) (Supplementary Information 1).

A synthetic fault zone was created by sandwiching 2 g of simulated fault gouge between two stainless steel cylinders (25 mm in diameter), whose ends were machined with radial grooves 500 µm high to grip the sample surface (Supplementary Information 1 – Fig. SI2). The experiments were run under drained conditions, and to limit gouge loss during the experiments, the sample assembly was confined using a Teflon ring. Teflon rings were cut and tightened onto the stainless steel cylinder using a hose clamp. The inner edges of the rings were machined to reduce their sharpness, and thus avoid ring damage and sample contamination by Teflon during the insertion of the stainless steel cylinders (Supplementary Information 1 – Fig. SI2).

Samples were recovered after each experiment to study the slip zone microstructures. Thin sections for optical microscope observations were taken from slices of the slip zone cut at 2/3 of the radius, to make observations consistent with calculated values of the velocity, v, and the displacement d (Supplementary Information 2).

3. Mechanical data

To identify the mechanisms controlling the evolution of friction, we performed a set of displacement-controlled experiments, with a target speed $v = 1$ m s^{-1}, normal stresses $\sigma_n = 12$–18 MPa, and arrested at displacements d from 0.007 to 1.46 m (Supplementary Information Table 1). Experiments arrested at different displacements show similar acceleration paths (Fig. 1a–b), showing that the conditions during our experiments are reproducible (Fig. 1c–d). It also means that microstructures developed at different stages/displacements can be used to study the evolution of deformation mechanisms in the slip zone, and how these may affect frictional strength evolution.

During experiments run up to 1.44–1.46 m total slip, the imposed target speed of 1 m s^{-1} was attained after 0.12 m of slip (Fig. 1a–b). The measured strength consistently showed a four stage evolution (e.g. Exp. Du304–307 in Fig. 1c–d, Supplementary Information Table 1): Stage I) attainment of initial friction values, $\mu_i = 0.67$, upon instantaneous acceleration toward target speed; Stage II) increase in friction up to peak values $\mu_p = 0.80$–0.88, attained just before acceleration to target speed was complete; Stage III) sudden decrease in friction to low steady-state values, $\mu_{ss} = 0.17$–0.21, attained during sliding at constant velocity $v = 1$ m s^{-1}; and Stage IV) sudden increase of friction to $\mu_f =$ 0.44–0.45, observed upon deceleration of the motor.

The temperature rise produced during the laboratory experiments has been estimated, to a first approximation, using (Rice, 2006)

$$\Delta T = \frac{\mu \sigma_n \sqrt{vd}}{\rho c_p \sqrt{\pi \kappa}} \tag{1}$$

where μ represents the friction coefficient, σ_n is the normal stress, d is the displacement, ρ is the rock density, c_p is the specific heat

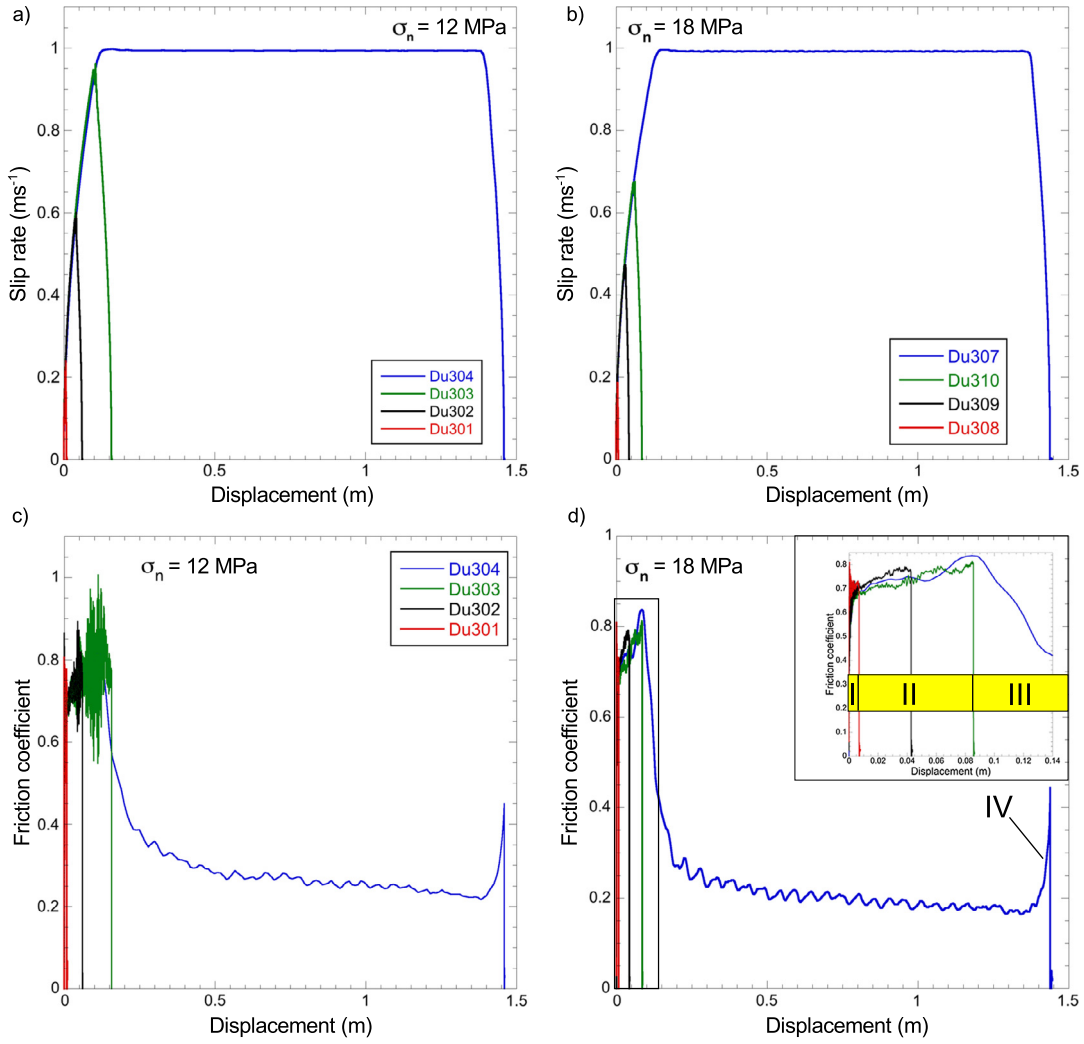

Fig. 1. Experimental data. a–b) Slip rate vs. displacement data for a set of displacement-controlled experiments performed at $\sigma_n = 12$, 18 MPa, and arrested before, during and after the attainment of target speed, $v = 1\ \mathrm{m\,s^{-1}}$. c–d) Friction coefficient vs. displacement data showing the evolution of friction during acceleration (Stages I–II), steady-state sliding (Stage III) and instantaneous deceleration to arrest (Stage IV) of the sample. The inset shows a blow-up of the data in the main graph.

capacity and κ is the thermal diffusivity. Microstructural evidence for slip localisation within slip zones with thickness $h < 150$ μm satisfies the condition $h \leq 4\sqrt{\kappa d/v}$, which allows to treat the slip zone as a plane of zero thickness and account for heat diffusion using Eq. (1). For experiments in which steady-state conditions were attained (e.g., Du304 and Du307 in Fig. 1c–d), temperatures were calculated up to the displacements, d_{tr}, attained at the end of the steep drop in friction observed during the transient stage of friction evolution to low, steady-state values, e.g., at $d_{tr} = 0.23$–0.08 m (Supplementary Information Table 1). The contribution to temperature increase by sliding from peak friction values to those attained at d_{tr} was calculated by using the mean value for μ in Eq. (1). The following physical properties of calcite, the main mineralogical component in the deformed rocks, were used for temperature calculations: $\rho = 2700\ \mathrm{kg/m^3}$, $\kappa = 1.48 * 10^{-6}\ \mathrm{m^2\,s^{-1}}$ and $c_p = 700\ \mathrm{J\,kg^{-1}\,K^{-1}}$ (Di Toro et al., 2011 and references therein). The mechanical parameters d, μ, σ_n and v used for the temperature calculations are those reported in Supplementary Information Table 1, and the temperatures calculated by Eq. (1) are plotted vs. the measured friction coefficients in Fig. 2. It is observed that friction values are in accord with the range of values predicted by Byerlee's rule for temperatures $\leq 554\,^{\circ}\mathrm{C}$ ($\mu_f = 0.68$–0.80), but significantly lower ($\mu_{ss} = 0.17$–0.21) when $T \geq 979\,^{\circ}\mathrm{C}$ (Fig. 2).

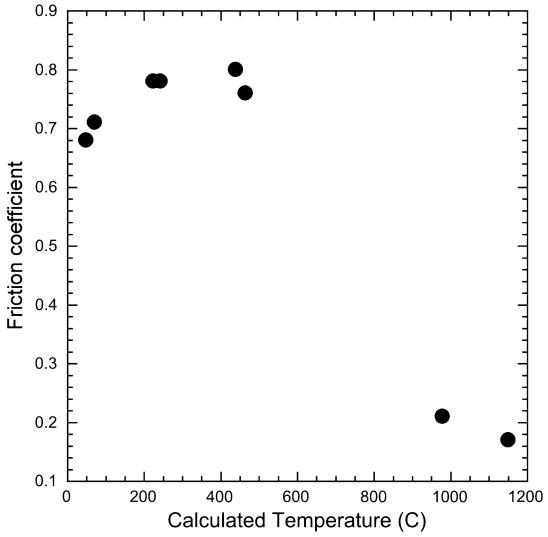

Fig. 2. Temperature vs. friction coefficient data. Temperatures calculated for localised, thin (<150 μm) slip zones plotted vs. the friction coefficient measured during laboratory experiments performed at seismic, target slip rates ($1\ \mathrm{m\,s^{-1}}$) on carbonate gouges (Table 1).

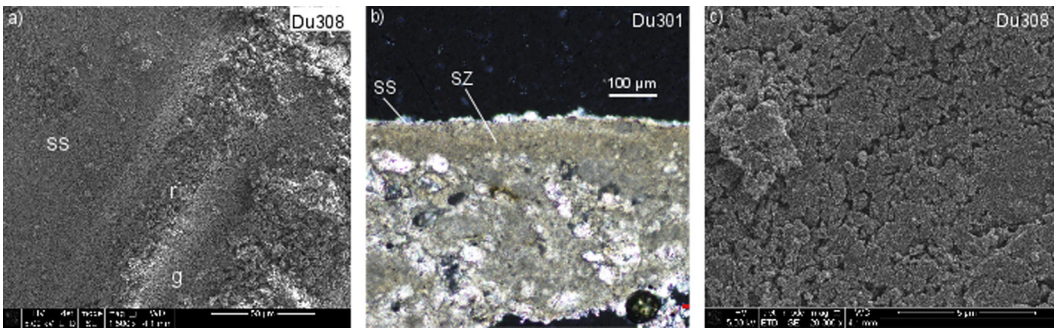

Fig. 3. Microstructural observations of experimental slip zones (Stage I). a) Scanning electron microscope (SEM) image showing in plan view the development of a rough SS, due to the presence of grooves (g) and ridges (r), oriented parallel to the slip direction. b) Optical microscope image showing in cross-section the formation of a continuous, immature slip zone (SZ) with variable thickness (20–200 µm), bounded on the upper part by a rough SS. c) SEM image in plan view showing a magnified, smooth portion of the SS made of fine-grained clasts ($1 < D < 5$ µm), which are sharply truncated against the SS.

4. Microstructural observations and interpretations

4.1. Experimental faults

Samples deformed during Stage I ($d = 0.007$–009 m, Fig. 1c–d) show the formation of an irregular slip zone (SZ) and rough slip surface (SS), due to the presence of grooves (up to 25 µm wide) and ridges, oriented parallel to the slip direction (Fig. 3a). A sharply defined, irregular slip surface (SS) bounds the upper part of the SZ, showing variable thickness (20–200 µm), whilst the lower bound between the SZ and less deformed material is sharp, but rather irregular and wavy (Fig. 3b). The SS is heterogeneous, displaying smooth compact areas interspersed with more granular porous areas (Fig. 3a). The granular portions of the SS appear to be coarser in grain size ($10 < D < 25$ µm) compared to the smooth regions. The smooth portions of the SS are made of fine-grained clasts ($1 < D < 5$ µm), which are sharply truncated against the SS (Fig. 3c). The shape of the clasts on the SS and in the SZ below the SS, is typically angular to sub-angular (Fig. 3c). In places, the smaller clasts display a sub-rounded shape. In the smooth and compact patches, the SS and SZ are still porous, but the porosity, like the grain size, seems finer. Overall, the SZ contains coarse- and fine-grained ($1 < D < 5$ µm), angular clasts, likely formed by brittle fracturing and cataclasis during frictional sliding at low temperatures $<100\,^{\circ}$C (Fig. 2).

During Stage II, samples show the development of a cohesive SZ, <150 µm thick (Fig. 4a), containing multiple SSs sandwiching thin layers (tl, ≈ 5 µm) of sub-rounded nanograins (Fig. 4b–c). TEM analyses show that tl contain slightly larger clasts of calcite ($D \leq 1$ µm) dispersed within a porous assemblage of calcite nanograins, ≤ 100 nm in size, with sub-rounded crystal shapes (Fig. 4d). The calcite clasts host dislocations, locally arranged to form dislocation walls separating subgrains ($D \leq 100$ nm) with small angular misorientations; this is typical of low temperature ($\leq 600\,^{\circ}$C) intragranular dislocation creep deformation (Rutter, 1995) (Fig. 4d). Bright-field TEM images show that, together with dislocation walls and subgrain boundaries, calcite clasts (CC) exhibit "damaged" rims, hosting rounded bubbles and lobate, low-contrast features (Fig. 4e). These nanostructures suggest concomitant decarbonation and amorphization processes, preferentially located within the strained calcite rims and at subgrain boundaries. This is where crystal structure defects are concentrated and where, it is suggested, calcite becomes more reactive. We propose that the occurrence of an amorphous phase along subgrain boundaries will facilitate clast disaggregation and the subsequent formation of nano-sized, calcite grain aggregates (Fig. 4d–e). The d-spacing measurements, obtained from the ring-shaped Selected Area Electron Diffraction (SAED) pattern of ultrafine-grained material, confirm that ultrafine grains are composed of calcite (Fig. 4f). In particular, rings I and II correspond to 3.82 and 3.00 Å spacing (Fig. 4f), in strong agreement with the 3.85 and 3.03 Å of reference calcite (012 and 104 reflections, respectively).

When deforming through Stage III, up to $d = 1.44$–1.46 m (Fig. 1c–d), samples show the localisation of slip in a cohesive SZ, <150 µm thick, and the formation of shiny, mirror-like SSs (Fig. 5a). The bulk slip zone configuration is similar to those seen during Stage II (Fig. 4a–b), but the grain scale textures are very different. Low porosity SSs ($D \approx 600$–700 nm) separate thin layers of nanograin ($D \approx 100$–600 nm) aggregates with markedly polygonal textures and straight grain boundaries (Fig. 5b–c). SEM images show that the SSs and the thin layers (tl) are composed of relatively compact, polygonal nanostructures of calcite grains, with 120° triple junction contacts between equiaxial grains (Fig. 5b–c). Patches of polygonal nanograins with coarser (600–700 nm, Fig. 5b) and finer (≤ 100 nm, Fig. 5c) grainsize are observed in the tl, in contrast to the polygonal nanograins on the SS which display a more uniform, but larger grainsize distribution (600–700 nm) (Fig. 5b–c). TEM analyses show that the finer and coarser calcite grains in the tl have low dislocation densities, as shown by their homogeneous TEM contrast, regardless of their crystal orientation (Fig. 5d). Relatively large cavities (e.g., C in Fig. 5e) occur along grain boundaries or at triple junctions, whereas smaller rounded bubbles are trapped within calcite grains (Fig. 5e). Calcite clasts from the tl in the SZ exhibit irregular, lobate crystal boundaries, surrounded by thin (<10 nm) rims of amorphous material of limited extent (Fig. 5f). Calcite grains do not show crystal preferred orientation, as they are characterised by ring-shaped SAED patterns (Fig. 5g). Measured d-spacing confirms that the polygonal grains are calcite (Fig. 5g).

4.2. Phase transformation and annealing processes

We found little evidence for phase transformations that might cause weakening in our experiments. Microstructural and mineralogical observations show that the development of degassing bubbles (Figs. 4e, 5e) and amorphization rims (Figs. 4e, 5f), indicative of decarbonation reactions, are limited to the boundaries of calcite grains in the SZ of samples deformed through Stage II and Stage III. In both cases, SAED pattern analyses revealed that the clasts in the SZ are composed of calcite (Figs. 4f, 5g), confirming that decarbonation reactions in the SZ of samples deformed up to Stage III were not quantitatively significant. We interpret this as being due to the kinetics of the decarbonation reaction requiring exposure to decomposition temperatures for periods much longer than the few fractions of a second that occurred during our experiments (De Paola et al., 2011a). This interpretation is supported by further microstructural evidence showing that widespread and

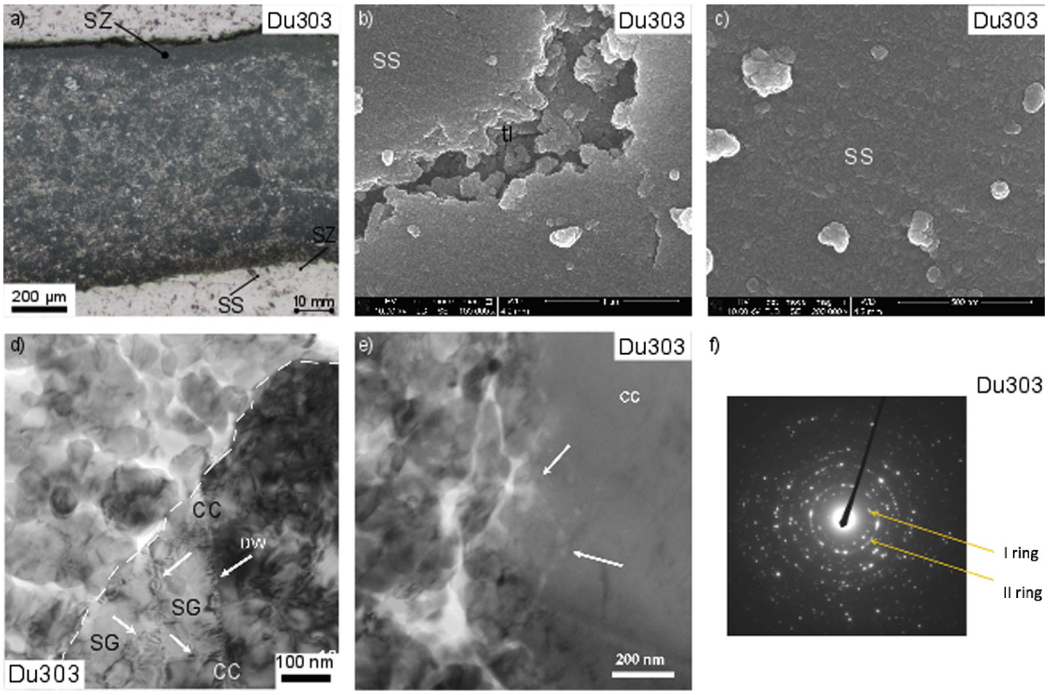

Fig. 4. Microstructural observations of experimental slip zones (Stage II). a–c) Optical microscope (a, cross section view) and SEM (b–c, plan view) images show the development a cohesive slip zone (SZ), and striated slip surface (SS) sandwiching thin layers made of nanograin aggregates ($D \leq 100$ nm) with sub-rounded shape. d) TEM image showing calcite nanograins ($\leq$100 nm) in contact with a calcite clast (CC) hosting dislocations and dislocation walls (DW) separating subgrains (SG) ($D \leq 100$ nm). e) Calcite clasts (CC) exhibit "damaged" rims, hosting rounded bubbles and lobate, low-contrast features (arrows) (bright-field TEM images). f) Measured d-spacings from ring-shaped SAED pattern confirm that ultrafine grains are formed by calcite.

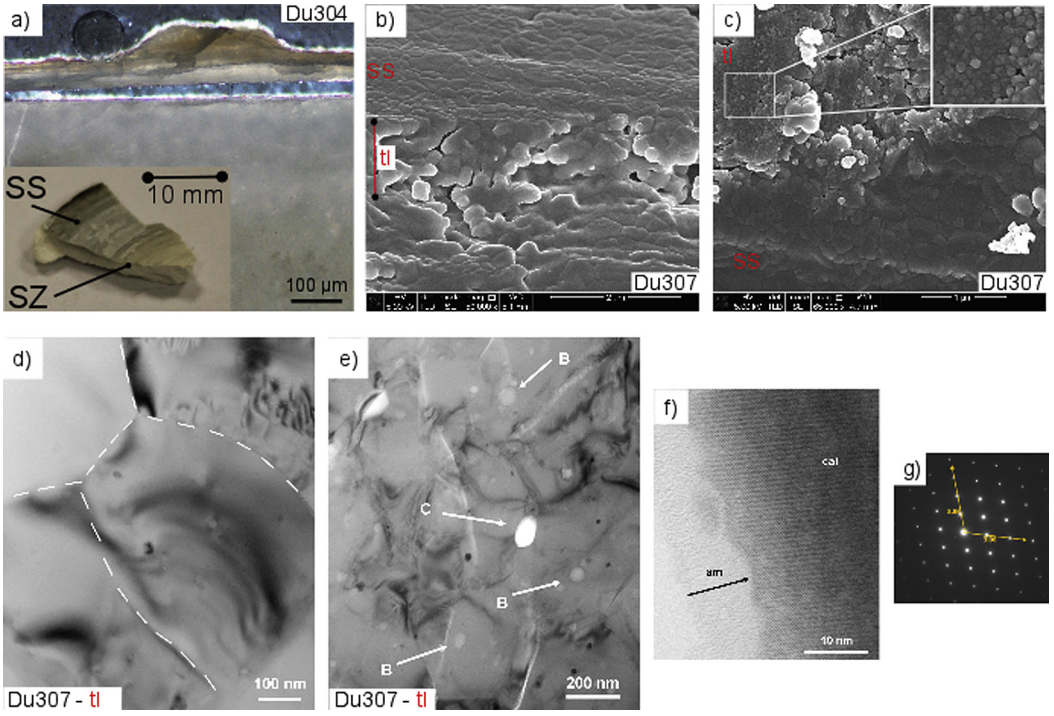

Fig. 5. Microstructural observations of experimental slip zones (Stage III). a–c) Optical microscope (a, cross section and inset oblique plan views) and SEM (b–c, plan view) images show the development of a cohesive slip zone (SZ) composed of stacked striated slip surfaces (SS), sandwiching thin layers (tl) of nanoscale grains. d) TEM images show that tl are associated with compact polygonal nanostructures of calcite grains, displaying low free dislocation densities. e) TEM image of relatively large cavities (C) formed along grain boundaries or at triple junctions, whereas smaller rounded bubbles are trapped within calcite grains (B). f) Calcite clast relic from the thin porous layers in the slip zone (see main text), exhibiting irregular, lobate crystal boundaries, surrounded by a 10 nm thick amorphous rim (am). g) Measured d-spacings from single-crystal SAED pattern of polygonal grains from the thin layers confirm that polygonal grains are formed by calcite (arrows show the corresponding reciprocal axes).

pervasive, intragranular thermal decomposition processes do affect polygonal calcite grains, when high temperatures are maintained for longer time periods (>2 s) during high displacement experiments ($d > 5$ m) (Supplementary Information 2). Thus we propose that the observed weakening is not caused by thermally activated phase transitions when fault displacements are <1.5 m.

Microstructural observations on samples deformed up to Stage III show the presence of localised patches of small (≤100 nm) polygonal nanograins in the tl of the SZ. The grainsizes are similar to those observed in the tl of samples deformed up to Stage II (Figs. 4b–d, 5b–c). However, slightly larger polygonal nanograins (600–700 nm) have also been observed on both the SS and in the tl of samples deformed up to Stage III (Fig. 5b–c), suggesting that grain growth processes occurred in the nanograins of the experimental SZ. Grain growth kinetics and the grainsize that can be attained by normal grain growth are described by the well know equation (e.g., Covey-Crump, 1997)

$$d^{\frac{1}{n}} - d_0^{\frac{1}{n}} = k_0 t e^{-\frac{H}{RT}} \quad (2)$$

where d is the grainsize, d_0 is the initial grainsize, t is the duration of the growth period, n is a dimensionless constant which depends on the process controlling the growth rate, k_0 is the pre-exponential factor, H is the apparent activation enthalpy of the process controlling the grain growth, R is the gas constant and T is the temperature. During sample deformation up to Stage II ($T = 500\,^{\circ}\mathrm{C}$) and Stage III ($T = 800$–$1000\,^{\circ}\mathrm{C}$) (Supplementary Information Table 1), the maximum temperatures inferred in the slip zone are only attained for a fraction of a second, and it takes <10 s for our sample to cool down to $T < 100\,^{\circ}\mathrm{C}$. Hence, we assume that $t = 1$ s is a conservative estimation of the time-scale upon which grain growth, due to static recrystallisation, may occur in the slip zone. The parameters $n = 0.5$, $k_0 = 3.5502 * 10^{-10}\ \mu\mathrm{m}^{1/n}\,\mathrm{s}^{-1}$ (obtained from $k_{979\ \mathrm{K}} = 5.5626 * 10^{-3}\ \mu\mathrm{m}^{1/n}\,\mathrm{s}^{-1}$), $H = 240 * 10^3\ \mathrm{J\,mol}^{-1}$, $R = 8.3145\ \mathrm{J\,K}^{-1}\,\mathrm{mol}^{-1}$, obtained by Covey-Crump (1997) for the pore-fluid absent conditions, were used to solve Eq. (2), and to calculate the maximum theoretical increase in grain size, d, from an initial grain size $d_0 = 0.1$ μm, when growth time $t = 0.1$, 1, 10 s and temperature $T = 500$, 800, 900, 1000 °C (Fig. 6). The results show that, for conditions similar to those attained in samples deformed up to Stage II (e.g. $T = 500\,^{\circ}\mathrm{C}$ and initial grain size $d_0 = 0.1$ μm), no grain growth should occur in our samples (Fig. 6). Under these conditions, the activation of grain boundary migration processes requires timescales significantly longer than the overall duration and quenching phase of our experiments (Fig. 6). These results agree well with our microstructural observations on SS and tl nanograin aggregates showing $D \leq 100$ nm and a lack of diagnostic large and dislocation-free grains that would be expected to form during annealing.

For conditions similar to those attained in samples deformed up to Stage III (e.g. $T = 800$–$1000\,^{\circ}\mathrm{C}$ and initial grain size $d_0 = 0.1$ μm), grain growth is predicted to occur for the range of time $0.1\ \mathrm{s} \leq t \leq 10$ s considered (Fig. 6). At these conditions, grain boundary migration processes could be activated within 0.1 s from the attainment of the high temperatures reached in our experiments when deformed up to Stage III (Fig. 6). Our microstructural observations of polygonal, nanograin aggregates on the SS and in the tl show grain growth from initial values of $d_0 \leq 100$ nm up to $D = 600$–700 nm, which is lower than the maximum grainsize $d = 2.25$ μm predicted by grain growth calculations at $T = 1000\,^{\circ}\mathrm{C}$ and $t = 1$ s (Fig. 6). TEM analyses show that the polygonal calcite grains do have low dislocation density, but there is still a lack of diagnostic large and dislocation-free grains, which would be expected to form during complete annealing. We conclude that static recrystallisation and growth of the nanograin aggregates on the SS and within localised patches in the tl may have occurred after the experiments, during the cooling stage of samples deformed up to Stage III, although the integration of microstructural and theoretical data show that grain growth may only have caused a partial annealing of the original fabric. Elements of this fabric may still be preserved in the tl as patches of fine grainsize polygonal nanograins (see Fig. 5c). The attainment of high T for short durations ($t \leq 1$ s) and the presence of second-phase materials (e.g., amorphous decomposed material, Fig. 5f) and pores (e.g., degassing bubbles, Fig. 5e) pinning the grain boundaries (Olgaard and Evans, 1986), may have limited grain growth during our experiments. This plausibly explains the local preservation of patches of finer polygonal nanograins and the lower grainsizes observed than those theoretically predicted (Fig. 6).

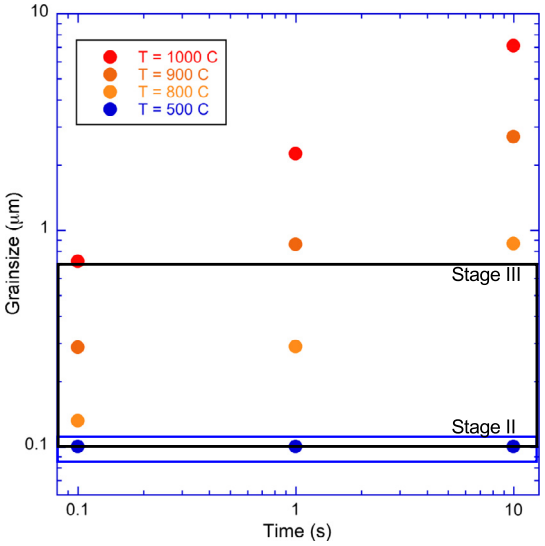

Fig. 6. Modelled grainsize vs. time during static crystallisation. The graph shows the maximum, theoretical increase in grain size, obtained by solving Eq. (2) in the main text for range of temperatures, initial grain sizes and timescales representative of those attained during sample deformation up to Stage II ($T = 500\,^{\circ}\mathrm{C}$) and Stage III ($T = 800$–$1000\,^{\circ}\mathrm{C}$). The blue (Stage II) and black (Stage III) rectangles show the range of grainsizes observed in the experimental slip zones.

5. Natural faults

In the last decade a series of studies have documented the nucleation and/or propagation of significant earthquakes through thick sequences of carbonates (e.g. Valoroso et al., 2014). Motivated by these observations, several workers have focused on the study of carbonate-bearing faults exhumed from the seismogenic crust in order to improve the characterisation of fault zone structure and deformation processes (e.g. De Paola et al., 2008; Smith et al., 2011; Rowe et al., 2012; Collettini et al., 2013; Siman-Tov et al., 2013; Bullock et al., 2014). Here as a natural example, we use a large-offset (≈600 m) fault exposed in the seismic belt of the Apennines, Italy. The fault is 10 km long with a maximum width of about 1.5 km and consists of 5 sub-parallel segments (Collettini et al., 2014). At the outcrop scale the fault structure is characterised by striated and mirrored SSs (Fig. 7a), similar to those observed in other carbonate-hosted, seismically active faults (Smith et al., 2013; Siman-Tov et al., 2013). Sampling and microstructural studies across the SS reveal a natural cohesive SZ (<150 μm thick) characterised by parallel SSs (Fig. 7b, c).

SEM investigations of the SZ show calcite grains with lobate and faint grain boundaries. Grain boundaries are characterised by the concentration of voids and/or vesicles, indicating limited thermal decomposition of calcite (Fig. 7b and Collettini et al., 2014). TEM analyses show that some portions of the SSs and the SZ material are made of micrometre-sized calcite crystals, which commonly show nanoscale polysynthetic twinning. High dislocation densities and subgrain boundary formation indicate that twin lamellae have experienced intense strain. The pervasive occurrence of subgrain boundaries along twinning planes suggests that twinning predates the development of dislocations, dislocation walls and calcite nanograins ($D = 200$–300 nm). Other portions of the SSs and SZ material show calcite nanograin ($D \leq 100$ nm) aggre-

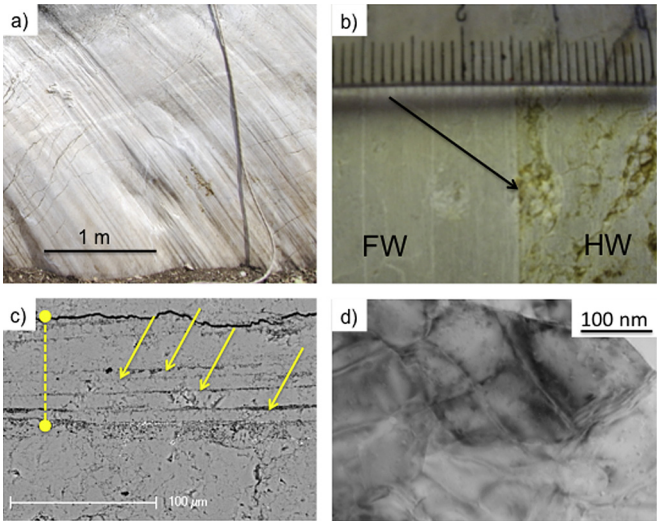

Fig. 7. Mesoscale and microstructural observations from natural slip zones. a) Outcrop photograph of the M. Maggio fault plane, located in the Apennines of Italy (details in Collettini et al., 2014), showing its naturally polished, reflective glossy surface. b) Rock sample cross section including hanging-wall, HW, and footwall, FW, blocks together with the principal slipping zone (indicated by the arrow) where we performed the microstructural studies. c) BSE-SEM image in cross section showing that the principal slipping zone is about 100 mm thick (dashed yellow line) and, here, the slip is accommodated along sub-parallel SSs indicated by yellow arrows. d) Nanostructure composed of polygonal calcite grains in close association with strain-free calcite crystals.

gates with a polygonal texture; the nanograins have straight grain boundaries with 120° triple junction contacts between equiaxial grains, and display no preferred elongation (Fig. 7d). These natural microstructures are strikingly similar to those observed in the experimentally deformed samples during Stage III (Fig. 5c).

6. Discussion

6.1. Micro-scale deformation mechanisms during earthquake propagation

In the experimental samples, a localised slip zone, up to 150 μm thick, develops in the early stages of deformation (Stage I) when the SZ material is poorly consolidated, bounded by slip surfaces, and made of fine-grained, angular clasts ($1 \leq D \leq 5$ μm). Brittle fracturing and cataclasis are the dominant deformation mechanisms observed in samples deformed up to Stage I, at relatively low temperatures ($\leq$100 °C), and it is these mechanisms that likely control shear localisation and grain size reduction in the slip zone (Fig. 3) (Bullock et al., 2015; Smith et al., 2015). In our experiments – unlike those of Verberne et al. (2014) – we do not observe the development of shiny, mirror-like slip surfaces and of nanoscale materials in the SZ of samples deformed up to Stage I (up to 7 mm slip). Sliding friction values predicted by Byerlee's rule (Byerlee, 1978) match those measured during experiments arrested in Stage I (Fig. 1).

SEM analyses of samples deformed up to Stage II show that the SZ material becomes cohesive and contains multiple SSs, which sandwich thin ($\approx$ 5 μm) porous layers of sub-rounded nanograins (Fig. 4). TEM analyses show larger clasts of calcite ($D \approx 1$ μm) dispersed within a porous assemblage of calcite nanograins, $\leq$100 nm in size. These larger calcite clasts exhibit a high density of free dislocations and host subgrains ($D \leq 100$ nm) (Fig. 4d–e). As temperatures rise during Stage II, due to frictional heating ($T \approx 550$ °C), intracrystalline plasticity mechanisms, active at $T \leq 600$ °C, start to accommodate intragranular strain and the development of nanoscale subgrains ($D \leq 100$ nm) in the thin layers of the slip zone (Fig. 4d–e).

When deformation progresses through Stage III, samples show a bulk slip-zone configuration similar to Stage II, but the grain-scale microstructures are very different. SEM and TEM analyses of thin layers of nanograin ($D \approx 100$–600 nm) aggregates between the SSs exhibit polygonal grain boundaries, showing 120° triple junctions between equiaxial grains (Fig. 5b–e). The grains display no preferred elongation, no crystal preferred orientation (based on SAED measurements) and low dislocation densities (Fig. 5d–g), possibly due to high temperature ($\geq$900 °C) GBS deformation mechanisms. The observed micro-textures in experimental (Fig. 8a) and natural slip zones (Fig. 8b) are strikingly similar to those predicted by theoretical studies (Fig. 8c, Ashby and Verrall, 1973), and those observed during experiments on metals (Chandra, 2002) and fine-grained carbonates (Walker et al., 1990; Schmid et al., 1977), at temperatures $\leq$1000 °C, where superplastic behaviour due to grainsize-sensitive GBS has been inferred. Hence, we propose that the preservation of equiaxial polygonal nano-grains ($D \leq 100$ nm), with low dislocation densities, is diagnostic of GBS mechanisms associated with superplastic behaviour (Verberne et al., 2013, 2014).

Our SEM and TEM observations show that the synthetic carbonate gouges deformed up to Stage III in our experiments preserve microstructural evidence for the operation of GBS accommodated by *both* diffusion and dislocation creep (Fig. 5c–e). The polygonal nanograins developed during Stage III are characterised by a much lower dislocation density compared to those observed during Stage II. This may be due to the establishment of less favourable

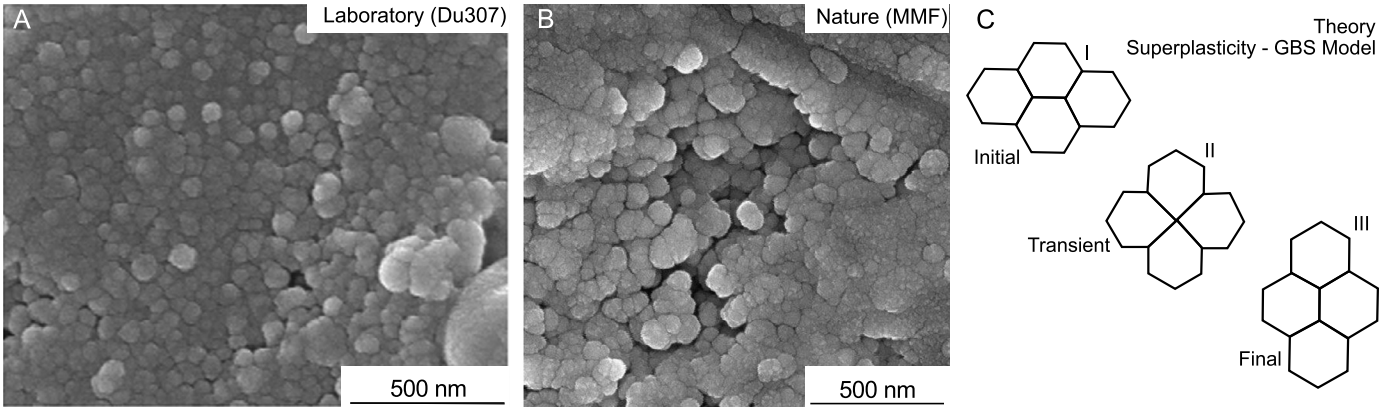

Fig. 8. Microstructures diagnostic of superplastic behaviour: theory vs. experimental/natural slip zone samples. a–b) SEM images of experimental (a) and natural (b) slip zones made of compact calcite nanograin aggregates with a polygonal texture, diagnostic of grainsize sensitive grain boundary sliding (GBS) mechanisms. c) Diagnostic microstructures predicted by superplastic flow accommodated by grainsize sensitive GBS, showing different stages (I–III) of the neighbour switching process (after Ashby and Verrall, 1973).

conditions for the operation of dislocation creep (i.e., high T, small grain size) attained at the transition from Stage II to Stage III in our experiments. Despite microstructural evidence for the simultaneous occurrence and operation of both diffusion- and dislocation-dominated GBS, more microstructural work is needed to quantify their relative contribution to the deformation of nanoscale materials at high strain rates and temperatures. Overall, the distinctive textures observed indicate a switch from low-temperature plasticity and cataclasis (Stages I, II) to GBS mechanisms (Stage III).

Finally, we suggest that the re-strengthening observed during deceleration at the end of the friction experiments (Stage IV, Fig. 1c–d) results from a decrease in the activity of slip zone-localised GBS associated with decreasing temperatures.

6.2. Slip zone strength: can grain size sensitive creep control fault strength during earthquake propagation?

Our experimental results and microstructural observations reveal evidence for the operation of both intracrystalline plasticity and GBS-accommodated flow processes in slip zones deformed at earthquake velocities. The evolution of distinctive micro-textures observed in the slip zone suggests that the transition from low-temperature plasticity and cataclasis ($T \leq 500\,^{\circ}C$ during Stages I and II, Figs. 2–4) to GBS-accommodated flow ($T \geq 800\,^{\circ}C$ during Stage III, Figs. 2, 5, 8) coincides with the onset of the weakening measured in the tested materials at seismic conditions (Figs. 1–2). Verberne et al. (2014) were the first to speculate that GBS-accommodated flow could occur at high strain rates and temperatures during rupture propagation in carbonate rocks. Green et al. (2015) produced further experimental evidence for the occurrence of phase transformation and GBS-accommodated flow in carbonate rocks shearing at seismic slip rates and temperatures, and proposed that these mechanisms could be associated with the onset of dynamic weakening in carbonate rocks. In our experiments, phase transformations, such as decarbonation of calcite, that might lead to weakening are of limited extent. Hence, whilst we agree with the previous hypotheses that GBS-accommodated flow can weaken faults at seismic slip rates (Green et al., 2015; Verberne et al., 2014), we suggest that the onset of the observed weakening does not require thermally-activated phase transitions to occur in carbonate rocks.

We now calculate flow stresses to add new evidence to the hypothesis that GBS-accommodated flow can weaken faults at high strain rates and temperatures, prior to the onset of phase transformations, and thus control earthquake propagation in the shallow crust. We use published constitutive flow laws for both dislocation creep and diffusion-dominated GBS in carbonates at temperatures $\geq 500\,^{\circ}C$ (Ashby and Verrall, 1973; Schmid et al., 1977; Walker et al., 1990), applying a range of strain rates and grain sizes representative of our experimental conditions (Supplementary Information Table 1).

6.2.1. Flow laws and state variables

The predicted flow stress for end-member type deformation mechanisms, dislocation creep and diffusion creep, can be modelled by the constitutive flow law

$$\dot{\gamma} = A^* D^{-b} e^{-\frac{H}{RT}} \tau^n \tag{3}$$

where $\dot{\gamma}$ is the shear strain rate, A^* is a pre-exponential factor, H is the apparent activation energy for creep, R is the gas constant, T is the absolute temperature, τ is the shear stress, n the stress exponent, D is the grain size and b is the grain size exponent. For dislocation creep, b is 0 and $3 < n < 7$, whereas for diffusion creep (which must include GBS) $2 < b < 3$ and $n = 1$. For dislocation-accommodated GBS, b and n lie somewhere between these two end members, so that $1 < n < 3$ values are predicted for grainsize-sensitive creep regimes (Ashby and Verrall, 1973), when the superposition of the two end-member mechanisms accommodates viscous flow (Ashby and Verrall, 1973; Schmidt et al., 1977). In the latter case ($1 < n < 3$), the overall creep rate should be given, to a sufficient approximation, by their relative contribution (Ashby and Verrall, 1973).

The parameters $b = 0$, $n = 4.70$, $A = 0.046$ ($s^{-1}\,bar^{-n}$), $H = 71$ ($kcal\,mol^{-1}$), $R = 1.987 * 10^{-3}$ ($kcal\,K\,mol^{-1}$), and $b = 3$, $n = 1.7$, $A^* = 9.55 * 10^4$ ($s^{-1}\,bar^{-n}$), $H = 51$ ($kcal\,mol^{-1}$), $R = 1.987 * 10^{-3}$ ($kcal\,K\,mol^{-1}$), obtained for deformed calcite aggregates from Schmid et al. (1977), were used to solve Eq. (3) and to calculate the flow stress τ predicted for dislocation creep and grainsize-sensitive GBS-accommodated flow, respectively, when $T = 600$, $1000\,^{\circ}C$ and $\dot{\gamma} = 1\text{–}3 * 10^3\ s^{-1}$ (Fig. 9).

The average shear strain, γ, values have been calculated by $\gamma = \tan\phi = r\theta/2h$, where ϕ is the angular shear, r is the outer diameter of the sample, θ is the angular displacement in radians and h is the average slip zone thickness. Shear strain rate, $\dot{\gamma}$, can then be calculated as the ratio $\dot{\gamma} = \Delta\gamma/\Delta t$, where Δt is the duration of each experiment from the onset of a specific deformation mechanism. An average value, $h = 150$ μm, has been assumed during shear strain calculations, based on optical and scanning electron microscope images, which show the development of a slip zone, due to shear localisation, from the very early stages of deformation when d is only a few mm (Fig. 3a). Strain rate values calculated for each deformation mechanism observed during the different stages of the experiments have been used as reference values during the flow stress calculations (Fig. 9, Table 1). The grain size range $D = 10$–600 nm was used during flow stress calculation of grainsize-sensitive GBS-accommodated flow, based on microstructural observations of the slip zone material produced during Stage II and Stage III deformation (Figs. 4–5).

6.2.2. Flow stress values and interpretation of results

Flow stress calculations, performed using Eq. (3), show that dislocation creep mechanisms operate at higher flow stress values ($\tau > 100$ MPa) than grainsize-sensitive GBS in the range of temperatures ($T = 600$–$1000\,^{\circ}C$) and strain rates ($\dot{\gamma} = 1\text{–}3 * 10^3\ s^{-1}$) considered, when grain size $D < 600$ nm (Fig. 9). For a given temperature, the flow stress increases with strain rate at a steeper gradient during GBS than during dislocation creep (Fig. 9). For a given temperature and a fixed strain rate, the flow stress due to GBS decreases with grain size (Fig. 9). At $T = 600\,^{\circ}C$ and high strain rates ($\dot{\gamma} \geq 1000\ s^{-1}$), the two mechanisms would operate at similar, very high flow stress values ($\tau \approx 3000$ MPa) for a grain size of about 100 nm (Fig. 9a). Under these conditions, the calculated flow stress values are always significantly higher than the values measured during our laboratory experiments (Fig. 9a). At $T = 1000\,^{\circ}C$ and high strain rates ($\dot{\gamma} \geq 1000\ s^{-1}$), grainsize-sensitive GBS flow would operate at much lower flow stress values ($\tau \leq 12$ MPa) than dislocation creep ($\tau \approx 100$ MPa), for grainsize $D \leq 100$ nm (Fig. 9b). Under these conditions, the shear stress values measured during our laboratory experiments are between the calculated flow stress values for grainsize $10 < D < 100$ nm (Fig. 9b).

Our microstructural observations suggest that brittle fracturing and cataclasis are the mechanisms that control shear localisation and grain size reduction in the slip zone at relatively low temperatures ($\leq 100\,^{\circ}C$). Stress levels predicted by Byerlee's sliding friction values (Byerlee, 1978) match those measured during Stage I (Fig. 10). Very little is known about how grain size reduction to submicron levels actually occurs under the conditions attained during our experiments ($T \geq 500\,^{\circ}C$), where samples have been deformed up to Stage II (Green et al., 2015; Verberne et al., 2013, 2014). Here, we propose that, as temperatures rise during Stage II, due to frictional heating ($\geq 500\,^{\circ}C$), dislocation creep

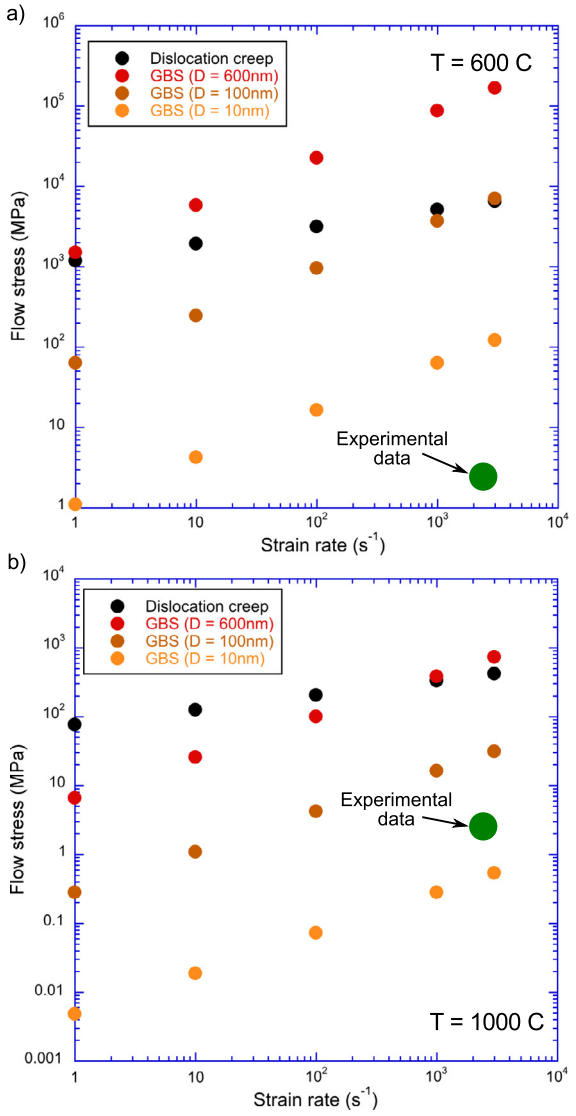

Fig. 9. Measured and predicted flow stresses. a–b) Calculated flow stresses for dislocation creep and grainsize sensitive GBS creep (Eq. (2) in the main text) are plotted vs. strain rates for a range of grain sizes (GBS only) and temperatures, representative of the conditions attained during sample deformation up to Stage II (a) and Stage III (b). The green dots represent the measured shear stress attained in our experiments at steady state during deformation up to Stage III.

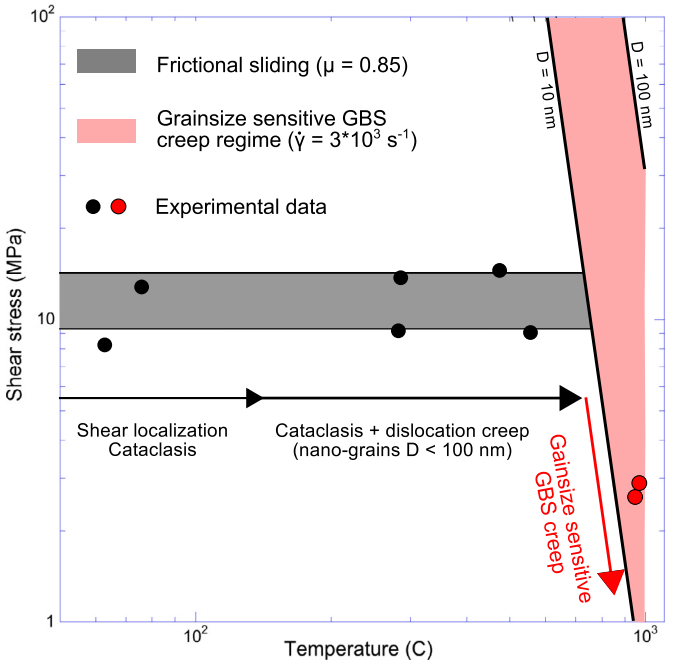

Fig. 10. Fault strength evolution with increasing temperatures at high strain rates. Shear stresses predicted by frictional sliding (Byerlee, 1978) match those measured during laboratory experiments at seismic slip rates during Stages I–II (temperature $\leq$600 °C). Flow stress values predicted by a regime of grainsize-sensitive GBS creep (Eq. (2) constitutive law in the main text) at temperatures $\geq$600 °C, strain rates $= 3 * 10^3$ s^{-1} and grainsize $D < 100$ nm, observed in the slip zone at the onset of weakening, are lower than those predicted by Byerlee's friction, and within the same order of magnitude as the values measured during the experiments during Stage III.

mechanisms start to accommodate intragranular strain and play a key role in producing nanoscale subgrains ($D \leq 100$ nm) in the slip zone (Fig. 4). Note that during Stage II, nanoparticles are present in the slip zone and seismic slip rates have been attained. However, the measured frictional strength of the experimental faults still lies within Byerlee's range of values $\mu = 0.68$–0.80 (Fig. 1, Supplementary Information Table 1). In the absence of microstructural evidence for the operation of pressure solution or diffusion creep (e.g., Verberne et al., 2014), it is suggested that the slip zone bulk strength at this stage is still controlled by cataclastic frictional sliding rather than by dislocation creep or nanopowder lubrication mechanisms. This is in accord with our flow stress calculations, which predict flow stresses for dislocation creep that are up to about 3 orders of magnitude higher than the measured ones at $T = 600$ °C and $\dot{\gamma} \geq 1 * 10^2$ s^{-1} (Figs. 9a, 10). When $T \approx 1000$ °C and $\dot{\gamma} \approx 3 * 10^3$ s^{-1} are attained during Stage III, micro-textures diagnostic of both dislocation creep and grainsize-sensitive GBS are observed, the latter becoming widespread within the slip zone (Fig. 5). Under these temperature and strain rate conditions, the flow stresses predicted for grainsize-sensitive GBS-accommodated flow, for grain size $D < 100$ nm observed in the slip zone at the onset of weakening, are lower than those predicted by Byerlee's friction and, within the same order of magnitude as the values measured during the experiments (Fig. 10).

Our microstructural observations are similar to those of previous studies showing that, under certain conditions, fine-grained geological materials deform by diffusion-accommodated GBS and dislocation-accommodated GBS (Schmid et al., 1977; Walker et al., 1990). This combination of mechanisms appears to be capable of explaining not only the observed relation between strain rate and stress (Schmid et al., 1977; Walker et al., 1990; Hirth and Kohlstedt, 2003; Mecklenburgh et al., 2010; Goldsby and Kohlstedt, 2001), but also most of the microstructural and topological features of materials displaying superplastic behaviour (Ashby and Verrall, 1973; Schmid et al., 1977; Walker et al., 1990; Hirth and Kohlstedt, 2003; Mecklenburgh et al., 2010; Goldsby and Kohlstedt, 2001; Verberne et al., 2014; Green et al., 2015).

We propose therefore that the activation of grainsize-sensitive GBS deformation mechanisms in the nanograin aggregates ($D <$ 100 nm) of the localised slip zone, at high temperatures ($T \approx$ 1000 °C) and strain rates $\dot{\gamma} \geq 1000$ s^{-1}, controls the onset of dynamic weakening of carbonate faults at seismic slip rates (Fig. 10). Note, however, that the cataclasis and intragranular dislocation creep operating during the earlier stages of slip are critical, precursory processes needed to produce the nanoscale grain sizes required to activate grainsize-sensitive creep mechanisms. Finally, the re-strengthening observed during the decelerating phase of deformation can be explained by the falling temperature "switching off" slip zone-localised GBS flow, leading to a return to frictional sliding.

6.2.3. Limitations and approximation of flow stress calculations and interpretations

The calculated flow stress values have been obtained by extrapolating published constitutive flow laws for grainsize-sensitive GBS in carbonates to the conditions attained during our experiments (Fig. 9, Supplementary Information Table 1). The flow stress values obtained for the temperatures, strain rates and grain sizes attained during our experiments, at the onset of weakening, are within about one order of magnitude of those measured during our experiments (Figs. 9–10). The remaining discrepancies are likely due to the approximation of the estimated slip zone parameters (e.g., grain size and SZ thickness), the experimental conditions (γ), and the simplistic extrapolation of existing flow laws to smaller, submicron grain sizes and to strain rates which are a few orders of magnitude higher than those at which they were obtained.

In our study we provide evidence that the onset of weakening during shearing at high velocity coincides with the activation of thermally-induced deformation mechanisms (e.g., grainsize-sensitive GBS) within thin layers of nanograins sandwiched by slip surfaces. To a first approximation, the measured drop in strength is in agreement with our flow stress calculations, suggesting that strain could be accommodated more efficiently by these mechanisms within the weaker thin layers than by frictional sliding along the SS (Fig. 5b–c). A quantitative estimation of the strain partitioning between sliding along the SS and deformation within the thin layers will allow the conceptual model described above to be proven, and provide more constrained strain rate values to be applied in the flow stress calculations. At the present stage, these tasks still present some significant practical challenges in rotary shear apparatus experiments and advanced microstructural studies on the deformed materials.

7. Conclusions

Our observations of experimentally and naturally produced carbonate faults suggest that grainsize-sensitive GBS deformation mechanisms can operate in geological materials deformed at high strain rates along frictionally heated seismogenic slip surfaces at the onset of dynamic weakening after a few centimetres of slip ($d > 10$ cm), before the occurrence of bulk phase transformations. The observed microstructures are similar to those seen at low and high strain rates in carbonates (Verberne et al., 2014; Green et al., 2015), and at high strain rates for a range of nanophase alloys and ceramics in association with superplastic behaviour, where grainsize-sensitive creep regimes develop due to the combined operation of dislocation/diffusion creep. Our findings provide a plausible explanation for both the low flow stresses measured at seismic slip rates in carbonate rocks, and most of the microstructural and topological features of the deformed materials. A regime of frictionally-induced grainsize-sensitive GBS can thus account for the self-lubrication and dynamic weakening of carbonate faults during earthquake propagation in nature.

Acknowledgements

This study was supported by the Natural Environment Research Council (NERC Standard Grant NE/H021744/1 awarded to NDP and REH), and the ERC Starting Grant GLASS No. 259256. L. Bowen (G.J. Russell Microscopy Facility, Durham University, UK) provided invaluable assistance during SEM and TEM analyses. J. Mecklenburgh, L. Hansen and C. Spiers are thanked for providing helpful comments improving the quality of the text and of our interpretations.

Appendix A. Supplementary material

Supplementary material related to this article can be found online at http://dx.doi.org/10.1016/j.epsl.2015.09.002.

References

Ashby, M.F., Verrall, R.A., 1973. Diffusion-accommodated flow and superplasticity. Acta Metall. 21, 149–163.
Ashby, M.F., Verrall, R.A., 1977. Micromechanics of flow and fracture, and their relevance to the rheology of the upper mantle. Philos. Trans. R. Soc. Lond. 288, 59–95.
Boullier, A.M., Gueguen, Y., 1975. Sp-mylonites – origin of some mylonites by superplastic flow. Contrib. Mineral. Petrol. 50, 93–104.
Bullock, R.J., De Paola, N., Holdsworth, R.E., Trabucho-Alexandre, J., 2014. Lithological controls on the deformation mechanisms operating within carbonate-hosted faults during the seismic cycle. J. Struct. Geol. 58, 22–42.
Bullock, R.J., De Paola, N., Holdsworth, R.E., 2015. An experimental investigation into the role of phyllosilicate content on earthquake propagation during seismic slip in carbonate faults. J. Geophys. Res., Solid Earth 120 (5), 3187–3207.
Byerlee, J., 1978. Friction of rocks. Pure Appl. Geophys. 116, 615–626.
Chandra, N., 2002. Constitutive behavior of superplastic materials. Int. J. Non-Linear Mech. 37, 461–484.
Collettini, C., Viti, C., Tesei, T., Mollo, S., 2013. Thermal decomposition along natural faults during earthquakes. Geology 41, 927–930. http://dx.doi.org/10.1130/G34421.1.
Collettini, C., Carpenter, B.M., Viti, C., Cruciani, F., Mollto, S., Tesei, T., Trippetta, F., Valoroso, L., Chiaraluce, L., 2014. Fault structure and slip localization in carbonate bearing normal faults: an example from the Northern Apennines of Italy. J. Struct. Geol. 67, 154–166. http://dx.doi.org/10.1016/j.jsg.2014.07.017.
Covey-Crump, S.J., 1997. The normal grain growth behaviour of nominally pure calcitic aggregates. Contrib. Mineral. Petrol. 129, 239–254.
De Paola, N., 2013. Nano-powder coating can make fault surfaces smooth and shiny: implications for fault mechanics? Geology 41, 719–720.
De Paola, N., Collettini, C., Faulkner, D.R., Trippetta, F., 2008. Fault zone architecture and deformation processes within evaporitic rocks in the upper crust. Tectonics 27. http://dx.doi.org/10.1029/2007TC002230.
De Paola, N., Chiodini, G., Hirose, T., Cardellini, C., Caliro, S., Shimamoto, T., 2011a. The geochemical signature caused by earthquake propagation in carbonate-hosted faults. Earth Planet. Sci. Lett. 310 (3–4), 225–232.
De Paola, N., Hirose, T., Mitchell, T., Di Toro, G., Viti, C., Shimamoto, T., 2011b. Fault lubrication and earthquake propagation in thermally unstable rocks. Geology 39, 35–38.
Di Toro, G., Han, R., Hirose, T., De Paola, N., Nielsen, S., Mizoguchi, K., Ferri, F., Cocco, M., Shimamoto, T., 2011. Fault lubrication during earthquakes. Nature 471, 494.
Fondriest, M., Smith, S.A.F., Candela, T., Nielsen, S.B., Mair, K., Di Toro, G., 2013. Mirror-like faults and power dissipation during earthquakes. Geology 41, 1175–1178.
Goldsby, D.L., Kohlstedt, D.L., 2001. Superplastic deformation of ice: experimental observations. J. Geophys. Res., Solid Earth 106, 11017–11030.
Goldsby, D.L., Tullis, T.E., 2011. Flash heating leads to low frictional strength of crustal rocks at earthquake slip rates. Science 334, 216–218.
Green, H.W., Shi, F., Bozhilov, K., Xia, G., Reches, Z., 2015. Phase transformation and nanometric flow cause extreme weakening during faulting. Nat. Geosci. http://dx.doi.org/10.1038/NGEO2436.
Han, R., Hirose, T., Shimamoto, T., 2010. Strong velocity weakening and powder lubrication of simulated carbonate faults at seismic slip rates. J. Geophys. Res., Solid Earth 115 (B3). http://dx.doi.org/10.1029/2008JB006136.
Hiraga, T., Miyazaki, T., Tasaka, M., Yoshida, H., 2010. Mantle superplasticity and its self-made demise. Nature 468, 1091–1490.
Hirose, T., Shimamoto, T., 2005. Growth of molten zone as a mechanism of slip weakening of simulated faults in gabbro during frictional melting. J. Geophys. Res., Solid Earth 110 (B5). http://dx.doi.org/10.1029/2004JB003207.
Hirth, G., Kohlstedt, D.L., 2003. In: Eiler, J. (Ed.), Inside the Subduction Factory. American Geophysical Union, Washington, DC, pp. 83–105.
Kohlstedt, D.L., Evans, B., Mackwell, S.J., 1995. Strength of the lithosphere – constraints imposed by laboratory experiments. J. Geophys. Res., Solid Earth 100, 17587–17602.
Lankford, J., 1996. High strain rate compression and plastic flow of ceramics. J. Mater. Sci. Lett. 15, 745–750.
Mecklenburgh, J., Heidelbach, F., Mariani, E., Mackwell, S., Seifert, F., 2010. Rheology and microstructure of $(Ca_{0.9},Sr_{0.1})TiO_3$ perovskite deformed in compression and torsion. J. Geophys. Res., Solid Earth 115 (B5). http://dx.doi.org/10.1029/2009JB006520.
Olgaard, D.L., Evans, B., 1986. Effect of second-phase particles on grain growth in calcite. Contrib. Mineral. Petrol. 69, C272–C277.
Passchier, C.W., Trouw, R.A.J., 2005. Micro-Tectonics. Springer, pp. 1–365.
Poirier, J.P., 1985. Creep of Crystals. Cambridge Earth Sciences Series, pp. 1–258.

Reches, Z., Lockner, D.A., 2010. Fault weakening and earthquake instability by powder lubrication. Nature 467, 452–502.
Ree, J.H., Ando, J.I., Han, R., Shimamoto, T., 2014. Coseismic microstructures of experimental fault zones in Carrara marble. J. Struct. Geol. 66, 75–83.
Rice, J.R., 2006. Heating and weakening of faults during earthquake slip. J. Geophys. Res., Solid Earth 111 (B5). http://dx.doi.org/10.1029/2005JB004006.
Rowe, C.D., Fagereng, A., Miller, J.A., Mapani, B., 2012. Signature of coseismic decarbonation in dolomitic fault rocks of the Naukluft Thrust, Namibia. Earth Planet. Sci. Lett. 333, 200–210. http://dx.doi.org/10.1016/j.epsl.2012.04.030.
Rutter, E.H., 1995. Experimental study of the influence of stress, temperature, and strain on the dynamic recrystallization of Carrara marble. J. Geophys. Res., Solid Earth 100, 24651–24663.
Rutter, E.H., 1999. On the relationship between the formation of shear zones and the form of the flow law for rocks undergoing dynamic recrystallization. Tectonophysics 303, 147–158.
Rutter, E.H., Brodie, K.H., 1988. The role of tectonic grain-size reduction in the rheological stratification of the lithosphere. Geol. Rundsch. 77, 295–307.
Rutter, E.H., Casey, M., Burlini, L., 1994. Preferred crystallographic orientation development during the plastic and superplastic flow of calcite rocks. J. Struct. Geol. 16, 1431–1446.
Schmid, S.M., Boland, J.N., Paterson, M.S., 1977. Superplastic flow in finegrained limestone. Tectonophysics 43, 257–291.
Scholz, C.H., 1998. Earthquakes and friction laws. Nature 391, 37–42.
Schubnel, A., Brunet, F., Hilairet, N., Gasc, J., Wang, Y.B., Green, H.W., 2013. Deep-focus earthquake analogs recorded at high pressure and temperature in the laboratory. Science 341, 1377–1380.
Sibson, R.H., 1977. Fault rocks and fault mechanisms. J. Geol. Soc. Lond. 133, 191–213.
Siman-Tov, S., Aharonov, E., Sagy, A., Emmanuel, S., 2013. Nanograins form carbonate fault mirrors. Geology 41, 703–706.
Smith, S.A.F., Billi, A., Di Toro, G., Spiess, R., 2011. Principal slip zones in limestone: microstructural characterization and implications for the seismic cycle (Tre Monti Fault, Central Apennines, Italy). Pure Appl. Geophys. 168, 2365–2393. http://dx.doi.org/10.1007/s00024-011-0267-5.
Smith, S.A.F., Di Toro, G., Kim, S., Ree, J.H., Nielsen, S., Billi, A., Spiess, R., 2013. Coseismic recrystallization during shallow earthquake slip. Geology 41, 63–66.
Smith, S.A.F., Nielsen, S., Di Toro, G., 2015. Strain localization and the onset of dynamic weakening in calcite fault gouge. Earth Planet. Sci. Lett. 413, 25–36.
Tisato, N., Di Toro, G., De Rossi, N., Quaresimin, M., Candela, T., 2012. Experimental investigation of flash weakening in limestone. J. Struct. Geol. 38, 183–199.
Valoroso, L., Chiaraluce, L., Collettini, C., 2014. Earthquakes and fault zone structure. Geology 42, 343–346.
Verberne, B.A., De Bresser, J.H.P., Niemeijer, A.R., Spiers, C.J., De Winter, D.A.M., Plumper, O., 2013. Nanocrystalline slip zones in calcite fault gouge show intense crystallographic preferred orientation: crystal plasticity at sub-seismic slip rates at 18–150 °C. Geology 41, 863–866.
Verberne, B.A., Plümper, O., Matthijs de Winter, D.A., Spiers, C.J., 2014. Superplastic nanofibrous slip zones control seismogenic fault friction. Science 346 (6215).
Walker, A.N., Rutter, E.H., Brodie, K.H., 1990. Experimental-study of grain-size sensitive flow of synthetic, hot-pressed calcite rocks. In: Deformation Mechanisms, Rheology and Tectonics, vol. 54, pp. 259–284.